# New methodologies for the NMR study of calcium phosphate biomaterials and bone mineral

Adam Nelson

SORBONNE UNIVERSITÉ

**ÉCOLE DOCTORALE 397 Physique et Chimie des Matériaux**
**Laboratoire de Chimie de la Matière Condensée de Paris (LCMCP)**

# New methodologies for the NMR study of calcium phosphate biomaterials and bone mineral

Thèse de doctorat présentée par :

**Adam Nelson**

pour obtenir le grade de
Docteur de Sorbonne Université
Discipline : Chimie des matériaux

Présentée et soutenue le 8 octobre 2024 devant un jury composé de :

| | | |
|---|---|---|
| M. Franck FAYON | Directeur de recherche CNRS, CEMHTI Orléans | Rapporteur |
| M. Jérôme CUNY | Maitre de conférence, Université Paul Sabatier | Rapporteur |
| Mme Melinda DUER | Professor, University of Cambridge | Examinatrice |
| M. Thibault CHARPENTIER | Directeur de recherche CEA, Saclay | Examinateur |
| Mme Christel GERVAIS | Professeur, Sorbonne Université, LCMCP | Directrice de thèse |
| Mme Danielle LAURENCIN | Directrice de recherche CNRS, ICGM | Co-directrice |
| M. Gaël DE PAEPE | Directeur de recherche CEA, Grenoble | Invité |

*Es muss sein!*

## Acknowledgements

I would first like to thank the members of the jury and referees who agreed to review this work. I can only hope that this work will interest and intrigue them.

I am indebted to my two thesis supervisors, Danielle and Christel, for having offered an entry door into this field and supporting me at every step of this project.

I would also like to express my gratitude for the members of the ANR TOGETHER that have contributed to this project. Thank you Wassilios Papawassiliou, Paul Subhradip, Isabelle Gennero, Sara Laurencin-Dalicieux, Gaël De Paëpe, Sabine Hediger, Christian Bonhomme, Hugo Petitjean.

I would like to extend this thanks to the numerous researchers, engineers and technicians that have been generous with their time, knowledge and patience. A special thanks goes to the team of NHMFL Ivan Hung, Zhehong Gan, Amrit Venkatesh, and to the NMR engineers who have spent days and nights fighting against broken hardware, buggy software and many, many user errors. Thank you, Guillaume Laurent, Philippe Gaveau, David Gajean, Dinu Iuga, Trent Franks, Cristina Coelho and Nicolas Birlirakis. Thanks to Benoit Baptiste for the low-temperature XRD measurements.

Thanks also goes to the directors and members of the LCMCP, ICGM and CEA labs for the hospitality, productive discussions, support and help that they extended at every turn. Special thanks to Cesar Leroy for his NMR insights and sequences, Sebastien Mittelette for his work on enrichment protocols and Rishit Yadav for shared time and struggles at the spectrometer and in the lab.

Great thanks to the ANR for funding that made this research possible. The thanks also extend to the INFRANALYTICS and Panacea networks, for hosting us and making large instruments available to all.

I would also like to thank my friends, family and loved ones for believing in my success stronger than I ever did. Very, very special thanks to Lili.

## Glossary

Biominerals and bones

| Initialism | Meaning |
|---|---|
| ACP | Amorphous calcium phosphate |
| DCPA | Dicalcium phosphate anhydrous (Monetite) |
| DCPD | Dicalcium phosphate dihydrate (Brushite) |
| HAp | Hydroxyapatite |
| LPA | Lysophosphatidic acid |
| $LPA(R)_1$ | Lysophosphatidic acid receptor 1 |
| MCPM | Monocalcium phosphate monohydrate |
| OCP | Octacalcium phosphate (pentahydrate) |
| TCP | Tricalcium phosphate |

NMR sequences

| Initialism | Meaning |
|---|---|
| BD | Bloch Decay |
| CPMAS | Cross Polarization Magic Angle Spinning |
| CW | Continuous Wave |
| DEPTH | Distortionless Enhancement by Polarization Transfer |
| DFS | Double Frequency Sweep |
| D-HMQC | Dipolar Heteronuclear Multiple-Quantum Correlation |
| DQ-SQ | Double Quantum – Single Quantum |
| D-RINEPT | Dipolar-mediated Refocused Insensitive Nuclei Enhancement by Polarization Transfer |
| FSLG | Frequency-Switched Lee-Goldburg |
| HETCOR | HETeronuclear CORrelation |
| MAS | Magic Angle Spinning |
| SPINAL-64 | Small Phase INcremental ALternation with 64 phases |
| TPPM | Two Pulses Phase Modulation |
| WURST | Wideband, Uniform Rate, Smooth Truncation |

## General introduction

The ingeniousness with which living beings turn inorganic and organic precursors into new functional materials is a source of constant interest for material scientists. From a limited selection of starting materials, organisms have developed an ability to build a wide range of materials, from thin porous membranes to tough woods. Through natural selection, these materials have become exceptionally well suited to fulfilling the roles for which they are specialized. One among many is bone, the scaffold of most land vertebrates.

Bone is a complex material with a unique composition that incorporates a large portion of inorganic material in its structure. It can be described as a hybrid inorganic-organic composite, mainly composed of calcium phosphate minerals, collagen and water, with the mineral phase comprising two thirds of the dry weight of human bone. On a nanometric scale, it is composed of nanocrystals of an apatite-like mineral, interwoven with strands of type I collagen. The study of those nanocrystals is of paramount importance to understand the properties and also the possible defects of bone mineral. Developing new methodologies for the solid-state NMR investigation of this mineral phase will be the central focus of this thesis.

This study was financed by the ANR project TOGETHER (The Observation of low Gyromagnetic ratio nuclei in biomaterial Environments Through Hyperpolarization Enhanced magnetic Resonance) regrouping labs from ICGM (CNRS Montpellier), INSERM (Toulouse research units), Sorbonne Université (Paris) and IRIG/CEA (Grenoble). The ultimate objective is an in-depth study by $^{43}$Ca DNP-NMR of bones of normal and genetically engineered mice, in view of expanding our understanding of bone pathologies. For this purpose, synthetic bone-related biominerals (hydroxyapatites HAp, and octacalcium phosphate OCP) were used for methodological NMR developments. The investigation was then extended to biological samples.

This manuscript is split into four chapters.

Firstly, a rapid overview on bone, and prior studies of biominerals and bone mineral is presented. This will give a general introduction to the structure of bone and its importance in health. We then describe $LPA_1$ deficiency, a model mutation that we will study later in this manuscript. This is followed by a presentation of bone mineral, with an in-depth look at the information provided by solid state NMR. Lastly, the NMR sequences and computational methods used throughout this study are detailed.

A second part corresponds to a study published in *Faraday Discussions*, in which the effect of low-temperatures on the structure of OCP is discussed. For this, a combination of isotopic enrichment, multiple-magnetic field multinuclear ssNMR analyses (at room temperature and down to 100 K), DNP-enhanced NMR, molecular dynamics simulations, and GIPAW calculations of NMR parameters are used. The study provides new evidence of water mobility in OCP, which can explain a number of NMR observations. A tentative assignment of the low-temperature structure using NMR crystallography methods is then provided.

A third part is dedicated to a comparative NMR investigation of the composition of mice bone mineral, comparing mutant $LPA_1$ receptor deficient to wild type non deficient specimens. For

this purpose, new methods for the analysis of the 2D signals of variable-$t_{cp}$ $^{1}H$-$^{31}P$ CP-HETCOR spectra are explored, demonstrating the utility of homemade solutions for the processing of large numbers of spectra. Thanks to this, it is shown that evolutions in NMR parameters at different contact times are a telling sign of the presence of a collection of environments in bone mineral with close NMR characteristics.

Finally, we investigate synthetic apatites and bone mineral *via* DNP-enhanced $^{43}Ca$ NMR. The chapter provides a description of the experimental challenges and successive improvements which led to the first DNP-enhanced $^{1}H$-$^{43}Ca$ CP MAS NMR experiments on bone samples.

NMR acquisition, parameters and signal fitting

| Initialism | Meaning |
|---|---|
| ADC | Analog to Digital Converter |
| ASR | Absolute Sensitivity Ratio |
| $C_Q$ | Quadrupolar coupling constant |
| CSA | Chemical Shift Anisotropy |
| FHWM | Full Width at Half Maximum |
| I and S | Abundant and rare spins (in CP NMR) |
| lb | Line broadening |
| $\nu_r$ | Rotation frequency |
| ns | Number of scans |
| NUS | Non-Uniform Sampling |
| $R^2$ | Coefficient of determination |
| RD | Relaxation delay |
| SI | Size of real spectrum |
| si/no | Signal to Noise ratio |
| $T_1$ | Longitudinal relaxation time |
| $T_{1\rho}$ | Spin lattice relaxation time constant |
| $T_{amb}$ | Ambient temperature |
| $T_{CP}$ | CP rate constant |
| $t_{CP}$ | Contact time |
| TD | Time Domain |
| $t_{exp}$ | Experimental time |
| US | Uniform Sampling |
| $\delta_{iso}$ | Isotropic chemical shift |
| $\eta_Q$ | Quadrupolar asymmetry parameter |

# CHAPTER I

## Bibliography

## Summary

# I. Introduction to bone structure and health

## I.1. Presentation of bone

Bone is the scaffolding material of many vertebrates. It is one of four hard (mineralized) tissues in the human body, with the others being enamel, dentin and cementum. All except bone are located solely within the teeth. All of these "hard tissues" are distinguished by their composite nature, as their hardness and flexibility come from the interweaving of a mineral phase and a collagen matrix. This gives them a number of desirable properties: them rigid and tough while retaining some flexibility. Bone stands out among those, as, unlike other hard tissues, it can easily repair itself through a constant cycle of biomineralization and resorption.

These properties have made it the dominant structuring material for vertebrates, although it is not the only one. Cartilage is an important part of our skeletal structure, and fills the role of bone among Chondrichthyes (also called cartilaginous fish, which includes shark and rays). How mineralized tissue evolved in vertebrates seems to still be a matter of debate,[1,2]although we know that cartilaginous skulls and teeth predate the apparition of mineralized tissue.[3] From the late Cambrian (500 Ma) onwards, new species show mineralized teeth and jaws.[4] Bony fish (Osteichthyes) then diverged from cartilaginous fish to form their own clade, which became dominant and led to the bony vertebrates we know (and belong to). Bone therefore appeared early in the evolutionary process of vertebrates, and is most likely the result of mineralization appearing within cartilage.

Bone, as we know it, is mostly composed of mineral, collagen matrix, and water. Human bone is, by weight, ca. 67% mineral and 33% organic.[5] The organic part of bone includes small proportion (ca. 10% w/w) of non-collagenous organic compounds (e.g. citrate, proteins, and lipids). Cartilage, in comparison, is composed of a collagen and proteoglycan matrix with a large proportion of water[6] (up to 80% by weight!), and is completely devoid of blood vessels and nerves. This comparison of cartilage and bone serves to highlight the numerous features that distinguish bone from other structural tissues: it repairs and reforms constantly, meaning it can heal up to full strength in case of a break. Damaged cartilage, in comparison, is slow to heal and can only recover from superficial damage. However, cartilage is a much more elastic material, whereas bone is flexible but stiff, making it prone to breaking rather than tearing. Bone is also a porous material, which contains not only vascularity and nerves but also bone marrow, which produces blood cells in most vertebrates (notably, the blood cells of cartilaginous fish are produced in the spleen[7]). Lastly, bone is the body's largest reservoir of calcium and phosphate ions. Precise control of calcium levels is required for cellular activity, whereas phosphates regulate the pH of the bloodstream. Bone is therefore both a structural element and an organ, which grows, evolves and ages along with the rest of the body.

To understand this complex organ in more detail, we must take a closer look at how it is structured.

## I.2. Structure of bone

There are 213 bones in the human body.[8] They serve a variety of roles, most being structural, but also serving as protective shells, hinges, levers and acoustic conductors. On a macroscopic level, bone is separated into two parts, an outer shell of cortical bone and a core made of trabecular bone. Cortical bone is dense and tough, giving bone most of its mechanical strength. Trabecular bone is spongy and light. Their relative proportion depends on the bone and its role within the human body. Vertebra are 25% cortical and 75% trabecular bone by volume[8] whereas the average human bone is 80%/20% cortical/trabecular and structural bones can reach up to 95% cortical bone. The entire bone is wrapped in a thin (2-3 mm[9]) tissue layer called the periosteum. It is composed mostly of collagen and contains many of the blood vessels and nerves of the bone. It also contains a number of osteoblasts and fibroblasts, allowing it to repair the surface of bone at an elevated rate. This is the layer responsible for radial bone growth.

We will continue our description of bone looking only at the typical structures found in mature, compact, cortical bone. Describing the microstructure of every type of bone that exists within the human body is a lengthy endeavor, beyond the scope of this work. It should be noted that we describe a mature bone: growing bone, trabecular bone, bone undergoing repair and other types of bone come in a variety of differently ordered or disordered states.[10]

Delving deeper into the structure of bone shows that it is composed of channels called osteons or Haversian systems (Figure 1). The channel is made of a central canal surrounded by a layer of dense bone tissue. The Haversian canals are formed by blood vessels, along which bone remodels and matures in a concentric pattern. These canals form a branching network which is predominantly oriented along the principal axis of the bone. The bone tissue surrounding a mature canal is composed of successive layers of lamellae. The lamellae are 3-7 µm thick, and a mature osteon will be surrounded by 4-8 layers of lamellae.[11]

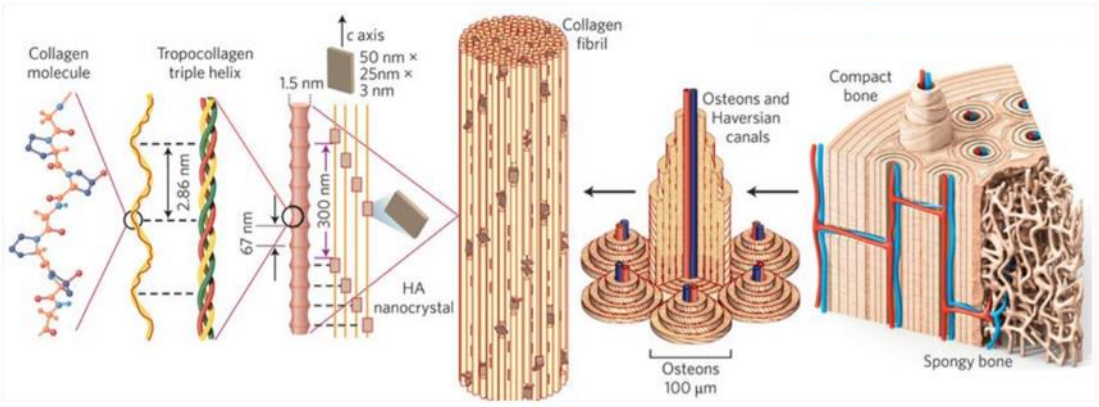


*Figure 1: Hierarchical structure of bone, reproduced from Liu* et al.[12]

The lamellae are a highly isotropic layer made of unidirectionally aligned bundles of mineralized collagen fibrils. The orientation of this tissue varies in successive layers. This means that the lamellae form a structure reminiscent of plywood,[10] where layers of opposing orientation are assembled together to strengthen the overall structure. The space between these lamellae is filled by disordered collagen fibrils, binding the layers together.

Looking closer at the isotropic tissue making up the lamella, we find fibrils arranged in bundles, 1-3 µm in diameter. These bundles run parallel to one another, and are separated by thin layers of disordered fibrils. The bundles are assembled from dozens of collagen fibrils that run along the length of the bundle. These fibrils, 80-100 nm in diameter and up to millimeters in length, are woven from strands (or nanofibrils) of highly mineralized type-I collagen in its typical triple-helix configuration, about 1.5 nm wide and 300 nm long. Embedded around the nanofibrils are nanometric crystals of bone mineral, made of a highly-substituted, apatitic calcium phosphate. The exact morphology of the mineral has been the subject of intense debate, but recent studies[13] have proven that the "platelets" of bone mineral, about 5 nm x 25 nm x 100 nm in size, are assembled from thin, acicular crystals, no wider than 5 nm in width. Thereby, we come to the smallest structuring units of bone, the collagen nanofibril and the needle-shaped nanocrystal. The study of these fundamental elements of bone are necessary to understand the formation, growth, makeup and possible defects of bone.

Bone defects can have severe consequences on living organisms. The next section will detail the importance of bone in human health and the prevalence of bone disease.

### I.3. Bone and health

Bone remodels itself constantly. This exceptional organ, which may seem inactive and stable on the surface, is on the contrary subject to a continuous cycle of formation and destruction.[14] Due to its structure, the mineral of bone has a vast surface area that is in equilibrium with extracellular fluids. These fluids contain calcium and phosphate ions that can precipitate under the action of osteoblasts, specialized cells that fix mineral ions to the bone. Osteoclasts have the opposite function, taking care of the resorption of bone. The balance between these two mechanisms is key to regulating the quantity of mineral present in bone, and therefore in maintaining its strength.

By far the most common bone diseases come from disruptions in this equilibrium. These conditions, referred to as "metabolic bone disease", may have very different causes but have similar impacts on the health of the individual. Indeed, the prevalence and causes of metabolic bone disease have changed drastically over the past two centuries. The industrial revolution saw a drastic increase in a condition commonly known as "rickets", which was characterized by brittle and soft bones. Rickets is usually caused by a vitamin-D deficiency, which causes osteoclasts to release calcium from the body at an elevated rate. This was coupled to widespread calcium deficiencies due to malnourishment. It is estimated that 50-80%[15] of children in early industrial Europe suffered from Rickets. This disease was nearly eradicated in the 1930s[16] by fortification with vitamin-D of common foodstuffs like margarine and milk. However, metabolic bone disease has not subsided, and is facing a resurgence as an aging population is now facing increasing rates of osteoporosis. Osteoporosis is a type of metabolic bone disease, characterized by decreasing bone strength with age due to lower mineralization. The causes of osteoporosis are multifactorial, with old age and gender being the most important predictors (osteoporosis is twice as common in women).[17] Other major risk factors include calcium and vitamin-D deficiency, genetic factors, low physical activity and hormonal imbalances, among many. The impact on public health is severe, as a large portion of the population will experience an osteoporosis-induced fracture in their lifetime (13% of

men and 40% of women is US cohorts[18]), leading to a serious reduction in quality of life and life expectancy, as well as an increased risk for a second fracture. With an aging and increasingly sedentary population, bone disease is therefore surging once again, and will become epidemic if the risk factors are not mitigated as populations around the world get older.

Other types of metabolic bone disease are endemic in the population, like Paget's disease, with an estimated prevalence of 2-5% in western cohorts.[19] An increased activity of the osteoclasts lead to bones becoming progressively weaker and more disordered over time. It may be caused by genetic factors or by prior infections[20], but, like most metabolic bone disease, can be managed if diagnosed early enough. Treatments like bisphosphonates[19] are effective at slowing down osteoblastic activity, leading to increased bone density and reduced risk of fractures.

Other non-metabolic bone diseases also exist. They are typically caused by imperfect formation of type-I collagen, leading to a significant weakening of the organic fraction of bone. One of such disease, Osteogenesis imperfecta, leads to an extreme weakness of the bones from birth. This disease is rare (one in 15000-20000),[21] and is caused by a variety of mutations to genes controlling the formation of collagen. Like other collagen malformations, it affects a large portion of the body, leading to joint, dental, circulatory and hearing issues, among others.

We can therefore categorize bone disease in two classes depending whether they affect the mineral of bone or the collagen matrix surrounding it. Diseases relating to bone mineral are usually metabolic in nature. They can (and often do) manifest later in life and have a myriad of possible causes, including environmental ones. On the other hand, diseases affecting the collagen strands are usually genetic in origin, affect the body at large and weaken bone significantly.

It is useful to note that not all discussions of bone health can be approached so directly (in terms of metabolic or non metabolic disease), especially in cases where a clear causality between a specific condition and a weakened bone structure in unclear. We can give the example of Type II diabetes (T2D): unlike Type I diabetes which leads to lowered bone density[22] and therefore weakens the bone, T2D has no negative impact on bone density,[23] yet still leads to an increased risk of fracture. The mechanism for this has not been uncovered, and many hypotheses have been put forward to explain this correlation. It has been proposed that diabetes can cause falls simply due to comas or the higher average BMI (Body Mass Index) of patients. On the other hand, micro-indentation studies have shown that T2D bone has a significantly lower hardness than control bone with a similar density. It was also discovered that the biochemical markers linked to bone turnover were lower in T2D patients,[24] meaning that both osteoclasts and osteoblasts had a slower activity. Last but not least, it was also shown that the accumulation of advanced glycation end-products (AGEs), byproducts of the Maillard reaction that can accumulate in diabetic patients, causes brittleness of the bones.[25–28]

This illustrates that the issue of "bone quality" can be separate, and often more elusive, than simple issues of bone mineralization. Therefore, measurements of bone mineralization that are common and non-invasive, cannot give a full picture of bone health, since they do not account for the quality of the bone on a nanostructural level. It is also difficult with current imaging and analytical techniques to understand the link between a pathology and a decrease in bone quality, as the changes to the composition of bone are often not apparent from medical imaging. We will continue our discussion by covering one such case from the literature: $LPA_1$ deficiency. This mutation is the subject of our study of bone mineral composition *via* solid-state NMR (Chapter III).

### I.4. Bone and health: the case of LPA1 deficiency

Lysophosphatidic acid (LPA, Figure 2) is a small bioactive phospholipid with a variety of biological functions. It is produced in majority during the synthesis of cell membranes.[29] It is present in a number of biological media, including blood, plasma, brain and fluid.[30] There are nine receptors that can react to LPA, six of them being G protein-coupled receptors (or GPCRs, a type of receptor that can initiate responses inside of the cells to receptors outside of it). The six GPCRs in question are named sequentially $LPAR_1$ to $LPAR_6$ (often simply $LPA_1$ to $LPA_6$). These are targeted in a wide array of studies due to the suspected role of LPA signaling in a number of common afflictions, including cancer, neurodegenerative diseases and neuropathic pain.[29]

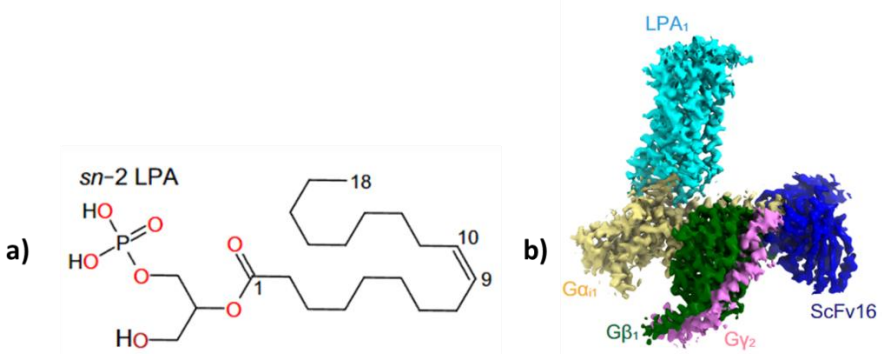


Figure 2*: a) Lysophosphatidic acid (LPA). b) Structure of the $LPA_1$ – G-protein complex. Reproduced from Akasaka* et al.[31]

The number of systems in the human body relying on LPA signaling are too many to enumerate. During development, LPA plays a crucial role in the formation of the nervous, circulatory, reproductive and immune system, and most crucially in the context of our study, the osteoblasts and osteoclasts.[32] Of the nine receptors yet known, the first of them, namely $LPA_1$, was originally identified in 1992:[33] it was found to be expressed all throughout the human body, but predominantly in neuronal cells. Since then, the role of $LPA_1$ in various biological processes has been a source of constant study. We now know that $LPA_1$ signaling has roles in cellular proliferation, inhibition of adenylyl cyclase (an enzyme that regulates ATP consumption) and $Ca^{2+}$ mobilization, among others.

The role of $LPA_1$ signaling in the development of the skeleton has been regularly studied from the early 2000s onwards. It was shown in 2000 that $LPA_1$ deficient mice had significant craniofacial deformations and were noticeably smaller than their wild-type congeners.[34] The authors hypothesized that this was caused by lowered milk uptake of the mice pups, possibly from defective olfaction. However, later evidence would open the possibility that the $LPA_1$ receptor has a direct influence on bone growth. First, a direct link between the LPA signaling molecule and osteoblast formation was discovered.[35] Then, in 2010, Liu *et al.* evidenced a direct correlation between $LPA_1$ activity and the differentiation of osteoblasts *in-vitro*.[36] However, whereas the role of $LPA_4$ in bone formation was clearly established (it inhibits the differentiation of stem cells into osteoblasts), the mechanism linking $LPA_1$ to increased osteoblast count was unclear.

In 2011, a study (by our collaborators in the ANR project, I. Gennero, S. Laurencin-Dalacieux *et al.*)[37] confirmed that $LPA_1$ deficient mice have significantly altered bone structures compared to wild-type. This was especially obvious from the structure of the ribcage, where ribs were abnormally attached and fused (Figure 3).

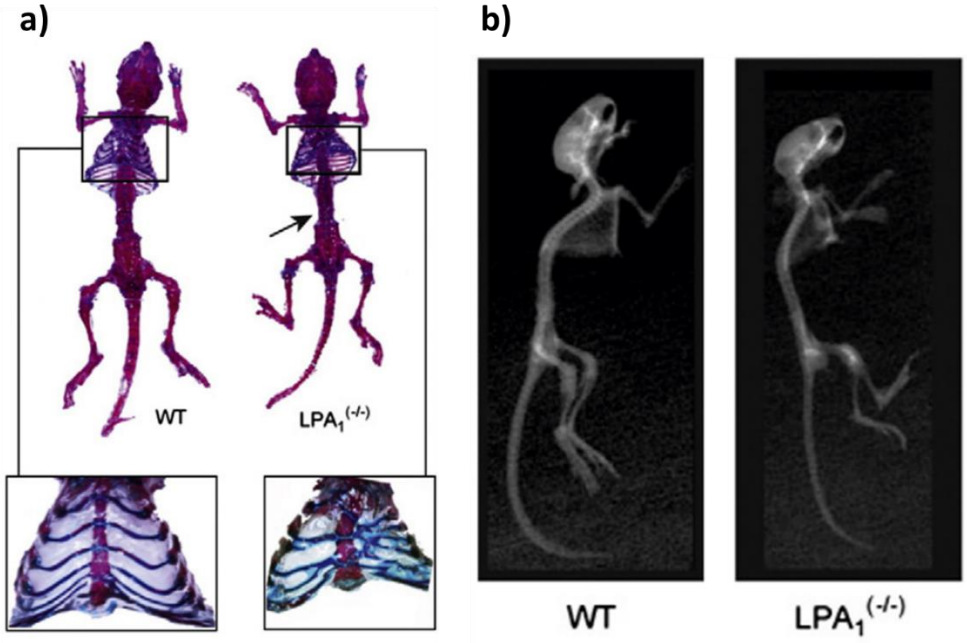


*Figure 3: Phenotype of 4 week-old WT and $LPA_1^{-/-}$ mice. a) histological analysis of the skeleton of young mice, stained with alizarin red (calcium) and alcian blue (cartilage and collagen). b) X-ray imaging of the two phenotypes, highlighting the lower overall length of the specimen. Reproduced from Gennero* et al.[37]

Similarly to what was previously discussed in the case of T2D and bone, the abnormally shaped and extremely weak bones had no statistically significant decrease in bone mineral quantity in comparison to collagen content. It was therefore concluded that $LPA_1$ deficiency was not a case of osteomalacia which would lead to undermineralized tissue, but rather an osteoporosis characterized by entirely missing bone tissue. It is therefore of interest to us to try to better understand this decrease in bone quantity, and whether the mineral composition and/or structure is significantly affected by the mutation.

Before we introduce solid-state NMR (ssNMR) as a technique for the analysis of bone mineral, we must introduce the main characteristics of its composition. We will therefore detail the techniques used for the analysis of bone mineral and our current knowledge about its structure and content.

# II. Short history and description of bone mineral

## II.1. Early observations

Before we give a description of bone mineral, we shall give a short retrospective look at the observations on which they were built. As the story of the study of bone long and rich in experimental observations, we will limit this section to descriptions of the different groundbreaking observations that shaped our actual understanding of bone mineral. In conclusion, a summary of the information about bone mineral gathered from non-NMR based analysis will be presented.

The study of bone is as old as the scientific method itself. As the material is widely available and of great interest to the field of medicine, bone was among the very first to be studied using scientific apparati. Antonie van Leeuwenhoek, often referred to as the "Father of Microbiology", reported to the Royal Society of London In 1674 that he observed in calf bone "*several small bones, passing from without inwards;"* and then hypothesized*, "that this Bone had divers small pipes going longways: But I have since observed the Tooth of a Cow, and found it made up of transparent Globuls, which I can see very perfectly*".[38] A modern reader can recognize this as a description of the Haversian canal of bone, and possibly the first observation of the microscopic structure of bone on record. As the microscope travelled over Europe and improved throughout the late 18th, the possibility of studying bone *via* microscopy led to better and more detailed observations. Most notably, Clapton Havers wrote a treaty on bone[39] in 1691, describing in detail the various aspects of bone he could observe with his (already much improved) microscope: this included descriptions of the *Laminae* (or lamella), the *Cancelli* (canals), cortical and trabecular bone. It also described teeth as mineral in nature, and observed that they are, unlike other stones, soluble in sulfuric acid (and recommended the reader to avoid using it as a whitener).

The mineral aspect of bone is therefore not a recent discovery. It was known by the earliest sources that bony tissue, unlike the rest of the body, leaves behind bone ash when burnt ("*I will not turn away the punishment thereof, because he burned the bones of the King of Edom into lime*", Book of Amos, 2:1, King James Bible, 1611. Note that the original word used for "lime", שִׂיד, can also be translated to plaster or gypsum, showing the strong association between bone ash and other calcareous minerals since early history). However, it would take until the end of the 18th century for bone mineral to be recognized as a calcium orthophosphate,[40] thanks to the pioneering work of Johan Gahn in 1769, who proved that orthophosphoric acid could be obtained from the dissolution bone mineral (published by Scheele in 1771).[41]

The end of the 18th and beginning of the 19th century would not only see extensive work on the chemical composition of bone and teeth, but also the successive discovery of most of the

calcium orthophosphates[40] (Dicalcium phosphate dihydrate DCPD, its anhydrous form DCPA, apatite HAp, monocalcium phosphate monohydrate MCPM, tricalcium phosphate TCP, etc.). We note that the composition of the orthophosphate ion was still a matter of debate at the time (often written either $PO_5$ or simply Ꝑ). This did not stop enterprising biochemists from making careful and exact accounts of the chemical makeup of bone. A growing field was the chemical analysis of bone ash for medical and archeological studies. A notable of example of this comes from an 1844 publication by Ernst von Bibra.[42] In an effort to understand the origin of bone calcification, he had rigorously dosed the combustion products of bone and teeth, in a wide variety of animals, humans, at different ages, with or without bone disease. We can see here (possibly) the first attempt at comparing diseased bone to healthy bone *via* the analysis of its chemical composition (Figure 4). These analyses were limited by the lack of spectroscopic tools, but the gravimetric analysis of the combustion products of bone still gave an accurate dosage of the organic and inorganic components of bone. From this analysis as well as others, it therefore became known that bone is an organic-inorganic aggregate corresponding to a calcified organic scaffold.

Die Analyse der beiden Femura ergab:

| | FEMUR *des atrophischen Fusess.* | FEMUR *des gesunden Fusses.* |
|---|---|---|
| Phosphorsaure Kalkerde . | 59.21 | 59.22 |
| Kohlensaure Kalkerde . . | 12.99 | 13.89 |
| Phosphorsaure Talkerde . | 1.30 | 1.43 |
| Salze . . . . . | 0.72 | 0.72 |
| Knorpelsubstanz . . . . | 24.37 | 23.22 |
| Fett . . . . . | 1.41 | 1.52 |
| | 100.00 | 100.00 |
| Organische Substanz . . | 24.74 | 25.78 |
| Anorganische Substanz . | 75.26 | 74.22 |
| | 100.00 | 100.00 |

*Figure 4: Elemental analysis of bone mineral via combustion, from Ernst von Bibra.[42] Here, a rabbit foot bone with restricted blood supply (first column) is compared to a healthy bone (second column), showing similar degrees of mineralization in both samples.*

Concerning the elemental composition of bone mineral, the 19th century was rich in debate and disagreement, made more obscure by the varying descriptions of the stoichiometry of common calcium phosphates. We will skip ahead in time to the direct experimental confirmation of the presence of apatite in bone: in 1926, an early X-Ray setup allowed De Jong to record the first known diffraction patterns of bone mineral.[43] This signaled the emergence of XRD (X-Ray Diffraction) as a technique capable of characterizing bone mineral.

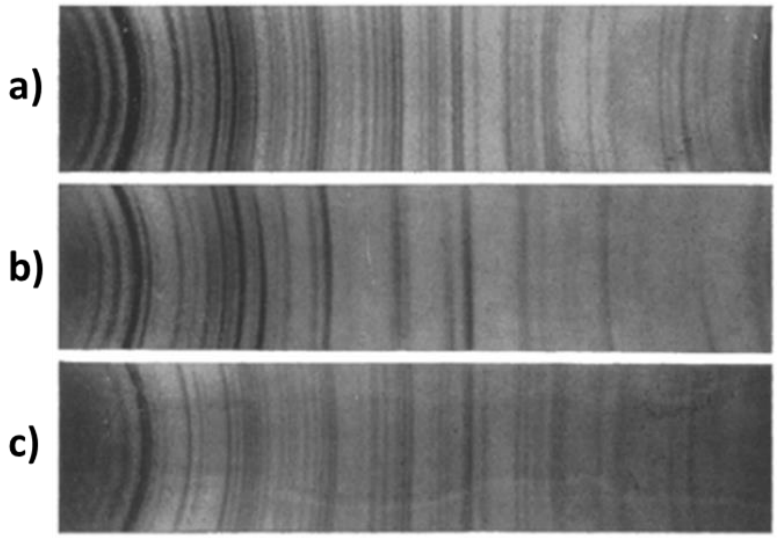


*Figure 5: Early X-ray diffraction patterns of a) hydroxyapatite, b) enamel and c) dentin by Möller* et al.*[44]*

The technique would quickly become ubiquitous to analyze biominerals: in 1933, Möller and Trömel measured the size of the crystallites in teeth using XRD diffraction patterns (Figure 5), estimating them to be micrometric[44] in size, and later proving them to be aligned into a unified axis.[45] Here, we see the important role that X-ray diffraction had in understanding the scale and arrangement of tissue mineralization. Contemporary estimates would revise down the size of biological mineral to place it in the nanometric range.[40]

This, however, did not solve the issue of bone mineral composition. As reported by Schmidt and Greenberg in 1935:[46] "*The further general conclusion that has been drawn from the X-ray work is that bone salt belongs to the apatite series of mineral. Beyond this there is no general agreement.*" Despite the widespread disagreement, some had nearly matched the modern formula for carbonated apatite. As an example, Hendricks *et al.*[47] concluded in 1932: "*The results of numerous biological experiments indicate that the organic compound of bone proximates the composition* $Ca_{10}CO_3(PO_4)_6.xH_2O$*, and that it forms solid solutions with hydroxy apatite.*" This conclusion was the synthesis of old data on the elemental analysis of bone ash and new XRD data on the crystallographic space group of bone mineral.

### II.2. Structural models of bone and apatite

1930 and 1932 saw the first two reportings of the apatite structure by Náray-Szabó and Mehmel,[48,49] and was a breakthrough for the study of bone mineral. They elucidated the position of the atoms within the fluoroapatite cell, giving rise to the first atomic model of the apatite mineral (Figure 6). This aroused great interest from other crystallographers who finally had the tools to understand the various substitutions of the structure. Yet there still existed a discrepancy between the composition of the crystal cell and that of bone mineral, often theorized to be a separate carbonated phase. In 1938, McConnell published a thorough review of contemporary evidence,[50] in which he hypothesized possible substitutions of the structure. It reviewed the plausibility of carbonate substitutions in place of the fluoride ($F^-$) of fluoroapatite (now known as A-type substitution), calcium (now excluded as a mechanism)

and phosphates (B-type substitution). The author, however, dismissed the possibility of A-type substitution despite experimental evidence, due to the fact that the carbonates were considered much too large to fit in place of the fluoride (along with other evidence that showed these substituted apatites did not follow the established stoichiometry). At the time, the author also concluded that B-type substitution is unlikely in isolation, as the charge difference would severely destabilize the structure.

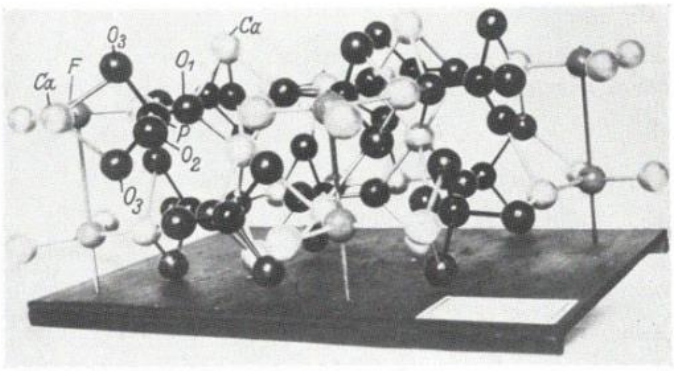


a

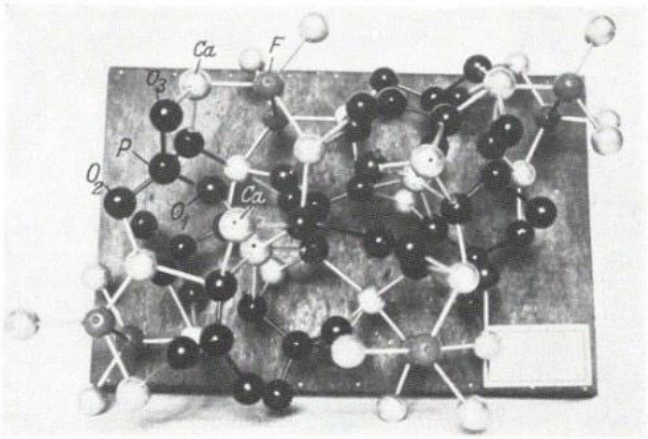


b

Fig. 6. Photographie des Modells der Apatitstruktur[1]).
a) Blickrichtung ungefähr auf die Fläche (1 0 $\bar{1}$ 0).
b) Blickrichtung ungefähr in Richtung der c-Achse.

*Figure 6: Atomic structure of the apatite cell, as published by Mehmel* et al. *in 1932.*[48]

The considerable range of possible substitutions in apatite means that even by knowing the elemental composition of an apatite, we do not have full knowledge of how it is substituted. Up to the 1950s, there was still disagreement as to whether bone apatite had carbonate substitutions, or whether the carbonates represented a separate phase. In fact, while it was widely believed that carbon could be substituted into apatite, it was not well understood whether this was under the form of carbonate ions or carbon dioxide. In 1952, McConnell would weigh again in the debate by showing that mineral apatites could, indeed, include carbonate substitutions without forming a separate phase.[51] The proposed mechanism was a complex substitution of three phosphates by four carbonates and a calcium by a water molecule. This convoluted system was an attempt to explain how substitutions that seemed

to severely destabilize the structure could be seen in mineral samples that were observably stable and well-crystallized.

Focusing back on the study of bone mineral, Robinson would make the first direct observation of the morphology of bone mineral using electron microscopy in 1952.[52] These micrographs showed crystals (dimensions : 500*250*100 Å) closely intertwined but distinct from the collagen strands (Figure 7). They were shown to be hydroxyapatite on the basis of XRD, but surprisingly showed a "*tabular*" or plate-like shape, not typical of micrometric apatite crystals. A striking aspect of these crystallites was their regular spatial arrangement: the crystals were regularly spaced along the axis of the collagen.

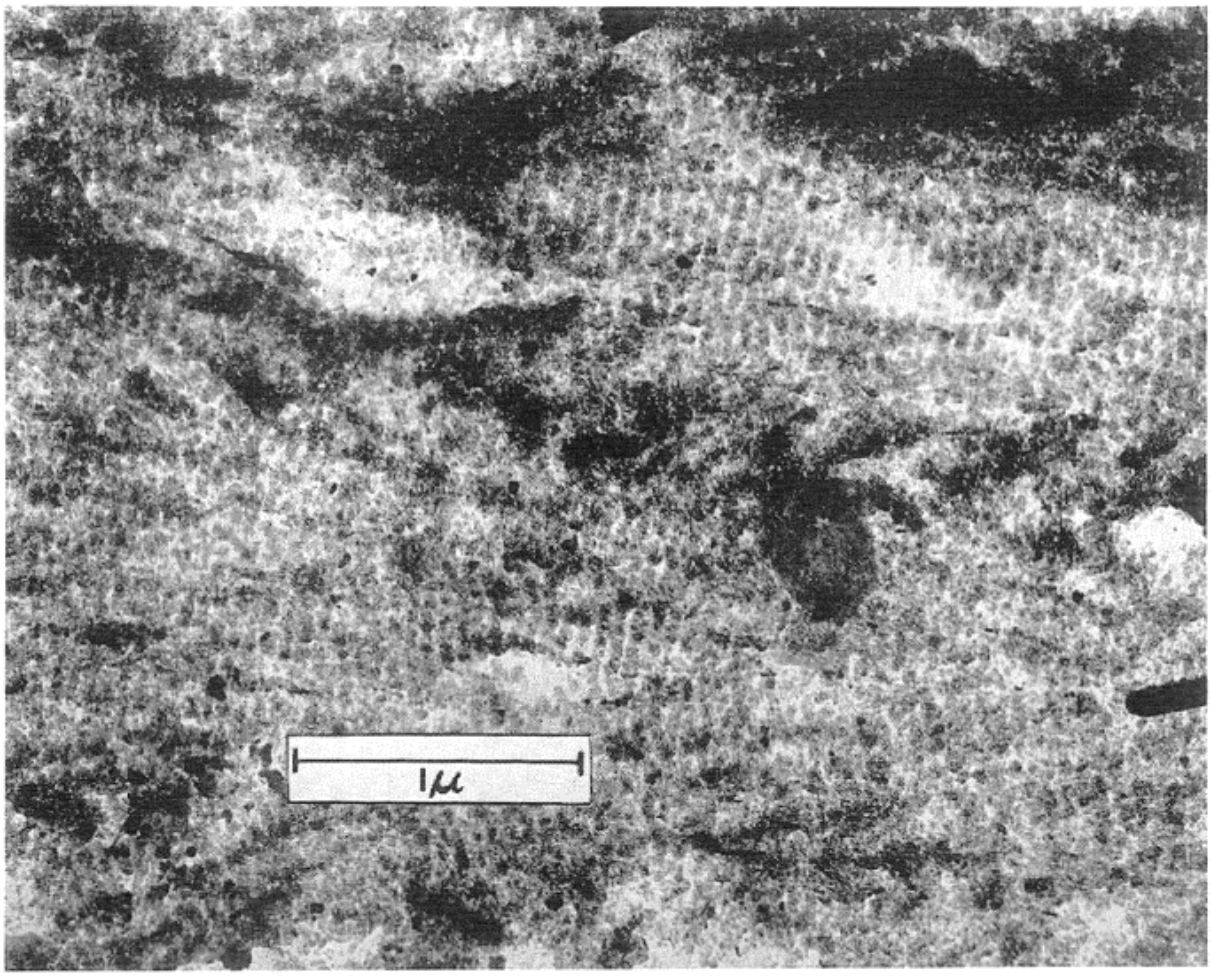


*Figure 7: Early electron micrograph of human bone, showing the regular spatial arrangement of the mineral platelets. Recorded by Robinson, reproduced by Neuman and Neuman.[53] Brightness corrected from the digital scan.*

Another important discovery relates to the water content of apatite. Even geological samples always contain a small amount of water.[54] In contrast, a 1952 study by Neuman *et al.* evidenced the presence of a large quantity of water, estimated to be above 20% of its dry weight. This was done using an ingenious combination of BET surface area measurements and high-speed centrifugation. The study was part of a long series of discoveries by Neuman, whose exceptional analyses of bone using the latest techniques (*in-vivo* radioisotope labeling, electron microscopy, precise recrystallization measurements, *etc.*) gave a detailed description

of the composition, ion substitution and reactivity of bone mineral. Another discovery, determined on the basis of the precipitation kinetics, was that the concentration of $HPO_4^{2-}$ ions governed the kinetics of the recrystallization of apatite, implying that bone apatite has a precursor rich in hydrogen phosphates. A review from the next year by Neuman and Neuman[53] presented the emerging consensus thusly: *"Whereas the size and shape of the crystals of bone are now known with some certainty, the chemical nature of these crystals is still poorly understood, after a century of investigation. A primary obstacle has been the variability in composition of the bones and teeth. In fact, there is no evidence that the crystals are comprised of a single compound, despite the proposal of at least ten "formulae""* and *"The apatite lattice is not a compound, but rather a space arrangement of atoms found in a number of minerals, of which fluorapatite may be considered the prototype"*. These statements, which in some part still hold true to this day, prefigured the difficulties that chemists would face for the next seventy years.

### II.3. Recent discoveries

We will skip over much of the incremental progress that was made in the latter part of the 20th century, as many of those discoveries are parallel to solid-state NMR investigations (discussed below). Yet we must note two important developments Firstly, the mode of substitution of carbonates in bone was widely debated in the 1980s and 1990s using a mix of XRD, FT-IR (Fourier Transform Infrared spectroscopy), TGA and NMR data.[55–57] A consensus formed that carbonate ions were present inside biological apatites, both as A-type (replacing $OH^-$ groups in the hydroxyl channels) and B-type substitutions (replacing phosphate groups), the latter being more common. However, controversies on the exact locations and orientation of carbonates in the HAp matrix are still present in the literature. A particular attention was paid to $CO_3^{2-}$ axial direction by XRD and FT-IR experiments.[58–60]

Another important finding by Reznikov *et al.* in 2018 concerned the structure of the mineral "platelets" in bone.[13] Using high-resolution TEM, it was decisively shown that the plate-like shape of bone mineral comes from the assembly of curved and merging crystals, forming a "lacy" motif of which the platelets were only a single level of hierarchical organization (Figure 8).

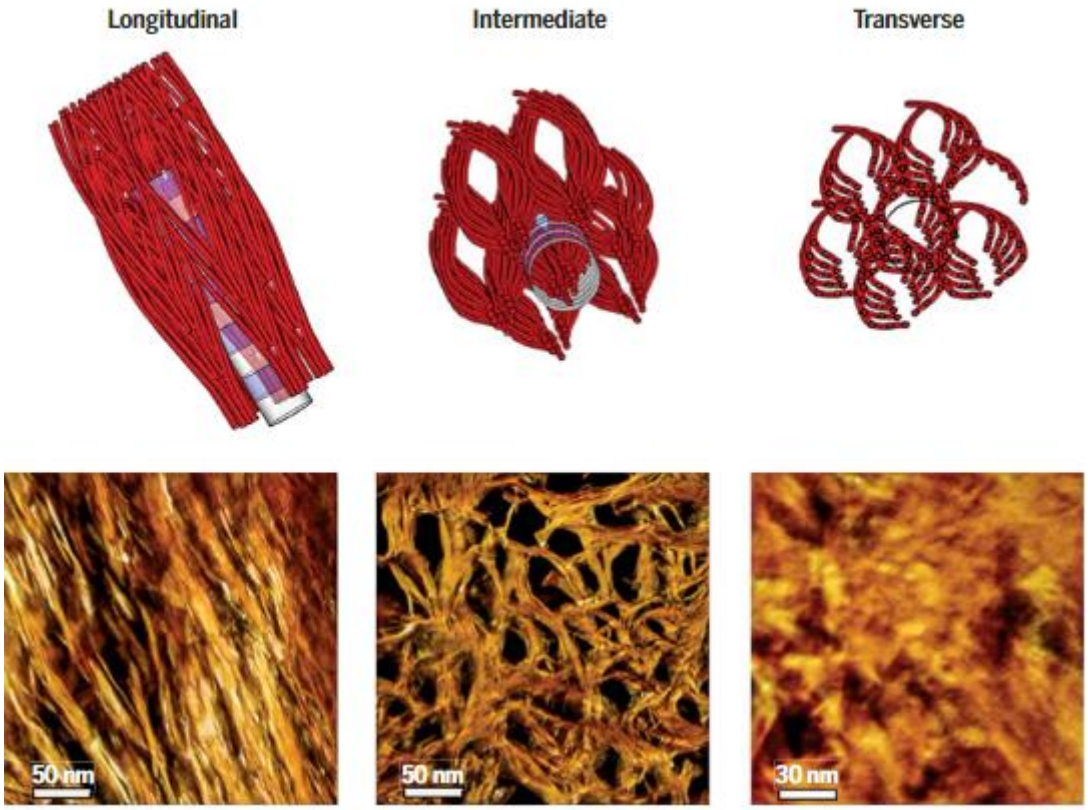


*Figure 8: New description of the nanostructure of bone mineral, based off of HRTEM findings. The different models describe arrangements observed at different points within the sample. Reproduced from Reznikov* et al.[13]

We therefore arrive at our modern description of bone,[61,62] which faces many of the same uncertainties that worried Neuman seventy years ago: it is an assembly of apatitic nanocrystals which lie in close contact with the collagen of bone. Their core is composed of a substituted, carbonated apatite. Their surface is hydrated with a large quantity of hydrogen phosphate ions, and is sometimes described as ACP (Amorphous Calcium Phosphate). The average composition of bone is still a matter of debate and greatly varies with the sample studied. Finally, many aspects of bone mineral remain difficult to measure and are still a subject of great interest: the exact nature of the surface, its interface with collagen, the proportion of surface water, *etc*. This is where we introduce nuclear magnetic resonance, a technique that has been at the forefront of bone mineral analysis and has given us insight into the more obscure aspects of bone mineral.

# III. NMR of the mineral phase of pristine bone and teeth

## III.1. Early NMR

The next section will be dedicated to understanding how NMR spectroscopy contributed to deepen our understanding of bone mineral. It will detail in a roughly chronological order a number of contributions with novel approaches to the study of bone mineral. We will put a particular emphasis on the study *via* solid-state MAS NMR of the mineral component of bone, especially those relating to the work presented in this manuscript. Through this, we explore the different NMR methods used to probe bone and their importance in our understanding of this complex material.

The first publications reporting NMR spectra of bone originate in the mid-1960s, a little more than a decade after the emergence of NMR as an analytical technique. We can point to H. M. Myer's 1965 study of bone mineral *via* wide-line $^{31}$P NMR[63] as the first published observation of bone (and enamel) mineral. At an extremely low field (78 mT!) and without Fourier-transform spectroscopy, it was barely possible to extract the $^{31}$P signal of the enamel from the background noise. We can presume that the even weaker signal of bone was impossible to observe, since it was not presented in the study. Nonetheless, a strong $^{1}$H resonance was visible in enamel and bone samples. In the case of enamel, $^{1}$H signal was shown to be insensitive to dehydration at 200°C over a week, leading the author to conclude that there was water tightly bound to the enamel.

Similar studies *via* $^{1}$H NMR of the water of dentin, enamel and bone would continue over the next ten years, but the lack of resolution in the spectra of solid samples remained a constant barrier in separating the signals originating from organic parts, which were usually assumed to be broader. Another similar study in 1972 by G. H. Dibdin[64] showed $^{1}$H spectra of enamel over time after hydrating. The author observed a small, wide signal not removed by dehydration, explained by the presence of bound water (estimated at 1.6-2.0% w/w) and hydroxyl ions (3.0-3.8 w/w). We know with hindsight that these values are close to contemporary estimations of the content of bound water in apatite.[65]

The first true high-resolution MAS studies of the $^{31}$P signal of bone would require the development of magic angle spinning (MAS), Fourier-transform spectrometry and higher magnetic fields. The first mention of a MAS spectrum of bone is from a 1979 study of embryonic bone by Roufosse *et al.*,[66] citing back to a 1978 Annual Report of the National Magnet Laboratory of the Massachusetts Institute of Technology (MIT).

The 1980s were a transformational decade for solid-state NMR, with a rapid increase in magnet field strength, MAS rotation rates and the widespread adoption of novel techniques like two-dimensional heteronuclear spectroscopy.[67] Bone was of particular interest in these early high-resolution studies, as the material contained two highly-sensitive nuclei ($^{1}$H and $^{31}$P) and because the observation of $^{31}$P nucleus allowed for the direct study of bone mineral in pristine bone. One of such studies was conducted by Roufosse et al. in 1984,[68] observing bone samples alongside reference calcium phosphates on a 7.0 T spectrometer. Using a MAS spinning rate of 2 kHz, the team was able to use the intensity of the spinning sidebands (and therefore, the chemical shift anisotropy of the $^{31}$P sites) as a basis of comparison between the

bone and calcium phosphate samples. The team also used a proton suppression sequence[69] (in essence, a measurement of the $T_{1\rho}$ relaxation under free precession) to indirectly measure the $^{1}H$ –$^{31}P$ dipolar couplings in the samples. As expected, it was found that this relaxation was faster in samples with stronger $^{1}H$ – $^{31}P$ couplings and in more disordered systems. It was concluded on the basis of the CSA (chemical shift anisotropy) and relaxation measurements that bone mineral contains a large amount (est. 5-10%) of $HPO_4^{2-}$ groups similar to those of DCPD, as well as a highly carbonated, B-type apatite with a $CO_3^{2-}$ content of 5-10%. One of the most striking results of the study is that ACP was discounted as the source of the acidic phosphate groups, as its CSA and relaxation were significantly different from that of the bone samples. Additionally, it was found that the spectra were notably different between embryonic and mature bone, as the older bones had a lowered $HPO_4^{2-}$ content. This early study proved the importance of NMR spectroscopy in the investigation of the structure of bone mineral. Its ability to distinguish between different local environments was providing insight into $HPO_4^{2-}$ sites that could not have been obtained using other analytical techniques. We can see the immediate impact that those findings had on the understanding of bone mineral in writings of M. J. Glimicher the same year,[70] who speculates that the "brushite-like"[69] $HPO_4^{2-}$ sites may be bridging the organic and inorganic phases of bone.

The decade also saw the emergence of $^{31}P$ NMR *in-vivo* for medical applications. Although the absence of MAS and the severe constraints in magnetic field limit the sensitivity of the system, NMR had the advantage of being non-invasive, and of using non-ionizing radiation that induces no risk for the patient. This led to a study[71] proving the feasibility of using $^{31}P$ NMR for the measurement of bone mineralization. Although we will not discuss it further in this work, multiple studies[72–74] would envision the use of $^{31}P$ NMR for MRI applications. So far, the idea does not seem to have found widespread medical application. However, this idea has been transposed to MAS NMR. The combination of MAS NMR and micro-imaging has been investigated and allows for the detailed spatial imaging of biological samples.[75]

### III.2. First high-resolution NMR studies

The continual improvements of spectrometers in the late 1980s and early 1990s would lead to a multiplication of the number of studies exploring the $^{31}P$ NMR of bone mineral. In 1990, Miquel *et al.*[76] recorded high-resolution $^{1}H$ and $^{31}P$ spectra on a 7.0 T spectrometer with the help of high-power heteronuclear decoupling and higher spinning speeds (5.0 to 6.5 kHz) than previously achieved. This study produced a series of better-resolved $^{1}H$ and $^{31}P$ spectra for bone and a number of synthetic calcium phosphates (several hydroxyapatites, brushite, monetite, octacalcium phosphate, $\beta$-tricalcium phosphate). The study reported a highly resolved $^{1}H$ spectrum of pristine bone, for which the masking effect of the organic phase over the mineral phase was apparent. The team also reported a series of values for the chemical shift and linewidth of mineral and bone samples, with and without high power decoupling. One of the notable features of the bone sample was the fact that the broad BD linewidth (123 Hz for healthy bone) was not reduced by heteronuclear decoupling. This was interpreted by the broadening from the distribution of chemical shifts being greater than the residual dipolar coupling, at the specific spinning speed and Larmor frequency of the study. This was found to be in stark contrast with DCPD and other hydrogen phosphate containing compounds, for

which the residual $^{1}H$-$^{31}P$ dipolar coupling significantly broadened the spectra (from 48 Hz when applying $^{1}H$ decoupling to 470 Hz in absence of decoupling). This also went against earlier studies describing bone mineral's $HPO_4^{2-}$ sites as "brushite-like".[66,68] The conclusion was that the $HPO_4^{2-}$ groups of bone are dissimilar to those present in monetite or brushite.

The improved resolution achieved in this study allowed the team to compare the spectra obtained from four diseased bones from human biopsies (affected by Paget disease, Hyperparathyrosis, Osteomalacia and Kahler disease). They observed a larger linewidth in $^{31}P$ ssNMR for Kahler and Paget disease affected tissues, and a larger static linewidth for the sample with Osteomalacia. This was attributed to a lowered crystallinity for the former, and a larger hydrogen phosphate content for the latter. This study illustrated the advancement of ssNMR and the new possibilities opened by the increased resolution of modern spectrometers. However, it also highlighted a weakness common to many ssNMR studies: because of the rather time-consuming experimental setup required for the analysis of each sample (compared to other spectroscopic methods like FTIR), and the difficulty of obtaining and handling human bones, the overall number of available samples tended to be small. This often led to weak conclusions and poor statistical significance regarding the pertinence of this analytical to be used for diagnosis purposes. This was especially true during the early days of ssNMR, when MAS systems proved more unreliable and prone to failure than today's systems.

The 1990s then saw a flurry of activities surrounding the study of calcium phosphates *via* ssNMR. A variety of studies focused on different aspects of bone: bone growth, bone disease, bone grafts and bone composition. A 1992 study by Roberts *et al.*[77] reported that embryonic bone had decreasing sideband intensity in $^{31}P$ MAS NMR as it matured. From a variety of measurements, including relaxation measurements in the manner of the above-described 1984 study,[69] it was concluded that the "transient precursor phase" of bone could not be ACP or DCPD. Instead, it was proposed to be mostly similar to very deficient apatite, with a lower carbonate content and higher acidity, which was once again described as "DCPD-like $HPO_4^{2-}$".

A new step in the analysis of bone mineral came in 1994 with the application of 2D CP-HETCOR NMR. As the $^{1}H$ signal of bone mineral is usually masked by the strong signal of the organic phase, it was impossible to obtain the $^{1}H$ spectrum of the mineral through direct acquisition without chemically altering the bone. As a workaround, Santos *et al.*[78] used a modified $^{1}H$-$^{31}P$ CP-HETCOR sequence alongside homonuclear decoupling (CRAMPS)[79] to obtain a series of $^{1}H$-$^{31}P$ correlation maps of bone and model calcium phosphates. Despite the low magnet field strength (4.7 T) and low spinning speeds (2.0-2.5 kHz), the spectra (Figure 9) were well resolved. They clearly showed the difference in the water and hydrogen phosphate content of apatite and bone. The team also attributed the 0 ppm ($^{1}H$) peak to the hydroxyl groups of apatite. This ability to distinguish the hydroxyl groups of bone through $^{1}H$-$^{31}P$ NMR was explored in more detail with accurate dosages of these ions by Ackerman *et al.* in 2003.[80]

However, the broadening due to dipolar coupling was still strong, showing that higher fields and MAS spinning rates would be required to observe this signal in greater detail.

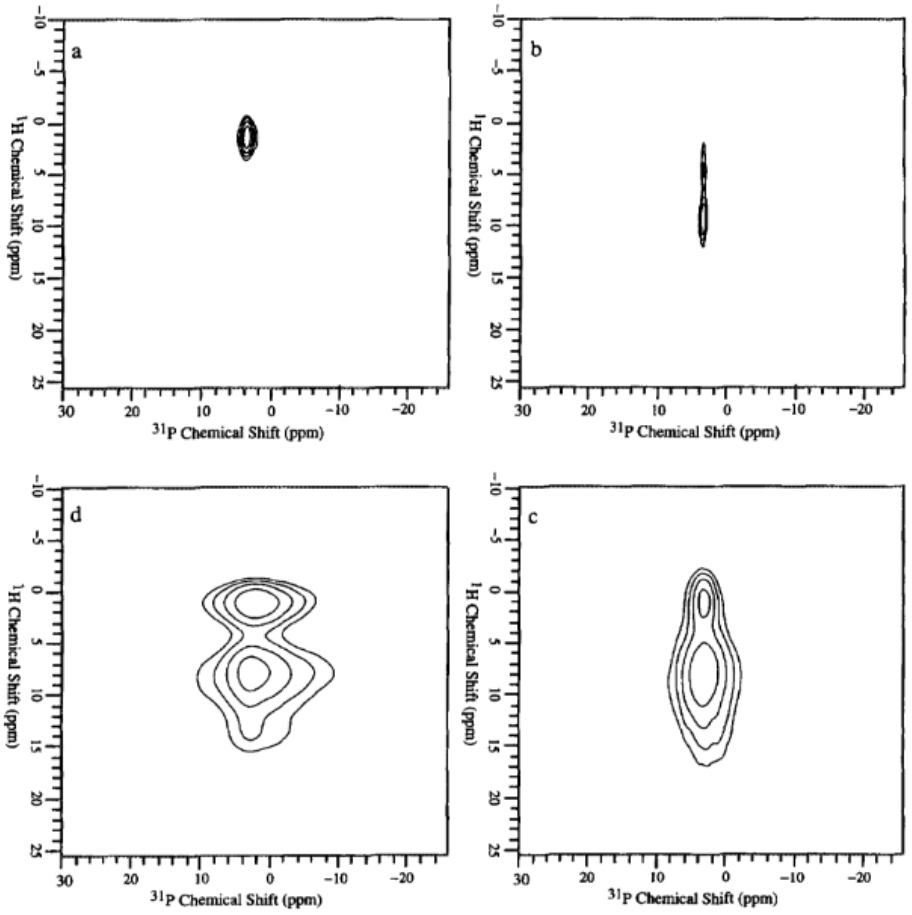


*Figure 9: First CP-HETCOR NMR signal of bone mineral, alongside other phases: a) hydroxyapatite, b) brushite, c) octacalcium phosphate d) animal bone standard (IAEA-H5).*[78]

Another method to distinguish multiple sites on a convoluted spectrum was demonstrated in 1994 by Wu *et al*.[81] Using a modified CP sequence (differential CP, or DCP), the team was able to suppress the $PO_4^{3-}$ signal of bone while conserving the $HPO_4^{2-}$ based on the difference of the characteristic time of magnetization transfer ($T_{cp}$) between the two ions. Once the $PO_4^{3-}$ is suppressed in this manner, a second fine peak appears at – 0.5 ppm in the $^{31}$P dimension, attributed to the hydrogen phosphate groupings in bone. The authors noted that whereas the isotropic chemical shift matches that of hydrogen phosphates in OCP, the CSA is nearly identical to that of brushite. The authors conclude that the $HPO_4^{2-}$ and $PO_4^{3-}$ environments in bone may in fact coexist within the same structure, with a few Å of distance. We note that this observation of a $^{31}$P signal at -0.5 ppm was not reproduced in later NMR studies. Nevertheless, the study demonstrated the usefulness of $T_{cp}$ as a method for discriminating different chemical environments in bone.

Because of the limitation inherent to the 1D NMR observations of bone (a single asymmetric peak in $^{31}$P NMR, and the masking superposition of the organic phase signal in $^{1}$H NMR), alternative methods were sought to differentiate samples. This can be seen in a 1998 publication by Kaflak *et al*.[82] that studied in detail the cross-polarization dynamics of human bone samples. While the field strength and spinning rate were still limited (4.7 T, 3 kHz), the use of a 7 mm rotor increased the amount of signal per scan so that the authors were able to

record a large number of experiments in a short timeframe. By using a combination of variable contact time CP and depolarization measurements, they were able to measure the number of components of the CP buildup curve of bone mineral. Their conclusion was that the CP kinetics resulted from the sum of two components, a “proton rich” domain and a “proton deficient” one with drastically different dynamics. This went to confirm the earlier suspicions of a bone mineral with two distinct phases, one of which contains a significant number of protons. The authors did not propose a chemical composition for the « proton-rich » phase.

A recurring difficulty with the study of CP dynamics in bone is the complexity of the polarization transfer mechanisms during the length of the spinlock which prevents the simple extraction of P-H short distances. This problem can be overcome by suppressing the homonuclear spin diffusion during a variable cross-polarization study, as was proved in 2005 by Wilson *et al.*[83] who used a Frequency-switched Lee-Goldburg (FSLG) decoupling sequence.[84] This limits the polarization transfer to rely solely on direct $^{1}H - ^{31}P$ dipolar coupling, as the $^{1}H - ^{1}H$ spin diffusion is suppressed. The resulting buildup curves thus resemble those of isolated spin-pairs, and give an estimation of the H – P distance. This, alongside the observation of dehydrated samples, led the team to conclude that bone includes an ordered layer of strongly bound water embedded within the bone mineral, in close proximity to the phosphorus sites. Unlike the bulk water bound to the organic phase, this hydration could not be fully restored once it was removed. Looking back at the studies of the late 1990s and early 2000s, we can now see a common trend in the conclusions reached by the authors. It becomes clear at this point that the mineral phase of bone cannot be characterized as a single apatitic phase. Rather, bone mineral is being increasingly being described as the combination of “hydrated” or “DCPD-like” phase with a “non-hydrated” or “apatitic” phase. If the nature of the apatitic phase seems clear from NMR, XRD and other evidence (it is a carbonated, deficient apatite), the description of the “hydrated phase” was still made in analogies, being alternatively likened to OCP, TCP, ACP or DCPD, but with no definite composition.

### III.3. A new model for bone mineral

While we have not mentioned them specifically so far, the studies of apatite phases were yielding results of particular interest for our understanding of bone. The study of nanocrystalline biomimetic synthetic apatites was pushed forwards by the same technological and methodological advancements as that of bone. It was also facing issues characterizing an amorphous hydrate that was found to have similar behavior as the “mysterious” hydrated phase of bone.

In 2005, Lin *et al.*[85] studied the growth of apatite on bioactive glass using a number of different analytic techniques, including XRD, FT-IR spectroscopy and a variety of $^{1}H - ^{31}P$ correlation methods already discussed before (e.g. LG-CP HETCOR and variable contact time CP). The team found that apatite also forms from a hydrated, amorphous calcium phosphate of unknown composition. The year afterward, an investigation focused on NMR measurements of mature apatite nanocrystals by Jäger *et al*.[86] confirmed the location of this disordered phase. By using $^{1}H - ^{1}H$ EXSY measurements, typically used in polymer NMR to study domain sizes, it was shown that the disordered “hydrated layer” of bone mineral was an integral part

of the apatite nanocrystal. By extracting the NMR parameters (frequency, peakwidth) of the crystalline and disordered domains, the team could quantify the two domains, estimating an equal split of the $^{31}P$ content between surface and core. Lastly, the two domains were quantified on a variable contact time CP-HETCOR experiment, showing the extreme difference in the CP dynamics characterizing these two domains. Combining the quantifications established in $^{1}H$ BD NMR and $^{31}P$ BD decomposition, the authors were then able to established an approximate composition of the surface layer, estimating it to be similar to that of OCP ($Ca_8(PO_4)_4(HPO_4)_2{\cdot}4H_2O$, missing only a single water molecule!). As the particles were relatively monodisperse and of known size (thanks to TEM measurements), the team was able to directly calculate the thickness of the "hydrated" domain, estimating it to be ≈ 1 nm thick on an apatite nanocrystal ≈ 10 nm wide (Figure 10).

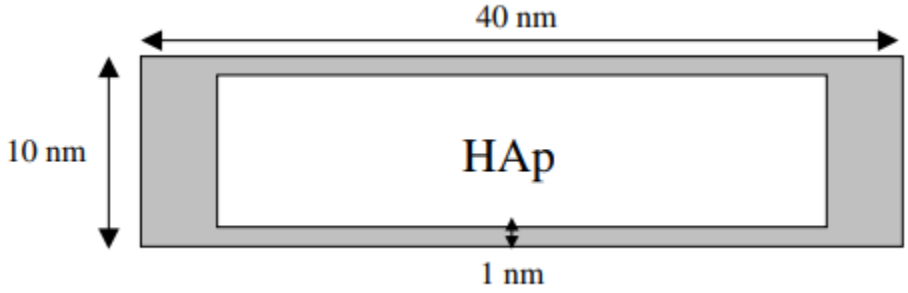


*Figure 10: Structural scheme of the elongated calcium phosphate nanoparticles.*[86]

The confirmation of this core-shell model of nanocrystalline apatite had important implications for the structure of bone mineral. Given the NMR similarities between the apatite of this model and that of bone, it is tempting to believe that bone mineral has a similar organization, which would go a long way to explaining all of the results seen above.

It did not take long for those methods to be applied to biological samples. Just a year later, in 2007, Tseng *et al.* ran a similar analysis on the incisors or rats to determine the relative amount of "amorphous" and "apatitic" phosphates. Unlike the previous study, it was impossible to use $^{1}H$ BD spectra to quantify the proton content of either phase due to the presence of collagen signal. However, as seen before, the $^{1}H - {}^{31}P$ CP-HETCOR still allowed the discrimination of the signal of the surface and that of the core of the mineral (assuming that the core of the apatite has no $^{1}H$ signal aside from the $OH^-$ resonance, which is a risky assumption!). Yet using this method, the researchers were able to prove that the relative quantity of the phases changed drastically over the lifetime of the individual rat. The evolution of the crystallinity of biological minerals over the lifetime of the individual was already well established *via* XRD measurements, but could now be correlated to a relative decrease of the amorphous surface of the mineral.

Gradually, we see a consensus emerging: a new description of bone and other biological minerals according to a core-shell model, with a disordered calcium phosphate at the surface gradually converting to the crystalline apatite of the core as the mineral grows. Therefore, by the end of the 2000s, the broad strokes of our modern description of bone mineral were

solidly established, owing in large part to the evidence from solid-state NMR showing that the two distinct chemical environments belonged to neighboring but distinct phases.

## III.4. Refining the model, pushing boundaries

This new model of bone mineral still left gaps and asked new questions about this complex phase. The composition of the surface of bone mineral was still poorly understood. A review of the evidence from 2009 (Rey *et al.*)[61] described the limitations of the model of bone mineral: a hydrated phase that is poorly defined, with contradictory evidence describing it alternatively as being most similar to OCP or DCPD. It also highlighted the wide array of conflicting evidence about what constitutes the precursor phase of bone. For this purpose, researchers were looking for new analytical methods that could delineate between closely related, disordered calcium phosphates.

### III.4.1. $^{1}H$-$^{31}P$ NMR investigation of the amorphous surface of apatitic bone mineral

After 2010, new NMR studies aimed at characterizing the disordered phases at the surface of bone. Von Euw *et al.*[62] had the idea to simplify the acquisition of a $^{1}H$ spectrum of bone mineral by using a straightforward $^{1}H$ – $^{31}P$ – $^{1}H$ double-CP sequence.[87] This back-and-forth transfer of the polarization would serve to filter the $^{1}H$ resonances further away from $^{31}P$ sites, *i.e.*, those of the organic phase. By this method, a non-quantitative $^{1}H$ NMR spectrum of bone mineral could be acquired relatively easily. The study of the CP dynamics in this sequence was revealing: by fitting a variable-CP experiment, varying solely the second contact time (from $^{31}P$ to$^{1}H$ direction), the team observed oscillations of the intensity over the contact time. This could be explained, as seen before, by a dipolar coupling, indirectly relating back to the distance of the P - H spin pair. By this method, it was possible to deduce the corresponding $d_{PH}$ distance for different bone mineral signals. Their findings are presented in Table 1.

| Sample | $^{1}H$ species | $\delta(^{1}H)$ (ppm) | $D_{PH}$ (Hz) | $d_{PH}$ (Å) | $T_{HP}$[a] (µs) | $T_{df}$[b] (µs) | $T_{1\rho}(^{1}H)$ (µs). |
|---|---|---|---|---|---|---|---|
| Bone mineral | $OH^-$ | 0.0 | — | — | 795 | — | ∞ |
| | $H_2O$ | 5.2 | — | — | 522 | — | ∞ |
| | $HPO_4^{2-}$ | 9.8 | 4050 ± 500 | 2.24 ± 0.07 | — | 788 | 1485 |
| | $HPO_4^{2-}$ | 14.0 | 4695 ± 500 | 2.14 ± 0.07 | — | 624 | 1224 |
| CHA-SBF | $HPO_4^{2-}$ | 7.0–17.0 | 4960 ± 500 | 2.10 ± 0.07 | — | 665 | 3531 |
| Monetite | $HPO_4^{2-}$ | 13.0 | 5275 ± 500 | 2.10 ± 0.07 | — | 626 | ∞ |
| | $HPO_4^{2-}$ | 15.8 | 6863 ± 900 | 1.92 ± 0.14 | — | 691 | ∞ |

*Table 1: Different fitting parameters of the variable-CP experiment. $D_{PH}$ = fitted dipolar coupling constant for each environment. $d_{PH}$ = calculated P - H internuclear distance. $T_{HP}$ = CP rate constant. $T_{df}$ = spin-diffusion rate constant. $T_{1\rho}$ ($^{1}H$) = spin-lattice relaxation rate in the rotating frame.*[62]

This method for the characterization of P - H interspatial distances led the team to conclude that the $HPO_4^{2-}$ sites contained within bone cannot be attributed to an OCP or monetite layer,

and are not present within the core of the mineral. Rather, they are concentrated at the surface in an ACP-like layer of thickness ≈0.8 nm (revising the $HPO_4^{2-}/PO_4^{3-}$ ratio of the bone mineral in its entirety from <0.5 to ≈1, see Figure 11). This was very similar to the previously described study of precipitated apatite placing it at ≈1 nm in thickness.[85] We note that the study was of the cortical femoral bone of a young, healthy sheep, and may not be applicable to all types of bone.

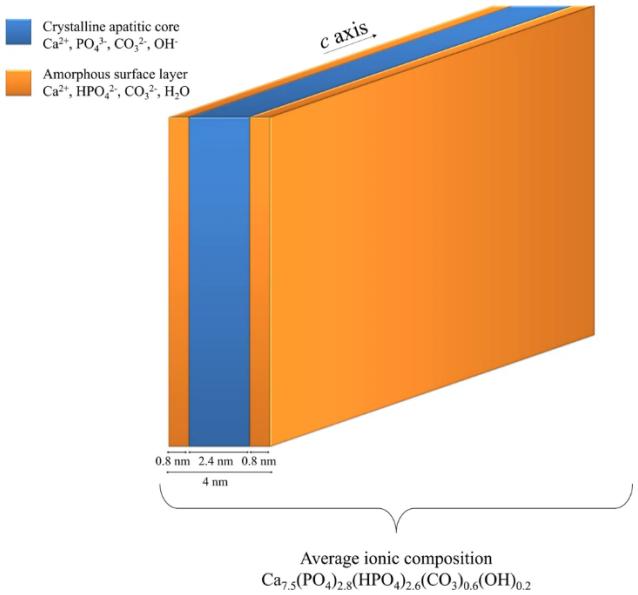


*Figure 11: Updated model of the structure and composition of bone mineral, reproduced from Von Euw* et al.[62]

In addition to $^{1}H$ and $^{31}P$ NMR, the observation of less sensitive nuclei was becoming possible thanks to higher field spectrometers. Thus, researchers expanded the NMR of bone to rare nuclei ($^{43}Ca$ and $^{17}O$) and substitutions ($^{13}C$ and $^{23}Na$) in biological samples. $^{43}Ca$ and $^{17}O$ nuclei in particular have a lower intrinsic sensitivity than $^{31}P$ and $^{1}H$, owing to their lower gyromagnetic ratio and natural abundance. Indeed, what makes the two isotopes particularly challenging, is their extreme rarity. $^{43}Ca$ and $^{17}O$ isotopes have a natural abundance of 0.135% and 0.037% respectively. When compared with a theoretical 100% abundant sample, a natural-abundance sample would require an acquisition respectively 5500 times and 73000 times longer to achieve the same signal/noise ratio (as the acquisition time increases with the inverse square of the signal). To acquire a sufficient signal, therefore, one must increase the signal and resolution by any means possible.

### III.4.2. $^{43}$Ca NMR

Already in 2008, Laurencin *et al.* showed that a natural abundance spectrum of $^{43}$Ca at 18.8 T could resolve the two calcium sites of hydroxyapatite.[88] This spectrum (Figure 12) was acquired over the course of more than a day on a 4 mm rotor. Spectra at lower fields required even larger volume MAS rotors (9.5 mm in diameter).

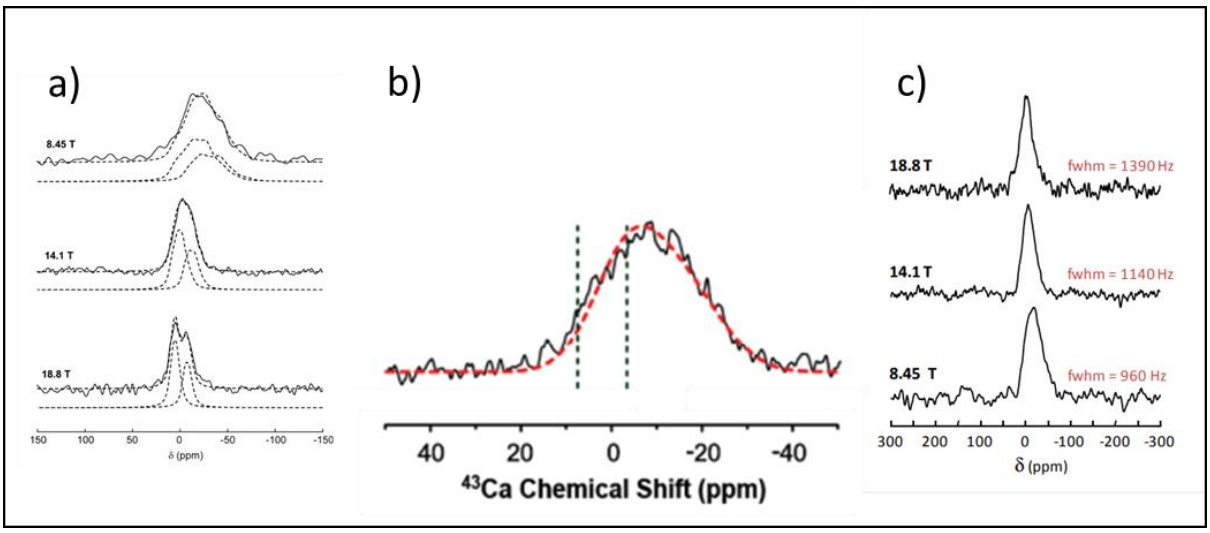


*Figure 12: $^{43}$Ca spectra of apatitic materials from three different publications. a) Laurencin* et al.*, 2008:[88] natural abundance $^{43}$Ca spectra of HAp at three different fields. b) Xu* et al.*, 2010[89] : natural abundance $^{43}$Ca spectrum of bovine cortical bone at 19.6 T. c) Laurencin* et al.*, 2010[90] : natural abundance $^{43}$Ca spectra of equine bone at three different fields.*

The observation of bones *via* natural-abundance $^{43}$Ca NMR was reported closely after. In 2010, Laurencin *et al.,* followed by Xu *et al.,* published natural abundance spectra of bone.[89,90] In stark contrast to crystalline HAp, the two calcium sites could not be resolved at high fields, the spectrum showing a single broad peak instead. This was attributed to a distribution of chemical shifts caused by the presence of substitutions (e.g. $Na^+$, $Mg^{2+}$, $CO_3^{2-}$) in the apatite crystal lattice and disordered environments in bone mineral. Because of the very long acquisition times of 1D MAS NMR spectra, trying to gain resolution through two-dimensional acquisitions such as MQMAS[91] would have been experimentally infeasible. 2D $^1$H – $^{43}$Ca correlation experiments would be similarly useless at natural abundance, due to the low sensitivity and the fact that extremely slow MAS speeds would add the additional constraint of a very broad spectrum due to strong residual dipolar couplings. The idea of studying bone through natural abundance $^{43}$Ca NMR therefore found itself at a standstill, given the lack of information of the 1D spectrum and the apparent severely poor sensitivity of 2D acquisitions.

### III.4.3. $^{17}$O NMR

Davies *et al.* completed the analysis of the major components of bone by acquiring a $^{17}$O NMR spectrum of pristine bone in 2014 (Figure 13).[92] Because of the larger quadrupolar constants, resulting in broader peaks, moderate to fast MAS rates are required for this nucleus, precluding the use of large diameter rotors. In the reported study, it was shown that at natural abundance, the signal of a $ZrO_2$ rotor was interfering with the observation of some of the bone

resonances, requiring the use of a special $Si_3N_4$ rotor. Despite extreme rarity of the $^{17}O$ nucleus, the high field (20.0 T) and a lengthy acquisition give resolved resonances for a number of compounds of bone. They observed the expected signals in zones expected for the components of bone mineral, $PO_4^{3-}$ and $HPO_4^{2-}$, visible as PO and POH resonances. Signals assigned to the organic matrix and citrates are also visible, although extremely noisy. This spectrum showcases the potential, but also the limitations of a $^{17}O$ NMR study of bone. Although the large chemical shift range gives relatively well-resolved signals for the organic and mineral phases, the extremely poor sensitivity required extremely long acquisition times to be able to distinguish the different signals. We can therefore conclude that $^{17}O$, like $^{43}Ca$, is a highly challenging nucleus to observe, even with the use of specialized probes, rotors and high-fields. Further studies of bone have therefore continued to primarily use $^{1}H$, $^{31}P$ and $^{13}C$ NMR. This may come to change with the development of sensitivity enhancement techniques like DNP applied to $^{17}O$ and $^{43}Ca$, a point that will be discussed later in this work (Chapter IV).

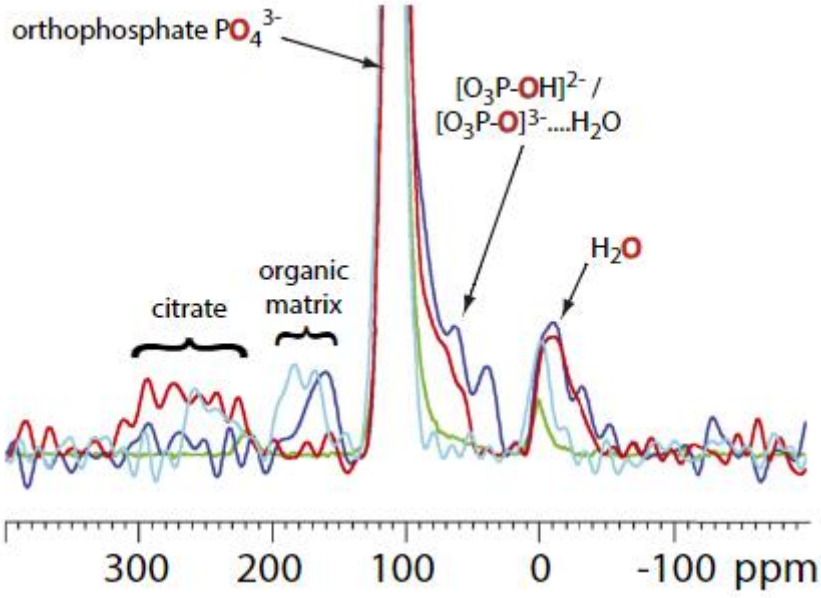


*Figure 13: $^{17}O$ direct acquisition NMR spectra of fresh sheep bone (blue), bone mineral soaked in a citric acid solution (light blue), OCP-citrate (red) and 5% $^{17}O$ enriched apatite (green), at 20.0 T.*[92]

### III.4.4. $^{13}C$ NMR

As mentioned previously, the location and geometry of carbonate substitutions in apatites is of great importance to the study of biominerals. This issue was studied using $^{13}C$ solid-state NMR as early as 1990 by Beshah *et al*.[93] In this contribution, synthetic apatite samples were studied alongside dental enamel. Thanks to the poor organic content of enamel, a spectrum of the carbonate resonances could be acquired using a simple $^{1}H$ – $^{13}C$ CP acquisition. This proved that $^{13}C$ NMR was able to distinguish A-type and B-type carbonate substitutions, with the enamel sample showing evidence of both. It was however impossible to measure the carbonate resonance of bone, as the resonances corresponding to the organic content could not be removed despite harsh chemical treatments.

This limitation was overcome by Yasar *et al.*[94] using $^{1}H \rightarrow {}^{31}P \rightarrow {}^{13}C$ polarization transfers. With a combination of CP-HETCOR, DCP and REDOR experiments, the team was able to isolate the signal of carbonates in bone. This showed the presence of two different types of B-type carbonate types, which were referred to as $B_1$ and $B_2$. Overall, the study of carbonate substitutions in bone is made somewhat challenging due to the low natural abundance of $^{13}C$, small amount of carbonate substituents in the mineral phase (5.8 %)[55] and the low dipolar couplings with more sensitive nuclei, but is achievable using moderate fields and commonly available probes. It provides precious information about the location of carbonate substitutions in a sample. The advent of DNP as a sensitivity enhancement technique also promises to make the observations of carbonation in bone mineral much less time consuming than ever before.[95,96]

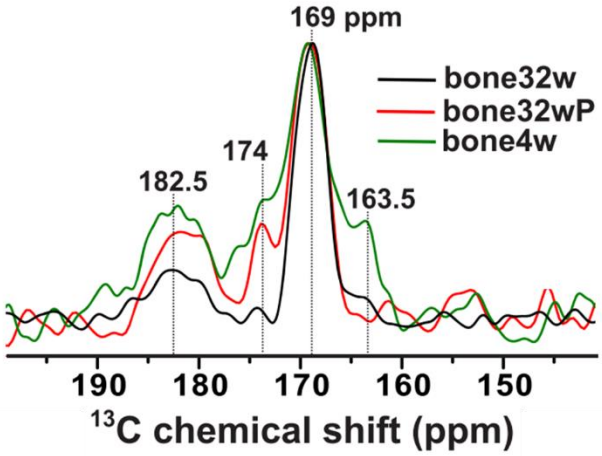


*Figure 14: $^{13}C$-{$^{31}P$} REDOR ΔS spectra of different dog bone samples. Bone4w corresponds to bone from a four week old specimen, bone32w to an adult dog and bone32wP to a powdered sample of the same specimen. Note the resonance at 182.5 ppm, which may belong to carboxylate groups (such as those of citrate ions). Reproduced from Yasar* et al.[94]

#### III.4.5. $^{23}$Na NMR

Laurencin *et al.*[90] also studied the incorporation of sodium ions within bone mineral using $^{23}Na$ NMR. Unlike $^{43}Ca$, $^{23}Na$ is a 100% abundant, moderately sensitive nucleus. Its signal in bone is therefore greater than that of $^{43}Ca$, despite making up a much smaller fraction of the total mass (0.7% and 24.5%[55] respectively). Therefore, the team was able to acquire a well resolved 2D $^{1}H$ – $^{23}Na$ $R^3$-HMQC[97] correlation spectrum, showing that the sodium content of bone correlates strongly with the $OH^-$ signal of bone apatite at $\delta_{iso}(^{1}H) = 0$ ppm. However, this does not discard the possibility of finding sodium ions in the disordered phase of bone as well. There are a number of reasons why this second correlation peak might be more difficult to observe, first and foremost $T_{1\rho}$ relaxation of the protons of the hydrated layer, which may be induced by the greater hydration of this disordered phase.

## III.5. 1D $^{31}$P and 2D $^{1}$H-$^{31}$P NMR analyses for comparative studies of the impact of diseases on bone mineral samples

At this point, solid-state NMR had only rarely been used for the comparative study of different bone samples, although it has a unique ability to provide information on the structure of the mineral of pristine bone. In spite of this, studies observing the variation of the mineral's signal with specific bone diseases are still sparse.

One such study to be mentioned is that of Nikel *et al.* in 2013,[98] probing composition of the bone mineral in intact bones of genetically engineered mice lacking osteocalcin (OC) and osteopontin (OPN). These two non-collagenous proteins are play an important role on the mechanical properties of bone, and have also been proven to inhibit the formation of mineral *in vitro*.[99] As a consequence, the authors sought to compare the mineral component of OC/OPN deficient mice to that of healthy individuals. The study was made more challenging by the intrinsic occlusion of the $^{1}$H signal of the mineral by organic species, and the lack of resolution of the $^{31}$P spectrum. The comparison was therefore made on the basis of the 2D CP-HETCOR spectra, which could not be considered directly quantitative due to the possibility for varying polarization transfer dynamics. The acquisition was run at varying contact times in order to estimate the CP dynamics for each sample. However, due to the large number of 2D experiments required for each sample, the number of samples was reduced to n = 2 for each group. The number of contact times were also much reduced compared to previously discussed studies running this analysis on 1D experiments, with only six contact times. Despite these limitations, the team was able to make a first estimate of the time constants of the magnetization transfer ($T_{cp}$) and of the spin-lattice relaxation ($T_{1\rho}$) with a relatively small error interval (Figure 15, Table 2). The issue with this comparison was that the small number of samples, low number of points in the variable CP dimension and large variation between samples led to a (here unquantified) uncertainty on the statistical significance of the data presented. Consequently, despite some discrepancies in the CP dynamics, no strong conclusion could be made by the authors on the difference between the two types of bone samples.

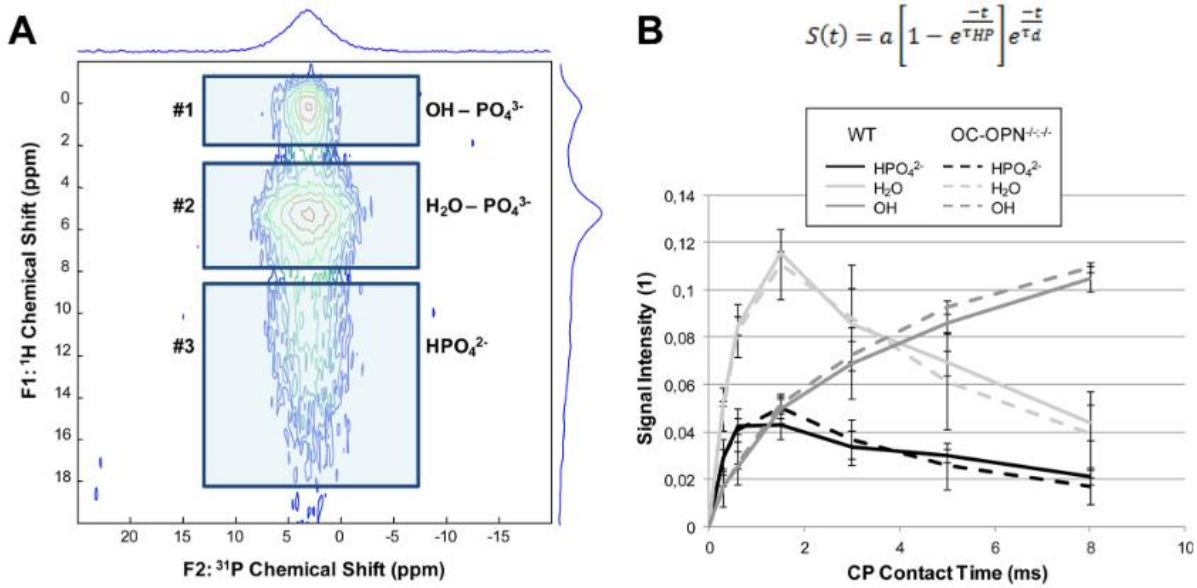


*Figure 15: Comparison of healthy and OC/OPN deficient bone samples on the basis of CP-HETCOR acquisitions. A) $^{1}H$-$^{31}P$ CP-HETCOR correlation map divided into three environments. B) Evolution of the intensity of the three components (spectrum summed over F2) with a varying contact time.*[98]

| | | WT | OC–OPN$^{-/-/-}$ | ESB |
|---|---|---|---|---|
| $HPO_4^{2-}$ | $\tau_{HP}$ (ms) | 0.3 ± 0.1 | 0.5 ± 0.1 | 0.4 ± 0.2 |
| | $\tau_d$ (ms) | 8.9 ± 1.2 | 5.5 ± 0.5 | |
| $H_2O$–$PO_4^{3-}$ | $\tau_{HP}$ (ms) | 0.6 ± 0.1 | 0.7 ± 0.1 | 0.6 ± 0.1 |
| | $\tau_d$ (ms) | 6.2 ± 0.9 | 5.3 ± 0.5 | |
| OH–$PO_4^{3-}$ | $\tau_{HP}$ (ms) | 2.5 ± 0.4 | 2.6 ± 0.3 | 2.9 ± 0.5 |
| | $\tau_d$ (ms) | $>10^5$ | $>10^5$ | |
| total | $\tau_{HP}$ (ms) | 0.4 ± 0.1 | 0.5 ± 0.1 | |
| | $\tau_d$ (ms) | 17.5 ± 3.4 | 15.9 ± 3.3 | |

[a]The errors correspond here to errors of fitting and do not reflect the experimental error.

*Table 2: Estimated time constants of the different components of the CP-HETCOR spectrum of healthy bone (WT), OC/OPN deficient bone (OCP-OPN -/-,-/-) and equine subchondral bone (ESB).*[98]

Another study by Kaflak *et al.*[100] from 2016 compared bone samples affected by different metabolic diseases through NMR relaxometry parameters. Instead of comparing time-consuming 2D acquisitions, the team instead chose to study the $^{31}P$ spin-lattice relaxation times ($T_1$) on static samples, using saturation-recovery experiments. The investigation included eighteen human bone samples from patients suffering from either osteoarthritis (OA) and osteoporosis (OP) or osteopenia (OPA, which corresponds to bone density below normal values but above the threshold for OP). The $^{31}P$ static spectra were deconvoluted into a wide "surface layer" signal and a narrower "apatitic core" signal. The study showed a strong correlation between the different NMR parameters studied (surface/core ratio *vs* $T_1$ and surface/core ratio *vs* peak width). The various parameters were combined into a common score, which was compared to the one for all of the clinical markers of osteoporosis. It was

found that the score obtained through NMR analysis did correlate with different clinical markers. This showed the potential for careful analysis of NMR markers to help in understanding the effect of bone disease on bone mineral composition. However, the conclusions of the study were limited by the absence of a true control group.

Skipping ahead in time, we will mention one last study of bone disease relevant to our analysis in the literature. In 2021, Zeng *et al.*[101] analyzed a number of bone samples originating from diseased mice, rats and human patients. Cohorts were modified to express severe cases of osteopetrosis (increased bone density) and osteoporosis (through RANKL overexpression). Another cohort received an ovariectomy, inducing osteoporosis due to estrogen deficiency. The bones of the rats and mice were compared to control specimens through solid-state $^{31}$P BD and $^{1}$H-$^{31}$P CP-HETCOR NMR. They were compared based on linewidth and on the relative intensities of the "core HA" and "surface ACP" signals in CP-HETCOR spectra. The team found that the core signal of osteoporotic bones was weaker relative to that of the surface, with wider peaks compared to control samples. This finding showed that osteopetrosis through lowered bone resorption increased the thickness of the disordered layer relative to the crystalline core. Similarly, osteoporotic bones had a narrower linewidth than that of control specimens, both for osteoporosis induced by RANKL overexpression and estrogen deficiency. Lastly, human samples from osteoporotic (OP) patients were compared to those of osteoarthritic (OA) patient, showing results consistent with those of the animal models (Figure 16). The study therefore proved a link between the presence of metabolic bone disease in an individual and the neo-formation of bone mineral on a nanostructural scale. The relatively large sample size (n = 3 to 10) for each cohort allowed for statistical significance to be achieved. This study therefore confirmed that solid-state NMR is a relevant tool for the study of metabolic bone disease, but requires large number of samples given the inherent diversity of biological specimens.

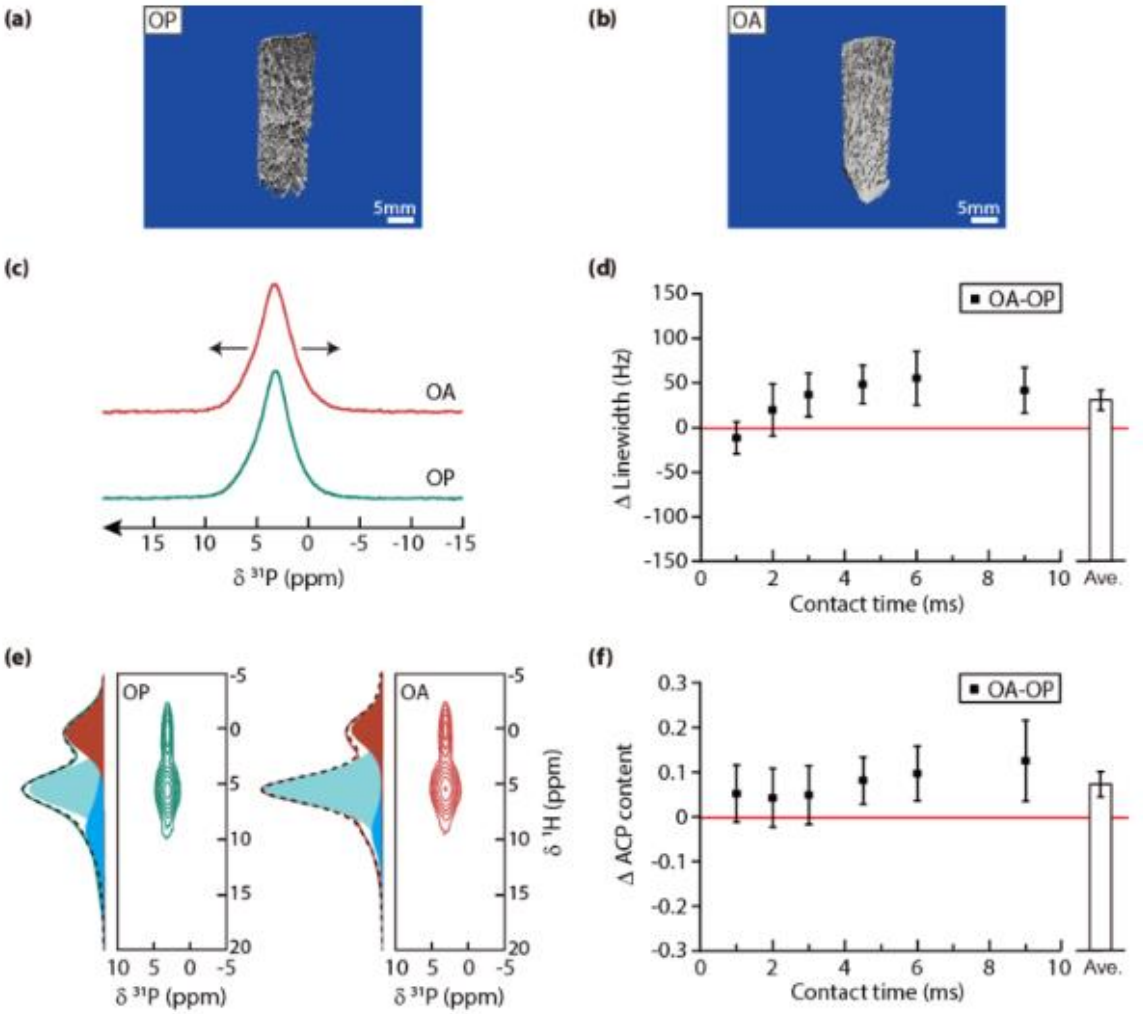


*Figure 16: Comparison between human bone samples of osteoporotic (OP) and osteoarthritic (OA) patients (n=3). a) Micro-CT images of the osteoporotic and b) Osteoarthritic femur bones. c) Comparison of the 1D $^{1}H$ – $^{31}P$ CP spectra with a contact time of 3 ms, showing a wider peak for OA samples. d) Comparison of the linewidth of the 1D CP spectra at different contact times. e) Comparison of the CP-HETCOR measurements between OP and OA samples. f) Difference in measured "surface layer" signal between OA and OP samples, showing the increased surface signal of OA samples. Reproduced from Zeng* et al.[101]

### III.6. Conclusion on the NMR studies of bone mineral

This broad-strokes overview of the literature relating to NMR's investigations of bone mineral has shown that this is a valuable technique for the characterization of bone mineral. It distinguishes itself by its ability to study of pristine bone mineral without chemical treatment, and to give information about its disordered surface. Although this surface is an exceptionally complex environment, a wealth of information can potentially be obtained for each isotope (intensity, chemical shift, CSA, broadening, CP and BD relaxometry, quadrupolar parameters for $^{17}O$, $^{23}Na$, $^{43}Ca$).

This is however hampered by the difficulties inherent to each isotope of bone: $^{17}O$ and $^{43}Ca$ are extremely insensitive, and despite being major components of bone, have not been studied beyond 1D acquisitions. Their direct acquisition spectra are also rather poorly

resolved, even at high fields. Filtered by $^{31}P$, $^{1}H$ signal gives the highest resolution of all of the nuclei, being able to distinguish the surface and core signals of bone. It also has an extremely high sensitivity and can be observed using nearly every probe. However, the CP-based sequences required to observe solely the mineral phase prevents quantitativity of the signal. The $^{1}H$-$^{1}H$ dipolar couplings in bone mineral are also hard to overcome, requiring homonuclear decoupling sequences that further obscure the quantitative information. $^{31}P$ NMR of bone can be extremely straightforward, as a signal specific to bone mineral can be acquired in a few BD scans. The spectrum, unfortunately, is completely unresolved, showing a single asymmetric peak. This peak is presumably composed of two components of different widths, but quantifying each of them requires us to precisely know the NMR parameters of each component. This can be perilous, as we will see in further discussions.

The application of solid-state NMR to the study of bone disease is still at its beginnings. A few studies[100,101] have demonstrated that practical applications exist for the technique. However, the studies are usually held back by the large sample sizes required to obtain a statistically significant result. The time constraints and experimental difficulties inherent to NMR studies also make the prospect of such a study daunting. These issues are being gradually overcome by higher performance spectrometers and more reliable probes. Better established methodologies and more experimental applications will be required for the methods to propagate beyond the solid-state NMR community.

As a conclusion, a number of questions regarding bone mineral have already been answered by a variety of creatively constructed studies. Yet our understanding of this complex phase remains partial. In this thesis, we will therefore attempt to find solutions to some of the current limitations of NMR studies of bone mineral and put them into practice.

# IV. NMR sequences

The work presented in this manuscript relied on NMR experiments acquired using a variety of sequences. In order to maintain the continuity of our argumentation, these NMR sequences will be summarized briefly in this chapter.

## IV.1. 1D sequences

### IV.1.1. Hahn Echo

The Free-Induction Decay (FID) of a nucleus starts from the moment its spin is brought out of equilibrium. In an NMR probe, this is made difficult by the acoustic ringing[102] resulting from the high-power current circulating through the coil moments before the acquisition. Even with an excellent control of the pulse, it can cause eddy currents in the conductive surfaces of the probe that can return to the probe at the beginning of the acquisition. This ringing imposes a minimum delay before signal acquisition which can be problematic in the case of wide signals with short FIDs, where the lost data points can cause severe baseline distortions.

A common solution to this problem is the Hahn-Echo sequence (Figure 17).[103] This simple sequence consists of a 90° excitation pulse, the transverse magnetization is refocused using a 180° pulse. The echo delay τ is set to a multiple of the rotation period under MAS conditions. The refocused polarization can be acquired after a second echo delay, while the magnetization is at its maximum. This comes at the cost of quantitativity, as the signals will decay at different rates during the echo. Another advantage of the Hahn Echo is its ability to filter out signals with short FIDs: wide background signals can be gradually eliminated from the sample by increasing the length of the echo delay.

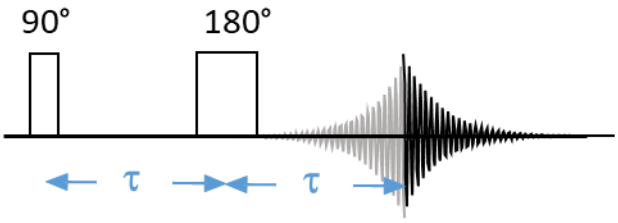


*Figure 17: Hahn-Echo sequence involving 90° excitation pulse and 180° refocusing pulse separated by an echo delay τ.*

### IV.1.2. DEPTH

The DEPTH[104] sequence provides an alternative to the Hahn-Echo for the suppression of background signals, without the refocusing delay. This relies on the use of a composite pulse, chaining a 90° excitation pulse with two 180° refocusing pulses, cycled using the EXORCYCLE scheme. This reduces the background signal of the probe without affecting the quantitativity of the signal. This is valuable to distinguish broad signals from the sample from those of the polymeric components of the probe in $^{1}$H NMR.

### IV.1.3. Cross-polarization

Cross-polarization (CP) is a polarization transfer sequence with broad applications in solid-state NMR. Introduced by Hartmann and Hahn in 1962,[105] the sequence relies on the dipolar coupling between two nuclei to equalize their spin temperatures. Especially useful in the case

of insensitive or slow-relaxing nuclei, for which the superior magnetization of abundant nuclei (noted I) can afford more signal than direct acquisition of the dilute nucleus (noted S).

Cross-polarization was soon after combined with magic-angle spinning, under which the condition is altered.[106] Under MAS conditions, a transverse radiofrequency field is applied on I and S simultaneously (at frequencies $\nu_{1I}$ and $\nu_{1S}$) which must closely match the Hartman-Hahn (HH) condition:

$$\nu_{1I} = \nu_{1S} + n\nu_r$$

with $\nu_r$ the rotation rate in a MAS experiment, and n an integer number, usually ranging from -2 to 2. The cross-polarization sequence is a staple of solid-state NMR, both due to its experimental simplicity and its high efficiency for I = ½ nuclei. In a basic CP sequence (Figure 18), the transverse magnetization is created on the x axis with a 90° pulse on I (generally $^1$H). The radiofrequency fields are then applied along the y axis for a duration $t_{cp}$. The resulting magnetization of S is then acquired, typically with a decoupling sequence applied to I. Different shapes can be applied to the I spin-lock pulse. Commonly, a ramp in the amplitude of the rf field is used to broaden the HH condition, making the CP more robust to small experimental variations.

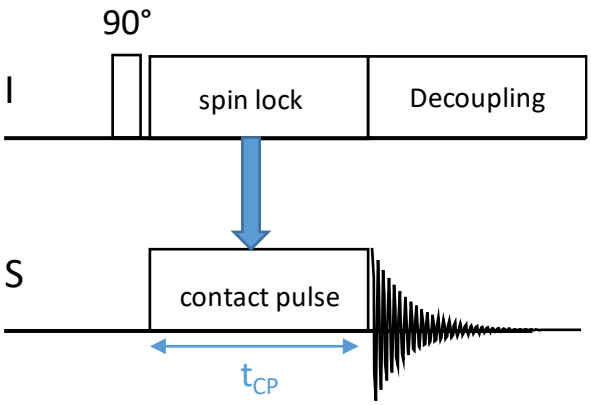


*Figure 18: Cross-polarization pulse sequence with heteronuclear decoupling.*

## IV.2. Decoupling and population transfer schemes

### IV.2.1. Heteronuclear decoupling

Because of the presence of residual dipolar couplings in solid samples, the resonances of a dilute spin S can often be broadened by the presence of a neighboring spin of high gyromagnetic ratio I (usually $^1$H). This can be alleviated by the use of dipolar decoupling sequences that reduce the spatial coherence of the two spins.

The simplest of the heteronuclear decoupling schemes is the continuous wave (CW).[107] The application of a radiofrequency field on the I spin during the precession of the S spin reduces their alignment in space. This leads to a reduced interaction between the two spins, leading to a narrower resonance. This type of decoupling is however suboptimal at higher spinning rates, and is weak to inhomogeneities of the field.

An exceptionally vast array of decoupling schemes have been devised to improve the resolution of solid-state spectra during acquisition. The following will appear in this study:

- SPINAL-64 (Small Phase Incrementation Alternation with 64 steps)[108] is a ubiquitous sequence in solid-state NMR due to a favorable combination of robust performance in most conditions (rf field inhomogeneity, pulse-width imperfections, large offsets) and ease of use. It consists of a series of ≈ 165° pulses of alternating phase angles (10°, -10°, 15°, -15°, 20°, -20°). This scheme is used in nearly all applicable acquisitions in this study.
- $SW_f$-TPPM (SWept-frequency Two-Pulse Phase Modulation)[109] is a modification to the popular TPPM[110] decoupling scheme. TPPM is one of the earliest decoupling sequences written for MAS conditions, which alternates a series of ≈ 165° pulses that switch between phases of +ϕ/2 and - ϕ/2 repeatedly for the length of the acquisition (with ϕ usually between 10 and 50°). The $SW_f$-TPPM variation introduces a sweep of the $^1$H radiofrequency near the HORROR condition ($\nu_{1I} = 0.5\nu_r$). This reintroduces homonuclear rotational recoupling while efficiently reducing heteronuclear dipolar coupling, enhancing the spin-diffusion and in turn the decoupling efficiency. This comes at the cost of a limited choice of rf frequencies, which necessitates more calibrations before the acquisition.

### IV.2.2. Homonuclear decoupling

When recording a $^1$H NMR spectrum, the limiting factor for the resolution is often the homonuclear dipolar coupling, due to the $^1$H high gyromagnetic ratio. Using a cycle of switching phases and variable rf frequencies, the FSLG (Frequency-Switched Lee-Goldberg) scheme[84] cancels out the homonuclear dipolar coupling term. This makes possible the acquisition of highly resolved $^1$H spectra in indirect acquisition experiments, by replacing the evolution time by an FSLG scheme of the same duration. This has a few important limitations: it requires relatively strong radiofrequency fields (> 100 kHz), which must be maintained for the duration of the evolution time, and scales the spectrum by a known factor ($\sqrt{3/2}$). The sequence also eliminates spin-diffusion, which can be useful when measuring the distance of spin pairs in combination with cross-polarization sequences.

### IV.2.3. Double frequency sweep

The DFS (Double Frequency Sweep)[111] serves to enhance the magnetization of the central transition of half-integer quadrupolar nuclei. By sweeping a low-power field over the frequencies of the satellite transitions, the technique inverts the energy levels of the outer and inner satellite transition. This increases the population differential at the central transition, increasing the acquired signal. Theoretically, the maximum enhancement is 2I for a nucleus of spin I. Under MAS, the effect is closer to the saturation of the populations, meaning the maximum enhancement is equal to (I + ½). The DFS scheme can be applied to nearly any sequence where the magnetization starts on a quadrupolar nucleus, providing valuable increase in signal for insensitive nuclei. It is relatively robust, and requires little optimization. Because of this, we have applied it to many experiments involving quadrupolar nuclei, in particular in Chapter II.

## IV.3. 2D sequences

### IV.3.1. CP-HETCOR

The CP-HETCOR[67] sequence is a 2D adaptation of the CP sequence that uses an evolution delay to modulate the I magnetization by its amplitude at a time $t_1$ of its FID (Figure 19). By recording the I-S CP spectrum for different values of $t_1$, the FID of the I nucleus can be reconstructed indirectly. This allows us to build a heteronuclear correlation "map" where I and S nuclei with a strong enough dipolar coupling (i.e. a close spatial proximity) will show a correlation peak. More details on this sequence will be given during Chapter III, which uses it extensively.

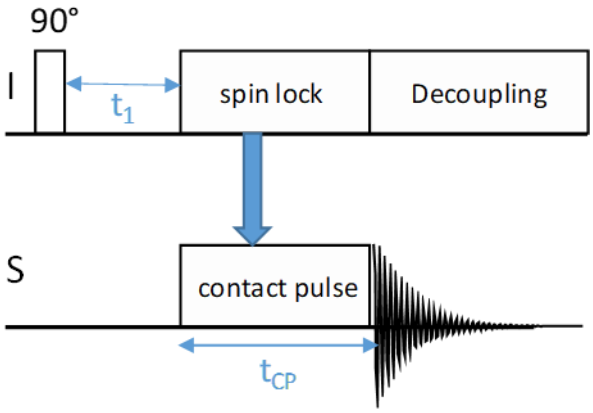


*Figure 19: 2D CP-HETCOR sequence with heteronuclear decoupling during the acquisition.*

### IV.3.2. D-HMQC

For quadrupolar nuclei, the CP sequence can be inefficient for polarization transfer. In those cases, rotor-synchronized dipolar recoupling sequences can be employed in a similar manner to create a heteronuclear correlation spectrum. Based on the ubiquitous HMQC[112] sequence (relying on J coupling), the D-HMQC (Dipolar Heteronuclear Multi-Quantum Correlation, Figure 20) uses an $SR4_1^2$ recoupling block[113] on the I nucleus, which reintroduces heteronuclear dipolar couplings without additional homonuclear couplings. The D-HMQC is particularly suited to the correlation between abundant spin ½ nuclei and quadrupolar nuclei, and has the advantage of requiring no prior optimization on the S nucleus, of importance for insensitive nuclei.[114,115]

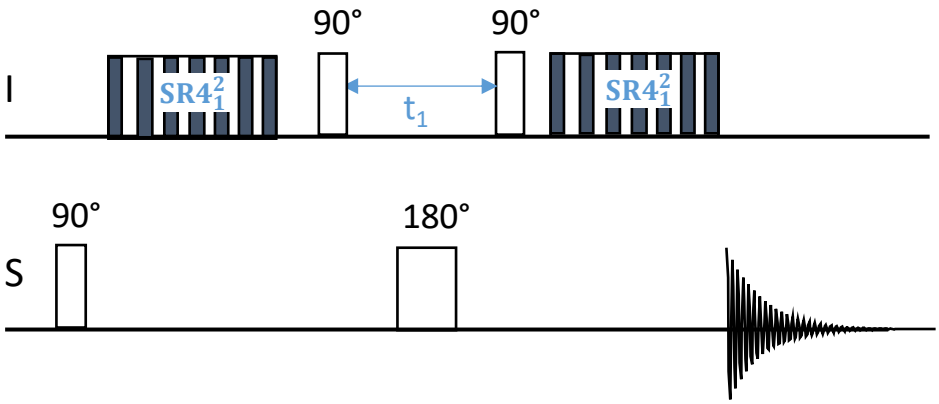


*Figure 20: 2D D-HMQC sequence. S corresponds to the quadrupolar nucleus, the recoupling block is applied to the I = ½ nucleus.*

### IV.3.3. D-RINEPT

Similarly to the D-HMQC sequence, the D-RINEPT[116] sequence (Figure 21) provides a second method to record HETCOR experiments between spin ½ and quadrupolar nuclei. Although slightly more complex than the D-HMQC sequence, it provides an alternative which can prove to be experimentally more robust.[117]

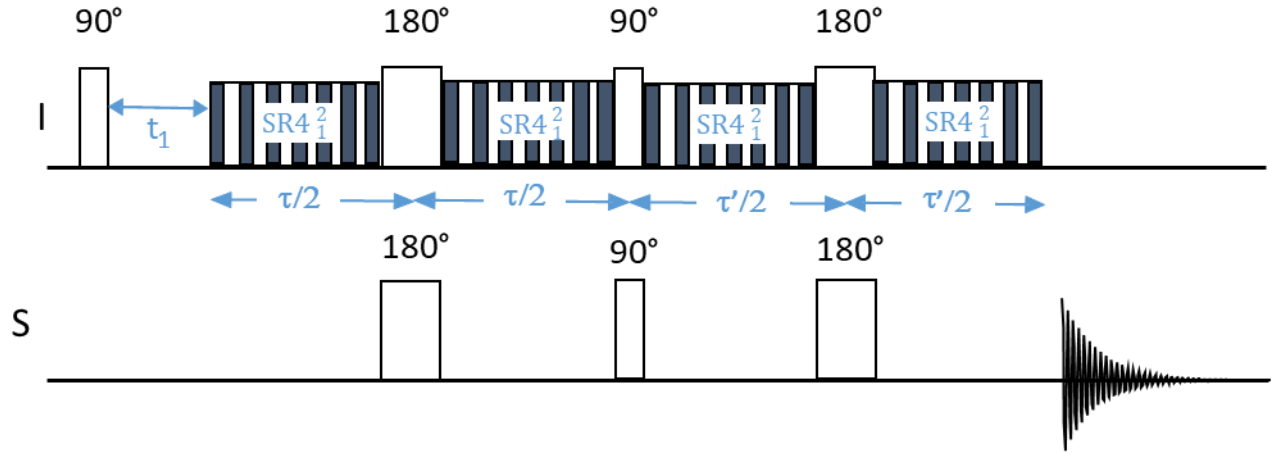


*Figure 21: 2D D-RINEPT sequence. I = ½, S > ½*

## IV.4. DNP (Dynamic Nuclear Polarization)

The DNP method is an extremely powerful method for the enhancement of NMR signals. It relies on transferring the polarization from unpaired electrons to nuclei in a solid. Although the discovery of the DNP effect is nearly as old as the field of NMR itself,[118,119] DNP-NMR took over half a century to gain its importance in solid-state NMR. The method was used for MAS NMR in 1985[120] and 1992,[121] but was not applicable at magnetic fields such as those being used in solid-state NMR spectroscopy. This changed with the pioneering work of Griffin *et al*.[122,123], who extended its use to higher fields. DNP-enhanced NMR would then underwent a period of rapid growth in the 2010s, with the commercialization of DNP systems. DNP-NMR

has emerged as a method of choice for NMR in a number of extremely insensitive systems, reducing acquisition times by three to six order of magnitudes.

The most widespread method for using DNP in the case of solid-state NMR applications relies on the introduction of a nitroxide biradial in close contact with the sample. This radical is dissolved in a matrix / solvent, which is then impregnated onto the sample. An NMR spectrometer connected to a gyrotron then saturates the electron spin populations with a high-power microwave beam. Thanks to the Overhauser effect, the polarization can be transferred to nearby nuclei (usually $^{1}H$), which can then be used in any number of experiments. For this transfer to be effective, the sample must be cooled to temperatures near or below 100 K. This requires, in addition to the gyrotron, a set of specialized low-temperature probes that spin the sample using cold $N_2$ gas. DNP-enhanced NMR is at the moment of wring of this manuscript generally carried out at lower fields (≤ 9.4 T) and moderate MAS rates (≤ 40 kHz), above which the efficiency of common radicals drops precipitously.[124]

Although the $^{1}H$ theoretical magnetization gain is close to 660,[125] the effective increase varies from tens to hundreds. DNP is a highly sample-dependent method, which relies on the interaction between the sample and radical, which can only be determined experimentally. Therefore, finding the best combination of radical, radical concentration and matrix is an essential step in DNP studies. In chapter II and IV, we used the newly-developed radical AsymPol-POK[126] (Figure 22) to enhance the polarization of biominerals.

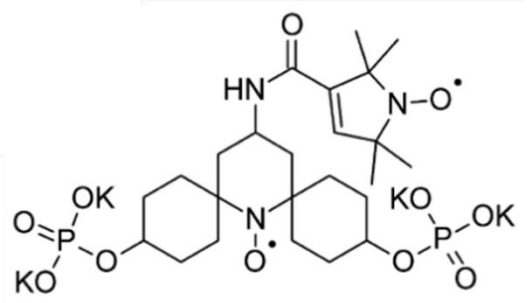


*Figure 22: The structure of the AsymPol-POK biradical, from Metink-Vigier* et al.[126]

# V. Predicting NMR parameters

Solid-state NMR is a powerful analytical technique to resolve the different chemical environments in a solid. However, linking these experimental measurements back to the local structure that they arose from can be challenging. This is because the NMR parameters are linked to the local magnetic field at the nucleus, which is influenced by the density of the electron cloud. Therefore, the possible correlations with the geometrical environment are not always straightforward. Predicting the electronic state of the system would therefore allow the calculation of the NMR parameters for a specific local environment in a structure.

Unfortunately, there is no analytical solution for the electron density in all but the most trivial of systems (a single hydrogen atom). In complex systems composed of a large number of electrons, the most we can do is approximate the electron density. A number of methods exist to compute this approximation, with the most common being Density Functional Theory (DFT).

## V.1. DFT

DFT is based on the theorems of Hohenberg and Kohn.[127] These state that (i) the external potential of a system is a unique functional of the electron density and (ii) The energy content of the Hamiltonian is minimized only when the electron density is that of the ground state. Therefore, the average value of an observable can be entirely determined by a calculation of the electron density n(**r**). The total energy of system can then be defined as:

$$E^{HK}[n] = F[n] + \int \mathrm{V_{ext}}(\mathbf{r}) n(\boldsymbol{r}) \mathrm{d}\boldsymbol{r}$$

with

$$F[n] = T[n] + V_{ee}[n]$$

With $T[n]$ the kinetic energy and $V_{ee}[n]$ the electron repulsion energy. In non-trivial cases, no analytical solution is known for $[n]$.

The Kohn-Sham[128] equations strive to simplify the problem of calculating the ground-state electronic density. The approximation reduces the problem by neglecting the interactions between electrons ($\mathrm{V_{ext}}$) and replacing them with an effective potential where the kinetic energy of the electrons can be expressed analytically ($\mathrm{T_s}$). Neglecting the interaction between electrons has a significant impact on the total energy of the system, which is corrected by an approximated expression called the exchange-correlation functional ($E_{xc}[n]$). This new term is meant to account for two effects: the exchange effects (repulsion between electrons of the same spin projection) and correlation effects (negative interaction between electrons of opposite spins). The earlier expression can then be decomposed into three terms:

$$F[n] = T_S[n] + E_H[n] + E_{xc}[n]$$

with $E_H[n]$ the Hartree energy (coulombic interaction between two electrons).

Although $T_S[n]$ and $E_H[n]$ can be determined analytically, $E_{xc}[n]$ can only be approximated. A number of methods exist for this purpose. In practice, the choice of exchange-correlation functional is highly system-dependent, as no single method is accurate in all circumstances.

The simplest of the density functionals all is the LDA (Local Density Approximation).[129] In this method, the energy of an infinitesimal volume depends solely on the electron density at that point, and is proportional to the energy of an electron gas of the same density:

$$E_{xc}^{LDA}[n] = \int n(\boldsymbol{r})\, \varepsilon_{xc}\,(n(\boldsymbol{r}))\mathrm{d}\boldsymbol{r}$$

where $\varepsilon_{xc}$ and is the exchange-correlation energy per particle of a homogenous electron gas of charge density $n$. LDA is the basis for a large family of functionals, which expand on this initial approximation to increase the accuracy of the results.

One step in that direction is the Generalized Gradient Approximation (GGA).[130] These formulas link the exchange-correlation energy to the electronic density $n(\boldsymbol{r})$ and its gradient $\nabla n(r)$.

$$E_{xc}^{GGA}[n] = \int n(\boldsymbol{r})\, \varepsilon_{xc}\left(n(r)\right), |\nabla n(r)|\mathrm{d}\boldsymbol{r}$$

Chief among them is the Perdew, Burke and Ernzerhof (PBE)[131] functional. This method is particularly pertinent for NMR as it gives generally accurate results in particular thanks to reliable determination of bond lengths and angles.

### V.2. NMR calculations

To translate these DFT calculations of electronic density into a set of NMR parameters, we must be able to calculate the electric field-gradient (EFG) at the nucleus. Because of the requirement for orthogonality, DFT wave functions vary strongly in proximity to the nucleus. To accurately map these features, we require a very large set of plane waves, which is computationally costly. This can be avoided thanks to the projector augmented-wave method (PAW).[132] In this method, the atomic potential is abstracted to a pseudopotential that approximates its effect on the free-electron gas. Using this method, Petrilli *et al.*[133] were able to calculate the EFG tensor E(**r**):

$$E(\boldsymbol{r}) = \int d^3\boldsymbol{r}.\, n(\boldsymbol{r}') \times \frac{\boldsymbol{r}-\boldsymbol{r}'}{|\boldsymbol{r}-\boldsymbol{r}'|^3}$$

For I > ½ nuclei, the EFG tensor gives information about the quadrupolar parameters of the nucleus. By convention, the three values obtained from the diagonalization of the 3*3 tensor are denoted $V_{zz}$, $V_{xx}$ and $V_{yy}$ with $|V_{zz}| \geq |V_{xx}| \geq |V_{yy}|$. The quadrupolar interaction is then expressed through the values of the quadrupolar coupling constant $C_Q = eQV_{zz}/h$ ith the quadrupole moments Q taken from recent experimental measurements [135–137] and the asymmetry parameter $\eta_Q = (V_{yy} - V_{xx})/V_{zz}$.

For periodic systems, the PAW approach can be extended to the Gauge-Including Projector Augmented Wavefunction (GIPAW).[134] This method, unlike PAW is translationally invarient in the presence of a uniform magnetic field, which is essential for NMR calculations in periodic systems. This allows us to accurately calculate the expected magnetic resonance properties in a crystalline system in a computationally efficient manner. The magnetic shielding tensor $\sigma(\boldsymbol{r})$ can then be calculated from the induced magnetic field $B_{ind}(\boldsymbol{r})$, which is obtained from the current density at the first order ($j^{(1)}(\boldsymbol{r})$). Since the variations induced by the external field $B_0$ on the wave functions are small, $j^{(1)}(\boldsymbol{r})$ can be obtained using a perturbative method.

This is established by the Biot-Savart relation:

$$B_{ind}(\boldsymbol{r}) = \frac{1}{c}\int d\boldsymbol{r}' j^{(1)}(\boldsymbol{r}') \times \frac{\boldsymbol{r}-\boldsymbol{r}'}{|\boldsymbol{r}-\boldsymbol{r}'|^3}$$

with $c$ the light velocity.

The shielding tensor is then given by:

$$\sigma(\boldsymbol{r}) = -B_{ind}/B_{ext}$$

It is then diagonalized into its three principal components ($\sigma_{11}$, $\sigma_{22}$, and $\sigma_{33}$), which describe the chemical shift anisotropy at the site. The average of the three components is the isotropic magnetic shielding $\sigma_{\mathrm{iso}}^{\mathrm{calc}}$. The isotropic chemical shift can finally be obtained as:

$$\delta_{\mathrm{iso}}^{\mathrm{calc}} = \frac{-(\sigma_{\mathrm{iso}}^{\mathrm{calc}} - \sigma_{\mathrm{ref}})}{1-\sigma_{\mathrm{ref}}} \approx -(\sigma_{\mathrm{iso}}^{\mathrm{calc}} - \sigma_{\mathrm{ref}})$$

with $\sigma_{\mathrm{ref}}$ a reference magnetic shielding, common for a set of compounds. This is calculated from a series of reference compounds as detailed in the next part.

### V.3. Application of GIPAW DFT calculations to bone-related biominerals

The first relevant study was conducted in 2007 by Pourpoint *et al.*[138] and reviewed in 2011.[139] This involved the study of a variety of minerals of interest in the field of biominerals. The compounds included a wide range of phosphates with different degrees of hydration, to estimate the accuracy of the method when estimating $^{1}$H, $^{17}$O and $^{31}$P NMR parameters. The study concluded a generally good agreement between experimental and calculated data. Notably absent from this study was our compound of interest for the next chapter, octacalcium phosphate (OCP). A purely $^{31}$P study of its NMR parameters would be proposed in 2012 by Ashbrook, Duer and co-workers,[140] which will be examined in more detail later-on.

GIPAW was used to calculate NMR parameters on a relaxed slab (~ 16 Å thick) of HAp showing that $OH^-$ groups experienced large rotations (up to 70°) at the surface. The range of the calculated $\delta_{iso}(^{31}P)$ was calculated to be ~ 11 ppm, compared to ~ 1 ppm for bulk HAp, suggesting that these values are highly sensitive to the local geometry, especially near the surface.[141] The method was also applied to the study of carbonate substitutions in apatites.[142–144] These mechanisms can be difficult to probe even with the information from IR spectroscopies and diffraction experiments. Here, NMR and GIPAW helped bridge the informational gap and provide useful information to help the identification of the different substitution mechanisms.

In addition to phosphates, pyrophosphates, which are present in pathological calcifications, would see the application of computational methods for NMR. The first example we can site comes from P. Gras[145] *et al.* in 2016. Through the study of amorphous and hydrated phases, it was established that the agreement of calculations with experimental parameters is generally good. Yet it was also shown that major discrepancies existed in the case of hydrates, which was explained by the existence of molecular motion in the solids. This would be followed by

studies[146,147] which would yet again highlight the value of combined experimental and computational methods.

The study of $^{43}Ca$ NMR parameters began in 2008 with Bryce *et al.*, who investigated them in $CaCO_3$ polymorphs (calcite, aragonite, vaterite), with a combination of high-field observations and DFT/GIPAW calculations.[148] $^{43}Ca$ continued to be a structural probe in the high-field investigation of monetite ($CaHPO_4$),[149] and in the study of intercalated metabolic acids in OCP.[150]

However, the difficulty of predicting NMR parameters in the case of hydrates would be once again apparent in a study of calcium-oxalates by Goldberga *et al*.[151] In this study, careful consideration was given to the influence of molecular dynamics on the NMR parameters, which was found to be significant. This highlights a shift in the approaches to NMR crystallography: as the study of simple crystals are being replaced by study of complex hydrates and disordered systems, researchers are developing methods to compensate for the inherent fluctuations of the new systems, particularly with temperature.

Various methods have been applied to account for the variations of NMR parameters with temperature.[152] As methods like GIPAW cannot be directly applied to a system in motion, we must describe it using a series of systems displaced by molecular motion. The new structures can be generated using several methods:

i) The introduction of vibrational modes (usually in molecular crystals) using the quasi-harmonic wavefunction vibration approximation[153,154] or vibration configuration interactions.[155]
ii) The introduction of phonon modes to perturb the system.[156,157]

These methods have the advantage of rapidly converging the averaged calculated properties, therefore requiring few configurations. On the other hand, it quickly becomes difficult to generate these configurations for large systems.

iii) For more complex systems, the use of a molecular dynamics (MD) simulation in the Born-Oppenheimer approximation is a possibility. This significantly lowers the computational cost compared to the previous methods, at the cost of information on long time-scales.[158–162]

We note that compared to the calculation of the NMR parameters of a static crystal, these methods are computationally costly and add an additional level of complexity to the study since the number of configurations is restricted. In the case of MD, timescale and sampling of the molecular motion can be adjusted in a limited range. Yet, these methods are proving unavoidable for the study of dynamical effects. A practical application will be shown in the following chapter.

## VI. References


(1) Berendsen, A. D.; Olsen, B. R. Bone Development. *Bone* **2015**, *80*, 14–18. https://doi.org/10.1016/j.bone.2015.04.035.

(2) Murdock, D. J. E.; Dong, X.-P.; Repetski, J. E.; Marone, F.; Stampanoni, M.; Donoghue, P. C. J. The Origin of Conodonts and of Vertebrate Mineralized Skeletons. *Nature* **2013**, *502* (7472), 546–549. https://doi.org/10.1038/nature12645.

(3) Zhang, G. An Evo-Devo View on the Origin of the Backbone: Evolutionary Development of the Vertebrae. *Integrative and Comparative Biology* **2009**, *49* (2), 178–186. https://doi.org/10.1093/icb/icp061.

(4) Brazeau, M. D.; Friedman, M. The Origin and Early Phylogenetic History of Jawed Vertebrates. *Nature* **2015**, *520* (7548), 490–497. https://doi.org/10.1038/nature14438.

(5) Quelch, K. J.; Melick, R. A.; Bingham, P. J.; Mercuri, S. M. Chemical Composition of Human Bone. *Archives of Oral Biology* **1983**, *28* (8), 665–674. https://doi.org/10.1016/0003-9969(83)90100-0.

(6) Sophia Fox, A. J.; Bedi, A.; Rodeo, S. A. The Basic Science of Articular Cartilage: Structure, Composition, and Function. *Sports Health* **2009**, *1* (6), 461–468. https://doi.org/10.1177/1941738109350438.

(7) Zapata, A. G. The Fish Spleen. *Fish & Shellfish Immunology* **2024**, *144*, 109280. https://doi.org/10.1016/j.fsi.2023.109280.

(8) Clarke, B. Normal Bone Anatomy and Physiology. *Clinical Journal of the American Society of Nephrology* **2008**, *3* (Supplement_3), S131. https://doi.org/10.2215/CJN.04151206.

(9) Maia Ferreira Alencar, C. H.; Sampaio Silveira, C. R.; Cavalcante, M. M.; Maia Vieira, C. G.; Diógenes Teixeira, M. J.; Neto, F. A.; de Abreu, A.; Chhabra, A. "Periosteum: An Imaging Review." *European Journal of Radiology Open* **2020**, *7*, 100249. https://doi.org/10.1016/j.ejro.2020.100249.

(10) Reznikov, N.; Shahar, R.; Weiner, S. Bone Hierarchical Structure in Three Dimensions. *Acta Biomaterialia* **2014**, *10* (9), 3815–3826. https://doi.org/10.1016/j.actbio.2014.05.024.

(11) Chang, B.; Liu, X. Osteon: Structure, Turnover, and Regeneration. *Tissue Eng Part B Rev* **2022**, *28* (2), 261–278. https://doi.org/10.1089/ten.teb.2020.0322.

(12) Liu, Y.; Luo, D.; Wang, T. Hierarchical Structures of Bone and Bioinspired Bone Tissue Engineering. *Small* **2016**, *12* (34), 4611–4632. https://doi.org/10.1002/smll.201600626.

(13) Reznikov, N.; Bilton, M.; Lari, L.; Stevens, M. M.; Kröger, R. Fractal-like Hierarchical Organization of Bone Begins at the Nanoscale. *Science* **2018**, *360* (6388), eaao2189. https://doi.org/10.1126/science.aao2189.

(14) Mankin, H. J. Metabolic Bone Disease. *JBJS* **1994**, *76* (5), 760.

(15) Hochberg, Z.; Hochberg, I. Evolutionary Perspective in Rickets and Vitamin D. *Front. Endocrinol.* **2019**, *10*. https://doi.org/10.3389/fendo.2019.00306.

(16) Rajakumar, K.; Greenspan, S. L.; Thomas, S. B.; Holick, M. F. SOLAR Ultraviolet Radiation AND Vitamin D. *Am J Public Health* **2007**, *97* (10), 1746–1754. https://doi.org/10.2105/AJPH.2006.091736.

(17) Pouresmaeili, F.; Kamalidehghan, B.; Kamarehei, M.; Goh, Y. M. A Comprehensive Overview on Osteoporosis and Its Risk Factors. *Therapeutics and Clinical Risk Management* **2018**, *14*, 2029–2049. https://doi.org/10.2147/TCRM.S138000.

(18) Riggs, B. L.; Melton, L. J. The Worldwide Problem of Osteoporosis: Insights Afforded by Epidemiology. *Bone* **1995**, *17* (5, Supplement 1), S505–S511. https://doi.org/10.1016/8756-3282(95)00258-4.
(19) Chung, P. Y. J.; Van Hul, W. Paget's Disease of Bone: Evidence for Complex Pathogenetic Interactions. *Semin Arthritis Rheum* **2012**, *41* (5), 619–641. https://doi.org/10.1016/j.semarthrit.2011.07.005.
(20) Mills, B. G.; Singer, F. R.; Weiner, L. P.; Holst, P. A. Immunohistological Demonstration of Respiratory Syncytial Virus Antigens in Paget Disease of Bone. *Proc Natl Acad Sci U S A* **1981**, *78* (2), 1209–1213.
(21) Forlino, A.; Marini, J. C. Osteogenesis Imperfecta. *The Lancet* **2016**, *387* (10028), 1657–1671. https://doi.org/10.1016/S0140-6736(15)00728-X.
(22) McCabe, L. R. Understanding the Pathology and Mechanisms of Type I Diabetic Bone Loss. *Journal of Cellular Biochemistry* **2007**, *102* (6), 1343–1357. https://doi.org/10.1002/jcb.21573.
(23) Hygum, K.; Starup-Linde, J.; Langdahl, B. L. Diabetes and Bone. *Osteoporosis and Sarcopenia* **2019**, *5* (2), 29–37. https://doi.org/10.1016/j.afos.2019.05.001.
(24) Shu, A.; Yin, M. T.; Stein, E.; Cremers, S.; Dworakowski, E.; Ives, R.; Rubin, M. R. Bone Structure and Turnover in Type 2 Diabetes Mellitus. *Osteoporos Int* **2012**, *23* (2), 635–641. https://doi.org/10.1007/s00198-011-1595-0.
(25) Tanaka, S.; Avigad, G.; Brodsky, B.; Eikenberry, E. F. Glycation Induces Expansion of the Molecular Packing of Collagen. *Journal of Molecular Biology* **1988**, *203* (2), 495–505. https://doi.org/10.1016/0022-2836(88)90015-0.
(26) Bai, P.; Phua, K.; Hardt, T.; Cernadas, M.; Brodsky, B. Glycation Alters Collagen Fibril Organization. *Connective Tissue Research* **1992**, *28* (1–2), 1–12. https://doi.org/10.3109/03008209209014224.
(27) Vashishth, D.; Gibson, G. J.; Khoury, J. I.; Schaffler, M. B.; Kimura, J.; Fyhrie, D. P. Influence of Nonenzymatic Glycation on Biomechanical Properties of Cortical Bone. *Bone* **2001**, *28* (2), 195–201. https://doi.org/10.1016/S8756-3282(00)00434-8.
(28) Snedeker, J. G.; Gautieri, A. The Role of Collagen Crosslinks in Ageing and Diabetes - the Good, the Bad, and the Ugly. *Muscles Ligaments Tendons J* **2014**, *4* (3), 303–308.
(29) Geraldo, L. H. M.; Spohr, T. C. L. de S.; Amaral, R. F. do; Fonseca, A. C. C. da; Garcia, C.; Mendes, F. de A.; Freitas, C.; dosSantos, M. F.; Lima, F. R. S. Role of Lysophosphatidic Acid and Its Receptors in Health and Disease: Novel Therapeutic Strategies. *Sig Transduct Target Ther* **2021**, *6* (1), 1–18. https://doi.org/10.1038/s41392-020-00367-5.
(30) Tokumura, A. Metabolic Pathways and Physiological and Pathological Significances of Lysolipid Phosphate Mediators. *Journal of Cellular Biochemistry* **2004**, *92* (5), 869–881. https://doi.org/10.1002/jcb.20147.
(31) Akasaka, H.; Tanaka, T.; Sano, F. K.; Matsuzaki, Y.; Shihoya, W.; Nureki, O. Structure of the Active Gi-Coupled Human Lysophosphatidic Acid Receptor 1 Complexed with a Potent Agonist. *Nat Commun* **2022**, *13* (1), 5417. https://doi.org/10.1038/s41467-022-33121-2.
(32) Sheng, X.; Yung, Y. C.; Chen, A.; Chun, J. Lysophosphatidic Acid Signalling in Development. *Development* **2015**, *142* (8), 1390–1395. https://doi.org/10.1242/dev.121723.
(33) van der Bend, R. L.; Brunner, J.; Jalink, K.; van Corven, E. J.; Moolenaar, W. H.; van Blitterswijk, W. J. Identification of a Putative Membrane Receptor for the Bioactive

Phospholipid, Lysophosphatidic Acid. *The EMBO Journal* **1992**, *11* (7), 2495–2501. https://doi.org/10.1002/j.1460-2075.1992.tb05314.x.
(34) Choi, J. W.; Lee, C.-W.; Chun, J. Biological Roles of Lysophospholipid Receptors Revealed by Genetic Null Mice: An Update. *Biochimica et Biophysica Acta (BBA) - Molecular and Cell Biology of Lipids* **2008**, *1781* (9), 531–539. https://doi.org/10.1016/j.bbalip.2008.03.004.
(35) Grey, A.; Banovic, T.; Naot, D.; Hill, B.; Callon, K.; Reid, I.; Cornish, J. Lysophosphatidic Acid Is an Osteoblast Mitogen Whose Proliferative Actions Involve G(i) Proteins and Protein Kinase C, but Not P42/44 Mitogen-Activated Protein Kinases. *Endocrinology* **2001**, *142* (3), 1098–1106. https://doi.org/10.1210/endo.142.3.8011.
(36) Liu, Y.-B.; Kharode, Y.; Bodine, P. V. N.; Yaworsky, P. J.; Robinson, J. A.; Billiard, J. LPA Induces Osteoblast Differentiation through Interplay of Two Receptors: LPA1 and LPA4. *Journal of Cellular Biochemistry* **2010**, *109* (4), 794–800. https://doi.org/10.1002/jcb.22471.
(37) Gennero, I.; Laurencin-Dalicieux, S.; Conte-Auriol, F.; Briand-Mésange, F.; Laurencin, D.; Rue, J.; Beton, N.; Malet, N.; Mus, M.; Tokumura, A.; Bourin, P.; Vico, L.; Brunel, G.; Oreffo, R. O. C.; Chun, J.; Salles, J. P. Absence of the Lysophosphatidic Acid Receptor LPA1 Results in Abnormal Bone Development and Decreased Bone Mass. *Bone* **2011**, *49* (3), 395–403. https://doi.org/10.1016/j.bone.2011.04.018.
(38) Leeuwenhoek, A. van. Microscopical Observations from Leeuwenhoeck, Concerning Blood, Milk, Bones, the Brain, Spitle, and Cuticula, &c. Communicated by the Said Observer to the Publisher in a Letter, Dated June 1. 1674. *Philosophical Transactions of the Royal Society of London* **1997**, *9* (106), 121–131. https://doi.org/10.1098/rstl.1674.0030.
(39) Havers, C. *Osteologia Nova, or Some New Observations of the Bones and Parts Belonging to Them with the Manner of Their Accretion and Nutrition. To Which Is Added a Fifth Discourse of the Cartilages.*; 1691.
(40) Dorozhkin, S. V. A Detailed History of Calcium Orthophosphates from 1770s till 1950. *Materials Science and Engineering: C* **2013**, *33* (6), 3085–3110. https://doi.org/10.1016/j.msec.2013.04.002.
(41) Scheele, C. W. *The Collected Papers of Carl Wilhelm Scheele*; G. Bell & Sons Limited, 1931.
(42) Bibra, F. E. von. *Chemische Untersuchungen Über Die Knochen Und Zähne Des Menschen Und Der Wirbelthiere: Mit Rücksichtnahme Auf Ihre Physiologischen Und Pathologischen Verhältnisse*; im verlage des Kunstverlags, 1844.
(43) de Jong, W. F. La Substance Minérale Dans Les Os. *Recueil des Travaux Chimiques des Pays-Bas* **1926**, *45* (6), 445–448. https://doi.org/10.1002/recl.19260450613.
(44) Möller, H.; Trömel, G. Röntgenographische Untersuchung über den Aufbau der anorganischen Zahnsubstanz. *Naturwissenschaften* **1933**, *21* (19), 346–348. https://doi.org/10.1007/BF01504488.
(45) Möller, H.; Trömel, G. Über die Kristallorientierung im Zahnschmelz. *Naturwissenschaften* **1936**, *24* (24), 377–378. https://doi.org/10.1007/BF01474771.
(46) Schmidt, C. L. A.; Greenberg, D. M. Occurrence, Transport and Regulation of Calcium, Magnesium and Phosphorus in the Animal Organism. *Physiological Reviews* **1935**, *15* (3), 297–434. https://doi.org/10.1152/physrev.1935.15.3.297.
(47) Hendricks, S. B.; Jefferson, M. E.; Mosley, V. M. The Crystal Structures of Some Natural and Synthetic Apatite-Like Substances. *Zeitschrift für Kristallographie -*

*Crystalline Materials* **1932**, *81* (1–6), 352–369. https://doi.org/10.1524/zkri.1932.81.1.352.
(48) Mehmel, M. Beziehungen zwischen Kristallstruktur und chemischer Formel des Apatits. *Zeitschrift für Physikalische Chemie* **1932**, *15B* (1), 223–241. https://doi.org/10.1515/zpch-1932-1517.
(49) Náray-Szabó, St. 27. The Structure of Apatite (CaF)$Ca_4(PO4)_3$. *Zeitschrift für Kristallographie - Crystalline Materials* **1930**, *75* (1), 387–398. https://doi.org/10.1515/zkri-1930-0129.
(50) McConnell, D. A Structural Investigation of the Isomorphism of the Apatite Group. *American Mineralogist* **1938**, *23* (1), 1–19.
(51) McConnell, D. The Problem of the Carbonate Apatites. IV. Structural Substitutions Involving CO3 and OH. **1952**. https://doi.org/10.3406/bulmi.1952.4786.
(52) Robinson, R. A. AN ELECTRON-MICROSCOPIC STUDY OF THE CRYSTALLINE INORGANIC COMPONENT OF BONE AND ITS RELATIONSHIP TO THE ORGANIC MATRIX. *JBJS* **1952**, *34* (2), 389.
(53) Neuman, W. F.; Neuman, M. W. The Nature of the Mineral Phase of Bone. *Chem. Rev.* **1953**, *53* (1), 1–45. https://doi.org/10.1021/cr60164a001.
(54) Pasteris, J. STRUCTURALLY INCORPORATED WATER IN BONE APATITE: A CAUTIONARY TALE; Nova Science Publishers Inc: New York, NY, 2013.
(55) Zapanta LeGeros, R. Apatites in Biological Systems. *Progress in Crystal Growth and Characterization* **1981**, *4* (1), 1–45. https://doi.org/10.1016/0146-3535(81)90046-0.
(56) Rey, C.; Collins, B.; Goehl, T.; Dickson, I. R.; Glimcher, M. J. The Carbonate Environment in Bone Mineral: A Resolution-Enhanced Fourier Transform Infrared Spectroscopy Study. *Calcif Tissue Int* **1989**, *45* (3), 157–164. https://doi.org/10.1007/BF02556059.
(57) Sauer, G. R.; Zunic, W. B.; Durig, J. R.; Wuthier, R. E. Fourier Transform Raman Spectroscopy of Synthetic and Biological Calcium Phosphates. *Calcif. Tissue Int.* **1994**, *54* (5), 414–420. https://doi.org/10.1007/BF00305529.
(58) Wilson, R. M.; Elliott, J. C.; Dowker, S. E. P.; Smith, R. I. Rietveld Structure Refinement of Precipitated Carbonate Apatite Using Neutron Diffraction Data. *Biomaterials* **2004**, *25* (11), 2205–2213. https://doi.org/10.1016/j.biomaterials.2003.08.057.
(59) Fleet, M. E.; Liu, X. Location of Type B Carbonate Ion in Type A–B Carbonate Apatite Synthesized at High Pressure. *Journal of Solid State Chemistry* **2004**, *177* (9), 3174–3182. https://doi.org/10.1016/j.jssc.2004.04.002.
(60) Leventouri, T.; Chakoumakos, B. C.; Papanearchou, N.; Perdikatsis, V. Comparison of Crystal Structure Parameters of Natural and Synthetic Apatites from Neutron Powder Diffraction. *Journal of Materials Research* **2001**, *16* (9), 2600–2606. https://doi.org/10.1557/JMR.2001.0357.
(61) Rey, C.; Combes, C.; Drouet, C.; Glimcher, M. J. Bone Mineral: Update on Chemical Composition and Structure. *Osteoporos Int* **2009**, *20* (6), 1013–1021. https://doi.org/10.1007/s00198-009-0860-y.
(62) Von Euw, S.; Wang, Y.; Laurent, G.; Drouet, C.; Babonneau, F.; Nassif, N.; Azaïs, T. Bone Mineral: New Insights into Its Chemical Composition. *Sci Rep* **2019**, *9* (1), 8456. https://doi.org/10.1038/s41598-019-44620-6.
(63) Myers, H. M. Wide Line Nuclear Magnetic Resonance (NMR) Studies on Enamel. *Experimental Cell Research* **1965**, *38* (3), 686–688. https://doi.org/10.1016/0014-4827(65)90397-6.

(64) Dibdin, G. H. The Stability of Water in Human Dental Enamel Studied by Proton Nuclear Magnetic Resonance. *Archives of Oral Biology* **1972**, *17* (3), 433–437. https://doi.org/10.1016/0003-9969(72)90058-1.
(65) Heimann, R. B. *Calcium Phosphate: Structure, Synthesis, Properties, and Applications*, 1st Edition.; Nova Science Publishers Inc: New York, NY, 2013.
(66) Roufosse, A. H.; Landis, W. J.; Sabine, W. K.; Glimcher, M. J. Identification of Brushite in Newly Deposited Bone Mineral from Embryonic Chicks. *Journal of Ultrastructure Research* **1979**, *68* (3), 235–255. https://doi.org/10.1016/S0022-5320(79)90157-6.
(67) Maudsley, A. A.; Ernst, R. R. Indirect Detection of Magnetic Resonance by Heteronuclear Two-Dimensional Spectroscopy. *Chemical Physics Letters* **1977**, *50* (3), 368–372. https://doi.org/10.1016/0009-2614(77)80345-X.
(68) Roufosse, A. H.; Aue, W. P.; Roberts, J. E.; Glimcher, M. J.; Griffin, R. G. Investigation of Mineral Phases of Bone by Solid-State Phosphorus-31 Magic-Angle Sample-Spinning Nuclear Magnetic Resonance. *Biochemistry* **1984**, *23* (25), 6115–6120. https://doi.org/10.1021/bi00320a033.
(69) Aue, W. P.; Roufosse, A. H.; Glimcher, M. J.; Griffin, R. G. Solid-State Phosphorus-31 Nuclear Magnetic Resonance Studies of Synthetic Solid Phases of Calcium Phosphate: Potential Models of Bone Mineral. *Biochemistry* **1984**, *23* (25), 6110–6114. https://doi.org/10.1021/bi00320a032.
(70) Glimcher, M. J.; Muir, H.; Miller, A.; Phillips, D. C.; Williams, R. J. P. Recent Studies of the Mineral Phase in Bone and Its Possible Linkage to the Organic Matrix by Protein-Bound Phosphate Bonds. *Philosophical Transactions of the Royal Society of London. B, Biological Sciences* **1998**, *304* (1121), 479–508. https://doi.org/10.1098/rstb.1984.0041.
(71) Brown, C. E.; Allaway, J. R.; Brown, K. L.; Battocletti, J. H. Noninvasive Evaluation of Mineral Content of Bone without Use of Ionizing Radiation. *Clinical Chemistry* **1987**, *33* (2), 227–236. https://doi.org/10.1093/clinchem/33.2.227.
(72) Brown, C. E.; Battocletti, J. H.; Srinivasan, R.; Allaway, J. R.; Moore, J.; Sigmann, P. In Vivo 31P Nuclear Magnetic Resonance Spectroscopy of Bone Mineral for Evaluation of Osteoporosis. *Clinical Chemistry* **1988**, *34* (7), 1431–1438. https://doi.org/10.1093/clinchem/34.7.1431.
(73) Cao, H.; Nazarian, A.; Ackerman, J. L.; Snyder, B. D.; Rosenberg, A. E.; Nazarian, R. M.; Hrovat, M. I.; Dai, G.; Mintzopoulos, D.; Wu, Y. Quantitative 31P NMR Spectroscopy and 1H MRI Measurements of Bone Mineral and Matrix Density Differentiate Metabolic Bone Diseases in Rat Models. *Bone* **2010**, *46* (6), 1582–1590. https://doi.org/10.1016/j.bone.2010.02.020.
(74) Kassey, V. B.; Walle, M.; Egan, J.; Yeritsyan, D.; Beeram, I.; Wu, Y.; Snyder, B. D.; Rodriguez, E. K.; Ackerman, J. L.; Nazarian, A. Quantitative 31P Magnetic Resonance Imaging on Pathologic Rat Bones by ZTE at 7T. *Bone* **2024**, *180*, 116996. https://doi.org/10.1016/j.bone.2023.116996.
(75) Yon, M.; Sarou-Kanian, V.; Scheler, U.; Bouler, J.-M.; Bujoli, B.; Massiot, D.; Fayon, F. Solid-State 31P and 1H Chemical MR Micro-Imaging of Hard Tissues and Biomaterials with Magic Angle Spinning at Very High Magnetic Field. *Sci Rep* **2017**, *7* (1), 8224. https://doi.org/10.1038/s41598-017-08458-0.
(76) Miquel, J. L.; Facchini, L.; Legrand, A. P.; Marchandise, X.; Lecouffe, P.; Chanavaz, M.; Donazzan, M.; Rey, C.; Lernaitre, J. Characterisation and Conversion Study into Natural Living Bone of Calcium Phosphate Bioceramics by Solid State NMR Spectroscopy. *Clinical Materials* **1990**, *5* (2), 115–125. https://doi.org/10.1016/0267-6605(90)90011-J.

(77) Roberts, J. E.; Bonar, L. C.; Griffin, R. G.; Glimcher, M. J. Characterization of Very Young Mineral Phases of Bone by Solid State 31Phosphorus Magic Angle Sample Spinning Nuclear Magnetic Resonance and X-Ray Diffraction. *Calcif Tissue Int* **1992**, *50* (1), 42–48. https://doi.org/10.1007/BF00297296.

(78) Santos, R. A.; Wind, R. A.; Bronnimann, C. E. 1H CRAMPS and 1H-31P HetCor Experiments on Bone, Bone Mineral, and Model Calcium Phosphate Phases. *Journal of Magnetic Resonance, Series B* **1994**, *105* (2), 183–187. https://doi.org/10.1006/jmrb.1994.1120.

(79) Gerstein, B. C.; Packer, K. J.; Richards, R. E.; Packer, K. J. High-Resolution n.m.r. in Solids with Strong Homonuclear Dipolar Broadening: Combined Multiple-Pulse Decoupling and Magic Angle Spinning. *Philosophical Transactions of the Royal Society of London. Series A, Mathematical and Physical Sciences* **1981**, *299* (1452), 521–546. https://doi.org/10.1098/rsta.1981.0033.

(80) Cho, G.; Wu, Y.; Ackerman, J. L. Detection of Hydroxyl Ions in Bone Mineral by Solid-State NMR Spectroscopy. *Science* **2003**, *300* (5622), 1123–1127. https://doi.org/10.1126/science.1078470.

(81) Wu, Y.; Glimcher, M. J.; Rey, C.; Ackerman, J. L. A Unique Protonated Phosphate Group in Bone Mineral Not Present in Synthetic Calcium Phosphates: Identification by Phosphorus-31 Solid State NMR Spectroscopy. *Journal of Molecular Biology* **1994**, *244* (4), 423–435. https://doi.org/10.1006/jmbi.1994.1740.

(82) Kaflak, A.; Chmielewski, D.; Górecki, A.; Kolodziejski, W. Kinetics of $^{1}H \rightarrow ^{31}P$ Cross-Polarization in Human Trabecular Bone. *Solid State Nuclear Magnetic Resonance* **1998**, *10* (4), 191–195. https://doi.org/10.1016/S0926-2040(97)00085-4.

(83) Wilson, E. E.; Awonusi, A.; Morris, M. D.; Kohn, D. H.; Tecklenburg, M. M.; Beck, L. W. Highly Ordered Interstitial Water Observed in Bone by Nuclear Magnetic Resonance*. *Journal of Bone and Mineral Research* **2005**, *20* (4), 625–634. https://doi.org/10.1359/JBMR.041217.

(84) Levitt, M. H.; Kolbert, A. C.; Bielecki, A.; Ruben, D. J. High-Resolution 1H NMR in Solids with Frequency-Switched Multiple-Pulse Sequences. *Solid State Nuclear Magnetic Resonance* **1993**, *2* (4), 151–163. https://doi.org/10.1016/0926-2040(93)90021-E.

(85) Lin, K. S. K.; Tseng, Y.-H.; Mou, Y.; Hsu, Y.-C.; Yang, C.-M.; Chan, J. C. C. Mechanistic Study of Apatite Formation on Bioactive Glass Surface Using 31P Solid-State NMR Spectroscopy. *Chem. Mater.* **2005**, *17* (17), 4493–4501. https://doi.org/10.1021/cm050654c.

(86) Jäger, C.; Welzel, T.; Meyer-Zaika, W.; Epple, M. A Solid-State NMR Investigation of the Structure of Nanocrystalline Hydroxyapatite. *Magnetic Resonance in Chemistry* **2006**, *44* (6), 573–580. https://doi.org/10.1002/mrc.1774.

(87) Schaefer, J.; McKay, R. A.; Stejskal, E. O. Double-Cross-Polarization NMR of Solids. *Journal of Magnetic Resonance (1969)* **1979**, *34* (2), 443–447. https://doi.org/10.1016/0022-2364(79)90022-2.

(88) Laurencin, D.; Wong, A.; Dupree, R.; Smith, M. E. Natural Abundance $^{43}$Ca Solid-State NMR Characterisation of Hydroxyapatite: Identification of the Two Calcium Sites. *Magnetic Resonance in Chemistry* **2008**, *46* (4), 347–350. https://doi.org/10.1002/mrc.2117.

(89) Xu, J.; Zhu, P.; Gan, Z.; Sahar, N.; Tecklenburg, M.; Morris, M. D.; Kohn, D. H.; Ramamoorthy, A. Natural-Abundance $^{43}$Ca Solid-State NMR Spectroscopy of Bone. *J. Am. Chem. Soc.* **2010**, *132* (33), 11504–11509. https://doi.org/10.1021/ja101961x.

(90) Laurencin, D.; Wong, A.; Chrzanowski, W.; Knowles, J. C.; Qiu, D.; Pickup, D. M.; Newport, R. J.; Gan, Z.; Duer, M. J.; Smith, M. E. Probing the Calcium and Sodium Local Environment in Bones and Teeth Using Multinuclear Solid State NMR and X-Ray Absorption Spectroscopy. *Phys. Chem. Chem. Phys.* **2010**, *12* (5), 1081–1091. https://doi.org/10.1039/B915708E.
(91) Frydman, L.; Harwood, J. S. Isotropic Spectra of Half-Integer Quadrupolar Spins from Bidimensional Magic-Angle Spinning NMR. *J. Am. Chem. Soc.* **1995**, *117* (19), 5367–5368. https://doi.org/10.1021/ja00124a023.
(92) Davies, E.; Müller, K. H.; Wong, W. C.; Pickard, C. J.; Reid, D. G.; Skepper, J. N.; Duer, M. J. Citrate Bridges between Mineral Platelets in Bone. *Proceedings of the National Academy of Sciences* **2014**, *111* (14), E1354–E1363. https://doi.org/10.1073/pnas.1315080111.
(93) Beshah, K.; Rey, C.; Glimcher, M. J.; Schimizu, M.; Griffin, R. G. Solid State Carbon-13 and Proton NMR Studies of Carbonate-Containing Calcium Phosphates and Enamel. *Journal of Solid State Chemistry* **1990**, *84* (1), 71–81. https://doi.org/10.1016/0022-4596(90)90185-Z.
(94) Yasar, O. F.; Liao, W.-C.; Mathew, R.; Yu, Y.; Stevensson, B.; Liu, Y.; Shen, Z.; Edén, M. The Carbonate and Sodium Environments in Precipitated and Biomimetic Calcium Hydroxy-Carbonate Apatite Contrasted with Bone Mineral: Structural Insights from Solid-State NMR. *J. Phys. Chem. C* **2021**, *125* (19), 10572–10592. https://doi.org/10.1021/acs.jpcc.0c11389.
(95) Lee, D.; Leroy, C.; Crevant, C.; Bonhomme-Coury, L.; Babonneau, F.; Laurencin, D.; Bonhomme, C.; De Paëpe, G. Interfacial Ca2+ Environments in Nanocrystalline Apatites Revealed by Dynamic Nuclear Polarization Enhanced 43Ca NMR Spectroscopy. *Nat Commun* **2017**, *8* (1), 14104. https://doi.org/10.1038/ncomms14104.
(96) Azaïs, T.; Von Euw, S.; Ajili, W.; Auzoux-Bordenave, S.; Bertani, P.; Gajan, D.; Emsley, L.; Nassif, N.; Lesage, A. Structural Description of Surfaces and Interfaces in Biominerals by DNP SENS. *Solid State Nuclear Magnetic Resonance* **2019**, *102*, 2–11. https://doi.org/10.1016/j.ssnmr.2019.06.001.
(97) Trebosc, J.; Hu, B.; Amoureux, J. P.; Gan, Z. Through-Space R3-HETCOR Experiments between Spin-1/2 and Half-Integer Quadrupolar Nuclei in Solid-State NMR. *Journal of Magnetic Resonance* **2007**, *186* (2), 220–227. https://doi.org/10.1016/j.jmr.2007.02.015.
(98) Nikel, O.; Laurencin, D.; McCallum, S. A.; Gundberg, C. M.; Vashishth, D. NMR Investigation of the Role of Osteocalcin and Osteopontin at the Organic–Inorganic Interface in Bone. *Langmuir* **2013**, *29* (45), 13873–13882. https://doi.org/10.1021/la403203w.
(99) Hunter, G. K.; Hauschka, P. V.; Poole, A. R.; Rosenberg, L. C.; Goldberg, H. A. Nucleation and Inhibition of Hydroxyapatite Formation by Mineralized Tissue Proteins. *Biochem J* **1996**, *317* (Pt 1), 59–64.
(100) Kaflak, A.; Chmielewski, D.; Kolodziejski, W. Solid-State NMR Study of Discrete Environments of Bone Mineral Nanoparticles Using Phosphorus-31 Relaxation. *Journal of Applied Biomedicine* **2016**, *14* (4), 321–330. https://doi.org/10.1016/j.jab.2016.07.001.
(101) Zeng, P.; Fu, Y.; Pang, Y.; He, T.; Wu, Y.; Tang, R.; Qin, A.; Kong, X. Solid-State Nuclear Magnetic Resonance Identifies Abnormal Calcium Phosphate Formation in Diseased Bones. *ACS Biomater. Sci. Eng.* **2021**, *7* (3), 1159–1168. https://doi.org/10.1021/acsbiomaterials.0c01559.

(102) Buess, M. L.; Petersen, G. L. Acoustic Ringing Effects in Pulsed Nuclear Magnetic Resonance Probes. *Review of Scientific Instruments* **1978**, *49* (8), 1151–1155. https://doi.org/10.1063/1.1135538.
(103) Hahn, E. L. Spin Echoes. *Phys. Rev.* **1950**, *80* (4), 580–594. https://doi.org/10.1103/PhysRev.80.580.
(104) Cory, D. G.; Ritchey, W. M. Suppression of Signals from the Probe in Bloch Decay Spectra. *Journal of Magnetic Resonance (1969)* **1988**, *80* (1), 128–132. https://doi.org/10.1016/0022-2364(88)90064-9.
(105) Hartmann, S. R.; Hahn, E. L. Nuclear Double Resonance in the Rotating Frame. *Phys. Rev.* **1962**, *128* (5), 2042–2053. https://doi.org/10.1103/PhysRev.128.2042.
(106) Stejskal, E. O.; Schaefer, J.; Waugh, J. S. Magic-Angle Spinning and Polarization Transfer in Proton-Enhanced NMR. *Journal of Magnetic Resonance (1969)* **1977**, *28* (1), 105–112. https://doi.org/10.1016/0022-2364(77)90260-8.
(107) Anderson, W. A.; Freeman, R. Influence of a Second Radiofrequency Field on High-Resolution Nuclear Magnetic Resonance Spectra. *The Journal of Chemical Physics* **1962**, *37* (1), 85–103. https://doi.org/10.1063/1.1732980.
(108) Fung, B. M.; Khitrin, A. K.; Ermolaev, K. An Improved Broadband Decoupling Sequence for Liquid Crystals and Solids. *Journal of Magnetic Resonance* **2000**, *142* (1), 97–101. https://doi.org/10.1006/jmre.1999.1896.
(109) Thakur, R. S.; Kurur, N. D.; Madhu, P. K. Swept-Frequency Two-Pulse Phase Modulation for Heteronuclear Dipolar Decoupling in Solid-State NMR. *Chemical Physics Letters* **2006**, *426* (4), 459–463. https://doi.org/10.1016/j.cplett.2006.06.007.
(110) Bennett, A. E.; Rienstra, C. M.; Auger, M.; Lakshmi, K. V.; Griffin, R. G. Heteronuclear Decoupling in Rotating Solids. *The Journal of Chemical Physics* **1995**, *103* (16), 6951–6958. https://doi.org/10.1063/1.470372.
(111) Kentgens, A. P. M.; Verhagen, R. Advantages of Double Frequency Sweeps in Static, MAS and MQMAS NMR of Spin *I*=3/2 Nuclei. *Chemical Physics Letters* **1999**, *300* (3), 435–443. https://doi.org/10.1016/S0009-2614(98)01402-X.
(112) Bax, A.; Griffey, R. H.; Hawkins, B. L. Correlation of Proton and Nitrogen-15 Chemical Shifts by Multiple Quantum NMR. *Journal of Magnetic Resonance (1969)* **1983**, *55* (2), 301–315. https://doi.org/10.1016/0022-2364(83)90241-X.
(113) Brinkmann, A.; Kentgens, A. P. M. Proton-Selective $^{17}$O-$^{1}$H Distance Measurements in Fast Magic-Angle-Spinning Solid-State NMR Spectroscopy for the Determination of Hydrogen Bond Lengths. *J. Am. Chem. Soc.* **2006**, *128* (46), 14758–14759. https://doi.org/10.1021/ja065415k.
(114) Hu, B.; Trébosc, J.; Amoureux, J. P. Comparison of Several Hetero-Nuclear Dipolar Recoupling NMR Methods to Be Used in MAS HMQC/HSQC. *Journal of Magnetic Resonance* **2008**, *192* (1), 112–122. https://doi.org/10.1016/j.jmr.2008.02.004.
(115) Lu, X.; Lafon, O.; Trébosc, J.; Tricot, G.; Delevoye, L.; Méar, F.; Montagne, L.; Amoureux, J. P. Observation of Proximities between Spin-1/2 and Quadrupolar Nuclei: Which Heteronuclear Dipolar Recoupling Method Is Preferable? *The Journal of Chemical Physics* **2012**, *137* (14), 144201. https://doi.org/10.1063/1.4753987.
(116) Fyfe, C. A.; Mueller, K. T.; Grondey, H.; Wong-Moon, K. C. Dipolar Dephasing between Quadrupolar and Spin-/12 Nuclei. REDOR and TEDOR NMR Experiments on VPI-5. *Chemical Physics Letters* **1992**, *199* (1), 198–204. https://doi.org/10.1016/0009-2614(92)80069-N.

(117) Martineau, C.; Bouchevreau, B.; Taulelle, F.; Trébosc, J.; Lafon, O.; Amoureux, J. P. High-Resolution through-Space Correlations between Spin-1/2 and Half-Integer Quadrupolar Nuclei Using the MQ-D-R-INEPT NMR Experiment. *Phys. Chem. Chem. Phys.* **2012**, *14* (19), 7112–7119. https://doi.org/10.1039/C2CP40344G.
(118) Overhauser, A. W. Polarization of Nuclei in Metals. *Phys. Rev.* **1953**, *92* (2), 411–415. https://doi.org/10.1103/PhysRev.92.411.
(119) Carver, T. R.; Slichter, C. P. Experimental Verification of the Overhauser Nuclear Polarization Effect. *Phys. Rev.* **1956**, *102* (4), 975–980. https://doi.org/10.1103/PhysRev.102.975.
(120) Wind, R. A.; Duijvestijn, M. J.; van der Lugt, C.; Manenschijn, A.; Vriend, J. Applications of Dynamic Nuclear Polarization in 13C NMR in Solids. *Progress in Nuclear Magnetic Resonance Spectroscopy* **1985**, *17*, 33–67. https://doi.org/10.1016/0079-6565(85)80005-4.
(121) Afeworki, M.; Schaefer, J. Mechanism of DNP-Enhanced Polarization Transfer across the Interface of Polycarbonate/Polystyrene Heterogeneous Blends. *Macromolecules* **1992**, *25* (16), 4092–4096. https://doi.org/10.1021/ma00042a007.
(122) Hall, D. A.; Maus, D. C.; Gerfen, G. J.; Inati, S. J.; Becerra, L. R.; Dahlquist, F. W.; Griffin, R. G. Polarization-Enhanced NMR Spectroscopy of Biomolecules in Frozen Solution. *Science* **1997**, *276* (5314), 930–932. https://doi.org/10.1126/science.276.5314.930.
(123) Becerra, L. R.; Gerfen, G. J.; Temkin, R. J.; Singel, D. J.; Griffin, R. G. Dynamic Nuclear Polarization with a Cyclotron Resonance Maser at 5 T. *Phys. Rev. Lett.* **1993**, *71* (21), 3561–3564. https://doi.org/10.1103/PhysRevLett.71.3561.
(124) Menzildjian, G.; Schlagnitweit, J.; Casano, G.; Ouari, O.; Gajan, D.; Lesage, A. Polarizing Agents for Efficient High Field DNP Solid-State NMR Spectroscopy under Magic-Angle Spinning: From Design Principles to Formulation Strategies. *Chemical Science* **2023**, *14* (23), 6120–6148. https://doi.org/10.1039/D3SC01079A.
(125) Barnes, A. B.; De Paëpe, G.; van der Wel, P. C. A.; Hu, K.-N.; Joo, C.-G.; Bajaj, V. S.; Mak-Jurkauskas, M. L.; Sirigiri, J. R.; Herzfeld, J.; Temkin, R. J.; Griffin, R. G. High-Field Dynamic Nuclear Polarization for Solid and Solution Biological NMR. *Appl Magn Reson* **2008**, *34* (3), 237–263. https://doi.org/10.1007/s00723-008-0129-1.
(126) Mentink-Vigier, F.; Marin-Montesinos, I.; Jagtap, A. P.; Halbritter, T.; van Tol, J.; Hediger, S.; Lee, D.; Sigurdsson, S. Th.; De Paëpe, G. Computationally Assisted Design of Polarizing Agents for Dynamic Nuclear Polarization Enhanced NMR: The AsymPol Family. *J. Am. Chem. Soc.* **2018**, *140* (35), 11013–11019. https://doi.org/10.1021/jacs.8b04911.
(127) Hohenberg, P.; Kohn, W. Inhomogeneous Electron Gas. *Phys. Rev.* **1964**, *136* (3B), B864–B871. https://doi.org/10.1103/PhysRev.136.B864.
(128) Kohn, W.; Sham, L. J. Self-Consistent Equations Including Exchange and Correlation Effects. *Phys. Rev.* **1965**, *140* (4A), A1133–A1138. https://doi.org/10.1103/PhysRev.140.A1133.
(129) Ceperley, D. M.; Alder, B. J. Ground State of the Electron Gas by a Stochastic Method. *Phys. Rev. Lett.* **1980**, *45* (7), 566–569. https://doi.org/10.1103/PhysRevLett.45.566.
(130) Perdew, J. P.; Wang, Y. Accurate and Simple Analytic Representation of the Electron-Gas Correlation Energy. *Phys. Rev. B* **1992**, *45* (23), 13244–13249. https://doi.org/10.1103/PhysRevB.45.13244.
(131) Perdew, J. P.; Burke, K.; Ernzerhof, M. Generalized Gradient Approximation Made Simple. *Phys. Rev. Lett.* **1996**, *77* (18), 3865–3868. https://doi.org/10.1103/PhysRevLett.77.3865.

(132) Blöchl, P. E. Projector Augmented-Wave Method. *Phys. Rev. B* **1994**, *50* (24), 17953–17979. https://doi.org/10.1103/PhysRevB.50.17953.
(133) Petrilli, H. M.; Blöchl, P. E.; Blaha, P.; Schwarz, K. Electric-Field-Gradient Calculations Using the Projector Augmented Wave Method. *Phys. Rev. B* **1998**, *57* (23), 14690–14697. https://doi.org/10.1103/PhysRevB.57.14690.
(134) Pickard, C. J.; Mauri, F. All-Electron Magnetic Response with Pseudopotentials: NMR Chemical Shifts. *Phys. Rev. B* **2001**, *63* (24), 245101. https://doi.org/10.1103/PhysRevB.63.245101.
(135) Pyykkö, P. Year-2017 Nuclear Quadrupole Moments. *Molecular Physics* **2018**, *116* (10), 1328–1338. https://doi.org/10.1080/00268976.2018.1426131.
(136) Sahoo, B. K. Nuclear Quadrupole Moment of 43Ca and Hyperfine-Structure Studies of Its Singly Charged Ion. *Phys. Rev. A* **2009**, *80* (1), 012515. https://doi.org/10.1103/PhysRevA.80.012515.
(137) Burgess, K. M. N.; Xu, Y.; Leclerc, M. C.; Bryce, D. L. Alkaline-Earth Metal Carboxylates Characterized by 43Ca and 87Sr Solid-State NMR: Impact of Metal-Amine Bonding. *Inorg Chem* **2014**, *53* (1), 552–561. https://doi.org/10.1021/ic402658d.
(138) Pourpoint, F.; Gervais, C.; Bonhomme-Coury, L.; Azaïs, T.; Coelho, C.; Mauri, F.; Alonso, B.; Babonneau, F.; Bonhomme, C. Calcium Phosphates and Hydroxyapatite: Solid-State NMR Experiments and First-Principles Calculations. *Appl Magn Reson* **2007**, *32* (4), 435–457. https://doi.org/10.1007/s00723-007-0040-1.
(139) Pourpoint, F.; Diogo, C. C.; Gervais, C.; Bonhomme, C.; Fayon, F.; Dalicieux, S. L.; Gennero, I.; Salles, J.-P.; Howes, A. P.; Dupree, R.; Hanna, J. V.; Smith, M. E.; Mauri, F.; Guerrero, G.; Hubert Mutin, P.; Laurencin, D. High-Resolution Solid State NMR Experiments for the Characterization of Calcium Phosphate Biomaterials and Biominerals. *Journal of Materials Research* **2011**, *26* (18), 2355–2368. https://doi.org/10.1557/jmr.2011.250.
(140) Davies, E.; Duer, M. J.; Ashbrook, S. E.; Griffin, J. M. Applications of NMR Crystallography to Problems in Biomineralization: Refinement of the Crystal Structure and 31P Solid-State NMR Spectral Assignment of Octacalcium Phosphate. *J. Am. Chem. Soc.* **2012**, *134* (30), 12508–12515. https://doi.org/10.1021/ja3017544.
(141) Chappell, H.; Duer, M.; Groom, N.; Pickard, C.; Bristowe, P. Probing the Surface Structure of Hydroxyapatite Using NMR Spectroscopy and First Principles Calculations. *Physical Chemistry Chemical Physics* **2008**, *10* (4), 600–606. https://doi.org/10.1039/B714512H.
(142) Su, Y.; Brigiano, F. S.; Petit, I.; Leroy, C.; Bonhomme, C.; Babonneau, F.; Tielens, F.; Gervais, C. Investigation of Carbonate Substitution in Hydroxyapatite by Combining Solid-State NMR and DFT Calculations. *Chemistry–Methods* **2023**, *3* (11), e202300007. https://doi.org/10.1002/cmtd.202300007.
(143) Yi, H.; Balan, E.; Gervais, C.; Segalen, L.; Fayon, F.; Roche, D.; Person, A.; Morin, G.; Guillaumet, M.; Blanchard, M.; Lazzeri, M.; Babonneau, F. A Carbonate-Fluoride Defect Model for Carbonate-Rich Fluorapatite. *American Mineralogist* **2013**, *98* (5–6), 1066–1069. https://doi.org/10.2138/am.2013.4445.
(144) Yi, H.; Balan, E.; Gervais, C.; Ségalen, L.; Roche, D.; Person, A.; Fayon, F.; Morin, G.; Babonneau, F. Probing Atomic Scale Transformation of Fossil Dental Enamel Using Fourier Transform Infrared and Nuclear Magnetic Resonance Spectroscopy: A Case Study from the Tugen Hills (Rift Gregory, Kenya). *Acta Biomaterialia* **2014**, *10* (9), 3952–3958. https://doi.org/10.1016/j.actbio.2013.12.049.

(145) Gras, P.; Baker, A.; Combes, C.; Rey, C.; Sarda, S.; Wright, A. J.; Smith, M. E.; Hanna, J. V.; Gervais, C.; Laurencin, D.; Bonhomme, C. From Crystalline to Amorphous Calcium Pyrophosphates: A Solid State Nuclear Magnetic Resonance Perspective. *Acta Biomaterialia* **2016**, *31*, 348–357. https://doi.org/10.1016/j.actbio.2015.10.016.
(146) Mayen, L.; Jensen, N. D.; Desbord, M.; Laurencin, D.; Gervais, C.; Bonhomme, C.; Smith, M. E.; Porcher, F.; Elkaim, E.; Charvillat, C.; Gras, P.; Rey, C.; Soulié, J.; Combes, C. Advances in the Synthesis and Structure of α-Canaphite: A Multitool and Multiscale Study. *CrystEngComm* **2020**, *22* (18), 3130–3143. https://doi.org/10.1039/D0CE00132E.
(147) Goldberga, I.; D. Jensen, N.; Combes, C.; Mentink-Vigier, F.; Wang, X.; Hung, I.; Gan, Z.; Trébosc, J.; Métro, T.-X.; Bonhomme, C.; Gervais, C.; Laurencin, D. $^{17}$O Solid State NMR as a Valuable Tool for Deciphering Reaction Mechanisms in Mechanochemistry: The Case Study on the 17 O-Enrichment of Hydrated Ca-Pyrophosphate Biominerals. *Faraday Discussions* **2023**, *241* (0), 250–265. https://doi.org/10.1039/D2FD00127F.
(148) Bryce, D. L.; Bultz, E. B.; Aebi, D. Calcium-43 Chemical Shift Tensors as Probes of Calcium Binding Environments. Insight into the Structure of the Vaterite CaCO3 Polymorph by 43Ca Solid-State NMR Spectroscopy. *J. Am. Chem. Soc.* **2008**, *130* (29), 9282–9292. https://doi.org/10.1021/ja8017253.
(149) Bonhomme, C.; Wang, X.; Hung, I.; Gan, Z.; Gervais, C.; Sassoye, C.; Rimsza, J.; Du, J.; Smith, M. E.; Hanna, J. V.; Sarda, S.; Gras, P.; Combes, C.; Laurencin, D. Pushing the Limits of Sensitivity and Resolution for Natural Abundance 43Ca NMR Using Ultra-High Magnetic Field (35.2 T). *Chem. Commun.* **2018**, *54* (69), 9591–9594. https://doi.org/10.1039/C8CC05193C.
(150) Laurencin, D.; Li, Y.; Duer, M. J.; Iuga, D.; Gervais, C.; Bonhomme, C. A $^{43}$Ca Nuclear Magnetic Resonance Perspective on Octacalcium Phosphate and Its Hybrid Derivatives. *Magnetic Resonance in Chemistry* **2021**, *59* (9–10), 1048–1061. https://doi.org/10.1002/mrc.5149.
(151) Goldberga, I.; Hung, I.; Sarou-Kanian, V.; Gervais, C.; Gan, Z.; Novák-Špačková, J.; Métro, T.-X.; Leroy, C.; Berthomieu, D.; van der Lee, A.; Bonhomme, C.; Laurencin, D. High-Resolution $^{17}$O Solid-State NMR as a Unique Probe for Investigating Oxalate Binding Modes in Materials: The Case Study of Calcium Oxalate Biominerals. *Inorg. Chem.* **2024**, *63* (22), 10179–10193. https://doi.org/10.1021/acs.inorgchem.4c00300.
(152) Ashbrook, S. E.; McKay, D. Combining Solid-State NMR Spectroscopy with First-Principles Calculations – a Guide to NMR Crystallography. *Chem. Commun.* **2016**, *52* (45), 7186–7204. https://doi.org/10.1039/C6CC02542K.
(153) Schmidt, J.; Sebastiani, D. Anomalous Temperature Dependence of Nuclear Quadrupole Interactions in Strongly Hydrogen-Bonded Systems from First Principles. *The Journal of Chemical Physics* **2005**, *123* (7), 074501. https://doi.org/10.1063/1.2000241.
(154) Salager, E.; Stein, R. S.; Pickard, C. J.; Elena, B.; Emsley, L. Powder NMR Crystallography of Thymol. *Phys. Chem. Chem. Phys.* **2009**, *11* (15), 2610–2621. https://doi.org/10.1039/B821018G.
(155) Dračínský, M.; Bouř, P. Vibrational Averaging of the Chemical Shift in Crystalline α-Glycine. *J Comput Chem* **2012**, *33* (10), 1080–1089. https://doi.org/10.1002/jcc.22940.
(156) Monserrat, B.; Needs, R. J.; Pickard, C. J. Temperature Effects in First-Principles Solid State Calculations of the Chemical Shielding Tensor Made Simple. *J Chem Phys* **2014**, *141* (13), 134113. https://doi.org/10.1063/1.4897261.

(157) Dumez, J.-N.; Pickard, C. J. Calculation of NMR Chemical Shifts in Organic Solids: Accounting for Motional Effects. *J Chem Phys* **2009**, *130* (10), 104701. https://doi.org/10.1063/1.3081630.
(158) Gortari, I. D.; Portella, G.; Salvatella, X.; Bajaj, V. S.; van der Wel, P. C. A.; Yates, J. R.; Segall, M. D.; Pickard, C. J.; Payne, M. C.; Vendruscolo, M. Time Averaging of NMR Chemical Shifts in the MLF Peptide in the Solid State. *J. Am. Chem. Soc.* **2010**, *132* (17), 5993–6000. https://doi.org/10.1021/ja9062629.
(159) Dračínský, M.; Bouř, P.; Hodgkinson, P. Temperature Dependence of NMR Parameters Calculated from Path Integral Molecular Dynamics Simulations. *J. Chem. Theory Comput.* **2016**, *12* (3), 968–973. https://doi.org/10.1021/acs.jctc.5b01131.
(160) Goldberga, I.; Patris, N.; Chen, C.-H.; Thomassot, E.; Trébosc, J.; Hung, I.; Gan, Z.; Berthomieu, D.; Métro, T.-X.; Bonhomme, C.; Gervais, C.; Laurencin, D. First Direct Insight into the Local Environment and Dynamics of Water Molecules in the Whewellite Mineral Phase: Mechanochemical Isotopic Enrichment and High-Resolution $^{17}O$ and $^{2}H$ NMR Analyses. *J Phys Chem C Nanomater Interfaces* **2022**, *126* (29), 12044–12059. https://doi.org/10.1021/acs.jpcc.2c02070.
(161) Dračínský, M.; Hodgkinson, P. Effects of Quantum Nuclear Delocalisation on NMR Parameters from Path Integral Molecular Dynamics. *Chemistry – A European Journal* **2014**, *20* (8), 2201–2207. https://doi.org/10.1002/chem.201303496.
(162) Robinson, M.; Haynes, P. D. Dynamical Effects in Ab Initio NMR Calculations: Classical Force Fields Fitted to Quantum Forces. *The Journal of Chemical Physics* **2010**, *133* (8), 084109. https://doi.org/10.1063/1.3474573.

# CHAPTER II

## Article

**Temperature-induced mobility in Octacalcium Phosphate impacts crystal symmetry: water dynamics studied by NMR crystallography**

# I. Preface to the article

## I.1. Why use OCP as a model for bone mineral?

Octacalcium phosphate pentahydrate (OCP, $Ca_8(HPO_4)_2(PO_4)_4{\cdot}5H_2O$) is a mineral phase bearing similarities to bone mineral. This calcium phosphate can directly transform into apatite and has therefore been proposed as a possible precursor for bone mineral. It has been observed to exist in biological samples,[1] forming small complexes with osteocalcin. It has still a poorly-understood role, making its study important for our understanding of biomineralization.

There are a striking number of commonalities between OCP and bone mineral. First, they are both calcium phosphates with a relatively similar Ca/P ratio (stoichiometric OCP has a Ca/P ratio of 1.33, compared to an estimated 1.5 for bone mineral. Note that this value is related to partial substitution of phosphate by carbonate as substitution, since Ca/P ratio in stoechiometric HAp is 1.66). OCP is formed in conditions somewhat similar to HAp: at moderate pH (4.5-7.0), moderate temperatures (from RT to 60°C), in a few hours or days stirring a stoichiometric solution of calcium and phosphate ions in water.

In addition, the phase is lamellar and incorporates a large amount of structural water. The water is located in the interlayer space, and the crystallographic structure is commonly described as having an “apatitic” layer and a “hydrated” interlayer (Figure 1).

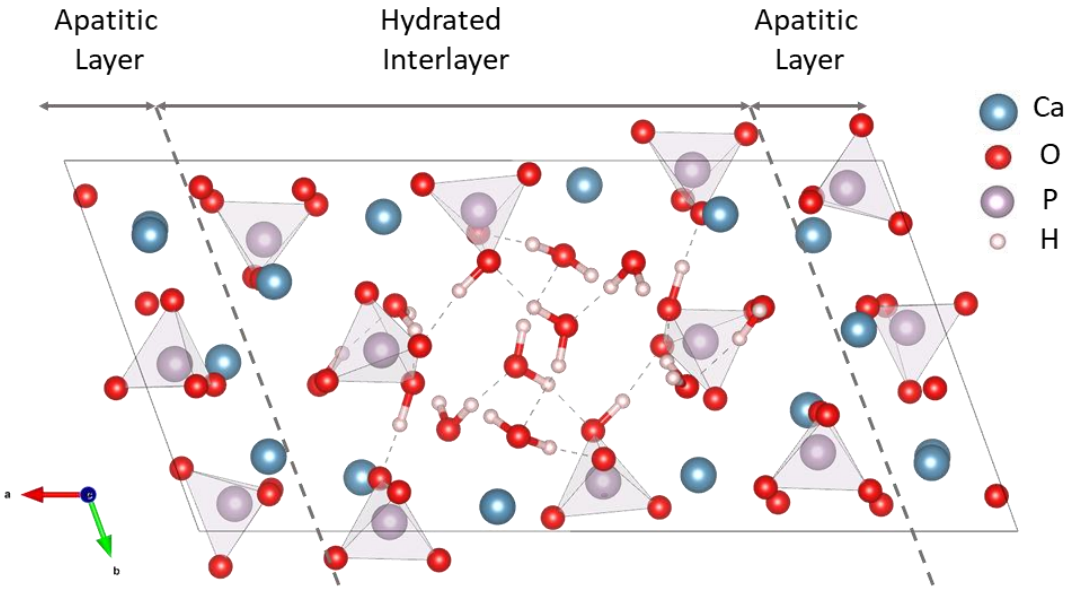


*Figure 1: The twinned cell of octacalcium phosphate ($Ca_{16}(PO_4)_8(HPO_4)_4{\cdot}10H_2O$), divided in two layers, as is commonly described.*

The contrasting “crystalline” and “hydrated” environments are observed in synthetic biomimetic apatites,[2] and are displayed prominently in the hydrated surface and crystalline core of bone mineral. OCP can also easily incorporate organic molecules, particularly dicarboxylates and citrates,[3,4,5] into its hydrated interlayer. Multiple studies have made parallels between the incorporation of organic molecules at the surface of OCP and the interface between bone mineral and its organic matrix,[4,5] going as far as to propose that the surface of bone mineral is OCP or an OCP-assimilated phase. Lastly, OCP has high osteoconductivity[6] and is widely studied as a biomaterial for bone substitution and repair.

These factors combined make OCP one of the prime materials to serve as one of our models of bone mineral in our studies. This is especially true when using surface-sensitive techniques like DNP-enhanced ssNMR, given that DNP’s efficiency is strongly influenced by the sample’s surface and its interaction with the hyperpolarized radical.[7] OCP therefore provides a good first approximation of the surface of bone mineral while avoiding the intricacies of biological samples.

However, it is important in the course of this argumentation to remember the differences that also exist between OCP and bone mineral. Firstly, OCP (or at least, pristine OCP synthesized through precipitation) is a highly crystalline and ordered environment, while the bone mineral surface has a high degree of disorder. The nanocrystalline bone mineral also has a very different morphology compared to the micrometric OCP platelets. While it could be tempting to make the parallel between the microscopic platelets of precipitated OCP and the mineral “platelets” of bone, the vast size difference and the earlier discussed evidence[8] of the “platelets” being assemblies of apatitic needles makes the comparison perilous. The presence of a tightly-intertwined organic matrix has also not been reproduced in OCP phases and the absence of carbonates substitution is noteworthy. Lastly, OCP has a surprising behavior when submerged in water: the compound is highly hydrophilic and forms a fluid paste, incorporating over ten time its weight in water. This is especially relevant in our DNP studies, where the surface impregnation of the solvent is tightly linked to DNP efficiency.[9] We can therefore expect OCP to serve as a relevant model material in the study of bone mineral. However, we need to remain cautious when drawing any parallels between the two, as they remain dissimilar in all but the most surface of levels.

Finally, we must note that the study of OCP holds interest in its own right, beyond its use as a model compound. It is widely studied (a rapid Google Scholar search shows 166 published studies with the term “octacalcium phosphate” in their title since 2020). However, our understanding of its structure is incomplete. Although the structure of the “apatitic” layer is well known due to a series of thorough XRD crystallography studies by W. Brown *et al.*,[10–12] the structure of the interlayer is poorly understood. Additionally, dynamical effects have been theorized at many points to explain the unexpected behavior of OCP, but has never been studied in detail. This point will be detailed in further detail in the following study.

## I.2. The synthesis and enrichment of OCP

The synthesis of OCP as a pure phase has proven a challenge in many (possibly all) previous studies. There are a number of reasons for this: firstly, it does not precipitate directly from solution in any meaningful amount. Because HAp is the thermodynamically favored product in all cases,[13] OCP can only be a reaction intermediate in the formation of HAp in water. Additionally, the synthesis of OCP in highly concentrated solutions usually involves the precipitation of a more kinetically favored calcium phosphate ($\alpha$-TCP and/or DCPD). The synthesis of pure OCP must therefore be carefully timed to stop after the precursor has been converted to OCP, but before it has a chance to form HAp in meaningful amounts. This is exacerbated by the fact that HAp impurities are extremely difficult to monitor in an OCP sample, as the XRD patterns of both compounds nearly completely overlap (and also because HAp produced from OCP tends to be poorly crystalline, with a wide diffraction pattern, as evidenced in a previous investigation where the OCP sample had a promising XRD pattern but very obvious HAp contamination in $^{31}$P NMR).[14]

To those challenges, our study adds the difficulties associated with isotopic enrichment in $^{43}$Ca and $^{17}$O (since they have a natural abundance of 0.135% and 0.037% respectively). Isotopically enriched precursors are expensive. Our protocol must therefore use the smallest possible amount of precursor and reliably produce a high yield, high purity product. The synthesis must consequently be run on a scale that is lower than that of other published protocols, typically by an order of magnitude or two (ca. 40 mg of OCP is required to fill a 3.2 mm rotor, whereas published protocols usually yield several grams). The selection of isotopically commercially-enriched precursors is also extremely limited. For example, whereas OCP precursors like $\alpha$-TCP and DCPD are commercially available from a number of manufacturers, the only commercially available source of $^{43}$Ca is $CaCO_3$. This makes the use of protocols starting from calcium nitrate or calcium acetate impractical, as they would require an initial transformation of the precursor that adds risk and incurs loss of precursor. Thankfully, protocols using $CaCO_3$ as a calcium source have been reported before, in the only previous study involving OCP enrichment.[5] However, in the latter case, the final product contained a large amount of $CaCO_3$ impurity, most likely explained by the large calcium excess at the beginning of the reaction (Ca/P = 1.60, well above stoichiometric OCP's Ca/P = 1.33). We can speculate that this excess was deemed preferable to a potential TCP/DCPD impurity. Here, we therefore worked on finding improvements to the low-scale OCP synthesis protocols, in order to create one focused on achieving high yields and high purity, reliably.

## I.3. Initial protocol and improvements.

The initial protocol to be improved was therefore a simple reaction involving the addition of $CaCO_3$ to a phosphate solution, adapted from a previous study of OCP.[15] It was the following:

"*A 200 mL solution containing 20 mmol of $H_3PO_4$ in distilled water is stirred and heated to 60°C in a round-bottom flask. 26.7 mmol (2.67 g) of $CaCO_3$ are added to the medium over five minutes, which rapidly forms a white precipitate in the solution. The medium is left to stir with an air-cooled reflux for six hours. Around three hours, the solution becomes completely opaque with solid and homogeneous stirring is no longer achieved using a stirring bar. After six hours of stirring, the solid is separated and air-dried on a fritted funnel. The powder is then dried in air at 50°C overnight.*"

This first attempted synthesis was relatively successful, producing a majority of OCP with a DCPD impurity visible in pXRD patterns. It was initially assumed that the poor stirring of the suspension was at fault, but the use of a wider stirring bar and a high stirring speed yielded a similar product. The Ca/P ratio was then increased to match a theorized Ca deficiency that would stop the complete formation of OCP. A slight excess of $CaCO_3$ (Ca/P ratio 1.37) improved the purity of the end product, with no detectable DCPD or $CaCO_3$ impurity over two syntheses.

Scaling down the reaction for an eventual enrichment protocol showed the reaction to be once again unreliable. In this alternate protocol, 0.71 mmol of $CaCO_3$ was added to 0.51 mmol of $H_3PO_4$ in 5 mL of water. The reaction was conducted, separated and dried in the same centrifuge tube in order to minimize losses. Although the reaction yielded a pure product in some syntheses, others would feature significant DCPD impurities.

We can explain the lack of reproducibility of the synthesis through a number of factors. Firstly, the reaction is run without any pH buffer, as all the phosphates in solution are expected to precipitate with the addition of calcium carbonate. This is problematic given the sensitivity of the OCP phase to pH (DCPD becomes significantly more stable than OCP at pH < 5, but OCP will rapidly hydrolyze into HAp at pH > 7). As mentioned before, controlling the kinetics of the reaction is also essential to the purity of the end product. Here, we speculate that the dissolution rate of $CaCO_3$ plays a major role in this regard. This was evidenced by ambient-temperature tests for which the product of the hydrolysis reaction was DCPD in sealed flasks, and an OCP-like precipitate in unsealed flasks (Figure 2). To flush out the $CO_2$ byproduct that may affect the kinetics of the reaction, we therefore chose to conduct the synthesis under a flowing Argon atmosphere. Lastly, it was speculated that the variable amounts of DPCD impurity that occurred unexpectedly in reproducibility tests may have been unreacted product that was deposited on the walls of the reactor, that would be slow to react due to the lowered surface area exposed to the reaction medium.

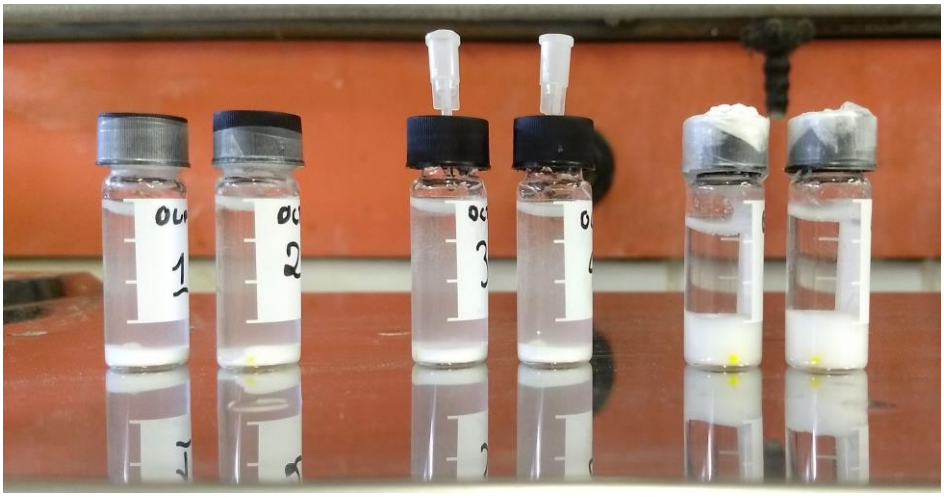

*Figure 2: Visual comparison of six OCP reactions run at room temperature with different degassing conditions, after 52 hours. From left to right: sealed flask, septum + syringe, open. Note the much larger volume of solid in the flasks open to air, later determined to be OCP.*

Ultimately, all of these factors were accounted for in the final protocol (featuring in the publication). The stirring was made reliable using a cross-head bar. The Argon gas flow was controlled with a bubbler and a metronome. Lastly, the most impactful change was the addition of regular sonication to the protocol. As we observed that the walls of the tube were often laden with a layer of precipitate, we chose to sonicate the reaction at regular intervals. This improved synthesis protocol allowed for the reliable synthesis of both calcium-43 (n = 2) and oxygen-17 (n = 1) enriched samples.

Following this preface, our study of water mobility in OCP, published in Faraday discussion, is reproduced in full. To help with ease of reading, the Supplementary Information section has been integrated in the article.

## References


(1) Simon, P.; Grüner, D.; Worch, H.; Pompe, W.; Lichte, H.; El Khassawna, T.; Heiss, C.; Wenisch, S.; Kniep, R. First Evidence of Octacalcium Phosphate@osteocalcin Nanocomplex as Skeletal Bone Component Directing Collagen Triple–Helix Nanofibril Mineralization. *Sci. Rep.* **2018**, *8* (1), 13696. https://doi.org/10.1038/s41598-018-31983-5.

(2) Jäger, C.; Welzel, T.; Meyer-Zaika, W.; Epple, M. A Solid-State NMR Investigation of the Structure of Nanocrystalline Hydroxyapatite. *Magn. Reson. Chem.* **2006**, *44* (6), 573–580. https://doi.org/10.1002/mrc.1774.

(3) Markovic, M.; Fowler, B. O.; Brown, W. E. Octacalcium Phosphate Carboxylates. 1. Preparation and Identification. *Chem. Mater.* **1993**, *5* (10), 1401–1405. https://doi.org/10.1021/cm00034a007.

(4) Davies, E.; Müller, K. H.; Wong, W. C.; Pickard, C. J.; Reid, D. G.; Skepper, J. N.; Duer, M. J. Citrate Bridges between Mineral Platelets in Bone. *Proc. Natl. Acad. Sci.* **2014**, *111* (14), E1354–E1363. https://doi.org/10.1073/pnas.1315080111.

(5) Laurencin, D.; Li, Y.; Duer, M. J.; Iuga, D.; Gervais, C.; Bonhomme, C. A 43Ca Nuclear Magnetic Resonance Perspective on Octacalcium Phosphate and Its Hybrid Derivatives. *Magn. Reson. Chem.* **2021**, *59* (9–10), 1048–1061. https://doi.org/10.1002/mrc.5149.

(6) Suzuki, O. Octacalcium Phosphate (OCP)-Based Bone Substitute Materials. *Jpn. Dent. Sci. Rev.* **2013**, *49* (2), 58–71. https://doi.org/10.1016/j.jdsr.2013.01.001.

(7) Perras, F. A.; Wang, L.-L.; Manzano, J. S.; Chaudhary, U.; Opembe, N. N.; Johnson, D. D.; Slowing, I. I.; Pruski, M. Optimal Sample Formulations for DNP SENS: The Importance of Radical-Surface Interactions. *Curr. Opin. Colloid Interface Sci.* **2018**, *33*, 9–18. https://doi.org/10.1016/j.cocis.2017.11.002.

(8) Reznikov, N.; Bilton, M.; Lari, L.; Stevens, M. M.; Kröger, R. Fractal-like Hierarchical Organization of Bone Begins at the Nanoscale. *Science* **2018**, *360* (6388), eaao2189. https://doi.org/10.1126/science.aao2189.

(9) Pump, E.; Bendjeriou-Sedjerari, A.; Viger-Gravel, J.; Gajan, D.; Scotto, B.; K. Samantaray, M.; Abou-Hamad, E.; Gurinov, A.; Almaksoud, W.; Cao, Z.; Lesage, A.; Cavallo, L.; Emsley, L.; Basset, J.-M. Predicting the DNP-SENS Efficiency in Reactive Heterogeneous Catalysts from Hydrophilicity. *Chem. Sci.* **2018**, *9* (21), 4866–4872. https://doi.org/10.1039/C8SC00532J.

(10) Walter E. Brown. Octacalcium Phosphate and Hydroxyapatite: Crystal Structure of Octacalcium Phosphate. *Nature* **1962**, *196* (4859), 1048–1050. https://doi.org/10.1038/1961048b0.

(11) Mathew, M.; Brown, W. E.; Schroeder, L. W.; Dickens, B. Crystal Structure of Octacalcium Bis(Hydrogenphosphate) Tetrakis(Phosphate)Pentahydrate, Ca8(HP04)2(PO4)4·5H2O. *J. Crystallogr. Spectrosc. Res.* **1988**, *18* (3), 235–250. https://doi.org/10.1007/BF01194315.

(12) Brown, W. E.; Lehr, J. R.; Smith, J. P.; Frazier, A. W. CRYSTALLOGRAPHY OF OCTACALCIUM PHOSPHATE. *J. Am. Chem. Soc.* **1957**, *79* (19), 5318–5319. https://doi.org/10.1021/ja01576a068.

(13) Pan, H.-B.; Darvell, B. W. Calcium Phosphate Solubility: The Need for Re-Evaluation. *Cryst. Growth Des.* **2009**, *9* (2), 639–645. https://doi.org/10.1021/cg801118v.

(14) Davies, E.; Duer, M. J.; Ashbrook, S. E.; Griffin, J. M. Applications of NMR Crystallography to Problems in Biomineralization: Refinement of the Crystal Structure and 31P Solid-State NMR Spectral Assignment of Octacalcium Phosphate. *J. Am. Chem. Soc.* **2012**, *134* (30), 12508–12515. https://doi.org/10.1021/ja3017544.

(15) Li, Y.; Reid, D. G.; Duer, M. J.; Chan, J. C. C. Solid State NMR - An Indispensable Tool in Organic-Inorganic Biocomposite Characterization; Refining the Structure of Octacalcium Phosphate Composites with the Linear Metabolic Di-Acids Succinate and Adipate. *Solid State Nucl. Magn. Reson.* **2018**, *95*, 1–5. https://doi.org/10.1016/j.ssnmr.2018.08.004.

# Temperature-induced mobility in Octacalcium Phosphate impacts crystal symmetry: water dynamics studied by NMR crystallography

Adam Nelson,[1,2] Wassilios Papawassiliou,[3] Subhradip Paul,[3] Sabine Hediger,[3] Ivan Hung,[4] Zhehong Gan,[4] Amrit Venkatesh,[4] W. Trent Franks,[5] Mark E. Smith,[5,6] David Gajan,[7] Gaël De Paëpe,[3] Christian Bonhomme,[1] Danielle Laurencin,[2,*] Christel Gervais[1,*]

[1] LCMCP, UMR 7574, Sorbonne Université, CNRS, Paris, France
[2] ICGM, Univ Montpellier, CNRS, ENSCM, Montpellier, France
[3] IRIG, MEM, Univ. Grenoble Alpes, CEA, CNRS, 38000 Grenoble, France
[4] National High Magnetic Laboratory (NHMFL), Tallahassee, Florida, USA
[5] Department of Physics, University of Warwick, Coventry, CV4 7AL, UK
[6] Department of Chemistry, University of Southampton, SO17 1BJ, UK
[7] CRMN Lyon, UMR 5082 (CNRS, ENS Lyon, Université Lyon 1), Villeurbanne, France

To whom correspondence should be addressed:
christel.gervais_stary@sorbonne-universite.fr
danielle.laurencin@umontpellier.fr

**Abstract**

Octacalcium phosphate (OCP, $Ca_8(PO_4)_4(HPO_4)_2{\cdot}5H_2O$) is a notable calcium phosphate due to its biocompatibility, making it a widely studied material for bone substitution. It is known to be a precursor of bone mineral, but its role in biomineralisation remains unclear. While the structure of OCP has been the subject of thorough investigations (including using Rietveld refinements of X-ray diffraction data, and NMR crystallography studies), important questions regarding the symmetry and H-bonding network in the material remain. In this study, it is shown that OCP undergoes a lowering of symmetry below 200 K, evidenced by $^{1}H$, $^{17}O$, $^{31}P$ and $^{43}Ca$ solid state NMR experiments. Using *ab-initio* molecular dynamics (MD) simulations and Gauge Including Projected Augmented Wave (GIPAW) DFT calculations of NMR parameters, the presence of rapid motions of the water molecules in the crystal cell at room temperature is proved. This information leads to an improved description of the OCP structure at both low and ambient temperatures, and helps explain long-standing issues of symmetry. Remaining challenges related to the understanding of the structure of OCP are then discussed.

## Introduction

Octacalcium phosphate (OCP, $Ca_8(PO_4)_4(HPO_4)_2{\cdot}5H_2O$) is a lamellar, hydrated calcium phosphate. It is a direct precursor of hydroxyapatite (HAp).[1] As HAp is the major component of bone mineral, the role of OCP in biomineralisation has been the subject of numerous investigations.[2,3,4,5,6] OCP is a plausible precursor to bone mineral for a number of reasons: it precipitates and further transforms into HAp at physiological pH,[7] and shares striking structural similarities with this phase.[8] Indeed, the lamellar structure of OCP is commonly described as being comprised of an "apatite-like" layer and a "hydrated" interlayer (Fig. 1), which is reminiscent of the hydrated layer found at the surface of bone mineral.[9,10] Yet, although OCP has now been observed *in vivo* in small quantities,[2] its prevalence in the human body and role in biomineralisation are still a matter of debate.

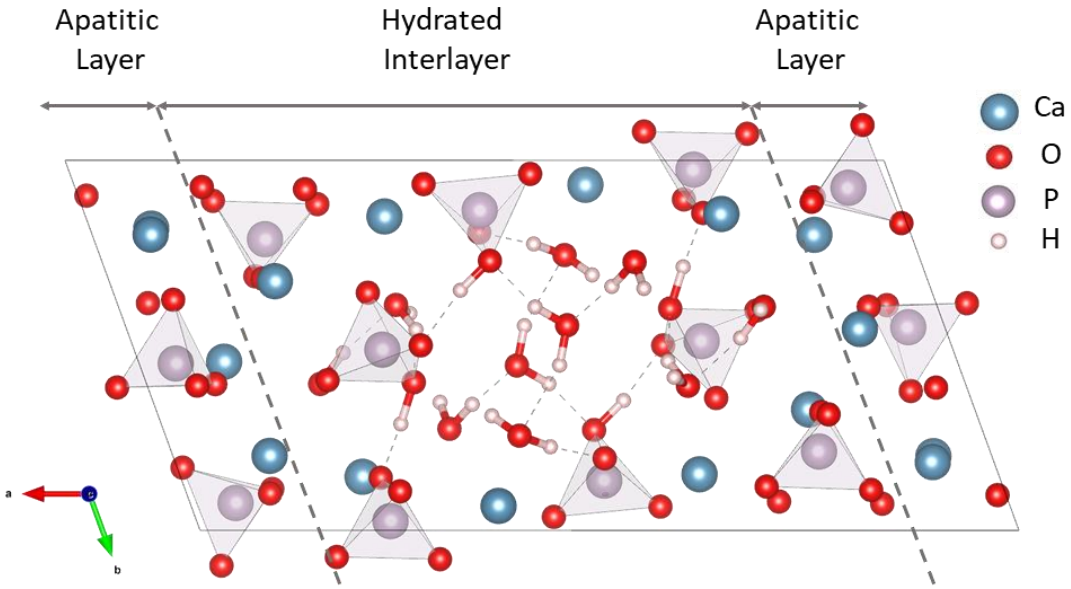


***Figure 1: The twinned cell of octacalcium phosphate ($Ca_{16}(PO_4)_8(HPO_4)_4{\cdot}10H_2O$), divided in two layers, as is commonly described.***

Key to OCP's study is an accurate description of its crystal structure. Although the first report of OCP as a distinct calcium phosphate dates back to 1950,[11] determination of its crystal structure was a clear challenge, owing to several unfavourable characteristics. The XRD crystallographic refinements of the phase by Brown *et al*.[1,8,12] faced a number of difficulties. Firstly, synthesising a pure sample of OCP is problematic, as the formation conditions allow its transformation into HAp,[1] and synthesis usually yields a mix of the two phases. The very similar powder X-ray diffraction (pXRD) patterns of OCP and HAp across a wide range of angles means determining the purity of a given synthesis product has been a challenge, until the first high-resolution solid state NMR experiments.[13] The issue of sample purity was addressed by Brown through the study of a single-crystal.[14] Its formation proved extremely difficult, as the synthesis of a sufficiently large crystal, measuring 0.2 mm in length,[12] could not be reproduced by the same team in later studies. Secondly, the large number of atoms (110) in the twinned unit cell, the important and variable number of water molecules clustered in the centre of the twinned cell, and the low symmetry group (*P*-1 or *P*1) mean that Rietveld refinements could only give a limited picture of the structure, particularly concerning the H-bonding network of the interlayer. The most notable issue with the XRD-refined structure of OCP is the lack of a clear symmetry group:

although the apatitic layer exhibits a central symmetry, it is unknown whether this holds true for the interlayer, as apparent disorder limits the accuracy with which the water molecules can be placed in the structure. This, in turn, leaves it with a fragmentary description of the interlayer, and particularly of its H-bonding network. Notably, a possible H-bond between the two central water molecules would preclude a *P*-1 symmetry at the local level, a point considered in more detail in this study.

Studies of OCP *via* solid-state NMR (ssNMR)[6,13,15,16] have offered more insight into its structure. Most importantly for the present work, a $^{1}$H and $^{31}$P high resolution NMR investigation by Davies *et al*.,[15] published in 2012, led to a revised structure of OCP, based on a combination of experimental assignments and first-principles calculations. This investigation sought to find a single structure that would simultaneously reduce the calculated strain on the structure through DFT relaxation, and could closely match the observed $^{31}$P NMR parameters of OCP. Nonetheless, the authors had to deal with several issues: not only was the synthesised OCP contaminated with HAp, but experimental $^{31}$P chemical shifts were also found to be dependent on temperature (varying by ~0.5 ppm over 100 K), suggesting possible mobility within the structure. Additionally, the ambiguous symmetry of previous studies remained, with the proposed structure having an assigned symmetry of *P*1, but with nearly identical atomic arrangements on either side of the cell. It was stated in the manuscript: "It is worth noting that the optimised structure is approximately consistent with *P*-1 symmetry (the maximum deviation from symmetry was determined by DFT to be $2.684 \times 10^{-5}$ Å); however, given the slight inconsistencies between the atomic positions and the symmetry operations of *P*-1, it is taken to be a *P*1 system."[15] The choice of starting from a *P*-1 structure may have been made because the calculated $^{31}$P NMR parameters on an asymmetric *P*1 cell showed strong splittings of the peaks, which is not consistent with ambient temperature $^{31}$P experimental data. Nevertheless, the proposed structure was a compromise between a Rietveld-refined structure,[12] featuring unrealistic bond angles and lengths, and the more realistic simulated interatomic distances and angles given by DFT relaxation. It also enabled a fairly close match to experimental $^{31}$P chemical shifts, although with a much larger error than that found for some related calcium phosphates ($CaH_2PO_4{\cdot}H_2O$, $CaHPO_4{\cdot}2H_2O$).[17] It therefore proved that an NMR crystallographic study was valuable when studying the structure of OCP, including for the assignment of the structure's phosphorus sites. The study did not, however, solve the issues of symmetry, nor explain the changes in chemical shifts with temperature. The recent advances in isotopic labelling, NMR instrumentation (low-temperature magic angle spinning (MAS) probes and high-field NMR spectrometers), and computational modelling, now allow us to further push the scope of NMR crystallographic studies of OCP.

The current study aims at expanding our understanding of the hydrated interlayer space of OCP and its potential mobility, using a combination of variable-temperature NMR spectroscopy (including at temperatures as low as 100 K), and molecular dynamics (MD) simulations. First, two improved protocols for the reproducible synthesis of high-purity OCP are described, both at gram-scale and in scaled-down quantities, for the purpose of isotopic enrichment. Notably, we propose an economical synthesis of $^{17}$O and $^{43}$Ca enriched samples. These samples are then analysed by multinuclear ssNMR at ambient and low temperature, demonstrating the existence of a significant change in the NMR signature. The origin of these changes is investigated with the help of computational modelling (MD simulations). Lastly, a new description for the structure of OCP is proposed, taking into account the presence of molecular motions in the cell, and assignment of some of the resonances recorded in the different NMR spectra obtained throughout the study. Remaining difficulties related to the OCP structure are also discussed.

**Experimental section**

**Materials and methods**

***Reagents***

The following reagents were used as received: phosphorus pentoxide ($P_2O_5$, Sigma-Aldrich, ≥ 99 %), orthophosphoric acid ($H_3PO_4$, Honeywell, 85 % w/w in water), and non-labelled calcite ($CaCO_3$, Acros Organics, ≥ 99%).

$^{17}O$-labelled water was purchased from Eurisotop, with a ~90% enrichment level. $^{43}Ca$-enriched $CaCO_3$ was purchased from Cortecnet, with a ~60% enrichment level.

***Gram-scale synthesis of octacalcium phosphate (OCP)***

Octacalcium phosphate was synthesised in water by adapting previously published protocols.[16] Because OCP is a reaction intermediate in the transformation of dicalcium phosphate dihydrate (DCPD, $CaHPO_4{\cdot}2H_2O$) into HAp, a precise control over the reaction kinetics is required to obtain a pure product. Since the $CaCO_3$ precursor's solubility is linked to the concentration of $CO_2$ in the reaction medium, the following improvements were made: (i) suppressing the accumulation of $CO_2$ gas in the reaction medium by using a flow of argon and (ii) avoiding the accumulation of DCPD on the walls of the reaction medium (where it can remain unreacted). As such, the following protocol was employed for the gram-scale synthesis of unenriched OCP.

A 100 mL solution of $H_3PO_4$ (0.100 mol.$L^{-1}$, 10 mmol, 1 eq) was heated to 60°C in a 250 mL round-bottom flask under argon. $CaCO_3$ (1.38 g, 13.87 mmol, 1.37 eq) was then gradually added over 5 minutes. A dense white precipitate appeared rapidly after the addition of $CaCO_3$. The reaction medium was stirred for 6 hours at 900 rpm, during which a flocculent white solid gradually filled the volume of the reaction medium. The solid was then filtered over a Büchner funnel and washed three times with 10 mL of water, yielding a large mass (≈ 12 g) of white paste. The paste was dried at 50°C overnight (under air), leading to the loss of a significant mass of water (≈ 10.5 g). The synthesis yielded 1.55 g (1.74 mmol, 96% yield) of a fluffy white powder, which was identified as OCP via IR spectroscopy, pXRD, and $^{31}P$ ssNMR. The powder was stored at –20°C until further analysis.

***Low-scale synthesis of $^{43}Ca$-enriched OCP***

A scaled-down protocol was developed for enriching OCP in either calcium-43 or oxygen-17. Given the high price and low availability of the enriched precursors, it was essential to reduce the synthesis scale while ensuring an optimal synthetic yield. To minimise losses in isotopically labelled product, all synthetic steps (precipitation, separation, washing and drying) were carried out in a single 50 mL round-bottom polypropylene centrifuge tube, as detailed below.

A 5 mL solution of $H_3PO_4$ (0.100 mol.$L^{-1}$, 0.508 mmol, 1 eq) in ultrapure $H_2O$ was added to the tube, heated to 60°C in an oil bath, and stirred with a PTFE crosshead stirring bar up to 800 rpm. A mixture of $^{43}Ca$-enriched $Ca^*CO_3$ and non-enriched $CaCO_3$ powders (~ 71 mg total mass, 0.70 mmol, 1.37 eq) was rapidly added to the reaction medium, causing the immediate formation of a dense white precipitate. The tube was sealed with a septum and placed under an Argon atmosphere, by inserting two 0.80 mm diameter needles into the rubber septum (one for Ar inlet, the other for Ar outlet). The reaction medium was then stirred at 60°C for 6 hours, during which it was sonicated four times (at t+ 0:30, 1:00, 1:30 and 2:30), to homogenise the reaction medium and favour the release of "trapped"

$CO_2$ bubbles. At the end of the reaction, the reaction medium was completely filled by a white, watery paste. After cooling back to room temperature, the solid was then separated from the reaction medium *via* centrifugation at 20k rpm for 10 minutes, then washed twice using 5 mL of ultrapure $H_2O$. The residual powder was dried inside the centrifuge tube overnight at 50°C (under air). This reaction was run twice, once using an average $^{43}$Ca-enrichment level of 5% for the starting $CaCO_3$, and the other of 15%. After drying, 80.9 mg and 78.4 mg of enriched OCP were isolated, which corresponds to synthetic yields of ca. 95% and 94%, respectively. The $^{43}$Ca-enriched products were stored at −20°C. The estimated cost for the $^{43}$Ca-labeling synthesis is ca. 900€ (for a 15% labelled sample, using ≈15 mg of enriched Ca*$CO_3$ precursor). As shown below, high quality 1D $^{43}$Ca MAS NMR spectra were collected in just an hour.

***Low-scale synthesis of $^{17}$O-enriched OCP (with enrichment on the PO and POH groups)***

OCP was enriched in oxygen-17 by synthesising a labelled $H_3PO^*_4$ precursor and using it in the previously described protocol. 175.7 mg of labelled $H_3PO^*_4$, was subsequently diluted in 1 mL $H_2O$ to yield a concentrated orthophosphoric acid solution. 345 μL of this solution were then further diluted to yield an aqueous solution of $H_3PO_4$ (5 mL, 100 mM, 0.51 mmol, 1 eq), which was in turn used as a precursor for the synthesis of the oxygen-17 enriched OCP, by adding unlabelled $CaCO_3$ (67.6 mg, 0.68 mmol, 1.37 eq.), and then following the protocol described above for $^{43}$Ca labelling. This produced 71.6 mg of labelled sample, with an 86% yield. The powder was stored at -20°C until further analysis.
The enrichment of OCP in $^{17}$O and $^{43}$Ca was successful for both isotopes on the first attempt, and provided a relatively inexpensive way to observe these rare nuclei with much reduced experimental times. The estimated cost of the labelled precursor for the $^{17}$O synthesis is ca. 65€. As shown below, high quality 1D $^{17}$O MAS NMR spectra were collected for each nucleus in just an hour.

***Infrared spectroscopy (IR)***

IR analyses were performed on a Perkin-Elmer Spectrum 2 FT-IR instrument. The ATR mode was used for measurements ranging from 400 to 4000 $cm^{-1}$.

***Powder X-ray diffraction (pXRD)***

Room temperature pXRD analyses were performed on an X'Pert MPD diffractometer using $CuK_{\alpha 1}$ radiation ($\lambda$ = 1.5406 Å), with the operating voltage and current maintained at 40 kV and 25 mA, respectively. X-ray diffractograms were recorded in Bragg-Brentano reflexion mode, in the $2\theta$ range from 3° to 60**°,** and a step size of 0.017°.
Variable-temperature pXRD analyses were performed on a similarly configured X'Pert MPD diffractometer equipped with a cryogenic chamber and a kapton window. The temperature was first gradually lowered from ambient down to 100 K, then gradually increased back to ambient temperature, with steps of 20 K, and 45 minutes acquisitions. The temperature is given with a ± 5°C error.

***SEM (Scanning Electron Microscopy), EDXS (Energy Dispersive X-ray Spectroscopy), and TEM (Transmission Electron Microscopy).***

SEM and EXDS analyses were carried out on a Zeiss Evo HD15 scanning electron microscope equipped with an Oxford Instruments X-MaxN SDD 50 $mm^2$ EDXS detector. Before the SEM analyses, samples were deposited on a double-sided conducting carbon tape.

TEM images were recorded at 100 kV on a JEOL 1400 Flash instrument. Samples for TEM were prepared by depositing a suspension of the OCP particles (dispersed in 1:1 EtOH/$H_2O$ by volume) onto carbon-supported copper grids and left to dry overnight at air, prior to analyses.

***Solid-state NMR (ssNMR)***

*$^1$H solid-state NMR*

A high resolution, high field, $^1$H MAS NMR spectrum was acquired on the 35.2 T series connected hybrid (SCH) magnet at the National High Magnetic Field Laboratory (NHMFL, Maglab),[18] using a Bruker Avance NEO NMR spectrometer operating at a $^1$H Larmor frequency of 1500.10 MHz, and a 1.3 mm narrow-bore NHMFL probe spinning at 50 kHz. The temperature was regulated to 0°C (temperature of the refrigerating unit). The spectrum was acquired using a Hahn-Echo sequence, with 90 and 180° pulse of 5 and 10 µs, respectively, separated by an echo delay of 1 rotor period (20 µs). A total of 8 scans were recorded with a recycle delay of 5 s.

Low and ambient temperature $^1$H NMR experiments were performed at the CRMN Lyon on an 18.8 T Avance NEO spectrometer operating at a $^1$H frequency of 799.66 MHz, equipped with a low-temperature 1.3 mm probe, achieving spinning rates of 40 kHz at ca. 100 K (temperature of the refrigerating unit). The room-temperature $^1$H spectrum was acquired using a Hahn-echo sequence, with 90 and 180° pulse of 3.7 and 7.4 µs, separated by an echo delay of 1 rotor period. A total of 32 scans were acquired, using a recycle delay of 8 s (which corresponds to full relaxation at room temperature). The low-temperature (100 K) $^1$H spectrum was acquired using a DEPTH background-suppression scheme, using 90° and 180° pulses of 2.25 and 4.5 µs, respectively.[19] A total of 16 scans were acquired with a recycle delay of 16 s (which does not correspond to full relaxation at 100 K, but the overall lineshape did not show significant difference between 16 and 64 s of recycle delay). $^1$H chemical shifts were referenced to the OH group of crystalline HAp at 0.0 ppm relative to adamantane (at 1.8 ppm).

*$^{31}$P solid-state NMR*

$^{31}$P MAS NMR experiments were performed at "close to ambient" temperature (temperature of the refrigerating unit set to 0°C), at 14.1 T on a Varian VNMRS spectrometer operating at $^1$H and $^{31}$P Larmor frequencies of 599.82 MHz and 243.12 MHz respectively, using a 1.6 mm HXY probe. The rotor spinning speed was set at 20 kHz. The Bloch decay, quantitative $^{31}$P NMR spectrum was acquired with a recycle delay of 750 s over four scans, with a 100 kHz SPINAL-64 $^1$H decoupling.

$^1$H – $^{31}$P cross-polarisation (CP) experiments in DNP conditions were performed at cryogenic temperatures (down to 100 K), using an Avance III NMR spectrometer (9.4 T) operating at $^1$H and $^{31}$P Larmor frequencies of 400.00 and 161.92 MHz respectively equipped with a 263 GHz gyrotron for microwave irradiation, and a low-temperature 3.2 mm probe in double resonance (HX) configuration. Radio frequency (rf) field strengths were set to 71.4 kHz in the case of $^{31}$P and 100 kHz on the $^1$H channel. A series of $^1$H-$^{31}$P CPMAS spectra at various temperatures were acquired without the presence of microwaves, with a CP contact time of 2 ms, a recycle delay of 5 s, and 8-16 scans per experiment at a MAS rate of 10 kHz, and using SPINAL-64 $^1$H decoupling[20] during acquisition, with a $^1$H decoupling power of 130 kHz. For DNP-enhanced NMR experiments, the sample was impregnated with a DNP matrix containing 10 mM of AsymPol-POK radical[21] in a 60/30/10 volume ratio of a $d_8$-glycerol/$D_2O$/$H_2O$ mixture. The $^1$H polarisation was then transferred to the $^{31}$P nuclei using a CP sequence with a contact time of 2 ms. The recycle delay was set to 2.3 s according to the optimal $^1$H-

$^{31}$P polarization build-up time under microwave irradiation. DNP enhancements for all $^{31}$P peaks obtained in this configuration were of $\varepsilon_{on/off}$ = 29 (Fig. S1).

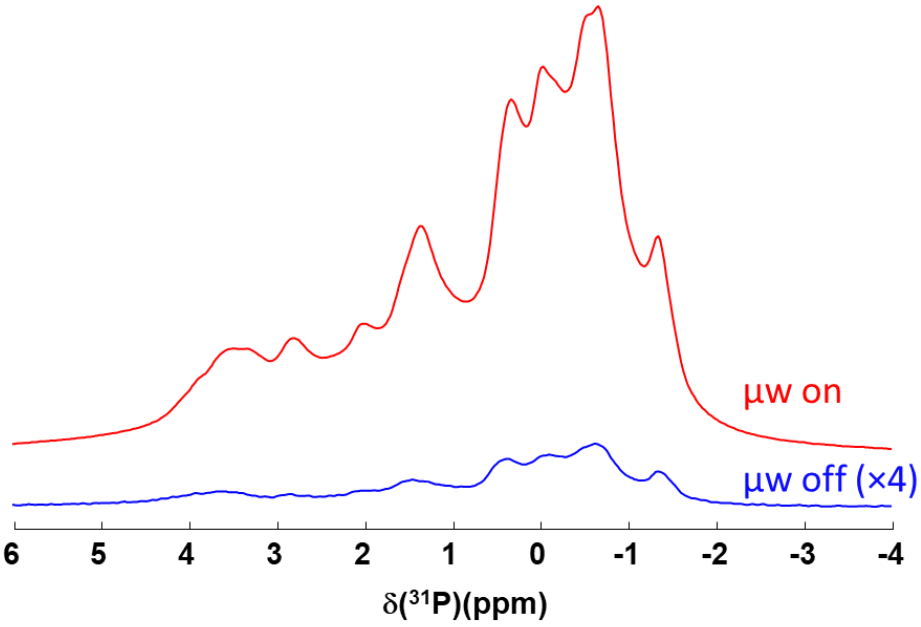


***Figure S1: $^{31}$P CPMAS NMR spectra of the unenriched OCP sample ($B_0$ = 9.4 T, $\nu_r$ = 10 kHz) recorded at ca. 100 K under DNP conditions, with (red) or without (blue) microwave irradiation suitable for DNP. The latter spectrum was scaled to four time its intensity. The measured $\varepsilon_{on/off}$ enhancement in this configuration is 29.***

Subsequently, a 2D $^{31}$P-$^{31}$P Double Quantum/Single Quantum (DQ/SQ) spectrum was acquired, with double-quantum excitation and reconversion of the $^{31}$P spins being achieved with the dipolar recoupling sequence S3.[22–24] The experimental temperature under microwave irradiation was approximately 100 K and the spinning speed was set to 13 kHz. A 100 kHz rf field strength $^{1}$H decoupling was used during direct detection period utilising the SW$_f$ – TPPM decoupling scheme,[25] whereas a 100 kHz rf SPINAL-64 scheme and continuous wave irradiation was used for the indirect detection period and the $S_3$ recoupling block, respectively. 256 points containing 16 transients each were acquired, corresponding to a total experimental time of approx. 2.5 h, with a mixing time of 7.4 ms. A $^{1}$H – $^{31}$P CP-HETCOR correlation spectrum was also recorded under identical DNP conditions. Enhancement was achieved by transferring magnetisation from the hyperpolarised proton with a CP contact time of 0.2 ms. The indirect acquisition was obtained with 196 slices with 8 scans each, with a 2.34 s recovery delay between each transient, for a total experimental time of 1 h. An FSLG decoupling scheme was applied during the evolution time (100 kHz rf field), while a SW$_f$ – TPPM $^{1}$H decoupling scheme was applied during the acquisition (100 kHz rf field).

High-field $^{31}$P MAS NMR experiments were recorded at low temperature (ca. 100 K – temperature of the refrigerating unit) using the 18.8 T Avance NEO spectrometer at ENS Paris, operating at $^{1}$H and $^{31}$P Larmor frequencies of 800.23 and 323.94 MHz respectively, and equipped with a low-temperature 3.2 mm probe, spinning at 8 kHz. A direct-excitation $^{31}$P NMR spectrum was recorded with a 30° pulse (1.6 μs, 52 kHz rf), and SPINAL-64 $^{1}$H decoupling during acquisition (ca. 70 kHz rf field strength). The recycle delay was set to 200 s, and 24 scans were acquired ($T_1$ was not measured precisely, but no change in relative intensities of the different OCP $^{31}$P signals was observed when using recycle delays of 60 s or

400 s). $^{31}$P CPMAS NMR spectra were recorded using a 90° (4.8 µs, 52 kHz rf) excitation pulse on the $^{1}$H, an array of contact times from 0.15 to 5.45 ms with 0.10 ms increments, and applying SPINAL-64 $^{1}$H decoupling during acquisition (52 kHz rf); the recycle delay was set to 60 s, and 16 scans were acquired at each contact time. $^{31}$P chemical shifts were referenced to the phosphate peak of crystalline HAp at 2.8 ppm or to an 85% $H_3PO_4$ solution at 0.0 ppm.

*$^{17}$O high-field solid-state NMR*

An ultra-high field $^{17}$O MAS NMR spectrum was recorded at the NHMFL in Tallahassee on the SCH magnet at 35.2 T, using a Bruker Avance NEO NMR spectrometer operating at $^{1}$H and $^{17}$O Larmor frequencies of 1500.10 and 203.36 MHz respectively. A NHMFL 1.3 mm narrow-bore solid-state NMR probe was used, spinning to 25 kHz. The spinning speed was chosen to minimise the overlap of spinning sidebands with the sample signal. The sample temperature was regulated to 0°C (temperature of the refrigerating unit). The spectrum was acquired using a Hahn-echo sequence, with central-transition (CT)-selective pulses (8 µs excitation and 16 µs refocusing pulses; for a power of 3.125 W) and an echo delay of 1 rotor period. The recycle delay was set to 1 s and 4096 scans were recorded. No decoupling was applied during the acquisition.

A 2D $^{1}$H – $^{17}$O correlation experiment was also recorded at the NHMFL, on an 18.8 T Bruker spectrometer operating at $^{1}$H and $^{17}$O Larmor frequencies of 799.71 and 108.42 MHz respectively, equipped with a low-temperature 1.3 mm probe, spinning at 50 kHz under ambient conditions. A D-RINEPT-based magnetisation transfer[26] was used, with the $SR4_1^2$ based recoupling sequence.[27] On the $^{17}$O channel, a WURST pulse was first applied (1 ms length, with a power of 8 W), followed by a 4 µs CT-selective pulse (corresponding to ca. 21 kHz rf field strength for the liquid). On the $^{1}$H channel, the total $SR4_1^2$ recoupling time was 480 µs. The recycle delay was set to 0.15 s. A total of 64 complex $t_1$ increments with 1792 transients were acquired. The total experimental time was ca. 10 h. No decoupling was applied during the acquisition.

Low and ambient temperature $^{17}$O NMR experiments were performed at the CRMN Lyon on an 18.8 T Avance NEO spectrometer operating at $^{1}$H and $^{17}$O Larmor frequencies of 799.66 and 108.42 MHz respectively, equipped with a low-temperature 1.3 mm probe, spinning at 25 kHz. $^{17}$O NMR spectra were recorded with a double frequency sweep (DFS)[28] enhancement scheme. The DFS-sweep had a length of 400 µs, starting at a frequency offset of 200 kHz and ending at 70 kHz; the power of this pulse was 10 W at ambient temperature, and 5 W at 100 K. The DFS pulse was followed by an excitation pulse of 2.33 µs at ambient temperature (1.5 µs at 100 K). No decoupling was applied on the $^{1}$H channel (when applying $^{1}$H decoupling at 100K, the PO region remains essentially unchanged, while the relative intensity of the POH region only increases by less than 15%). At both temperatures, the recycle delay was set to 1 s, and 24000 scans were acquired. A 2D $^{1}$H – $^{17}$O correlation experiment was also recorded at 100 K (temperature of the refrigerating unit), spinning at 30 kHz, and using a D-HMQC (dipolar-heteronuclear multiple-quantum coherence) sequence with the $SR4_1^2$ recoupling scheme.[27] The 90° pulses applied on the $^{17}$O and $^{1}$H were of 2.33 and 2.5 µs duration, respectively. The total $SR4_1^2$ recoupling time was 276 µs. The recycle delay was set to 0.8 s. A total of 62 slices with 3528 scans each were acquired, for an experimental time of ca 50 h. $^{17}$O chemical shifts were referenced to water ($H_2O$) at 0.0 ppm.

*$^{43}$Ca high-field solid-state NMR*

$^{43}$Ca MAS NMR experiments at ambient temperature were performed at multiple magnetic fields (18.8, 23.4 and 35.2 T) at different NMR facilities (ENS in Paris, UK NMR facility in Warwick, and NHMFL in

Tallahassee). All were direct $^{43}$Ca acquisitions on an enriched compound. The 35.2 T acquisition was recorded using a 5% enriched sample, whereas the others were recorded on a 15% enriched sample.
The 35.2 T spectrum was recorded on the NHMFL SCH magnet, using a Bruker Avance NEO NMR spectrometer operating at the $^{43}$Ca Larmor frequency of 100.96 MHz, using a NHMFL 3.2 mm probe spinning at 10 kHz, and setting the refrigerating unit to 10 °C. A total of 24634 scans were acquired with a recycle delay of 0.5 s, for an acquisition time of ca. 3h30. A DFS enhancement scheme was used, with a starting offset of 400 kHz, sweeping down to 50 kHz over 5 ms with a set power of 5 W. The DFS was followed by an 8 µs excitation pulse (31 kHz, solid 90°). A multi-DFS enhancement scheme[29] was applied, with four acquisitions per recycle delay. No decoupling was used during the acquisition.
The 23.4 T spectrum was recorded using an Avance NEO 1000 spectrometer, operating at the $^{43}$Ca Larmor frequency of 67.66 MHz, and equipped with a 1.9 mm probe spinning at 40 kHz, while setting the temperature of the refrigerating unit to 0°C. The DFS swept from an offset of 400 kHz to 50 kHz and had a duration of 2 ms and a set power of 10 W. The DFS was followed by a 1.8 µs excitation pulse (corresponding to a 22.5° tilt angle on a liquid). A total of 17848 scans were acquired with a recycle delay of 1 s, for an acquisition time of 5 h. No decoupling was used during the acquisition.
At 18.8 T, a low-temperature 3.2 mm probe was used, allowing for acquisitions both at room temperature and at 100 K using similar experimental parameters. The spectra were recorded with an Avance NEO spectrometer operating at a $^{43}$Ca Larmor Frequency of 53.86 MHz, using a low-temperature MAS probe spinning at 8 kHz. At both temperatures, a DFS enhancement scheme was used, with a 2 ms sweep duration (20 W power), starting with an offset of 400 kHz down to 50 kHz. This pulse was followed by a 3.75 µs excitation pulse (150 W power, corresponding to ca. 16 kHz rf on the liquid). No decoupling was used during the acquisition. Acquisitions at both temperatures were performed with a recycle delay of 0.8 s. A total of 55068 scans were acquired at ambient temperature, and 34088 scans at 100 K. $^{43}$Ca chemical shifts were referenced to a 1M $CaCl_2$ solution at 0.0 ppm.

***Processing and fitting of the $^{31}$P CPMAS build-up curves***

The series of 54 $^{31}$P CPMAS NMR spectra with varying contact times which had been recorded at 100 K were fitted sequentially using a sum of Pseudo-Voigt peaks. This was done using a homemade Python script, with the nmrglue[30] and scipy[31] modules for data reading and fitting respectively. The fit was optimised using the Levenberg-Marquardt method from the "curve_fit" function of the scipy module. The amplitudes of all component peaks were set as variables, and all other parameters (peak width, g/l ratio and position) were fixed. The value of the amplitude of each peak was estimated for each spectrum of the series, and the error calculated from the square root of the diagonalised covariance matrix. The values of the peak amplitudes over the contact time ($t_{cp}$) were then fitted with the simplified expression:[32]

$$I(t_{cp}) = \frac{I_0}{1 - T_{cp}/T_{1\rho}}\left(e^{\frac{-t_{cp}}{T_{1\rho}}} - e^{\frac{-t_{cp}}{T_{cp}}}\right)$$

with $I_0$ the absolute amplitude of the resonance, $T_{cp}$ the time constant of the magnetisation transfer and $T_{1\rho}$ the simplified time constant of the spin-lattice relaxation. In cases where $T_{1\rho}$ was large (> 50 ms) in comparison to the longest contact time recorded (5.55 ms), it was considered infinite and the terms scaling with a factor of $T_{1\rho}^{-1}$ were nullified. The optimised values and errors for $I_0$, $T_{cp}$ and $T_{1\rho}$ were likewise obtained using a Levenberg-Marquardt minimisation algorithm.

**DFT calculations**

***Molecular dynamics simulations and averaging***

Two molecular dynamics simulations were performed starting from the DFT-relaxed structure obtained in the previously published NMR-crystallography study of OCP by Davies *et al*.[15] The calculations were done using the CP2K package,[33] consisting in Born–Oppenheimer MD (BOMD) with PBE electronic representation, including the Grimme (D3) correction for dispersion,[34] GTH pseudopotentials,[35] combined plane-wave, and TZVP basis sets.[36] The simulation was carried out over 30000 steps, with a step time of 0.5 fs in an NVT canonical ensemble, periodic boundary conditions, fixed cell parameters and unconstrained atomic positions. For the calculation of the forces, we used a QUICKSTEP method with an analytical stress tensor and an energy cut-off of 400 Ry. The temperature of the ensemble was set using a Nosé-Hoover-chain thermostat[37] composed of three elements, with a set temperature of 100 K in the first MD simulation, and 300 K in the second. Although the initial structure exhibits a *P*-1 symmetry, no symmetry constraints were imposed during the simulation. Averaged structures of OCP over the 100 K and 300 K MD simulations were obtained by averaging the atomic positions of a given atom at each step of the MD (from step 1000 to 30000).

***NMR computations***

GIPAW calculations were performed with the QUANTUM-ESPRESSO[38] software, using a DFT formalism with a PBE gradient approximation.[39] The valence electrons were approximated using a norm-conserving pseudopotential. The wave functions are expanded on a plane wave basis set with a kinetic energy cut-off of 80 Ry with a Monkhorst-Pack grid of 1 × 2 × 3. For this study, the numbering of the sites is made consistent with a previously published structure.[15] Calculated NMR parameters over the duration of the MD simulations were determined by averaging the predicted shielding and electric field gradient tensors over a set number of evenly spaced structures. For this purpose, a GIPAW calculation was performed every 100 steps for the duration of the molecular dynamics simulation, starting from step 1100, for 290 GIPAW calculations per simulation. Time-averaged $\delta_{iso}$ values, calculated for each step, are the mean average of all $\delta_{iso}$ up to the specific time step. The principal components of the EFG tensor for a given site were then obtained by first averaging each individual components of the EFG tensor over the length of the simulation, and then diagonalising the averaged EFG tensor following the convention $|V_{zz}| \geq |V_{xx}| \geq |V_{yy}|$. The quadrupolar interaction is given with the values $C_Q = eQV_{zz}/h$ and $\eta_Q = (V_{yy} - V_{xx})/V_{zz}$, with the quadrupole moments Q taken from recent experimental measurements ($Q_{17O} = -25.58$ mb, $Q_{43Ca} = -44.4$ mb).[40,41,42] Based on $C_Q$ and $n_Q$, the $P_Q$ parameter which is also used in this contribution is defined by $P_Q = C_Q\left(1 + \frac{\eta_Q^2}{3}\right)^{1/2}$. All of the data treatment was facilitated using homemade Python scripts, using the Numpy[43] module for all numerical applications.

The isotropic chemical shift $\delta_{iso}$ is defined as $\delta_{iso} \approx -(\sigma_{iso}-\sigma_{ref})$, where $\sigma_{iso}$ is the isotropic shielding and $\sigma_{ref}$ is the isotropic shielding for the same nucleus in a reference system. $\sigma_{ref}$ was referenced internally as the difference between the average calculated $\sigma_{iso}$ and chemical shift values of the best resolved 300 K experimental spectra. Here, $\sigma_{ref}(^1H)$ = 29.9 ppm; $\sigma_{ref}(^{31}P)$ = 288.3 ppm; $\sigma_{ref}(^{17}O)$ = 230 ppm; $\sigma_{ref}(^{43}Ca)$ = 1110 ppm. Note that the reference value for oxygen-17 is close to the one recently used for calcium oxalates[44] and characteristic of the presence of Ca-O bonds leading to a partial Ca-3d O-2p hybridisation.[45]

**Results**

***Syntheses and characterisations at ambient temperature***

All syntheses (both gram-scale and low-scale) were tested for reproducibility and led to a crystalline OCP phase as confirmed by pXRD analysis (Fig. S2).

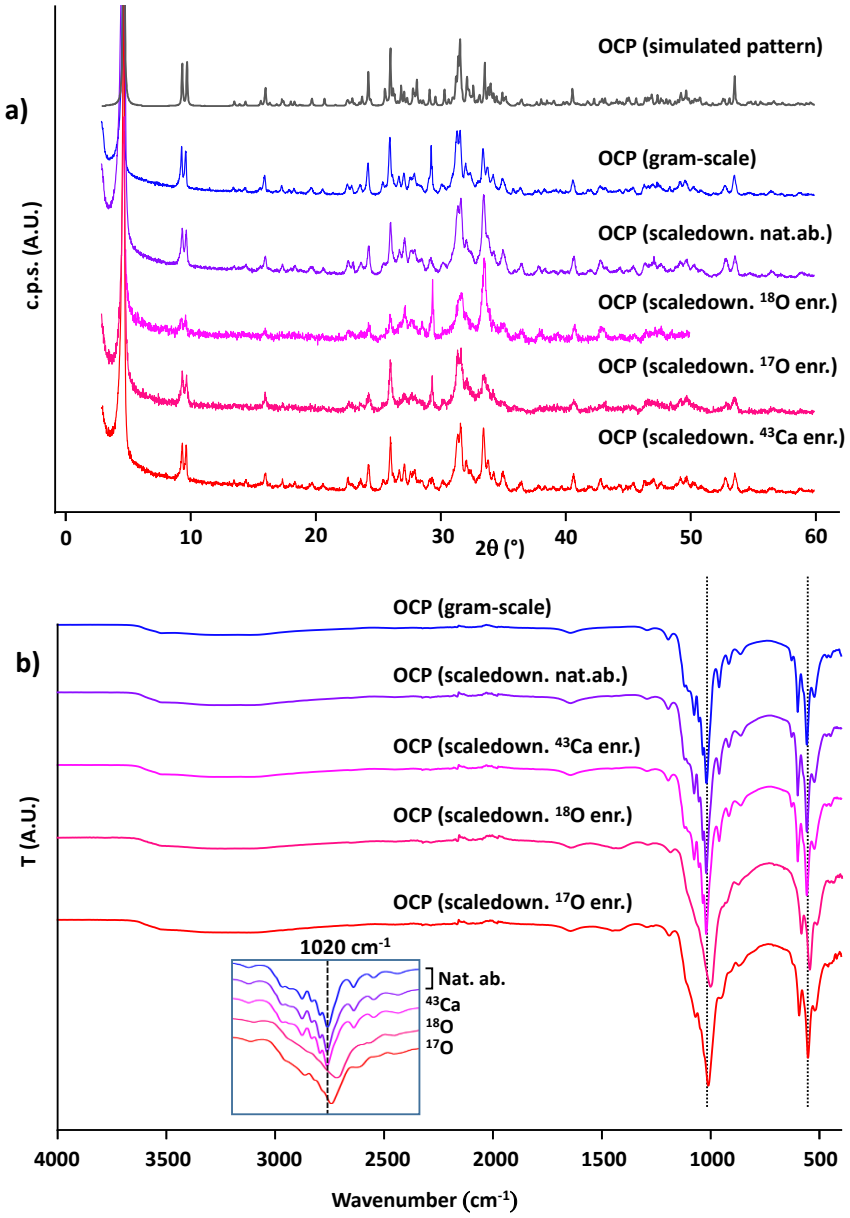


***Figure S2: a) pXRD patterns of samples synthesized using the different protocols described in this study. Patterns are scaled here so that the higher intensity diffraction peaks of OCP are compared (implying a "truncation" of the lowest diffraction peak of OCP, at ca 4.7 °). The simulated pXRD pattern of OCP (starting from the experimental .cif file ICSD 65347) is shown in dark grey at the top. b) ATR-IR transmission spectra of the different samples, scaled to match intensities. Magnified below is a comparison of the same spectra, highlighting the strong P-O stretching bands around 1020 $cm^{-1}$, and showing clear evidence of shifting due to the increased mass of the oxygen isotopes in the enriched samples (with, as expected, more significant shifts upon $^{18}O$-labeling compared to $^{17}O$-labeling). Because the enrichment is only partial (theoretically, ca. 40%), there are overlaps between resonances belonging to different oxygen isotopes, leading to a loss of resolution on the IR spectra.***

The main obstacles to a successful synthesis are the incomplete or excessive transformation of the DCPD precursor, leading to DCPD or HAp impurities, respectively. Whereas DCPD can easily be distinguished from OCP from its XRD powder pattern, HAp has similar diffraction peaks (in the intermediate angular range) and is more easily differentiated in $^{1}$H ssNMR spectra, where its OH resonance is found at 0.0 ppm (on a $^{31}$P spectrum, the HAp resonance is broad and centered at ca. 2.8 ppm). The Ca/P ratio of the compound synthesised via the scaled-up synthesis was estimated to be 1.41 ± 0.06 via EDXS microanalysis (Table S1), which is slighty above the theoretical value of 1.33, and to the ratio of the precursors during the synthesis (1.37).

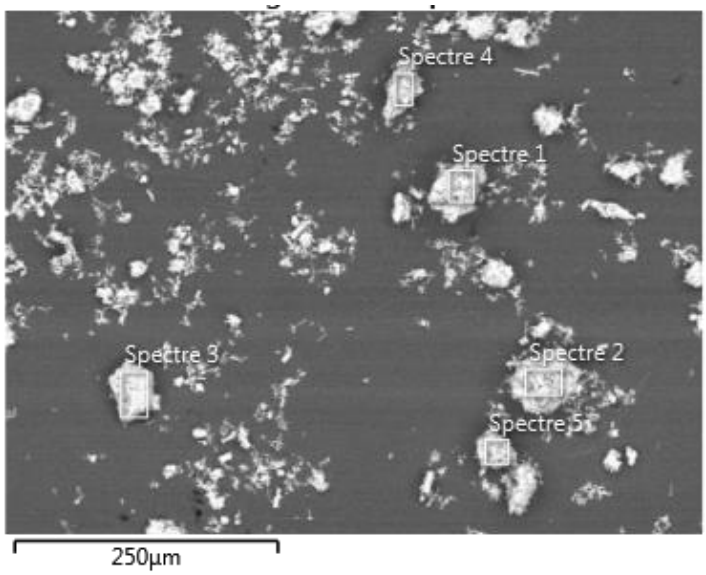


| | Spectrum 1 | Spectrum 2 | Spectrum 3 | Spectrum 4 | Spectrum 5 |
|---|---|---|---|---|---|
| Ca/P molar ratio | 1.42 | 1.37 | 1.34 | 1.55 | 1.38 |

| | |
|---|---|
| Average Ca/P molar ratio | 1.41 ± 0.06 |

***Table S1: EDXS analysis of gram-scale OCP, averaged over five spectra corresponding to different points of the sample.***

The Ca/P ratio of stoichiometric HAp is 1.67, and that of DCPD is 1.00. These observations lead us to believe that the OCP synthesised through these methods is of relatively good purity, with a possible presence of small amounts of HAp and/or $CaCO_3$ impurities. The samples were also analysed by SEM and TEM (Fig. S3), showing platelets characteristic of OCP. These are polydisperse, with particle lengths ranging from hundreds of nanometers to several micrometers. We note the extremely variable size and shape of the platelets, which may explain the variable relative intensities of different diffraction peaks obtained in XRD analysis for the different samples (Fig. S2a). In the case of the $^{17}$O-enriched sample, the success of the enrichment could be confirmed *via (i)* ATR-IR spectroscopy, where the increased atomic weight of the oxygen isotopes leads to lower frequency resonances for P-O vibration modes (e.g. bands at 1020 and 560 cm$^{-1}$) (Fig. S2b), *(ii)* $^{31}$P CPMAS NMR, where the additional $^{17}$O-$^{31}$P

couplings lead to changes and broadenings of the $^{31}$P resonances, in comparison to the non-labelled compounds (Fig. S3c), and *(iii)* $^{17}$O MAS NMR, as discussed later in this article.

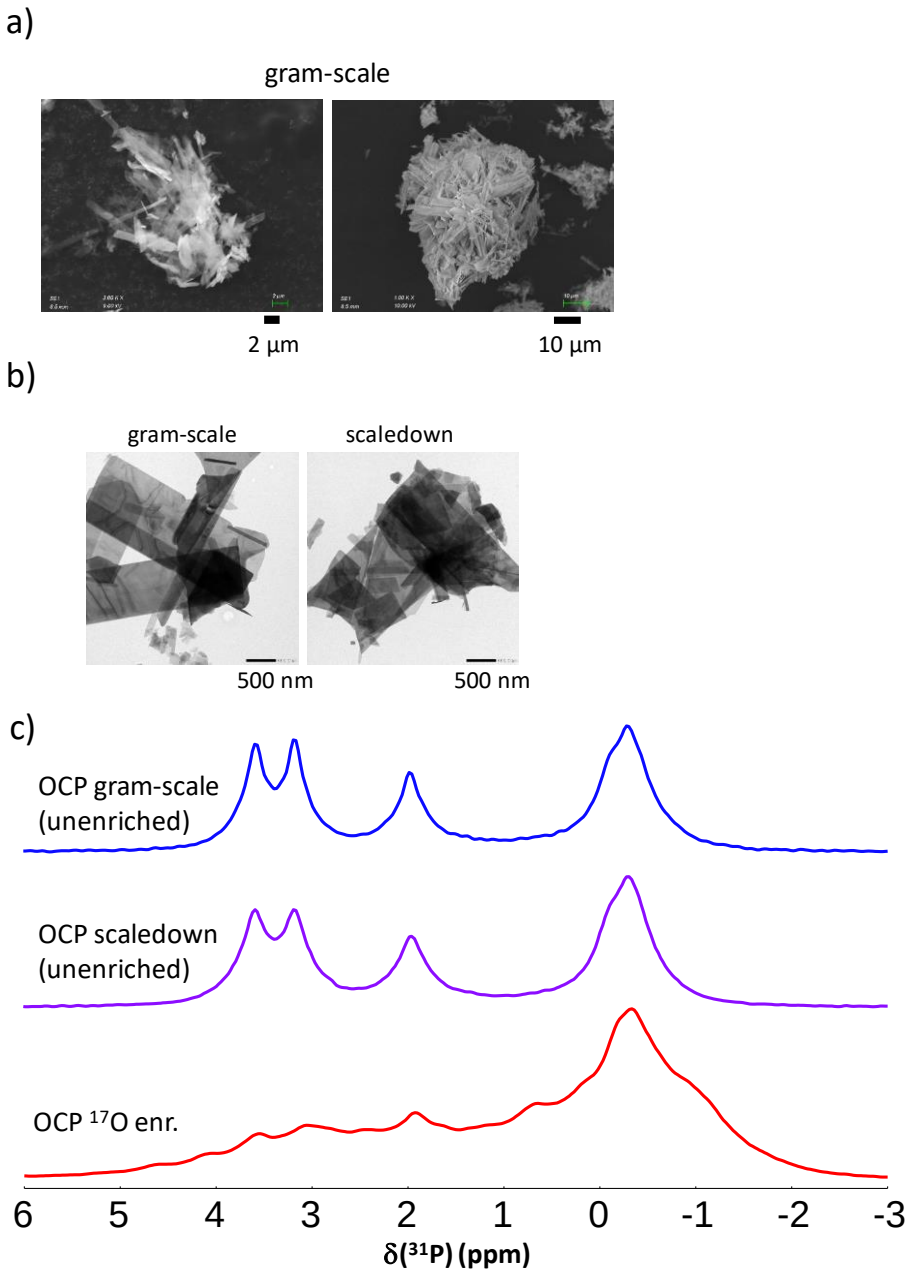


***Figure S3: a) SEM images of OCP particles. b) TEM images of OCP crystallites, obtained at natural-abundance with the two protocols described in this work. c) $^{31}$P CPMAS NMR spectra ($B_0$ = 14.1 T, $\nu_r$ = 20 kHz, $t_{CP}$ = 1 ms, refrigerating unit set to 0 °C) of three OCP samples. The couplings between the $^{17}$O and $^{31}$P isotopes are visible from the splittings observed for the $^{17}$O-enriched sample.***

The $^{31}$P MAS NMR spectrum of (non-labelled) OCP was recorded by direct excitation using a long recycle delay to enable relaxation of the different $^{31}$P sites (Fig. 2a). It could be decomposed into six resonances (as expected from the reported crystal structure), with integrated areas proportional to the amount of underlying sites, and considering three of the resonances almost superimposed, as already reported in previous NMR studies.[15]

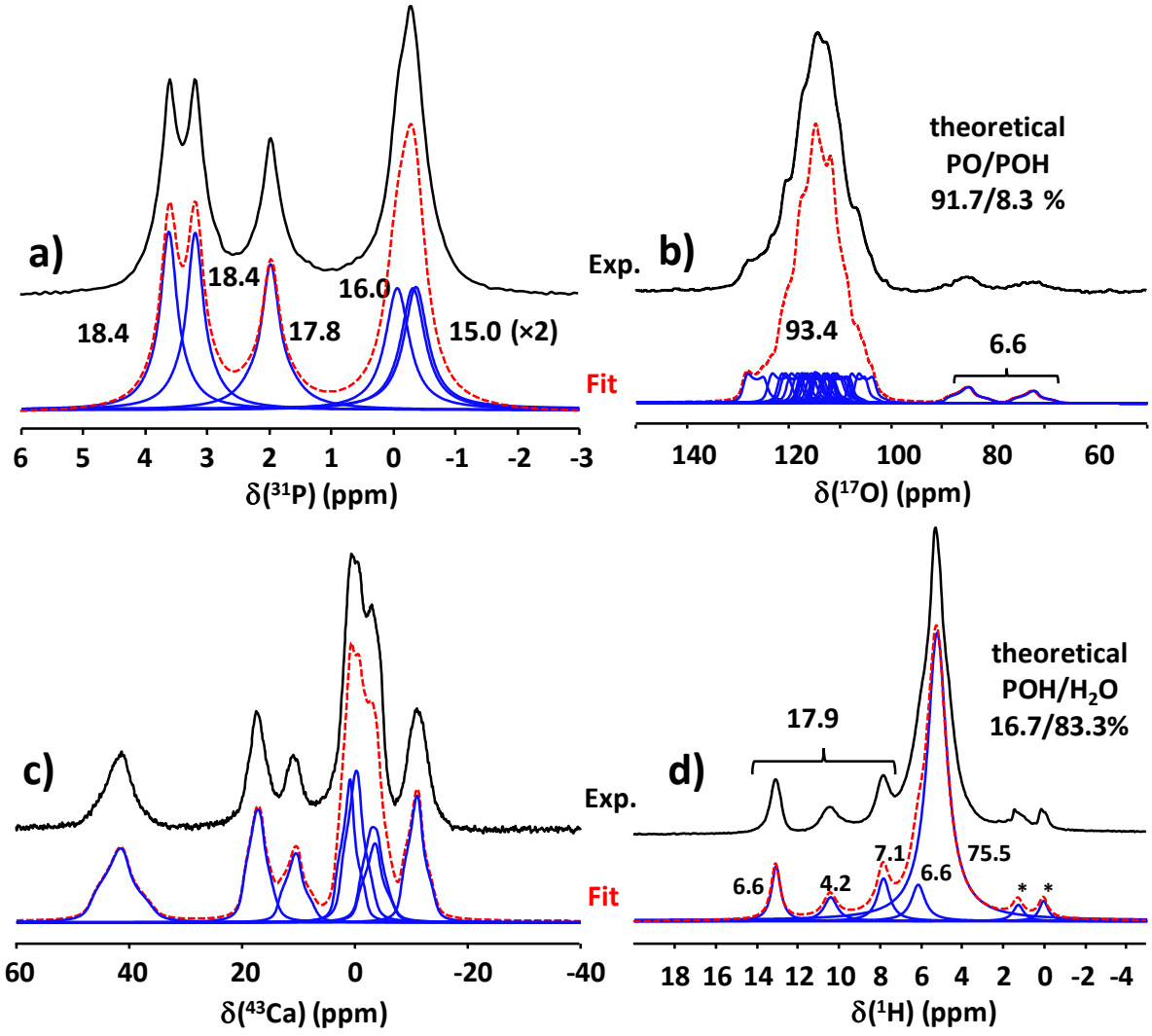


***Figure 2: Experimental (black) and fitted (red dashed) MAS NMR spectra of OCP : a) $^{31}$P single pulse spectrum recorded on the unenriched sample at $B_0$ = 14.1 T, $\nu_r$ = 20 kHz (refrigerating unit set to 0°C) ; b) $^{17}$O Hahn-Echo spectrum, refocused over one rotor period, recorded on the $^{17}$O enriched sample, $B_0$ = 35.2 T, $\nu_r$ = 25 kHz (refrigerating unit set to 0°C) ; c) $^{43}$Ca direct-excitation spectrum, recorded on the $^{43}$Ca enriched sample, $B_0$ = 35.2 T, $\nu_r$ = 10 kHz (refrigerating unit set to 10°C) ; d) $^{1}$H Hahn-Echo spectrum, refocused over one rotor period, and recorded on the $^{17}$O enriched sample, $B_0$ = 35.2 T, $\nu_r$ = 50 kHz (refrigerating unit set to 0°C). Relative proportions of signals (in %) are indicated in black. All NMR parameters used for fitting are summarised in Tables S2 to S4. (Two small $^{1}$H resonances, indicated by the "*" symbol are visible at ~ 0 and 1 ppm, which a priori do not belong to OCP; the former one is tentatively assigned to HAp).***

The $^{17}$O MAS NMR spectrum was recorded at 35.2 T (Fig. 2b). It clearly shows a main component ranging from 105 to 130 ppm (corresponding to PO sites), and two very distinct signals with $\delta_{iso}$ around 75 and 90 ppm respectively, accounting for about 6.6 % of the total signal. These can be safely assigned to the two POH environments expected in OCP. The P-OH/PO ratio is slightly lower than the expected value, possibly due to differences in T2 relaxation and/or in nutation rates of both types of sites during the spin-echo. The $H_2O$ molecules of the interlayer were not enriched, and therefore are not visible in $^{17}$O NMR under these conditions; their possible signature in $^{17}$O NMR will thus not be discussed here. A tentative fit of the spectrum in the PO region could be proposed based on a two-field simulation ($B_0$

= 35.2 T and 18.8 T), with 22 components of similar intensities and using similar quadrupolar parameters for all sites (Fig. S4), i.e. with $C_Q$ = 4.8 MHz and $\eta_Q$ = 0.2 values, as suggested by later experiments (Fig. 9), and in reasonable agreement with previously reported values.[46–48]

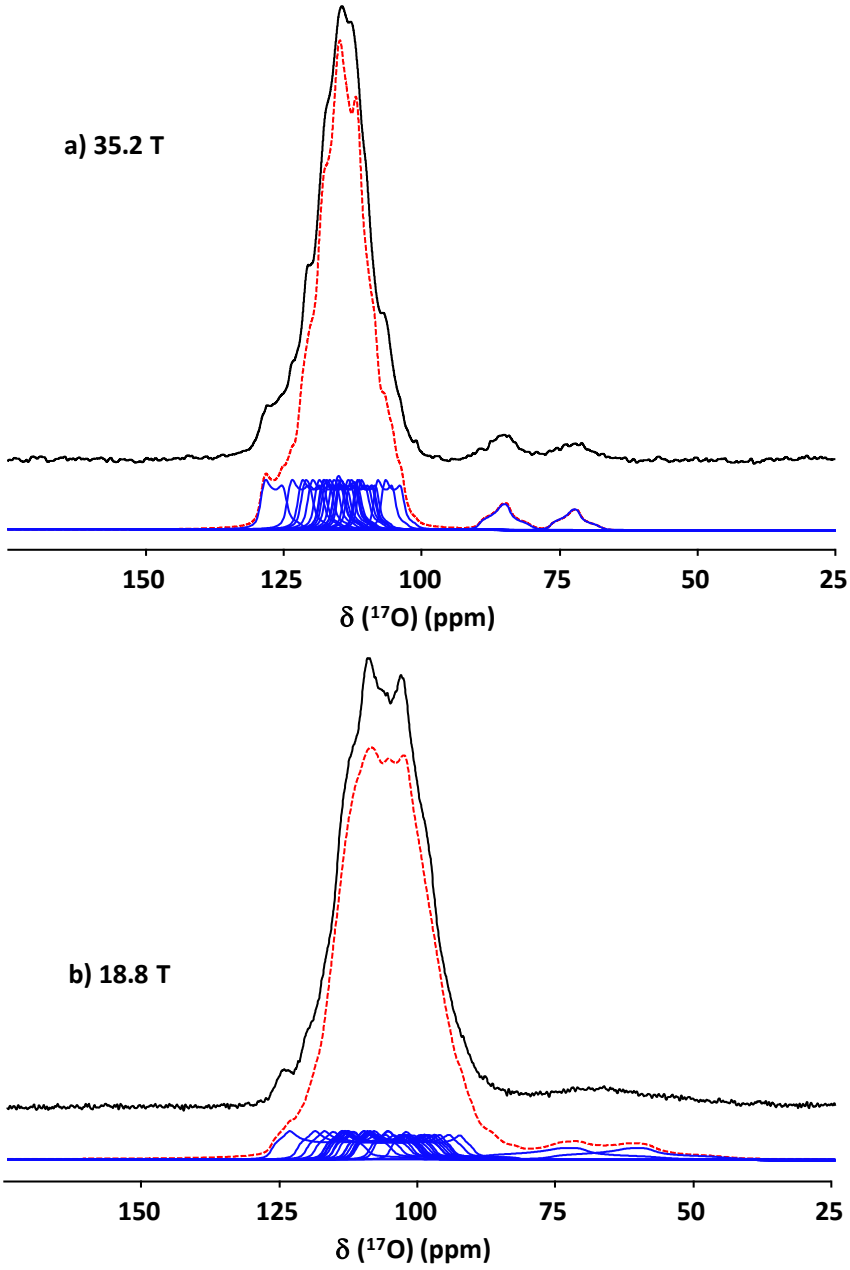


***Figure S4: Experimental $^{17}O$ Hahn-Echo MAS NMR spectra of OCP recorded at ambient temperature: a) $B_0$ = 35.2 T, $\nu_r$ = 25 kHz b) $B_0$ = 18.8 T, $\nu_r$ = 25 kHz (in black). A tentative fit is shown below each spectrum, with individual contributions of the PO and P-OH sites in blue, and their sum in red dashed line.***

At 35.2 T, the $^{43}Ca$ MAS NMR spectrum is still not fully resolved (Fig. 2c). Yet, it is consistent with the superposition of eight $^{43}Ca$ resonances, with some still slightly broadened by second-order quadrupolar effects. A tentative fit can be offered based on a multiple-field simulation with eight components (Fig. S5). It should be noted that this spectrum is close to the $^{43}Ca$ DOR (DOuble Rotation) NMR data previously reported in the literature.[16]

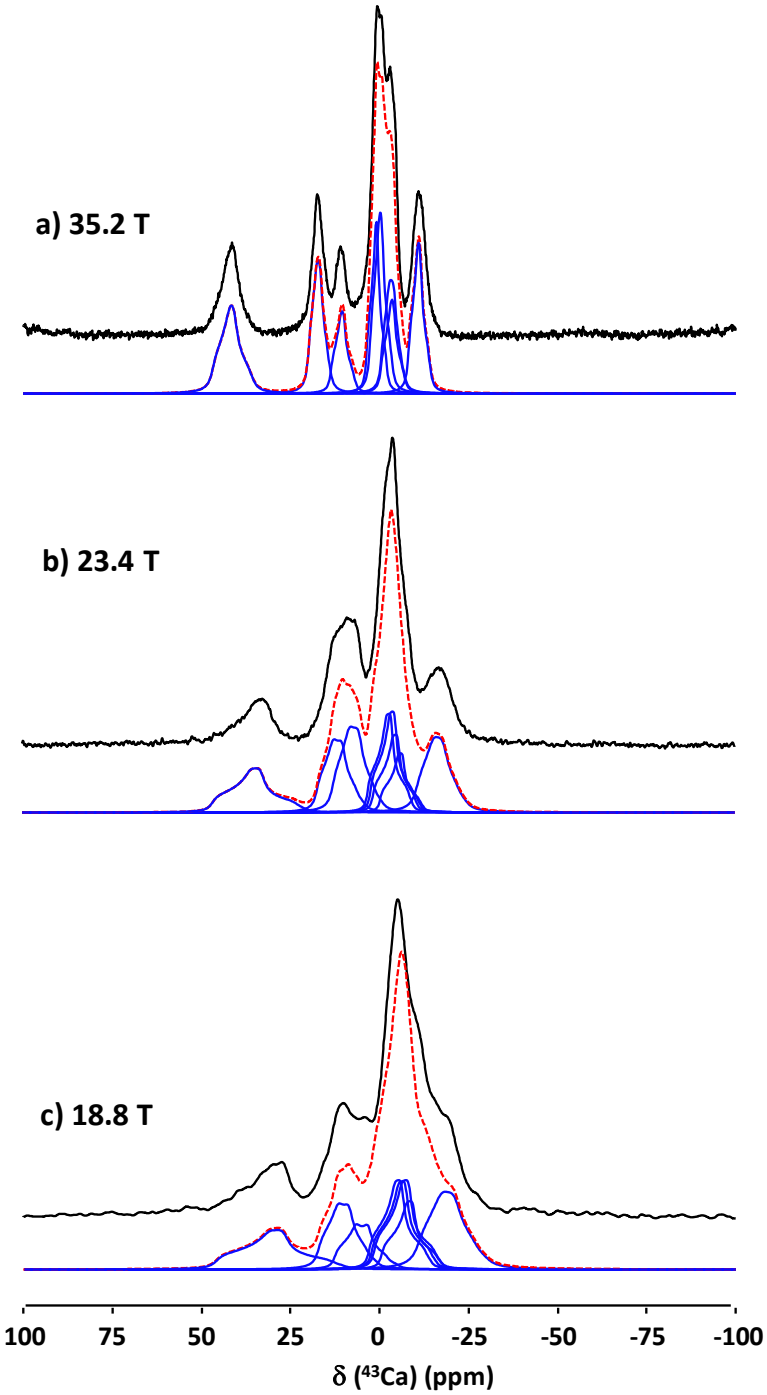


***Figure S5: Experimental $^{43}Ca$ MAS NMR spectra of OCP recorded at ambient temperature: a) $B_0$ = 35.2 T, $\nu_r$ = 10 kHz; b) $B_0$ = 23.4T, $\nu_r$ = 40 kHz c) $B_0$ = 18.8 T, $\nu_r$ = 8 kHz (in black). A tentative fit is shown below each spectrum, with individual contributions of the Ca sites in blue, and their sum in red dashed line.***

Finally, the $^{1}H$ MAS NMR spectrum (Fig. 2d) shows a main component centered about 4.5 ppm due to water molecules, and 3 minor signals around 13, 10 and 8 ppm consistent with POH sites involved in different H-bonds (presumably showing H---O distances ranging from 1.4 to 1.7 Å).[49] The presence of three signals compared to the two expected POH sites suggests a possible more complicated structure for OCP, as discussed below.

***Temperature and dynamics effects***

The $^{31}$P CPMAS NMR spectra of OCP at low temperatures show a significant change compared to room temperature. Between 220 K and 100 K, the four main peaks observed at room temperature (corresponding to six inequivalent sites, consistent with a *P*-1 cell symmetry) gradually split into a larger number of resonances, with at least ten individually resolved sites (Fig. 3a).

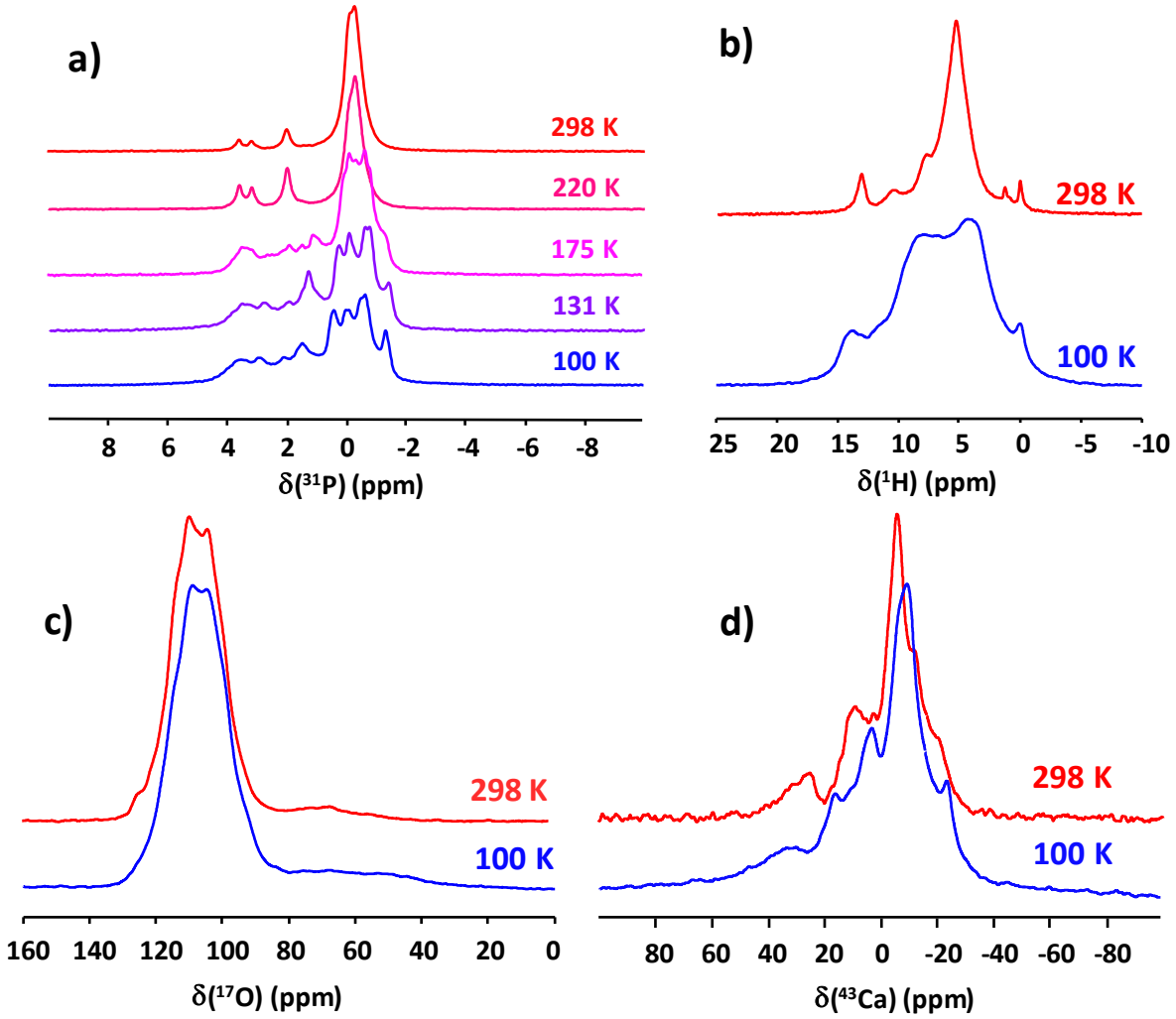


***Figure 3: Evolution with temperature of a) $^{31}$P CPMAS NMR spectra recorded on the unenriched OCP sample ($B_0$ = 9.4 T and $\nu_r$ = 10 kHz, b) $^{1}$H MAS NMR spectra recorded on the $^{17}$O enriched OCP sample ($B_0$ = 18.8 T and $\nu_r$ = 40 kHz), c) $^{17}$O Hahn-Echo NMR spectra (refocused over one rotor period), recorded on the $^{17}$O-enriched OCP sample ($B_0$ = 18.8 T and $\nu_r$ = 25 kHz) and d) $^{43}$Ca MAS NMR spectra recorded on the 15% $^{43}$Ca-enriched OCP sample ($B_0$ = 18.8 T and $\nu_r$ = 8 kHz). Indicated temperatures are those of the refrigerating units.***

During subsequent observations, these temperature-dependent changes were found to be fully reversible and repeatable over multiple OCP samples, prepared using both gram-scale and low-scale synthesis protocols. Further studies included the observation of OCP at low and ambient temperature *via* $^{1}$H (Fig. 3b), $^{17}$O (Fig. 3c) and $^{43}$Ca (Fig. 3d) NMR, using enriched samples. $^{1}$H resonances are much broader at 100 K, suggesting a reduction of mobility of the different OH groups compared to ambient

temperature. Although $^{17}O$ and $^{43}Ca$ NMR spectra also show an evolution of the signal between 100 K and close to ambient temperature, the most obvious changes were for the $^{1}H$ and $^{31}P$ NMR spectra. To go one step further, a series of XRD powder patterns were recorded, ranging from 100 K to 280 K in steps of 20 K (Fig. S6).

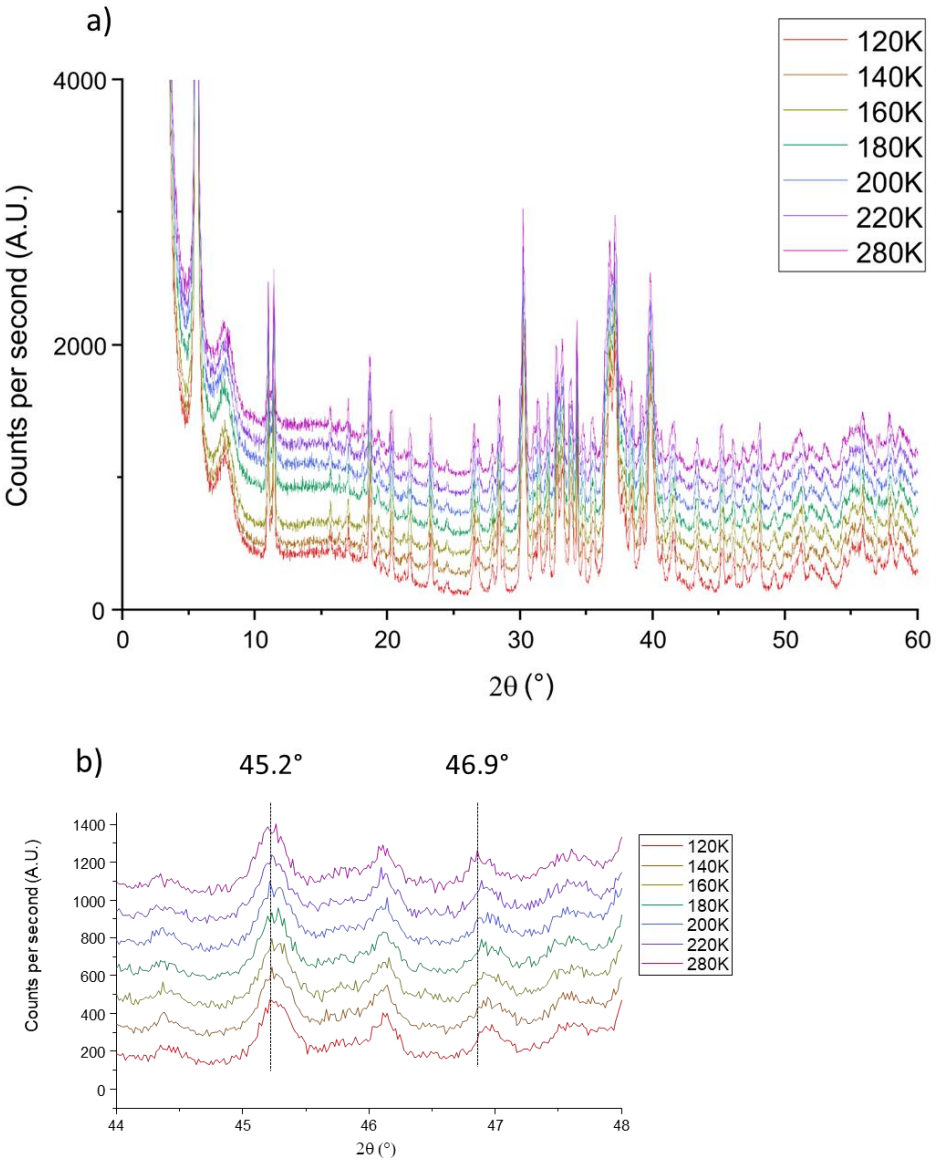


***Figure S6: a) Staggered pXRD patterns obtained at variable temperatures, starting at 120 K, and increasing the temperature incrementally to 280 K. b) Same patterns but focussing on the 2ϑ region from 44° to 48°, to highlight the gradual shift of the diffraction peaks with temperature.***

No evidence of a sudden change in OCP's complex pattern at any specific temperature was observed. Instead, a gradual shifting of the peaks occurred, consistent with a small change of the crystal cell parameters with temperature. This led us to hypothesise that the new signals observed in $^{31}P$ NMR were not the result of the appearance of a new phase or polymorph, but instead of a modification within the interlayer space caused by the change in temperature.

As mentioned in the introduction, previous studies[8,12] investigating the structure of OCP have had issues determining its symmetry group. With a high atom count, poor symmetry and a cluster of water

molecules in the interlayer that are difficult to locate *via* X-ray diffraction, the presence of central symmetry in the cell remained a hypothesis. A high-resolution, room temperature observation of OCP *via* $^{31}$P ssNMR seemingly confirms the *P*-1 symmetry group, as we only observe four distinct peaks, corresponding to the six equivalent positions of the lower symmetry (Fig. 2a). This is no longer true when observing OCP at temperatures below 175 K. Several mechanisms that may explain a symmetry break at low temperatures were considered in the literature: i) the asymmetric deprotonation of a water molecule to protonate a hydrogen phosphate (P6),[12] ii) the shifting of the position of a water molecule (whose oxygen atom is noted O19/O19', and has been shown to have high thermal parameters in previously reported XRD refinements),[12] or iii) the formation of an H-bond between the two central water molecules of O23 and O23' (Fig. 4).[12]

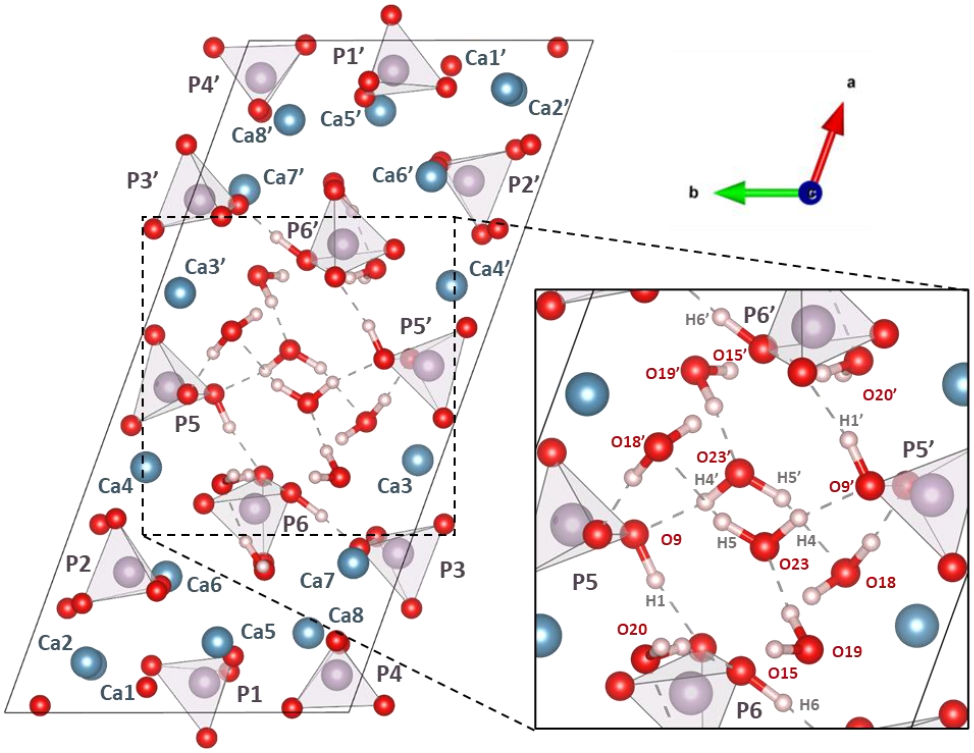


***Figure 4: DFT relaxed OCP structure,[15] with labels for calcium and phosphorus atoms (left) and relevant oxygen and hydrogen atoms of the interlayer (right). Each site is labelled with or without prime symbols, depending on its side relative to the cell's inversion centre.***

All these hypotheses are examined here, because they have been put forward in previous studies,[12,14] and are compatible with the observations by both XRD and NMR. As previous ssNMR analyses of OCP had shown the usefulness of *ab initio* calculations to help rationalise the experimental NMR spectra,[15,16] GIPAW calculations were also carried out as part of our work.

***DFT relaxation and molecular dynamics simulations***

A first series of numerical calculations were performed to investigate the possibility of explaining the symmetry break solely using "static" DFT relaxed-structures: GIPAW calculations of NMR parameters were performed on each model, and compared to the experimental data. A series of models were generated by selecting different relaxation parameters (relaxation of atomic positions only, or atomic positions and cell parameters). This did not result in a significant improvement of the calculated NMR

parameters compared to the previously reported ones,[15] nor in any "spontaneous" loss of symmetry from an initial *P*-1 structure, once the symmetry constraints removed. Instead, we observed that a DFT relaxation starting from a *P*-1 structure but without symmetry constraints would systematically produce a *P*-1 symmetrical structure, as already reported.[15]

Because of the difficulties of investigating potential temperature effects using static models of OCP, two molecular dynamics simulations were run, at 100 K and 300 K (which are relevant temperatures based on our experimental $^{31}$P NMR results). Starting from the same initial structure as for DFT relaxations (*P*-1 symmetry),[15] we simulated motions of all atoms in the structure, without any symmetry constraints, nor any change to the cell parameters. The GIPAW NMR parameters were then calculated every 100 steps, and averaged over the whole simulation, as previously described.[50]

At 100 K, a significant symmetry break was observed within the first 1000 steps (0.5 ps): the two central water molecules nearest the symmetry center (O23, O23') break symmetry to form an H-bond from O23-H4 to O23' (Fig. 5). This H-bond has an average H···O length of 1.95 Å, and remains stable at least at the time scale of this simulation (15 ps) (See Fig 6a and 6b). Because it requires the rotation of the O23 water molecule, this also breaks the H-bond present in the XRD-refined structure[12] between H4 and the hydrogen phosphate oxygen O9' (Fig. 5). Hence, this motion breaks the *P*-1 symmetry of the initial structure and leads to a stable *P*1 symmetry over the length of the simulation.

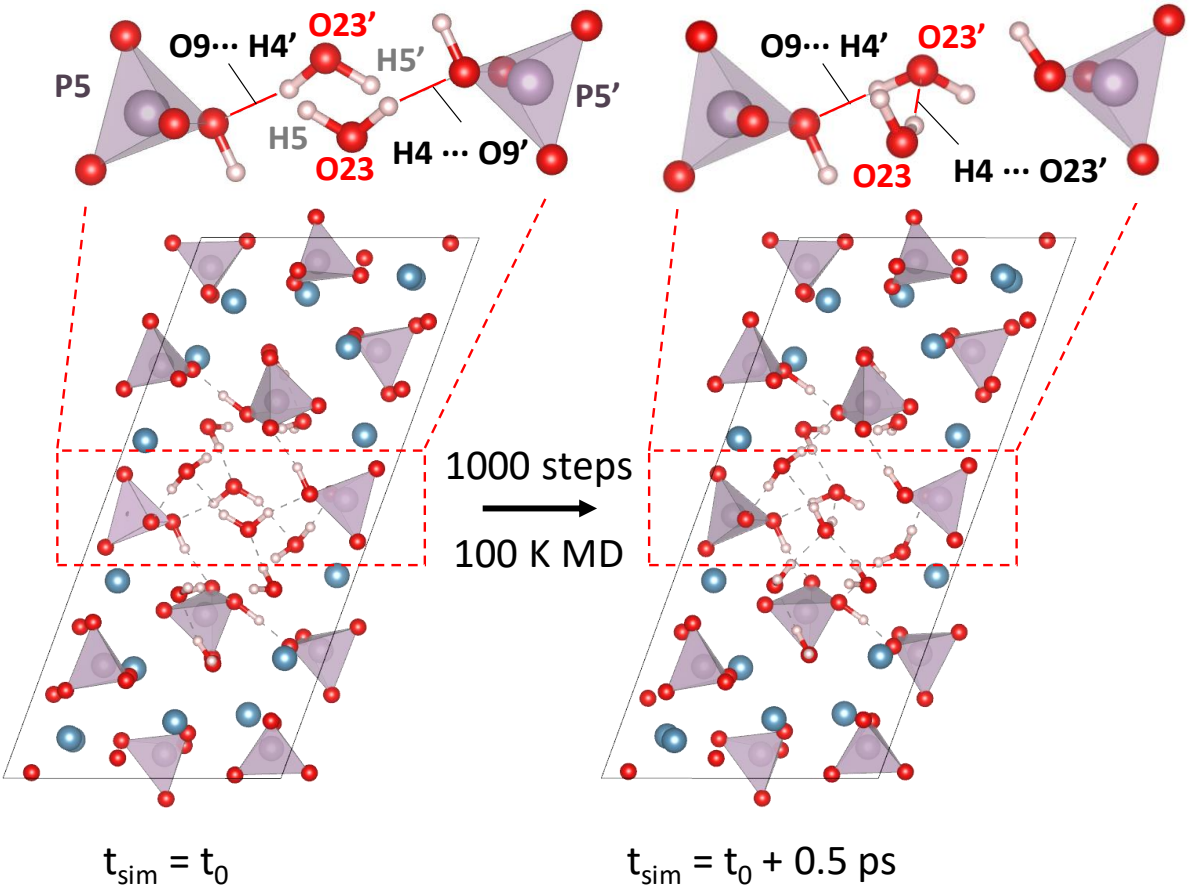


***Figure 5: Water molecule rotation inducing a symmetry break observed in the 1000 first steps of the 100 K molecular dynamics simulation.***

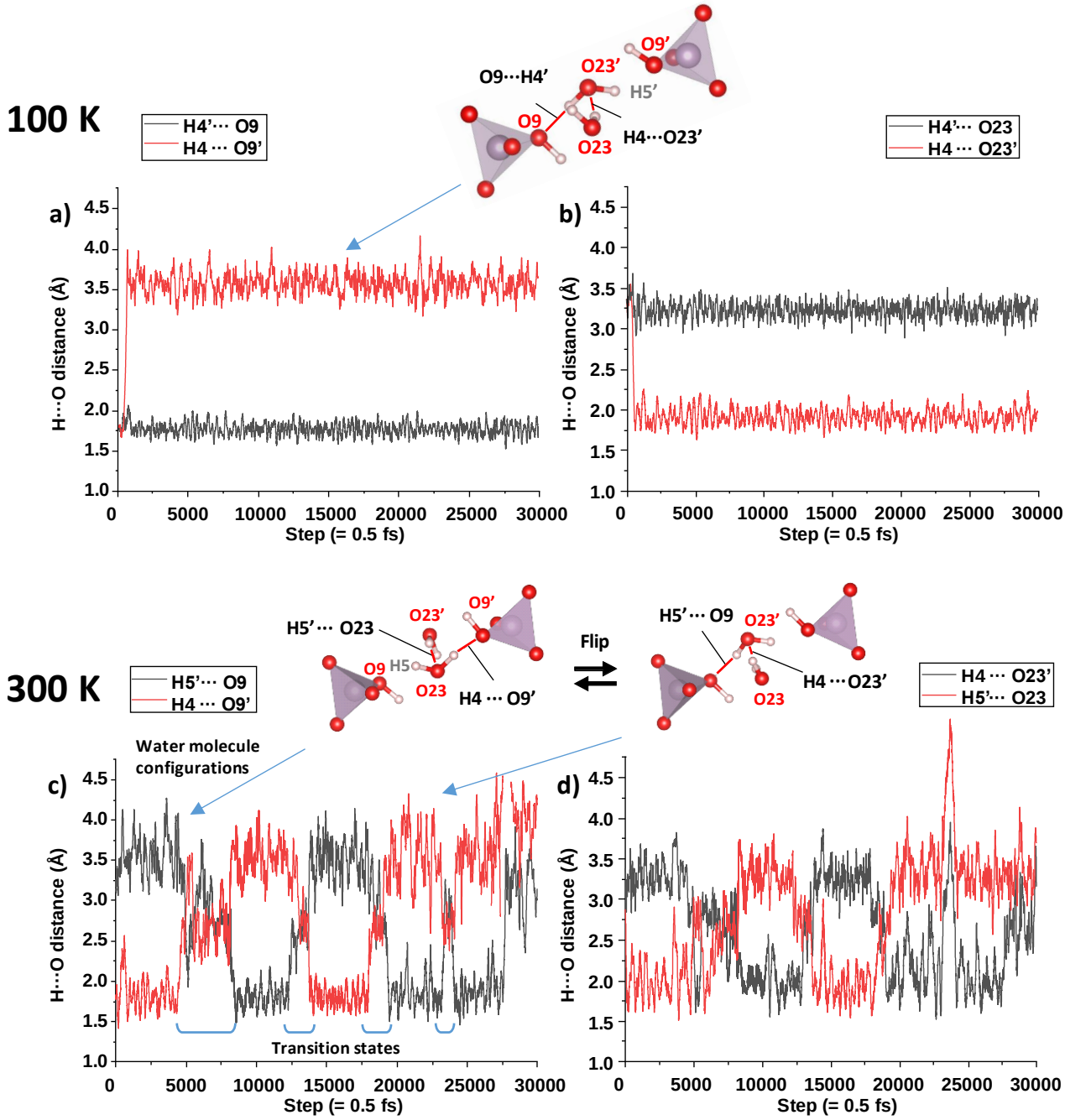


*Figure 6: Evolution of H-bonds starting from the central water molecules (H4-O23-H5 and H4'-O23'-H5') over the molecular dynamics simulations. a) H-bond with the nearest $HPO_4^{2-}$, at 100 K. b) H-bond with the symmetrically opposed water molecule, at 100 K. c) and d) show the same H-bond types, but at 300 K. Representations of the different water molecule configurations observed in the simulations are shown above the graphs. Note that the H4'-O23'-H5' water molecule rotates in opposite directions at the beginning of the MD simulations we performed at 100 K and 300 K, thereby "inverting" the roles of H4' and H5'. The simultaneous increased distances of the H4···O23' and H5'···O9 bonds observed at the end of the MD at 300 K comes from 180° flips of the H4-O23-H5 water molecule.*

At 300 K, the simulation starts similarly, with the formation of an H-bond between O23-H4 and O23'. However, at this temperature, the bond is not stable over time. Instead, it breaks and reforms asymmetrically multiple times throughout the simulation, as evidenced by the evolution of the bond lengths on opposite sides of the initial symmetry center (Fig. 6c and 6d).

This "flipping" motion has little visible impact on the total energy of the system (Fig. S7).

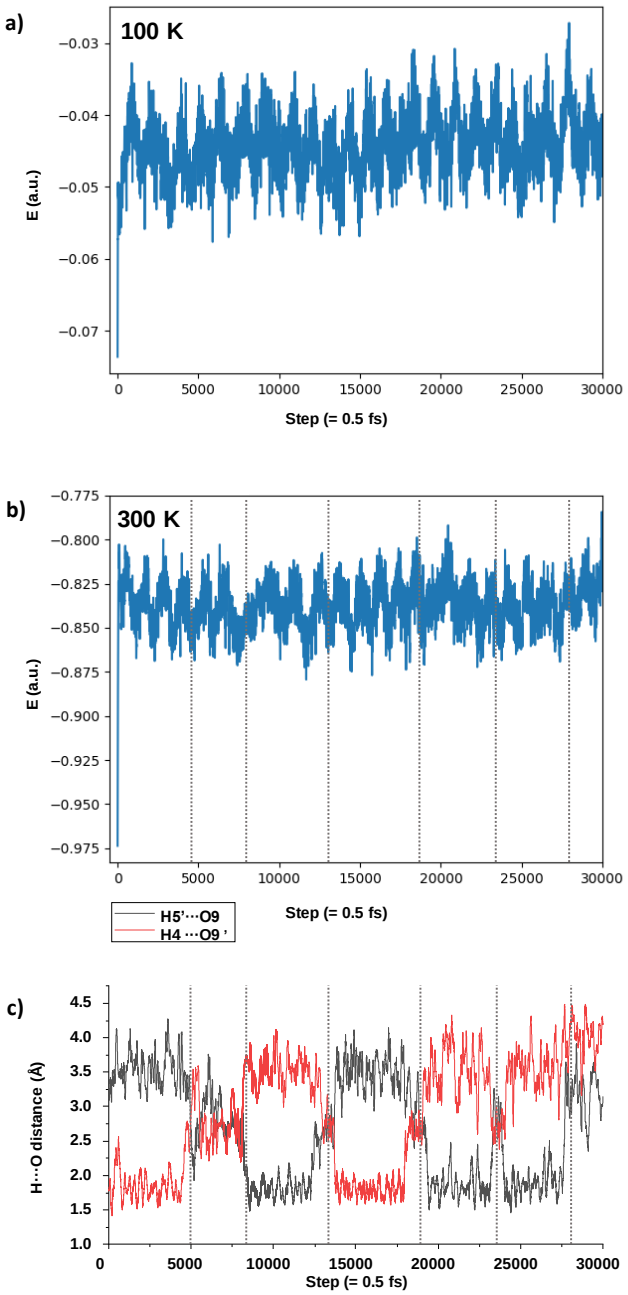


***Figure S7: Evolution of the total energy of the molecular dynamics simulations over the length of the simulation, at a) 100 K and b) 300 K. c) Evolution of H-bonds starting from the central water molecules (H4-O23-H5 and H4'-O23'-H5') to the nearest $HPO_4^{2-}$ (O9' and O9), at 300 K, highlighting their "flipping" motion. Changes in configuration are noted by dotted vertical lines, and reproduced on b), showing that this motion has little noticeable effect on the overall energy of the structure.***

Given that we observe four flips over a 15 ps simulation, we can approximate a frequency of the order of ca. $10^{12}$ Hz at room temperature. We can also note the appearance of an intermediate structure during the symmetry transition that exhibits the *P*-1 symmetry which is not observed at 100 K. About 25% of the length of the simulation is spent in this transitional metastable *P*-1 symmetry. We can therefore describe this simulation as an alternation of symmetric and asymmetric structures (each lasting a few hundreds of fs) which averages out to a pseudo *P*-1 symmetry at 300 K. This is in contrast with the stable *P*1 structure observed at 100 K. The fact that the symmetry is related to water mobility, which is dependent on temperature, would explain why the temperature changes observed *via* $^{31}$P NMR are gradual and fully reversible (and not visible in pXRD). Moreover, these simulations suggest that dynamics possibly affect NMR parameters of the phosphates in the hydrated interlayer (P3, P5 and P6) more strongly than those embedded further in the apatitic layers. This hypothesis will be used later in the manuscript when trying to assign the $^{31}$P NMR spectra.

***Averaged chemical shift calculations and effect of the water dynamics on NMR parameters***

As shown in Figure 3, we were able to record ssNMR spectra for each isotope at both room- and low-temperature. We thus compared them with the calculated averaged NMR parameters from MD simulations. First, regarding $^{31}$P NMR, the calculated isotropic chemical shifts of each $^{31}$P site were found to progressively converge towards a given value during the length of the MD simulation (15 ps), as shown in Figure 7.

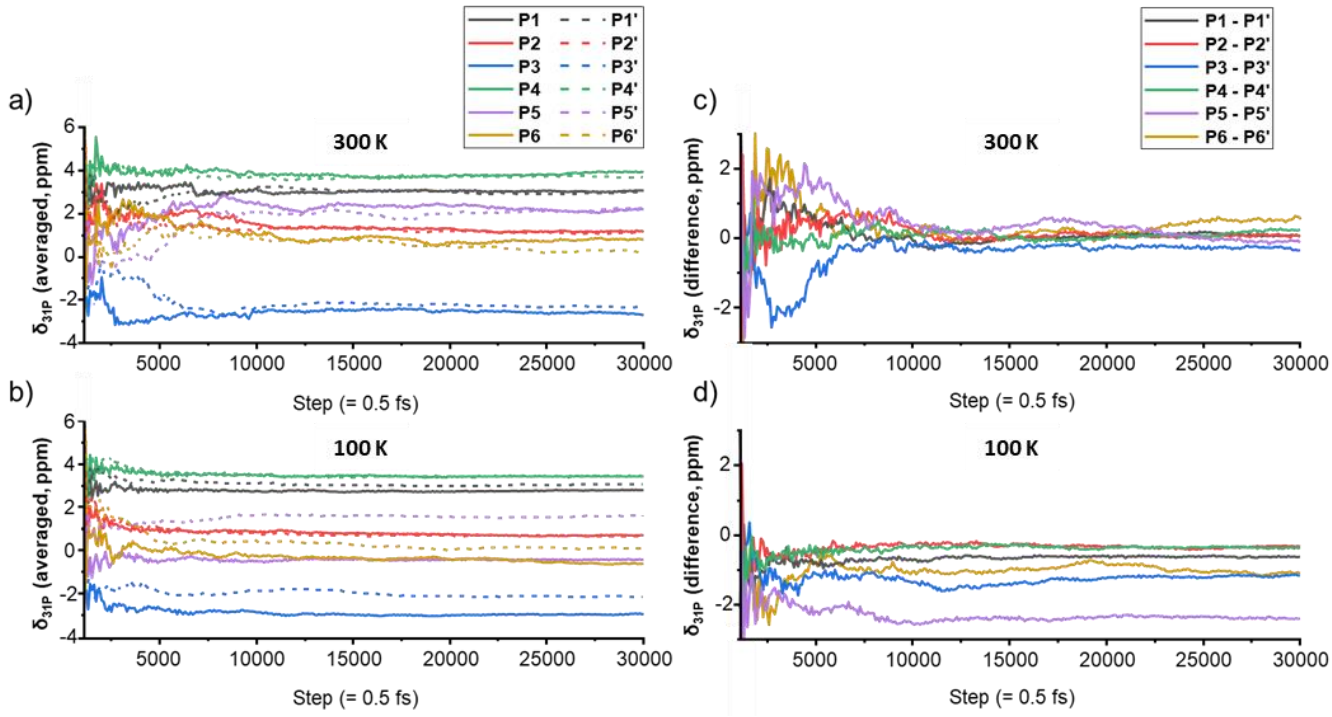


***Figure 7: Evolution of the time-averaged GIPAW-calculated $^{31}$P NMR isotropic chemical shifts a) at 300 K and b) at 100 K over the MD simulation. Difference in calculated $^{31}$P chemical shifts for a given site on both sides of the interlayer (Px and Px') c) at 300 K and d) at 100 K. It can be noted that the difference between Px and Px' chemical shifts is negative for every site of the 100 K simulation. Explanation of the averaging mode is detailed in the experimental part***

Indeed, after 30000 steps, we observe that whereas the individual snapshots can still show variations of chemical shifts as high as 30 ppm (Fig. S8), the time-averaged values converge towards a much smaller range, varying by less than 0.5 ppm in the last 10000 steps, at both temperatures (Fig. 7a and 7b). Importantly, the 100 K MD simulation exhibits a major difference compared to the 300 K simulation. Indeed, as shown in Fig 7d, the average differences in the $^{31}$P chemical shifts calculated at 100 K for P3/P3', P5/P5' and P6/P6' on both sides of the water interlayer are higher compared to those of the three other P sites (atoms labelled with or without a "prime" symbol on Fig. 4 are equivalent by *P*-1 symmetry). In contrast, in the simulation performed at 300 K (Fig. 7c), the average differences between Px and Px' chemical shifts converge towards zero for all sites, although slightly less completely for the P3 and P6 sites. Overall, these results are in line with both the splitting observed in $^{31}$P low-temperature NMR spectra as well as the observed *P*-1 symmetry at ambient-temperature.

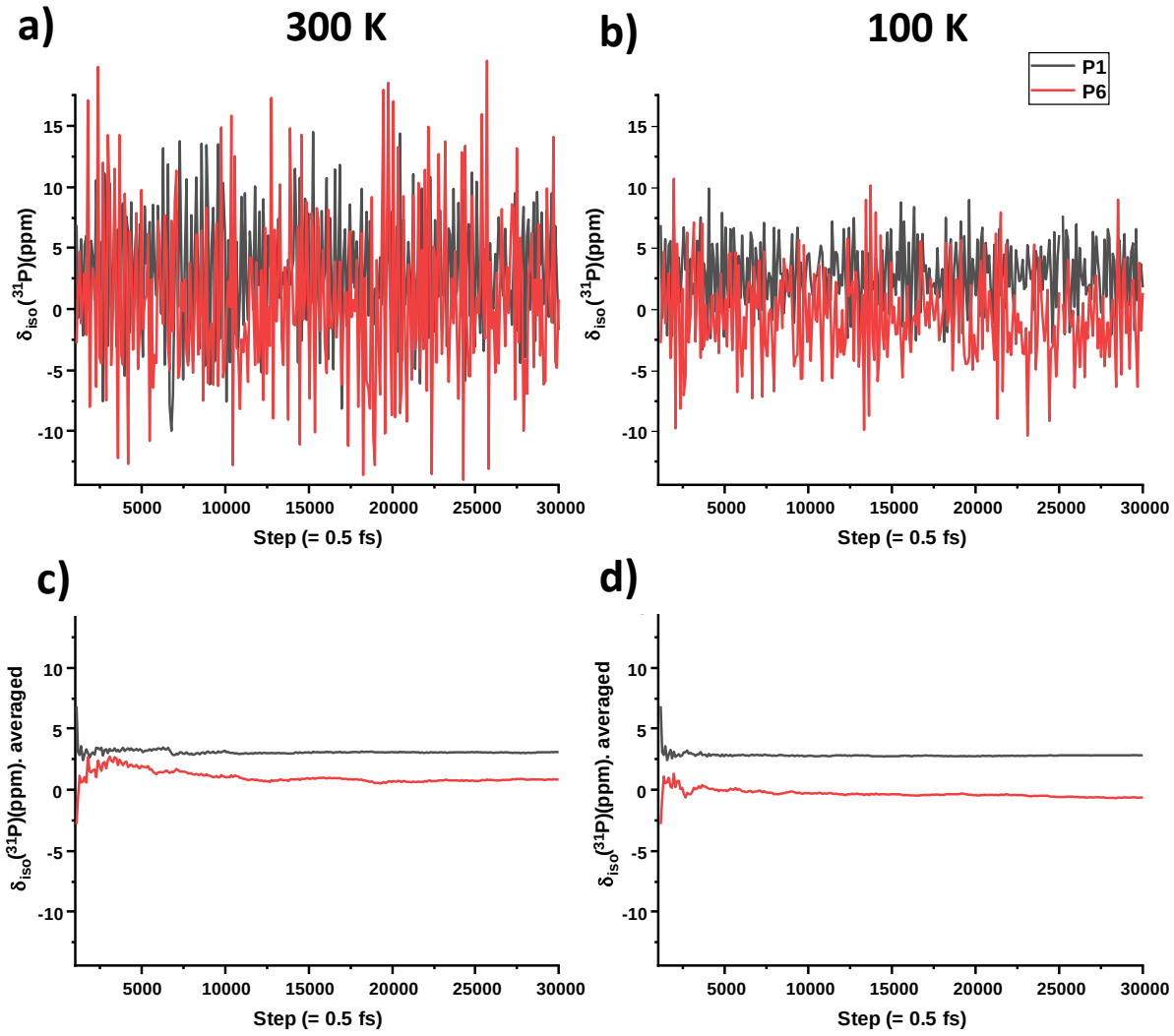


***Figure S8: GIPAW calculated $\delta_{iso}(^{31}P)$ of the P1 and P6 sites of OCP, along the MD simulation at a) 300 K and b) 100 K. Note the large variation of chemical shifts over the length of the simulation. Time-averaged $\delta_{iso}(^{31}P)$ values at c) 300 K and d) 100 K.***

.

Yet, the MD-averaged $^{31}$P NMR chemical shifts only partially agree with the experimental $^{31}$P NMR data at 300 K (Fig. 8a vs c). At this stage, it should be recalled that a first assignment of the experimental $^{31}$P MAS NMR spectrum of OCP had been proposed by Chan and co-workers in 2004,[13] based on the proximities established from $^{31}$P-$^{31}$P DQ-SQ and $^{1}$H-$^{31}$P CP-HETCOR experiments, but the proposed attribution (peaks at 3.7, 3.3, 2.0 and –0.2 ppm corresponding to P1, P2+P4, P3, P5+P6) did not match the experimental 1:1:1:3 intensity ratios observed in direct-excitation $^{31}$P NMR spectra (Fig. 2a). A new attribution was later proposed by Davies *et al.* in 2012, based on DFT calculations and $^{31}$P POST-C7 SQ–DQ correlation experiments with peaks at 3.6, 3.2, 2.0 and –0.3 ppm corresponding to P4, P1, P2, P3+P5+P6 (Fig. 8a),[15] which was consistent with the quantitative $^{31}$P NMR data.

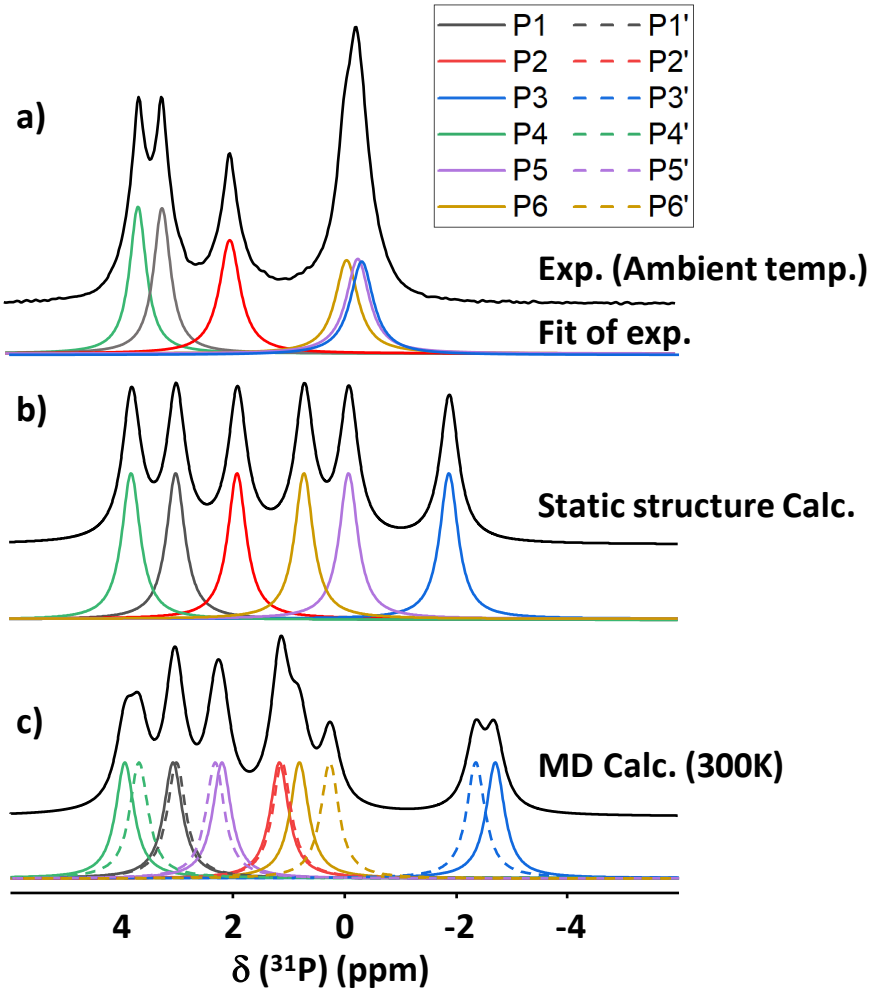


***Figure 8: a) Experimental and fitted $^{31}$P MAS NMR spectrum of OCP at "ambient temperature" (refrigerating unit set to 0°C), with resonances assigned according to Davies et al;[15] b) DFT-calculated $^{31}$P chemical shifts for the relaxed static structure extrapolated at 298 K;[15] c) Time-averaged calculated $^{31}$P chemical shifts after MD simulation at 300 K.***

Nonetheless, even if a satisfactory agreement was globally observed between experimental and calculated $^{31}$P values with this new assignment,[15] the P3 position was still calculated at –1.9 ppm (Fig. 8b) which is still far from the expected –0.3 ppm. Note that as previously mentioned, Davies *et al.* had

observed experimental $^{31}$P chemical shifts to be dependent on temperature (increasing by ~0.5 ppm over 100 K) and $^{31}$P reported calculated values (Fig. 8b) were extrapolated at 298 K from the 0 K raw data. Here, averaging $^{31}$P isotropic chemical shift values over the MD trajectory at 300 K does not improve the agreement (Fig. 8c).

This discrepancy could be due to a variety of factors, such as an incorrectly sized crystal lattice, the presence of partially occupied sites, small changes in the water content in the interlayer space, and/or dynamics effects on time scales not explored by MD simulations. However, because of the significant computational cost of the MD simulations, trying to improve chemical shift prediction by further increasing the size of the OCP model (to take into account defects), increasing the time range of the calculations, and/or further analyzing the effect of small changes in the temperature, is beyond the scope of this study.

The NMR parameters of the other nuclei ($^{1}$H, $^{17}$O, $^{43}$Ca) were also calculated by DFT, and averaged over the length of the MD simulations at 100 K and 300 K.

| | $\delta_{iso}$ (ppm) | | | | |
|---|---|---|---|---|---|
| Site | Exp amb. (Fig 2a) | Exp 100 K (Fig 10b) | Stat calc[1] | 300 K calc | 100 K calc |
| P1 | 3.2 | 2.8 | 3.0 | 3.1 | 2.8 |
| P1' | 3.2 | 3.9 | 3.0 | 3.0 | 3.1 |
| P2 | 2.0 | 3.5 | 1.9 | 1.2 | 0.7 |
| P2' | 2.0 | 3.2 | 1.9 | 1.1 | 0.6 |
| P3 | –0.3 | 1.4 | –1.9 | –2.7 | –3.0 |
| P3' | –0.3 | –0.7/2.0 | –1.9 | –2.4 | –2.2 |
| P4 | 3.6 | 3.5 | 3.8 | 3.9 | 3.5 |
| P4' | 3.6 | 3.2 | 3.8 | 3.7 | 3.4 |
| P5 | –0.3 | –1.3 | –0.1 | 2.2 | –0.4 |
| P5' | –0.3 | –0.2 | –0.1 | 2.3 | 1.6 |
| P6 | –0.1 | –0.6 | 0.7 | 0.8 | –0.6 |
| P6' | –0.1 | 0.3 | 0.7 | 0.2 | 0.1 |

***Table S2: $^{31}$P experimental chemical shifts (extracted from NMR spectra recorded at ambient temperature and 100 K), and GIPAW-DFT calculated parameters (on the static relaxed structure, after extrapolation at 298 K,[15] and after averaging by Molecular Dynamics at 100 K or 300 K). Note that the two positions proposed for P3' at 100 K correspond to the assignment hypothesis i) and ii) discussed at the end of the main text***

The calculated $^{43}$Ca NMR parameters ($\delta_{iso}$ and $C_Q$) for the MD-averaged structures similarly showed little variation between 100 K and 300 K (except for $\delta_{iso}$(Ca1'), which varies by ca. 6 ppm) (Tab. S3). Regarding $^{17}$O NMR, the largest difference between both temperatures was found for the calculated chemical shift values. Notably, O9 and O9' (from the PO*H groups involving P5 and P5') show a clear evidence of splitting at 100 K, but not at 300 K (differences in chemical shift values $\Delta\delta_{iso}(^{17}O)_{O9\text{-}O9',\,100\,K}$ = 16.0 ppm; $\delta_{iso}(^{17}O)_{O9\text{-}O9',\,300\,K}$ = 3.1 ppm) (Tab. S6). This significantly broadens the PO*H signal range, a change we can also observe on the experimental $^{17}$O NMR spectra (Fig. 3c). The experimental broadening is also probably due to the increase in $C_Q$ at low temperature, as suggested by the MD simulations and NMR calculations, which show an increase of 0.4 MHz for $|C_Q|$(O9') when lowering the temperature from 300 K to 100 K.

| | | $\delta_{iso}$ (ppm) | | | | $C_Q$ (MHz) | | | | $\eta_Q$ | | | |
|---|---|---|---|---|---|---|---|---|---|---|---|---|---|
| Site | Site[2] | Exp amb. | Stat calc[2] | 300K calc | 100K calc | Exp amb.[a] | Stat calc[2] | 300K calc | 100K calc | Exp amb. | Stat calc[2] | 300K calc | 100K calc |
| Ca1 | Ca1 | –0.4 | –12.6 | 0.3 | –3.0 | 2.9 | –2.2 | –2.4 | –2.7 | 0.8 | 0.9 | 0.6 | 0.5 |
| Ca1' | Ca2 | –0.4 | –12.6 | 0.1 | –5.6 | 2.9 | –2.2 | –2.4 | –2.6 | 0.8 | 0.9 | 0.6 | 0.5 |
| Ca2 | Ca3 | 19.9 | 7.8 | 20.7 | 19.3 | 3.1 | 2.8 | 2.6 | 2.7 | 0.6 | 0.5 | 0.5 | 0.7 |
| Ca2' | Ca4 | 19.9 | 7.8 | 21.2 | 21.3 | 3.1 | 2.8 | 2.6 | 2.8 | 0.6 | 0.5 | 0.5 | 0.7 |
| Ca3 | Ca5 | 2.6 | –8.7 | 6.0 | 5.3 | 2.9 | –3.2 | –3.3 | –3.3 | 0.8 | 0.5 | 0.0 | 0.2 |
| Ca3' | Ca6 | 2.6 | –8.7 | 5.9 | 6.1 | 2.9 | –3.2 | –3.3 | –3.5 | 0.8 | 0.5 | 0.1 | 0.1 |
| Ca4' | Ca7 | –0.5 | –11.0 | –2.7 | –6.5 | 2.8 | –2.6 | 2.8 | 2.8 | 0.8 | 0.9 | 0.3 | 0.7 |
| Ca4 | Ca8 | –0.5 | –11.0 | –1.2 | –1.0 | 2.8 | –2.6 | 2.8 | 2.8 | 0.8 | 0.9 | 0.3 | 0.5 |
| Ca5 | Ca9 | 3.5 | 3.8 | 6.8 | 4.8 | 2.8 | –2.5 | 2.3 | 2.4 | 0.8 | 0.9 | 0.2 | 0.1 |
| Ca5' | Ca10 | 3.5 | 3.8 | 7.7 | 8.6 | 2.8 | –2.5 | 2.2 | 2.4 | 0.8 | 0.9 | 0.2 | 0.4 |
| Ca6 | Ca11 | 46.8 | 27.7 | 38.2 | 36.3 | 4.1 | –4.6 | –3.4 | –3.4 | 0.8 | 0.9 | 0.8 | 0.7 |
| Ca6' | Ca12 | 46.8 | 27.7 | 37.7 | 34.8 | 4.1 | –4.6 | –3.4 | –3.5 | 0.8 | 0.9 | 0.7 | 0.7 |
| Ca7 | Ca13 | 13.6 | 8.2 | 13.1 | 10.7 | 3.1 | –2.4 | –2.1 | –2.1 | 0.6 | 0.1 | 0.2 | 0.1 |
| Ca7' | Ca14 | 13.6 | 8.2 | 13.6 | 14.9 | 3.1 | –2.4 | –2.2 | –2.1 | 0.6 | 0.1 | 0.2 | 0.1 |
| Ca8 | Ca15 | –8.2 | –18.2 | –8.3 | –8.9 | 3.1 | –2.8 | 2.7 | 2.8 | 0.6 | 0.9 | 0.8 | 0.9 |
| Ca8' | Ca16 | –8.2 | –18.2 | –8.3 | –11.0 | 3.1 | –2.8 | 2.7 | 2.7 | 0.6 | 0.9 | 0.8 | 0.8 |

[a] Experimentally, only the absolute value of $C_Q$ is extracted from the fitting (not its sign).

***Table S3: Experimental and fitted (Fig. S5) $^{43}$Ca NMR parameters (recorded at ambient temperature), compared to the calculated values (on the static relaxed structure,[2] and after averaging by Molecular Dynamics at 100 K or 300 K).***

As some of the $^{43}$Ca NMR lineshapes are featureless, it is difficult to determine precisely the quadrupolar parameters $C_Q$ and $\eta_Q$. Therefore, quadrupolar parameter $P_Q$ ( $P_Q = C_Q\left(1+\frac{\eta_Q^2}{3}\right)^{1/2}$ ) (1) and $\delta_{iso}$ were also obtained for comparison by plotting (see graphs below) the position of the maximum of the peaks $\delta_{max}$ at each magnetic field against $1/(\nu_0)^2$ (where $\nu_0$ is the Larmor frequency of $^{43}$Ca). $P_Q$ and $\delta_{iso}$ were then derived using the equation $\delta_{max} = \delta_{iso} - 10^6\left(\frac{1}{392}\right)\left(\frac{P_Q}{\upsilon_0}\right)^2$ (2).

| | $\delta_{iso}$ (ppm) | | $P_Q$ (MHz) | |
|---|---|---|---|---|
| | From Fig. S5 | From Eq. (2) and plot below | From Fig. S5 and Eq. (1) | From Eq. (2) and plot below |
| Ca1 | –0.4 | –1.9 | 3.2 | 2.1 |
| Ca2 | 19.9 | 20.3 | 3.3 | 3.7 |
| Ca3 | 2.6 | 3.0 | 3.2 | 3.4 |
| Ca4 | –0.5 | –1.9 | 3.1 | 2.1 |
| Ca5 | 3.5 | 3.0 | 3.1 | 3.0 |
| Ca6 | 46.8 | 47.2 | 4.5 | 4.9 |
| Ca7 | 13.6 | 13.7 | 3.3 | 3.4 |
| Ca8 | –8.2 | –7.2 | 3.3 | 3.9 |

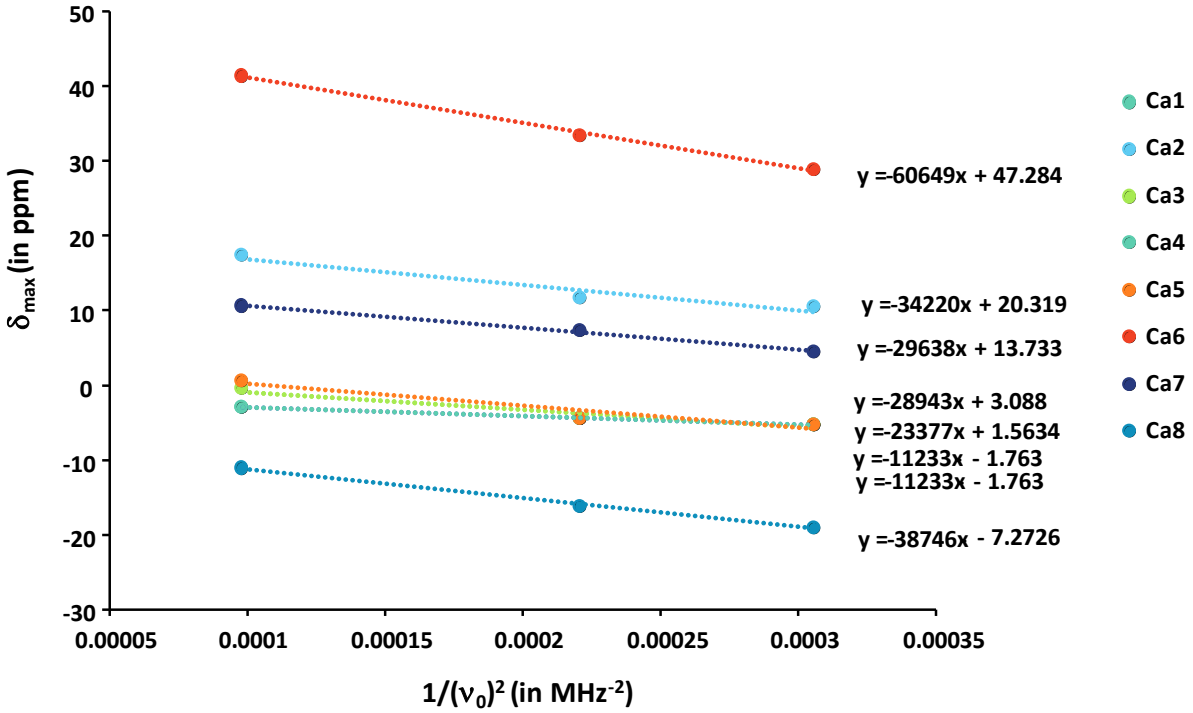


| Site | $\delta_{iso}$ (ppm) | $C_Q$ (MHz) | $\eta_Q$ |
|---|---|---|---|
| O15 (P-OH) | 89.5 | 5.0 | 0.8 |
| O9 (P-OH) | 76.6 | 4.9 | 0.8 |
| PO | 129.9 | 4.8 | 0.2 |
| | 125.1 | 4.8 | 0.2 |
| | 123.2 | 4.8 | 0.2 |
| | 122.6 | 4.8 | 0.2 |
| | 121.4 | 4.8 | 0.2 |
| | 118.9 | 4.8 | 0.2 |
| | 120.2 | 4.8 | 0.2 |
| | 118.4 | 4.8 | 0.2 |
| | 119.4 | 4.8 | 0.2 |
| | 119.3 | 4.8 | 0.2 |
| | 117.6 | 4.8 | 0.2 |
| | 116.4 | 4.8 | 0.2 |
| | 116.9 | 4.8 | 0.2 |
| | 116.8 | 4.8 | 0.2 |
| | 114.5 | 4.8 | 0.2 |
| | 115.0 | 4.8 | 0.2 |
| | 113.0 | 4.8 | 0.2 |
| | 112.8 | 4.8 | 0.2 |
| | 112.3 | 4.8 | 0.2 |
| | 116.0 | 4.8 | 0.2 |
| | 109.3 | 4.8 | 0.2 |
| | 108.0 | 4.8 | 0.2 |

***Table S4: $^{17}O$ experimental NMR parameters used for the tentative fit proposed on Figure S4.***

The calculated $^1$H NMR parameters showed only relatively small differences between MD-averaged values at 300 K and 100 K, with the maximum change being of 1.1 ppm (Tab. S5).

| Site | | $\delta_{iso}$ (Stat.) (ppm) | dOH---O (Å) | $\delta_{iso}$ (300K) (ppm) | dOH---O (Å) | $\delta_{iso}$ (100K) (ppm) | dOH---O (Å) |
|---|---|---|---|---|---|---|---|
| H1 | POH | 9.0 | 1.64 | 11.1 | 1.66 | 10.0 | 1.59 |
| H1' | POH | 9.0 | 1.64 | 9.1 | 1.65 | 8.1 | 1.69 |
| H2 | $H_2O$ | 7.4 | 1.75 | 9.0 | 1.85 | 7.9 | 1.75 |
| H2' | $H_2O$ | 7.4 | 1.75 | 8.3 | 1.84 | 7.2 | 1.76 |
| H3 | $H_2O$ | 9.0 | 1.61 | 9.2 | 1.65 | 8.1 | 1.65 |
| H3' | $H_2O$ | 9.0 | 1.61 | 9.8 | 1.66 | 8.7 | 1.62 |
| H4 | $H_2O$ | 4.7 | 1.79 | 6.1 | 2.49 | 5.0 | 1.91 |
| H4' | $H_2O$ | 4.7 | 1.79 | 6.4 | 2.02 | 5.3 | 1.76 |
| H5 | $H_2O$ | 3.9 | 1.96 | 4.4 | 1.98 | 3.3 | 2.00 |
| H5' | $H_2O$ | 3.9 | 1.96 | 5.9 | 2.59 | 4.8 | 1.86 |
| H6 | POH | 14.4 | 1.41 | 16.8 | 1.33 | 15.7 | 1.33 |
| H6' | POH | 14.4 | 1.41 | 16.7 | 1.34 | 15.7 | 1.34 |
| H7 | $H_2O$ | 2.8 | 2.12 | 5.1 | 1.99 | 4.0 | 1.89 |
| H7' | $H_2O$ | 2.8 | 2.12 | 5.1 | 1.97 | 4.0 | 1.92 |
| H8 | $H_2O$ | 9.3 | 1.61 | 11.2 | 1.59 | 10.2 | 1.56 |
| H8' | $H_2O$ | 9.3 | 1.61 | 10.2 | 1.60 | 9.1 | 1.61 |
| H9 | $H_2O$ | 7.0 | 1.69 | 8.1 | 1.68 | 7.0 | 1.70 |
| H9' | $H_2O$ | 7.0 | 1.69 | 8.7 | 1.68 | 7.7 | 1.66 |
| H10 | $H_2O$ | 9.2 | 1.59 | 7.9 | 1.78 | 6.8 | 1.74 |
| H10' | $H_2O$ | 9.2 | 1.59 | 5.9 | 1.79 | 4.8 | 1.87 |
| H11 | $H_2O$ | 6.4 | 1.71 | 5.9 | 1.97 | 4.9 | 1.79 |
| H11' | $H_2O$ | 6.4 | 1.71 | 7.0 | 2.49 | 6.0 | 1.76 |
| H12 | $H_2O$ | 4.0 | 1.95 | 7.7 | 2.12 | 6.6 | 1.81 |
| H12' | $H_2O$ | 4.0 | 1.95 | 4.3 | 2.42 | 3.2 | 2.54 |

***Table S5: Calculated $^1$H NMR parameters and shortest OH---O distances on the static relaxed structure[1] and after time-averaging by Molecular Dynamics at 100 K and 300 K.***

| | $\delta_{iso}$ (ppm) | | | $C_Q$ (MHz) | | | $\eta_Q$ | | |
|---|---|---|---|---|---|---|---|---|---|
| Site | Stat calc | 300K calc | 100K calc | Stat calc | 300K calc | 100K calc | Stat calc | 300K calc | 100K calc |
| O1 | 108.5 | 123.2 | 120.8 | –4.9 | –5.0 | –5.0 | 0.1 | 0.1 | 0.1 |
| O1' | 108.5 | 123.5 | 121.5 | –4.9 | –4.9 | –5.0 | 0.1 | 0.1 | 0.1 |
| O2 | 109.8 | 116.4 | 115.4 | –5.4 | –5.5 | –5.6 | 0.2 | 0.3 | 0.3 |
| O2' | 109.8 | 116.4 | 113.9 | –5.4 | –5.5 | –5.6 | 0.2 | 0.3 | 0.3 |
| O3 | 122.5 | 135.0 | 134.0 | –5.1 | –5.4 | –5.5 | 0.2 | 0.2 | 0.2 |
| O3' | 122.5 | 135.3 | 134.1 | –5.1 | –5.4 | –5.5 | 0.2 | 0.2 | 0.2 |
| O4 | 116.6 | 120.0 | 116.9 | –5.2 | –5.3 | –5.4 | 0.1 | 0.2 | 0.2 |
| O4' | 116.6 | 119.1 | 115.3 | –5.2 | –5.3 | –5.4 | 0.1 | 0.2 | 0.2 |

| | $\delta_{iso}$ (ppm) | | | $C_Q$ (MHz) | | | $\eta_Q$ | | |
|---|---|---|---|---|---|---|---|---|---|
| Site | Stat calc | 300K calc | 100K calc | Site | Stat calc | 300K calc | 100K calc | Site | Stat calc |
| O5 | 112.0 | 124.6 | 121.0 | –5.0 | –5.2 | –5.2 | 0.1 | 0.1 | 0.1 |
| O5' | 112.0 | 124.2 | 121.7 | –5.0 | –5.2 | –5.2 | 0.1 | 0.1 | 0.1 |
| O6 | 110.3 | 125.3 | 121.2 | –5.2 | –5.2 | –5.3 | 0.1 | 0.1 | 0.1 |
| O6' | 110.3 | 124.8 | 122.2 | –5.2 | –5.2 | –5.3 | 0.1 | 0.1 | 0.1 |
| O7 | 126.1 | 133.4 | 130.9 | –5.0 | –5.2 | –5.3 | 0.2 | 0.2 | 0.2 |
| O7' | 126.1 | 133.3 | 129.7 | –5.0 | –5.2 | –5.3 | 0.2 | 0.2 | 0.2 |
| O8 | 124.6 | 130.8 | 127.0 | –4.9 | –5.1 | –5.2 | 0.2 | 0.2 | 0.2 |
| O8' | 124.6 | 130.2 | 127.1 | –4.9 | –5.1 | –5.2 | 0.2 | 0.2 | 0.2 |
| O9 | 64.2 | 71.5 | 74.6 | –7.2 | –6.9 | –6.8 | 0.8 | 0.8 | 0.8 |
| O9' | 64.2 | 68.4 | 58.6 | –7.2 | –7.0 | –7.4 | 0.8 | 0.9 | 1.0 |
| O10 | 105.6 | 110.7 | 110.5 | –5.1 | –5.1 | –5.2 | 0.2 | 0.1 | 0.2 |
| O10' | 105.6 | 110.5 | 108.1 | –5.1 | –5.1 | –5.3 | 0.2 | 0.1 | 0.2 |
| O11 | 108.4 | 124.3 | 115.0 | –5.2 | –5.3 | –5.4 | 0.1 | 0.1 | 0.1 |
| O11' | 108.4 | 126.2 | 124.1 | –5.2 | –5.3 | –5.5 | 0.1 | 0.1 | 0.1 |
| O12 | 116.9 | 129.8 | 127.1 | –5.0 | –5.1 | –5.2 | 0.1 | 0.2 | 0.2 |
| O12' | 116.9 | 130.0 | 128.6 | –5.0 | –5.2 | –5.2 | 0.1 | 0.2 | 0.2 |
| O13 | 119.3 | 129.8 | 127.6 | –5.3 | –5.4 | –5.4 | 0.1 | 0.1 | 0.1 |
| O13' | 119.3 | 129.1 | 126.1 | –5.3 | –5.3 | –5.4 | 0.1 | 0.1 | 0.1 |
| O14 | 103.5 | 121.5 | 114.8 | –5.1 | –5.3 | –5.3 | 0.2 | 0.2 | 0.2 |
| O14' | 103.5 | 120.8 | 114.5 | –5.1 | –5.3 | –5.4 | 0.2 | 0.2 | 0.2 |
| O15 | 73.7 | 88.3 | 83.2 | –6.4 | –6.1 | –6.4 | 0.8 | 0.7 | 0.7 |
| O15' | 73.7 | 88.0 | 85.9 | –6.4 | –6.2 | –6.2 | 0.8 | 0.7 | 0.8 |
| O16 | 95.5 | 104.9 | 103.9 | –5.3 | –5.3 | –5.3 | 0.3 | 0.3 | 0.3 |
| O16' | 95.5 | 103.7 | 100.1 | –5.3 | –5.4 | –5.5 | 0.3 | 0.3 | 0.2 |
| O17 | 127.9 | 141.5 | 140.0 | –5.3 | –5.4 | –5.5 | 0.2 | 0.1 | 0.1 |
| O17' | 127.9 | 141.7 | 138.9 | –5.3 | –5.4 | –5.5 | 0.2 | 0.1 | 0.1 |
| O22 | 121.3 | 130.3 | 128.1 | –5.1 | –5.3 | –5.3 | 0.1 | 0.1 | 0.1 |
| O22' | 121.3 | 130.2 | 128.8 | –5.1 | –5.3 | –5.4 | 0.1 | 0.1 | 0.1 |
| O24 | 126.3 | 129.7 | 125.5 | –4.8 | –5.0 | –5.1 | 0.0 | 0.1 | 0.1 |
| O24' | 126.3 | 129.9 | 127.2 | –4.8 | –5.0 | –5.1 | 0.0 | 0.1 | 0.1 |
| O25 | 117.7 | 128.9 | 127.1 | –5.0 | –5.0 | –5.1 | 0.0 | 0.1 | 0.1 |
| O25' | 117.7 | 128.8 | 126.1 | –5.0 | –5.1 | –5.1 | 0.0 | 0.1 | 0.1 |
| O26 | 116.3 | 130.0 | 126.4 | –4.9 | –5.1 | –5.1 | 0.0 | 0.1 | 0.1 |
| O26' | 116.3 | 130.5 | 125.6 | –4.9 | –5.0 | –5.1 | 0.0 | 0.0 | 0.1 |
| O27 | 140.2 | 147.6 | 146.7 | –5.0 | –5.2 | –5.2 | 0.1 | 0.1 | 0.1 |
| O27' | 140.2 | 147.8 | 145.2 | –5.0 | –5.2 | –5.2 | 0.1 | 0.1 | 0.1 |
| O28 | 105.8 | 113.9 | 110.3 | –5.2 | –5.3 | –5.4 | 0.1 | 0.1 | 0.1 |
| O28' | 105.8 | 114.1 | 112.1 | –5.2 | –5.3 | –5.4 | 0.1 | 0.1 | 0.1 |
| O29 | 115.5 | 126.6 | 123.9 | –5.1 | –5.3 | –5.4 | 0.2 | 0.1 | 0.2 |
| O29' | 115.5 | 127.4 | 125.3 | –5.1 | –5.3 | –5.4 | 0.2 | 0.1 | 0.1 |

***Table S6: Calculated $^{17}O$ NMR parameters on the static relaxed structure[1] and after time-averaging by Molecular Dynamics at 100 K and 300 K. Green highlight P-O*-H sites. $H_2O$ oxygen sites are excluded.***

***Tentative assignment of calcium and oxygen sites in the ambient-temperature structures***

As previously mentioned, at 35.2 T, the $^{43}$Ca MAS NMR spectrum is still not fully resolved (Fig. 2c). Yet, it can be reasonably fitted at multiple fields with eight consistent components (Fig. S5), from which experimental $\delta_{iso}$, $C_Q$ and $\eta_Q$ parameters can be extracted for each site. The quadrupolar parameter $P_Q$, which is directly related to $C_Q$ and $\eta_Q$, was also estimated from complementary multifield analyses (see see supporting information Table S3 and related plots).

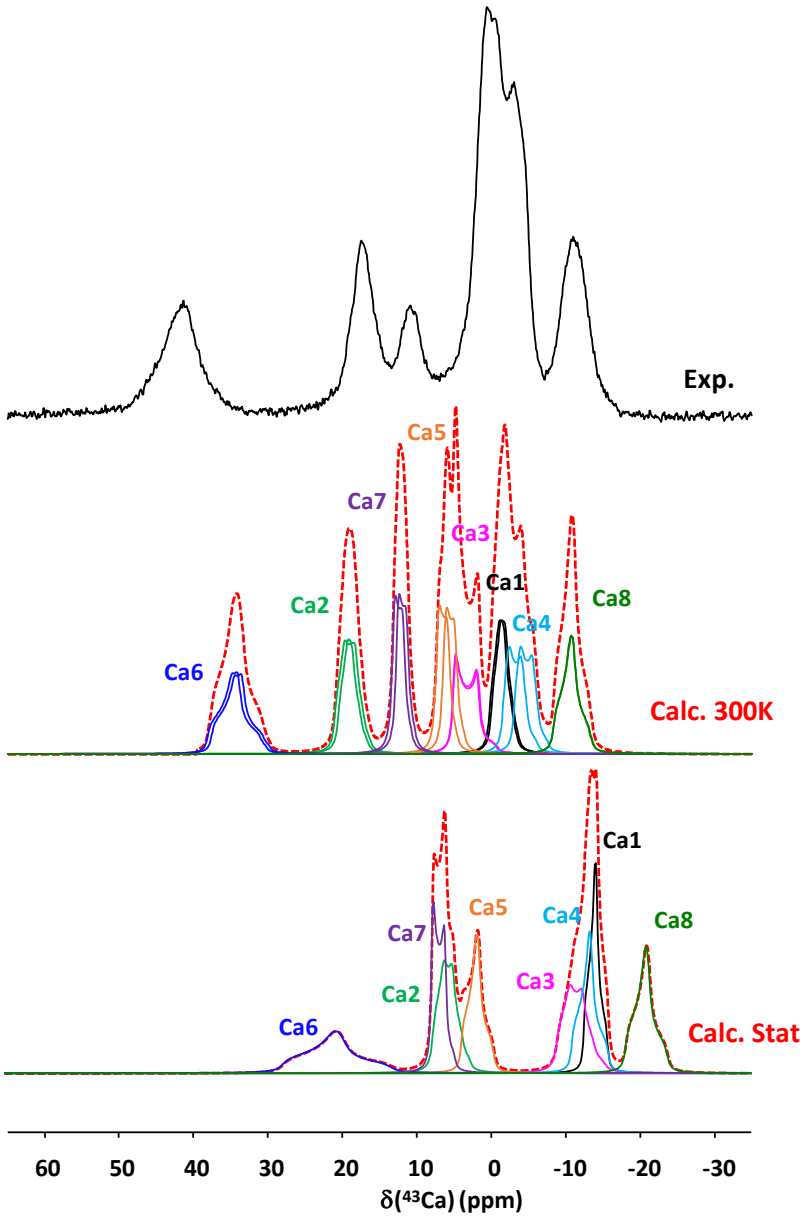


***Figure S9: Experimental $^{43}$Ca MAS NMR spectrum of OCP ($B_0$ = 35.2 T, $\nu_r$ = 10 kHz, refrigerating unit set to 10°C) (in black), in comparison to the spectrum simulated based on DFT-GIPAW calculated parameters on the static relaxed structure[16] and after averaging by Molecular Dynamics at 300 K. Calculated contributions from Ca individual sites are shown below the spectra in red dashed line. It should be noticed that the referencing used for both calculations is a bit different.***

In a previous study on OCP, a tentative assignment of some of the $^{43}$Ca resonances had been proposed, by comparison of experimental data with DFT-calculated values for a "static" model of the structure.[16] Here, to see if we could go further in the assignment of these signals, experimental values were

compared with the averaged parameters from the MD simulations at 300 K (Tab. S3 and Fig. S9). The signal with the highest $\delta_{iso}$ value (46.8 ppm experimentally) also shows the largest quadrupolar coupling constant ($C_Q$ > 4 MHz experimentally), in line with the calculated values for Ca6 and Ca6', which also show the highest $\delta_{iso}$ and $C_Q$, thereby allowing the safe assignment of this resonance. For the assignment of the other sites, the isotropic chemical shifts $\delta_{iso}$ were considered, because $\delta_{iso}$ has been shown to be a better criterion than quadrupolar parameters to discriminate $^{43}$Ca resonances.[51] In doing so, three of the remaining signals, with isotropic chemical shifts of 19.9, 13.6, and –8.2 ppm, can be assigned to Ca2, Ca7 and Ca8, respectively, based on the calculated values for these sites. Lastly, the 4 overlapping central $^{43}$Ca resonances can be divided into 2 groups, with the following assignments (based on calculations): one with $\delta_{iso}$ values at ~–0.5 ppm (Ca1 and Ca4), and the other with $\delta_{iso}$ values ~3 ppm (Ca3 and Ca5). This MD-proposed assignment remains consistent with our previously reported $^{43}$Ca{$^1$H} REDOR study of OCP.[16] To try to go even further in the assignments of the last 4 sites, calculated $\delta_{iso}$($^{43}$Ca) values for each site in the averaged structures over 100 K and 300 K MD simulations were plotted against the averaged corresponding Ca···O distance (with a cut-off of 2.9 Å, see Fig. S10), as already proposed in the literature.[51] However, no strong correlation could be established. Overall, at this stage, no more precise assignment of the Ca sites can be proposed. Nevertheless, it can be noticed that the averaged parameters from the MD simulations at 300 K allow a more precise assignment of Ca2 and Ca7 compared to the previous calculations we had reported on a static model of OCP,[16] in which some components were more superimposed (Fig. S9).

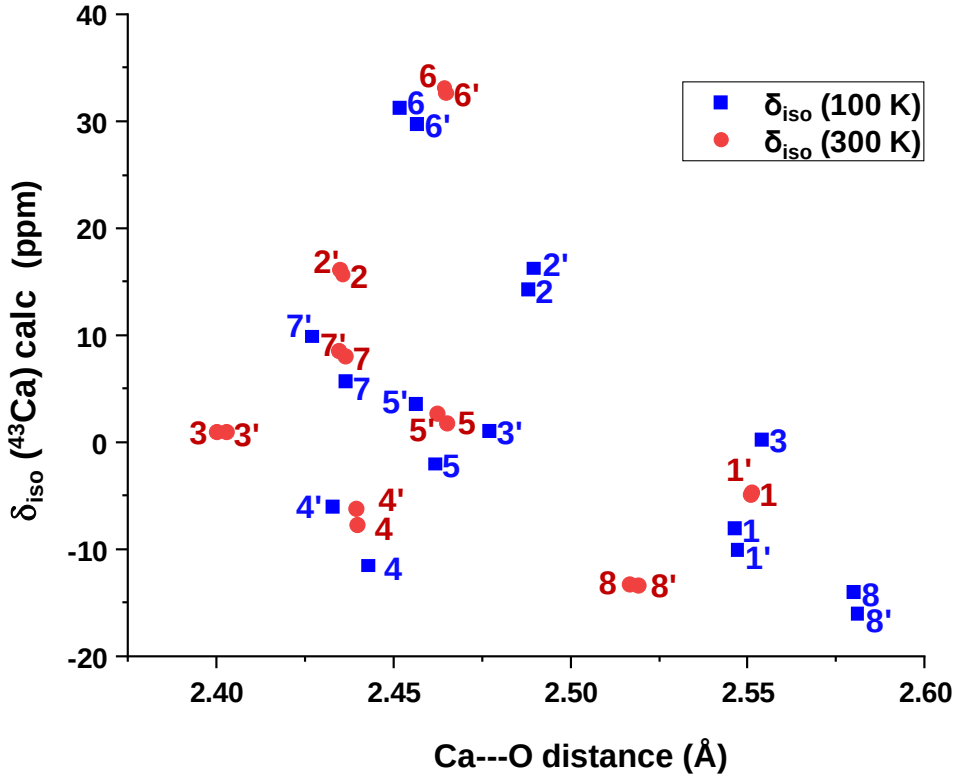


***Figure S10: Calculated $\delta_{iso}$($^{43}$Ca) for all calcium sites in OCP in the averaged MD structures for 300 K (red dots) and 100 K (blue square) simulations vs the average Ca···O distance for each Ca site (with a cut-off of 2.9 Å). In a number of previous studies,[16] $\delta_{iso}$($^{43}$Ca) could be related to a certain extent to the average Ca···O distance in the first coordination sphere of calcium. Here, data are scattered and no strong correlation can be established, apart from the fact that the most deshielded values tend to correspond to the shortest average Ca···O distances.***

.

| | | |
|---|---|---|
| Ca7 | H3 | 2.73 |
| Ca7' | H3' | 2.74 |
| Ca5' | H3' | 2.78 |
| Ca5 | H3 | 2.78 |
| Ca7 | H9 | 2.85 |
| Ca7' | H9' | 2.85 |
| Ca4 | H12 | 2.86 |
| Ca4' | H12' | 2.87 |
| Ca7 | H6 | 2.90 |
| Ca7' | H6' | 2.91 |
| Ca3 | H9 | 2.95 |
| Ca3' | H9' | 2.96 |
| Ca5' | H2' | 2.99 |
| Ca5 | H2 | 3.00 |
| Ca3' | H8' | 3.01 |
| Ca3 | H8 | 3.01 |
| Ca3 | H7 | 3.02 |
| Ca3' | H7' | 3.03 |
| Ca7 | H2 | 3.04 |
| Ca7' | H2' | 3.04 |
| Ca4 | H11 | 3.12 |
| Ca4' | H11' | 3.14 |
| Ca3 | H10 | 3.15 |
| Ca3' | H10' | 3.16 |
| Ca7' | H10' | 3.18 |
| Ca7 | H10 | 3.19 |
| Ca8' | H3' | 3.31 |
| Ca8 | H3 | 3.31 |
| Ca6' | H3' | 3.36 |
| Ca6 | H3 | 3.36 |
| Ca8 | H6 | 3.38 |
| Ca8' | H6' | 3.38 |

***Table S7: Selected Ca…H distances (shorter than 3.40 Å) for all crystallographically inequivalent calcium sites in the structure averaged by MD at 300 K***

Concerning the $^{17}O$ NMR data, the assignment of P-O sites (ranging from 105 to 130 ppm on the 1D $^{17}O$ MAS NMR spectrum) is too complicated considering the lack of resolution even at very high field (Fig. 2b) and the large number (22) of expected components. The two very distinct signals at around 75 and 90 ppm corresponding to POH environments can be safely assigned to O9 and O15 sites respectively, by comparison with calculated values (Tab. S6). The significant difference between both chemical shift values is potentially related to the differences in H-bonding, with O9-H1···O16 and O15-H6···O2 distances of 1.6 and 1.4 Å respectively in the 300 K MD simulation. This is also consistent with the $^{1}H$ – $^{17}O$ D-RINEPT experiment (Fig. 9), showing a stronger correlation of the $^{17}O$ P-OH signals of higher frequency with the $^{1}H$ peak at 13 ppm. The latter can be safely assigned to H6 according to calculations, and based on the shorter O15-H6···O2 distance (Tab. S5, Fig. S12).

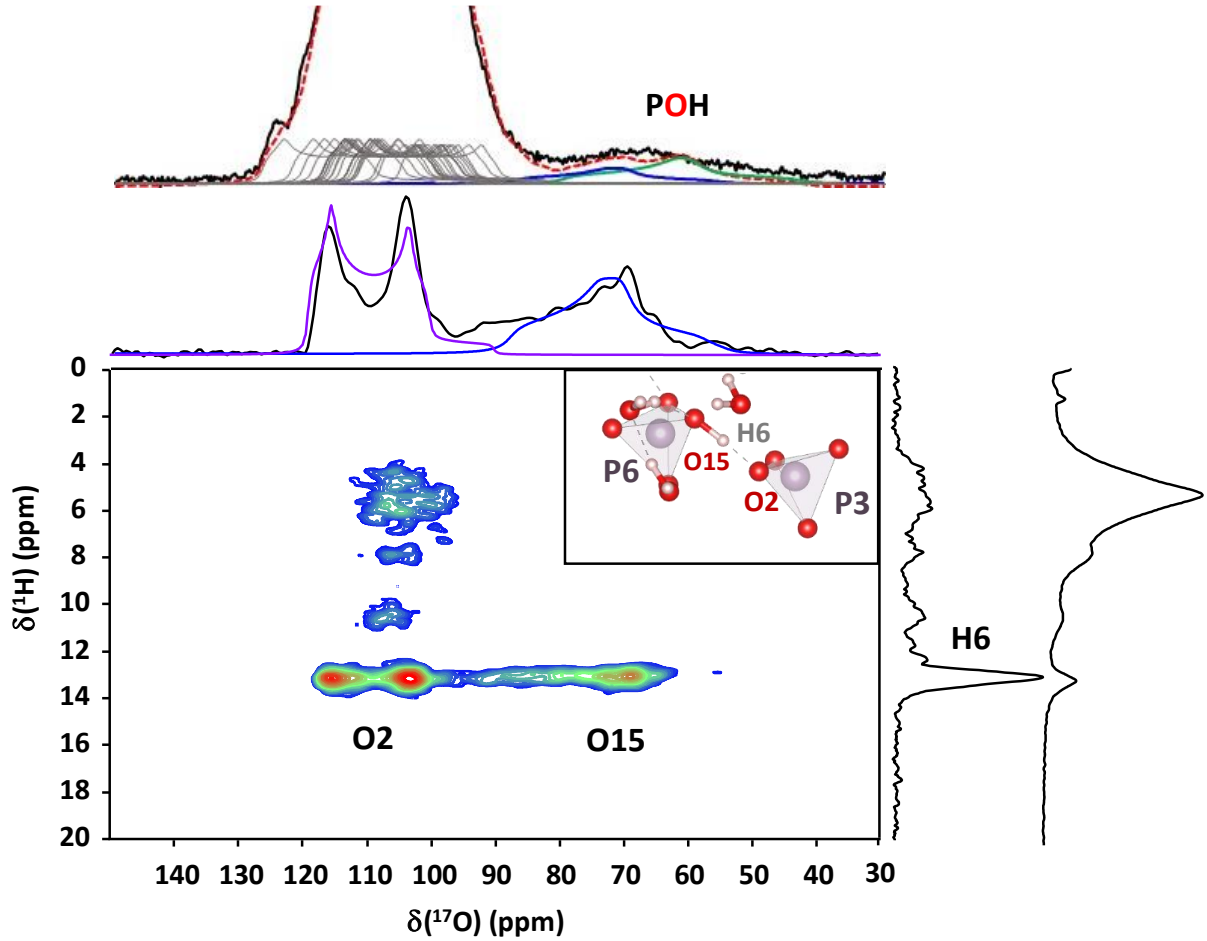


***Figure 9: 2D heteronuclear $^{1}H$-$^{17}O$ D-RINEPT spectrum of the $^{17}O$ enriched OCP sample recorded at $B_0$ = 18.8 T and $\nu_r$ = 50 kHz (refrigerating unit set to 5°C). Above the projections, the $^{1}H$ and $^{17}O$ direct acquisition NMR spectra are also presented in black. Regarding the $^{17}O$ projections, the direct excitation spectrum (top) was truncated to emphasize more the underlying individual components from PO (in grey) and POH groups (in blue and green), while the $^{17}O$ projection of the 2D data includes a fit of the H-bonded PO (O2, in purple) and POH (O15, in blue) sites.***

Surprisingly, only one clear cross-peak is observed for the POH groups in this D-RINEPT experiment. We would have expected two $^{17}O$ signals in the POH range, corresponding to O9 and O15 (respectively in green and blue on Figure 9). Yet, only O15 appears on the 2D, alongside the PO site that H6 is

H-bonded to, which involves O2. This site was fitted to extract chemical shift ($\delta_{iso}$ = 121.9 ppm) and quadrupolar parameters ($C_Q$ = 4.8 MHz and $\eta_Q$ = 0.2). The latter were subsequently used, as a first approximation, for all the other PO sites of OCP, in the fit proposed on Figure 2b.

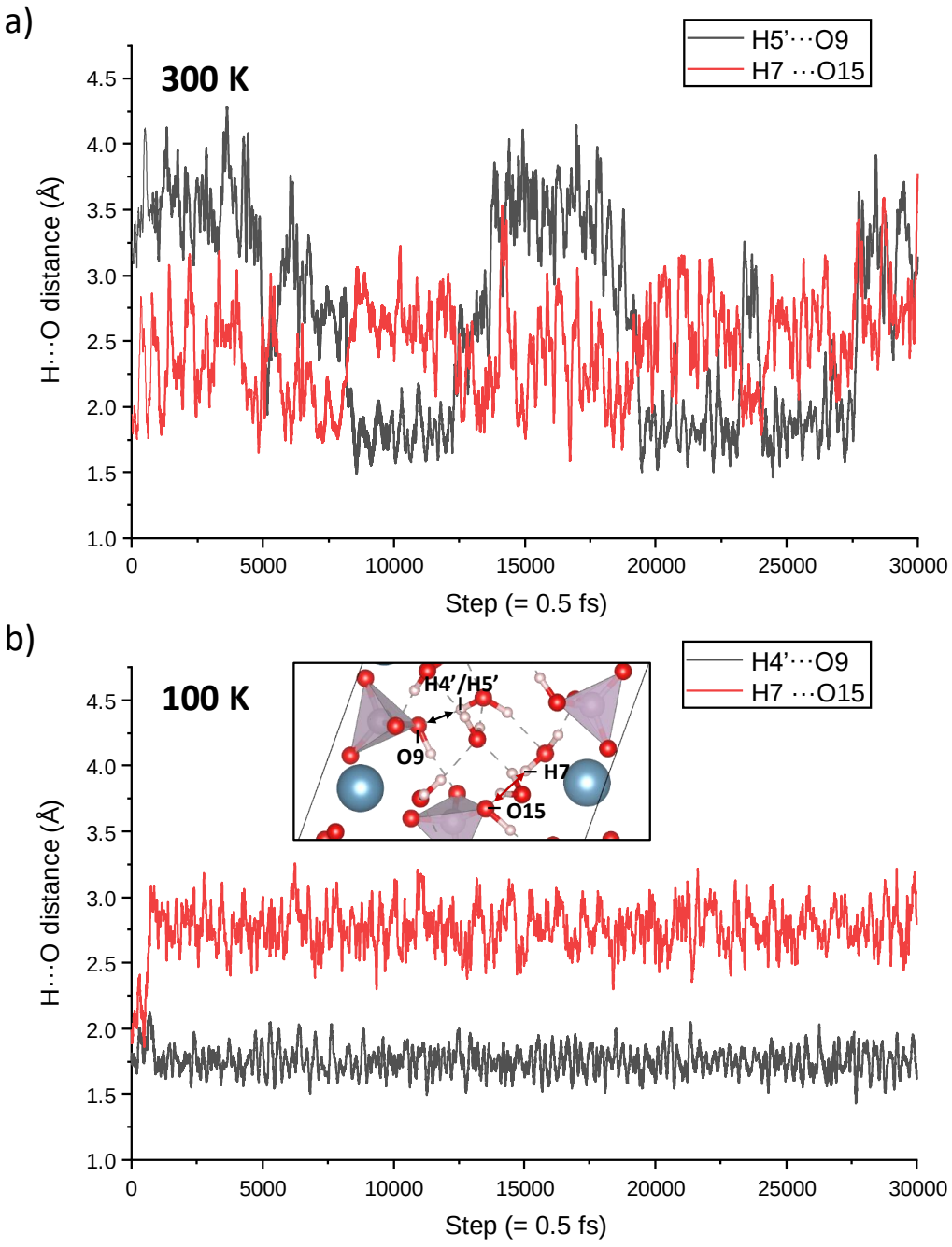


***Figure S11: Comparison of the relative stability of H-bonds involving the P3 PO*H (O9) and the P6 PO*H (O15), over the a) 300 K MD simulation, and b) the 100 K MD simulation. The increased instability around P3 (in black) at 300 K may explain the lack of correlation between O9 and H1, whereas the O15-H6 correlation is visible (see D-RINEPT experiment in Figure 9). An initial flip of the central water molecule H4'-O23'-H5' inverts the roles of H4' and H5' at 300 K. An inset illustrates the position of the relevant H-bonds within the structure.***

The lack of a cross peak for the other POH (involving O9) suggests that the dipolar recoupling between O9 and H1 must be significantly less efficient than that between O16 and H1, despite the similar distances in the static structure. This may be due to local motions around the POH, leading to an averaging of dipolar couplings and a faster relaxation. Indeed, rapid motions of water molecules around O9 are observed on the MD at 300 K (Fig. S11), which are more pronounced than for O15. This raises the question about the position of the H1 signal. Indeed, Figure 2d shows that the $^{1}$H signal at 13 ppm represents less than 7% of the overall signal, and therefore cannot correspond to both PO**H** peaks.

According to calculations (Tab. S5 and Fig. S12), the H1 chemical shift position is expected between 8 and 10 ppm, due to a weaker O···H bond (distance around 1.6 Å). Unfortunately, because of the superimposition of the $^{31}$P NMR resonances of P3, P5 and P6, the $^{1}$H-$^{31}$P CP-HETCOR experiment recorded at room temperature did not allow the unambiguous determination of the $^{1}$H chemical shift value of H1 (data not shown). However, it most likely sits at ca. 8 ppm: a $^{1}$H peak at this position is clearly visible in the high-field $^{1}$H NMR spectrum (Fig. 2d), which has a similar width and relative intensity as the peak at 13 ppm (H6 peak of the other POH). Our later study of the 100 K structure will further confirm this assignment (vide infra), with a similar $^{1}$H chemical shift for H1 at low temperatures observed both experimentally and on the GIPAW calculations of the MD structures at 100 K.

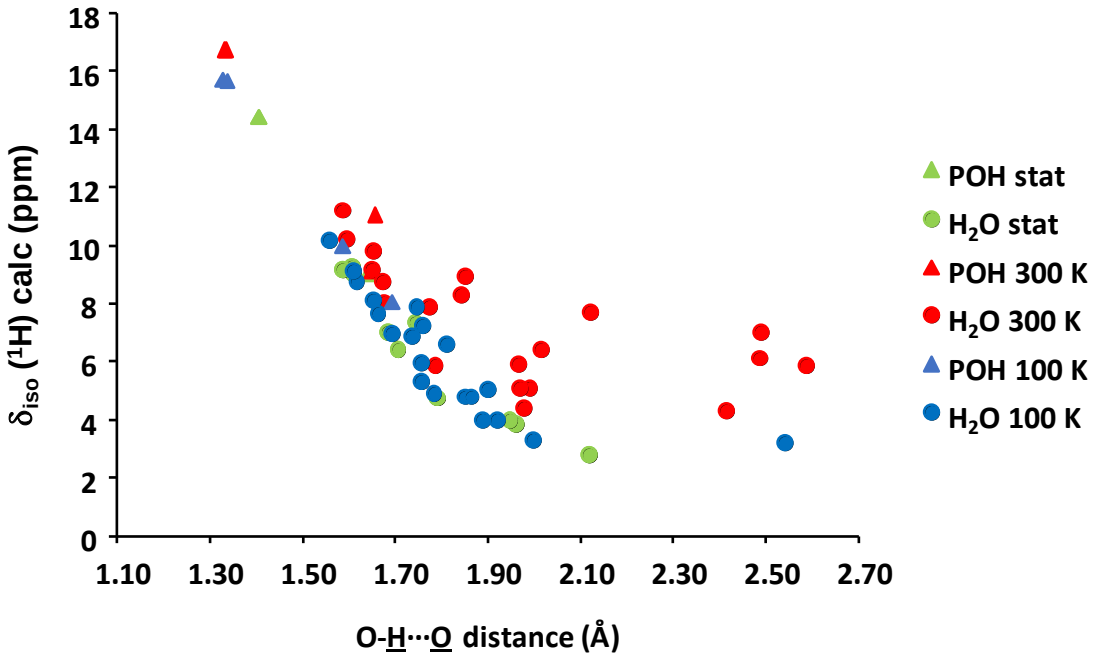


***Figure S12: Calculated $^{1}$H NMR chemical shifts plotted against the shortest OH---O distances for the static relaxed structure (in green), and in the averaged MD structures at 300 K (in red) and 100 K (in blue). Note that POH and HOH (H-bond donors) are plotted with triangles and dots respectively.***

***Tentative assignment of signals in the low-temperature structure***

The assignment of peak positions of the different P sites at 100 K was then examined. From the quantitative direct excitation $^{31}$P NMR experiments, it is possible to establish the following. Given a total integral for the signal of 12 a.u. (considering twelve resonances, as expected from the crystallographic structure in absence of symmetry), the rightmost peaks (from 1.0 to –2.0 ppm) integrate for 3.7 ± 0.3 a.u., the central peaks (from 2.5 to 1.0 ppm) integrate for 2.2 ± 0.2 a.u. and the leftmost peaks (from 4.5 to 2.5 ppm) integrate for 6.2 ± 0.2 a.u. leading to the fit presented on Figure 10a (with two peaks superimposed at 3.2 and 3.5 ppm, explaining their double intensity).

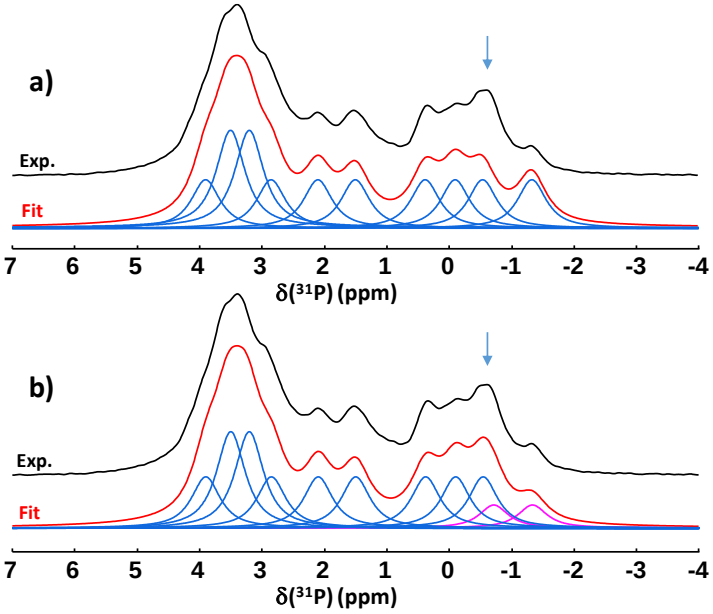


***Figure 10 : Experimental $^{31}$P MAS NMR spectrum of unenriched OCP sample at 100 K ($B_0$ = 18.8 T and $\nu_r$ = 8 kHz), and its fit (with Pseudo-Voigt peaks with a Gaussian/Lorentzian ratio of 0.4): a) attempts of fit with 12 sites of equal intensity (the resonances at 3.2 and 3.5 ppm have double intensity, due to the overlap of 2 sites at each of these positions), b) best fit, with the rightmost resonance split in two components of equal intensity (in pink) to match observed intensities. The blue arrow designates the area of the spectrum altered by the splitting of the resonance.***

It is almost possible to fit the experimental signal using 12 Pseudo-Voigt peaks of equal intensity and width, distributed to match these integrations. However, to obtain a more suitable fit in the low-frequency region, the rightmost resonance at –1.3 ppm must be reduced by half, and the missing intensity added as a new resonance at –0.7 ppm (see Fig. 10b, pink peaks; and Tab. S8 for fitting parameters). We will discuss the possible reasons for this splitting below.

A first clue for the assignment of the sites at 100 K can be obtained by comparing the relative intensities in the direct-excitation $^{31}$P MAS NMR spectrum to those in the $^{31}$P CPMAS NMR spectra, which were recorded at various contact times ($t_{cp}$) Figure 11 shows that the sites with the slowest CP build-up are between 2.0 and 4.0 ppm, while the other sites show higher relative intensities at shorter contact times. Since sites corresponding to $HPO_4^{2-}$ ions will have shorter build-up times, we can hypothesise that at least P5 and P6 sites (and their P5'and P6' counterparts) are among the lower chemical shift peaks (below 1.7 ppm), as is also the case at 300 K (Tab. S2).

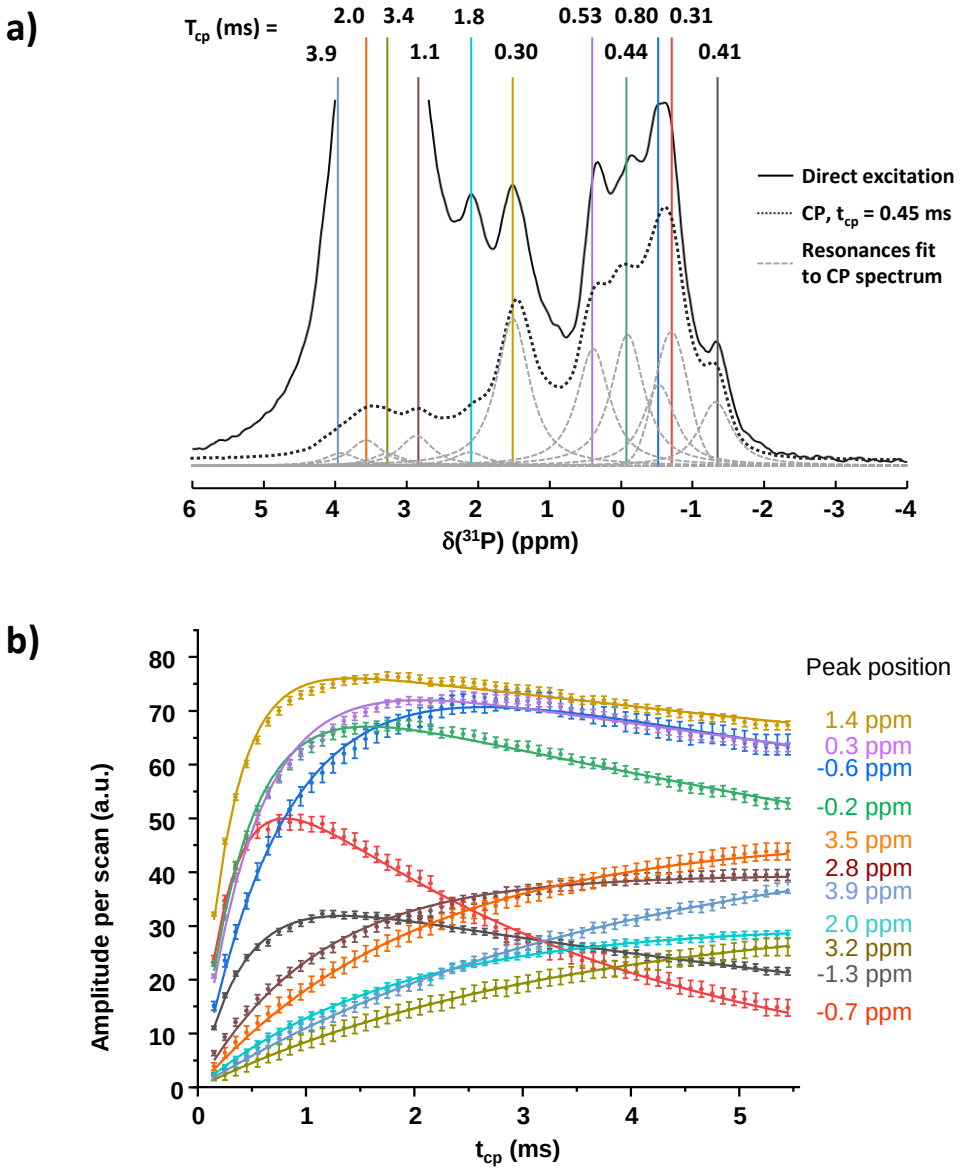


***Figure 11: a) $^{31}$P CPMAS spectrum (dotted black), recorded at ca. 100 K, using a contact time of 0.45 ms ($B_0$ = 18.8 T, $\nu_r$ = 8 kHz), in comparison to the direct-excitation $^{31}$P NMR spectrum recorded at the same temperature (in black, voluntarily truncated vertically, to enable comparisons in the low-frequency region). The individual components (dashed light-grey) correspond to the resonances shown in Fig. 10b, with intensities adjusted to match the experimental CPMAS spectrum. Above the resonances are the CP time constants ($T_{cp}$) calculated for each individual resonance. b) Evolution of the amplitude of the different resonances of the $^{31}$P CPMAS NMR spectra recorded on an unenriched OCP sample at ca. 100 K, at different contact times ($t_{cp}$). The curves correspond to a Levenberg-Marquardt regression of the data points using a simplified model for the transfer of polarisation from $^{1}$H to $^{31}$P (see experimental section for more details, and Table S9 for fitting parameters).***

| Site *i)* | Site *ii)* | $\delta_{iso}^{exp}$ (ppm) | FWHM (ppm) | Integration (a.u.) |
|---|---|---|---|---|
| P5 | P5 | –1.3 | 0.55 | 0.5 |
| P3’ | P° | –0.7 | 0.55 | 0.5 |
| P6 | P6 | –0.6 | 0.55 | 1.0 |
| P5’ | P5’ | –0.2 | 0.55 | 1.0 |
| P6’ | P6’ | 0.3 | 0.55 | 1.0 |
| P3 | P3 | 1.4 | 0.55 | 1.0 |
| P* | P3’ | 2.0 | 0.55 | 1.0 |
| P1 | P1 | 2.8 | 0.55 | 1.0 |
| P2’/P4’ | P2’/P4’ | 3.2 | 0.55 | 2.0 |
| P2/P4 | P2/P4 | 3.5 | 0.55 | 2.0 |
| P1’ | P1’ | 3.9 | 0.55 | 1.0 |

***Table S8: $^{31}$P resonances extracted from the simulation of the quantitative 1D NMR spectrum (Fig 10b), with chemical shift, linewidth and integration. Total sum of integrals is 12. Note that the two possible assignments of sites correspond to hypothesis i) and ii) discussed at the end of text.***

| $\delta_{iso}$ ($^{31}$P) (ppm) | $I_0$ (a.u.) | Tcp (ms) | T1ρ (ms) | $R^2$ |
|---|---|---|---|---|
| –1.3 | 36.9 ± 0.2 | 0.41 ± 0.01 | 9.1 ± 0.2 | 0.9964 |
| –0.7 | 63.5 ± 0.5 | 0.31 ± 0.01 | 3.4 ± 0.1 | 0.9959 |
| –0.6 | 81.3 ± 0.9 | 0.80 ± 0.01 | 18.9 ± 1.3 | 0.9972 |
| –0.2 | 74.8 ± 0.5 | 0.44 ± 0.01 | 14.5 ± 0.5 | 0.9953 |
| 0.3 | 78.5 ± 0.7 | 0.53 ± 0.01 | 23.5 ± 1.5 | 0.9951 |
| 1.4 | 79.4 ± 0.4 | 0.30 ± 0.01 | 32.6 ± 1.7 | 0.9949 |
| 2.0 | 30.1 ± 0.1 | 1.80 ± 0.01 | >> 50 | 0.9997 |
| 2.8 | 39.4 ± 0.2 | 1.11 ± 0.02 | >> 50 | 0.9958 |
| 3.2 | 32.7 ± 0.2 | 3.36 ± 0.04 | >> 50 | 0.9995 |
| 3.5 | 46.6 ± 0.3 | 2.03 ± 0.03 | >> 50 | 0.9982 |
| 3.9 | 48.2 ± 0.5 | 3.86 ± 0.07 | >> 50 | 0.9991 |

***Table S9: Characteristic CP dynamics parameters obtained by fitting the amplitude of different components of the $^{31}$P CPMAS NMR spectra of unenriched OCP at ca. 100 K (Fig. 11).***

To try to further assist in the assignment, $^{31}$P double quantum/single quantum (DQ-SQ) correlation spectra and $^{1}$H-$^{31}$P CP-HETCOR experiments were recorded at 100 K, under DNP conditions (Fig. 12).

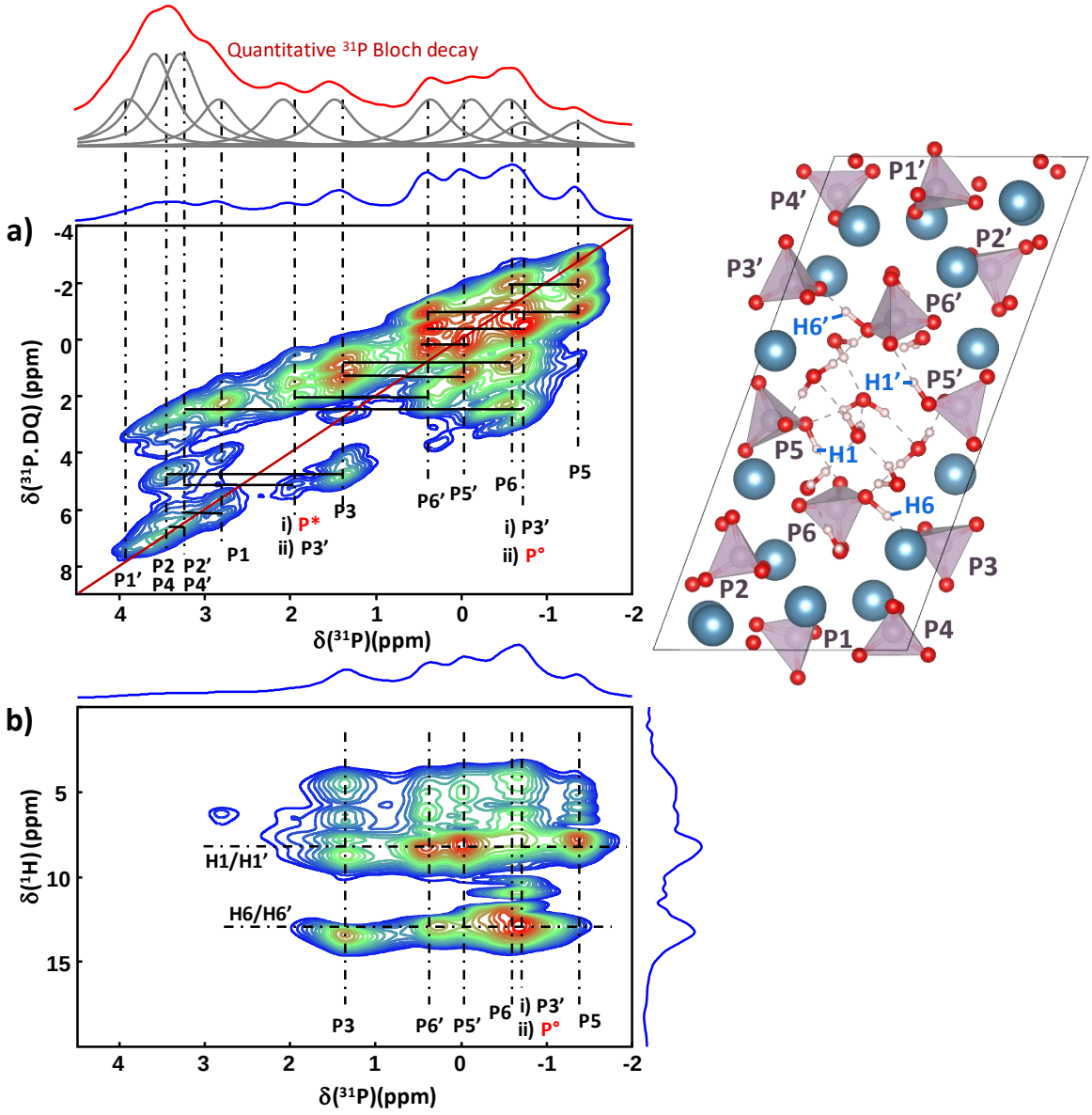


***Figure 12: 2D NMR experiments recorded on unenriched OCP at ca. 100 K (temperature of the refrigerating unit): a) {$^{1}$H} $^{31}$P -$^{31}$P DNP S3 DQ/SQ correlation spectrum recorded at 9.4 T, with a 7.4 ms recoupling time, and $\nu_r$ = 13 kHz. The fit of the quantitative direct-excitation (Bloch decay) $^{31}$P MAS NMR spectrum (recorded at 100 K) is shown in red above the figure. Small shifts in positions between DQ/SQ and direct-excitation MAS peaks are observed, possibly due to surface and/or DNP effects (as discussed in the manuscript). b) $^{1}$H-$^{31}$P DNP CP-HETCOR spectrum recorded at 9.4 T; $t_{cp}$ = 0.2 ms, $\nu_r$ = 13 kHz. The symbols i) /ii) and P*/P° signal correspond to the 2 tentative assignments discussed in the main text.***

Below, a tentative interpretation of these spectra is proposed. As a forenote, it should be noted that some of the cross-peaks on the DQ-SQ and HETCOR data are very slightly shifted compared to the peak-positions on the quantitative $^{31}$P NMR spectrum. DQ-SQ analyses were performed using different recoupling times (Fig. S13), systematically showing similar features.

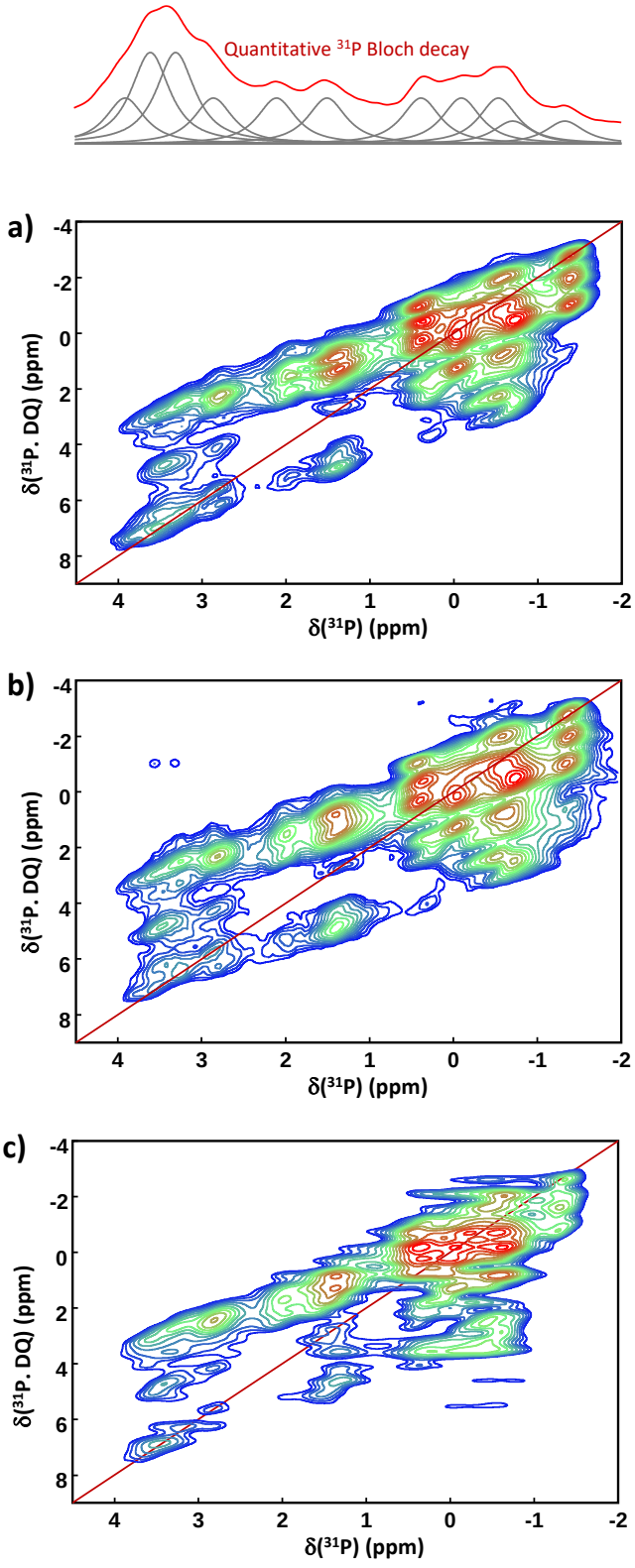


***Figure S13: {$^{1}$H} $^{31}$P -$^{31}$P DNP S3 DQ/SQ correlation spectra recorded on unenriched OCP at ca. 100 K ($B_0$ = 9.4 T, $\nu_r$ = 10 or 13 kHz) at three different recoupling times: a) 7.4 ms, b) 12.3 ms, c) 3.2 ms. The spectra show similar features at the different recoupling times (including very slight shifts in cross-peak positions, compared to the peak-maxima on the direct-excitation $^{31}$P MAS NMR spectra, as mentioned in main text).***

| Pair | Dist. (Å) | Pair | Dist. (Å) | Pair | Dist. (Å) | Pair | Dist. (Å) | Pair | Dist. (Å) | Pair | Dist. (Å) |
|---|---|---|---|---|---|---|---|---|---|---|---|
| **P1 - P1'** | 4.09 | **P2 - P3** | 3.96 | **P3 - P2** | 3.96 | **P4 - P4'** | 4.02 | **P5- P5'** | 4.02 | **P6 - P5** | 4.09 |
| P1 - P4' | 4.73 | **P2 - P4** | 4.15 | **P3 - P6** | 4.15 | **P4 - P2** | 4.15 | **P5 - P6** | 4.09 | **P6 - P3** | 4.15 |
| P1 - P2' | 4.76 | P2 - P1' | 4.76 | P3 - P4 | 5.10 | P4 - P1' | 4.73 | P5 - P3 | 5.61 | P6 - P2 | 5.08 |
| P1 - P2 | 5.03 | P2 - P1 | 5.03 | P3 - P1 | 5.40 | P4 - P1 | 5.03 | P5 - P2' | 5.88 | P6 - P1 | 5.09 |
| P1 - P6 | 5.09 | P2 - P6 | 5.08 | P3 - P4' | 5.56 | P4 - P3 | 5.10 | P5 - P2 | 6.05 | P6 - P3 | 5.75 |
| P1 - P3 | 5.40 | P2 - P5' | 5.88 | P3 - P5 | 5.61 | P4 - P3' | 5.57 | P5 - P3' | 6.65 | P6 - P4 | 5.99 |
| Pair | Dist. (Å) | Pair | Dist. (Å) | Pair | Dist. (Å) | Pair | Dist. (Å) | Pair | Dist. (Å) | Pair | Dist. (Å) |
| **P1' - P1** | 4.09 | **P2' - P3'** | 3.98 | **P3' - P2'** | 3.98 | **P4' - P4** | 4.02 | **P5'- P5** | 4.02 | **P6'- P5'** | 4.06 |
| P1' - P4 | 4.73 | P2'- P4' | 4.73 | **P3' - P6'** | 4.15 | P4' - P1 | 4.73 | **P5' - P6'** | 4.06 | **P6' - P3'** | 4.15 |
| P1' - P2 | 4.76 | P2' - P1 | 4.76 | P3' - P4' | 5.10 | P4' - P2' | 4.73 | P5' - P3' | 5.64 | P6' - P2' | 5.08 |
| P1' - P2' | 5.00 | P2' - P1' | 5.00 | P3' - P1' | 5.41 | P4' - P1' | 5.02 | P5' - P2 | 5.88 | P6' - P1' | 5.13 |
| P1' - P4' | 5.01 | P2' - P6' | 5.08 | P3' - P4 | 5.57 | P4' - P3' | 5.10 | P5 '- P3 | 5.88 | P6' - P4' | 6.02 |
| P1' - P6' | 5.13 | P2' - P5 | 5.88 | P3' - P5' | 5.64 | P4' - P1 | 5.54 | P5 '- P2' | 6.07 | P6 '- P5 | 6.71 |

***Table 1*: *Interatomic distances between phosphorus sites in the averaged structure of OCP obtained by MD simulation at 100 K. Distances below 4.5 Å are highlighted in green.***

First, based on the CP build-up times (Fig. 11) and the P-H distances (Tab. S10), we expect the P1(‘), P2(‘) and P4(‘) $^{31}$P signals to be positioned above 1.7 ppm, and P3(‘), P5(‘) and P6(‘) peaks below this value.

| **Site** | **P1** | **P2** | **P3** | **P4** | **P5** | **P6** |
|---|---|---|---|---|---|---|
| **Nearest proton** | H3 | H2 | H6 | H3 | H1 | H6 |
| **Distance (Å)** | 4.4 | 3.4 | 2.4 | 3.9 | 2.2 | 2.3 |
| **Next nearest** | H2 | H11 | H7 | H2 | H4’ | H3 & H1 |
| **Distance (Å)** | 5.2 | 3.8 | 3.3 | 4.6 | 2.7 | 2.6 |
| | | | | | | |
| **Site** | **P1’** | **P2’** | **P3’** | **P4’** | **P5’** | **P6’** |
| **Nearest proton** | H3’ | H2’ | H6’ | H3’ | H1’ | H6’ |
| **Distance (Å)** | 4.3 | 3.4 | 2.4 | 3.9 | 2.2 | 2.3 |
| **Next nearest** | H2’ | H11’ | H7’ | H2’ | H8 | H3’ & H1’ |
| **Distance (Å)** | 5.2 | 3.8 | 3.3 | 4.6 | 2.7 | 2.6 & 2.7 |

***Table S10: Distances between phosphorus sites to their nearest proton site in the 100 K averaged MD structure.***

The $^{1}$H-$^{31}$P CP-HETCOR experiment recorded using a short contact time of 0.2 ms (Fig. 12b) shows two main proton positions at ~ 8 ppm and ~ 13 ppm, that can be safely assigned to $HPO_4^{2-}$ resonances, based on the short P…H distances (Table S10). More precisely, they should correspond to H1/H1’ and H6/H6’, respectively, according to NMR calculations (Tab. S5). This is also consistent with the relative P5-O9-H1···O16-P6 and P6-O15-H6···O2-P3 distances, showing that there is a stronger H-bond in the latter case.[49] Consequently, P5(‘) and to a lesser extent P6(‘) sites are expected to show a cross-peak at ~ 8 ppm. Similarly, P6(‘) and P3(‘) sites should show a cross-peak at ~ 13 ppm. This means that the $^{31}$P signals observed at 0.3, –0.2 and –1.3 ppm can correspond to P5(‘) and P6(‘) sites, while those at 1.4, 0.3, –0.6, –0.7 could belong to P6(‘) and P3(‘) sites.

The DQ-SQ experiment shown on Fig. 12a was measured with a 2 ms CP polarisation transfer from $^{1}$H, and a recoupling time of 7.4 ms. Considering only the shortest calculated $^{31}$P-$^{31}$P interatomic distances (below 4.5 Å), 10 main cross-peaks are expected (Tab. 1), which we will focus on. P6 is supposed to have significant cross-peaks with P3 and P5. Therefore, we can propose that the signal at –0.6 ppm

belongs to P6, that shows cross-peaks with the signals at 1.4 and –1.3 ppm, that could thus belong to P3 and P5. Moreover, since P2, expected above 1.7 ppm, is close to P3, it could correspond to the peak at 3.5 ppm, showing cross-peak with the signal at 1.4 ppm. Note that two superimposed signals are suggested at 3.5 ppm by the quantitative $^{31}$P NMR spectrum (Fig. 10), and that a cross-peak is observed on the diagonal at 3.5 ppm. This suggests that P4, in close proximity to P2, may also observed at 3.5 ppm.

At this stage, we propose two possibilities for the Px(') assignments, both of which still present residual inconsistencies with the collected experimental data. Moreover, it should be noted that the $^{31}$P calculated values after averaging by MD at 100 K show unfortunately too many discrepancies with experimental data, making their use for spectral assignments impossible at this stage.

*i)* A first possibility is to assign the signal at –0.7 ppm to P3', based on the $^{1}$H-$^{31}$P CP HETCOR analysis. Since this signal shows cross-peaks with $^{31}$P signals at 3.2 and 0.3 ppm on the DQ-SQ spectrum, the latter would be assigned to P2' and P6', respectively. The remaining signal visible on the CP-HETCOR experiment at –0.2 ppm, showing a cross-peak with the signal at 0.3 ppm (P6') would then correspond to P5'. Finally, the signal at 3.2 ppm showing a cross-peak with the signal at –0.7 ppm (P3') could be assigned to P2', superimposed with P4' (as previously proposed for P2/P4). The $^{31}$P signal at 2.8 ppm showing cross-peaks with P4' and P2' (both at 3.2 ppm) is tentatively assigned to P1. P1 should show a cross-peak with P1', but no clear correlation is observed with the remaining signals. Here, it is proposed that the very low intensity peak at 3.9 ppm corresponds to P1' (its low intensity possibly preventing the observation of a cross-peak on the DQ-SQ experiment). A remaining $^{31}$P NMR signal centered at 2.0 ppm (noted P*) is observed. It is likely to be part of the OCP phase as well, as it shows small cross-peaks with other OCP signals. Yet its assignment is uncertain. Moreover, in all this reasoning, the relative intensities of the $^{31}$P resonances observed in the quantitative analysis (Fig. 10b) are not explained here.

*ii)* A second possibility is to take into account the fact that the intensity of the signal assigned to P5 (-1.3 ppm) is half of the others according to the quantitative spectrum (pink resonance on Fig 10b). This could suggest that the other half-intensity peak (at –0.7 ppm) is a P5-like site (noted P°), but with a different H-bonding for the POH since it shows cross-peaks with proton signals at ~ 13 ppm and ~ 10 ppm on the $^{1}$H-$^{31}$P CP-HETCOR experiment. This implies that the remaining $^{31}$P signals visible on the CP-HETCOR experiment at 0.3 and –0.2 ppm, showing a cross-peak on the DQ-SQ, would belong to P6' and P5' respectively. The small cross-peak between P6' (0.3 ppm) and the signal at 2.0 ppm on the DQ-SQ suggests the latter could be P3'. Finally, the signal at 3.2 ppm showing a cross-peak with the signal at 2.0 ppm (P3') could be assigned to P2', superimposed with P4' (as previously explained for P2/P4). By elimination and consistently with hypothesis *i)*, remaining signals at 3.9 and 2.8 ppm would possibly correspond to P1' and P1. However, in this second tentative assignment, P3' would not be visible on the $^{1}$H-$^{31}$P CP-HETCOR data, and would also show slower $^{1}$H-$^{31}$P CP dynamics, for unexplained reasons.

In both interpretations presented above, there are still common inconsistencies, like the unexpected presence of an on-diagonal cross-peak for P5, the absence of the expected cross-peak between P5 and P5', and the unexpected cross-peaks observed between P3 and P6, but also between P5 and P6'. In

addition, P* and P° assignments are difficult to confirm at this stage, and in hypothesis *ii),* P3' would also have a very different $^{1}$H-$^{31}$P CP dynamics than P3, for which we have no explanation.
Our reasoning above was based on the implicit hypotheses that OCP samples at ca. 100 K are perfectly stoichiometric, crystalline, with 110 well-defined and fully occupied atomic sites. The presence of unexpected cross-peaks indicates that there could be significantly more than 12 P sites, possibly due to an even smaller symmetry (at least in some crystals, and/or some unit cells). Moreover, surface effects may have an influence on the observations made by ssNMR. Indeed, even well-crystallised OCP platelets have a thickness of only a few unit cells (< 15 nm),[52] and the samples studied here also show a dispersion in the size of the particles (Fig. S3). Thus, the importance of the surface, particularly under DNP analysis conditions, may cause the observations made by NMR to partly diverge from those of an "ideal" model of OCP (which is built on experimental observations initially made on large single-crystals). These surface effects may not be apparent at ambient temperature, but the increased resolution and surface sensitivity of low-temperature DNP-enhanced experiments may have revealed (hydrogen)phosphate local environments that are not resolved under more standard analytical conditions. Simulating the surface of OCP separately from the bulk may be of interest in the case of OCP, although this is beyond the scope of our present study.

Lastly, regarding $^{17}$O NMR data, a $^{1}$H-$^{17}$O D-HMQC correlation experiment was performed at 100 K (Fig. 13).

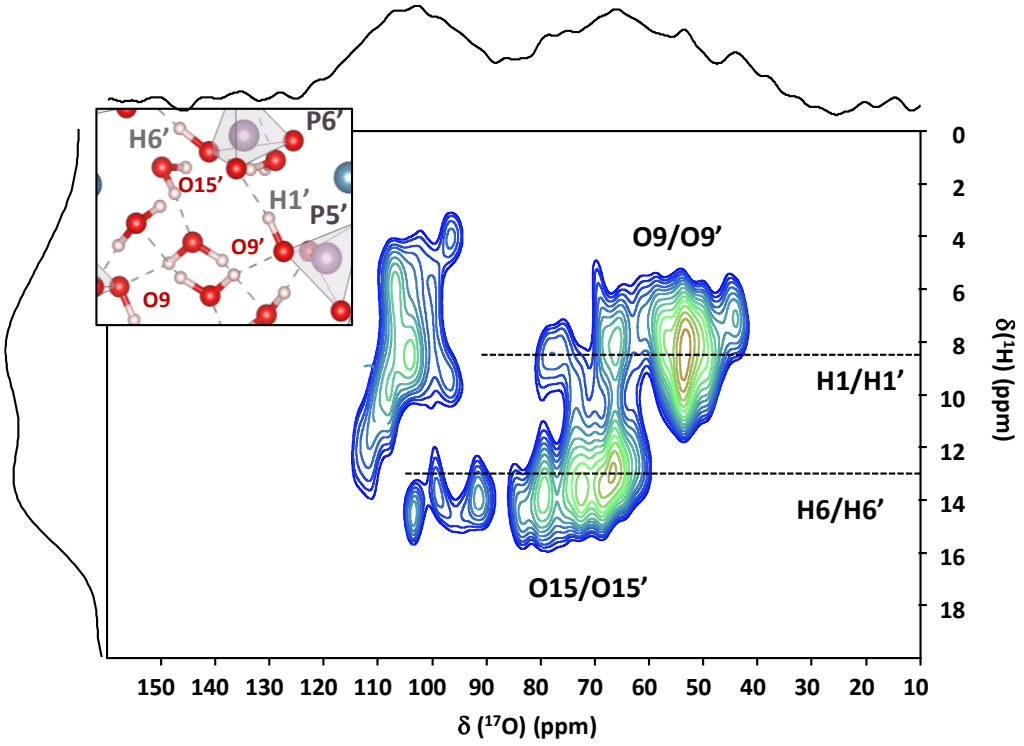


***Figure 13: 2D heteronuclear $^{1}$H-$^{17}$O D-HMQC spectrum of the $^{17}$O-enriched OCP sample recorded at ca. 100 K (temperature of the refrigerating unit), $B_0$ = 18.8 T and $\nu_r$ = 50 kHz.***

Here, contrary to the $^{1}H - {}^{17}O$ correlation D-RINEPT experiment recorded at ambient temperature (Fig. 9), two cross-peaks are now visible, correlating the $^{1}H$ positions around 13 and 8 ppm with the $^{17}O$ resonances in the POH region, with isotropic shifts around ca. 90 and 75 ppm respectively. According to calculations (Tab. S5 and S6) and to the assignments proposed at ambient temperature, these cross-peaks correspond to the H6/H6' (13 ppm) - O15/O15' (90 ppm) and H1/H1' (8.5 ppm) - O9/O9' (75 ppm) pairs, respectively. This suggests that at low temperature, motions around O9 and H1 are reduced, enabling a cross-peak to be observed the $^{1}H$-$^{17}O$ dipolar-recoupling experiment. This is confirmed by comparing the results of MD simulations around this site at 100 K and 300 K (Fig S11). This assignment is also consistent with $^{1}H$-$^{31}P$ HETCOR results, since the P6/P6' sites are linked to O15/O15', and show a cross-peak with H6/H6' at ~ 13 ppm, while the P5/P5' sites are linked to O9/O9' and show a cross-peak with H1/H1' at ~ 8 ppm (Fig. 12b). At this stage, no further information about the low-temperature form of OCP could be extracted from this $^{17}O$ NMR data.

**Conclusion**

We have demonstrated using solid-state NMR that OCP exhibits a significant mobility of water in the interlayer space, which is drastically reduced when cooled down at cryogenic temperatures. Using an "NMR crystallography" approach, involving variable-temperature ssNMR analyses, molecular dynamics simulations, and GIPAW-DFT calculations of NMR parameters, we propose that the OCP lattice can be found in different symmetry groups: *P*1 when observed at short timeframes or at low temperature, but *P*-1 when averaged over longer times or at high temperature. The lowered symmetry is caused by the asymmetric formation of low-energy H-bonds between water molecules, that become unstable at higher temperatures, due to reorientations of water molecules at a very short time scale.

While the reduction in crystal symmetry appears very clearly on the $^{31}P$ ssNMR data recorded at 100 K, several aspects of the OCP structre are nevertheless still unexplained. Indeed, molecular dynamics simulations help justifying the observed splitting of $^{31}P$ NMR peaks below 200 K, allow a more precise assignment of some $^{43}Ca$ sites at ambient temperature, and also help rationalise the differences observed on the $^{1}H$-$^{17}O$ dipolar-based correlations at 100 and 300 K. Nonetheless, MD does not facilitate the rationalisation of the low-temperature $^{1}H$-$^{31}P$ CP-HETCOR and $^{31}P$/$^{31}P$ DQ/SQ NMR data, nor help improve the quality of the agreement with the GIPAW calculated $^{31}P$ NMR parameters of the phosphorous sites in OCP. For this nucleus, it could be that NMR parameters are very sensitive to numerous effects, including the presence of partially occupied sites, small changes in local symmetry, small changes in the water content in the interlayer space, and/or dynamics effects on time scales not explored by MD simulations. While additional information on water dynamics may be accessible from $^{2}H$ experiments,[50] the synthesis of $^{2}H$-enriched OCP was not attempted as part of this contribution, as an overlap between 24 $^{2}H$ sites was expected, thereby requiring extensive complementary studies to ensure accurate interpretation.

All in all, the present work highlights the limitations in studying hydrated phases solely at ambient temperature and using static models, and the importance of low-temperature NMR and molecular dynamics simulations in such cases.[53] It also opens the possibility of studying the mechanism of transformation of OCP into HAp in even more detail, given the improved resolution afforded by low temperatures and new knowledge about the structure of OCP. It seems, however, that the periodic

boundary conditions usually used to analyse such structures may be a limiting factor in further computational studies of this phase. The use of more "costly" computational approaches, involving supercells and surface simulations, will probably be necessary for a deeper understanding of the OCP structure.

**Author Contributions**

The project was conducted by AN, in close interaction with DL and CG. AN carried out the syntheses and isotopic enrichment experiments, background characterisations, as well as the vast majority of ssNMR experiments. IH, AV and ZG performed the high-resolution ambient temperature experiments at 18.8 T and 35.2 T. SP and WP conducted and contributed to the analysis of the low-temperature $^{31}$P NMR experiments recorded at 9.4 T. TF participated to the ambient temperature $^{43}$Ca NMR experiments recorded at 23.4 T. DG participated to the low-temperature temperature $^{17}$O NMR experiments recorded at 18.8 T. AN and CG carried out GIPAW DFT computations and MD calculations. AN, CG, DL, CB, GP, SH, WP and SP participated in discussions on ssNMR data of OCP. AN, CG and DL wrote the initial draft of the manuscript, and all authors contributed to the final preparation of the article.

**Conflicts of interest**

In accordance with our policy on Conflicts of interest please ensure that a conflicts of interest statement is included in your manuscript here. Please note that this statement is required for all submitted manuscripts. If no conflicts exist, please state that "There are no conflicts to declare".

**Acknowledgements**

This project has received funding from the Agence Nationale de la Recherche (TOGETHER project – grant ANR-19-CE29-0021). DFT calculations were performed using HPC resources from GENCI-IDRIS (Grant AD010-097535). Financial support from the IR INFRANALYTICS FR2054 for conducting part of the NMR research at the facilities in Lyon (CRMN) and Paris (ENS) is gratefully acknowledged. Nicolas Birlirakis is warmly thanked for his help with the LT-NMR experiments at ENS-Paris. A portion of this work was also performed at the National High Magnetic Field Laboratory, which is supported by the National Science Foundation Cooperative Agreements Nos. DMR-1644779 and DMR-2128556 and the State of Florida**.** The 36 T SCH magnet and NMR instrumentation was supported by the NSF (DMR-1039938 and DMR-0603042) and NIH (BTRR 1P41 GM122698 and RM1GM148766). Ieva Golberga (LCMCP and ICGM) is thanked for her help while acquiring spectra at 35.2 T. The UK 1000 MHz solid-state NMR Facility was funded by EPSRC and BBSRC, as well as the University of Warwick including *via* part funding through Birmingham Science City Advanced Materials Projects 1 and 2 supported by Advantage West Midlands (AWM) and the European Regional Development Fund (ERDF). The variable temperature powder X-ray diffraction characterisation was performed at the XRD platform of IMPMC with the support of Benoît Baptiste.

**References**


1 W. E. Brown, J. R. Lehr, J. P. Smith and A. W. Frazier, *J. Am. Chem. Soc.*, 1957, **79**, 5318–5319.
2 P. Simon, D. Grüner, H. Worch, W. Pompe, H. Lichte, T. El Khassawna, C. Heiss, S. Wenisch and R. Kniep, *Sci. Rep.*, 2018, **8**, 1–17.
3 M. Robin, S. Von Euw, G. Renaudin, S. Gomes, J. M. Krafft, N. Nassif, T. Azaïs and G. Costentin, *Cryst. Eng. Comm.*, 2020, **22**, 2728–2742.
4 G. R. Sauer, W. B. Zunic, J. R. Durig and R. E. Wuthier, *Calcif. Tissue Int.*, 1994, **54**, 414–420.
5 N. J. Crane, V. Popescu, M. D. Morris, P. Steenhuis and M. A. Ignelzi, *Bone*, 2006, **39**, 434–442.
6 E. Davies, K. H. Müller, W. C. Wong, C. J. Pickard, D. G. Reid, J. N. Skepper and M. J. Duer, *Proc. Natl. Acad. Sci.*, 2014, **111**, E1354–E1363.
7 R. Horváthová, L. Müller, A. Helebrant, P. Greil and F. A. Müller, *Mater. Sci. Eng. C*, 2008, **28**, 1414–1419.
8 W. E. Brown, *Nature*, 1962, **196**, 1048–1050.
9 C. Rey, C. Combes, C. Drouet and M. J. Glimcher, *Osteoporos. Int.*, 2009, **20**, 1013–1021.
10 Y. Wang, S. Von Euw, F. M. Fernandes, S. Cassaignon, M. Selmane, G. Laurent, G. Pehau-Arnaudet, C. Coelho, L. Bonhomme-Coury, M. M. Giraud-Guille, F. Babonneau, T. Azaïs and N. Nassif, *Nat. Mater.*, 2013, **12**, 1144–1153.
11 P. W. Arnold, *Trans. Faraday Soc.*, 1950, **46**, 1061–1072.
12 M. Mathew, W. E. Brown, L. W. Schroeder and B. Dickens, *J. Crystallogr. Spectrosc. Res.*, 1988, **18**, 235–250.
13 Y. H. Tseng, J. Zhan, K. S. K. Lin, C. Y. Mou and J. C. C. Chan, *Solid State Nucl. Magn. Reson.*, 2004, **26**, 99–104.
14 W. E. Brown, J. P. Smith, J. R. Lehr, and A. W. Frazier, *Nature*, 1962, **196**, 1050–1055.
15 E. Davies, M. J. Duer, S. E. Ashbrook and J. M. Griffin, *J. Am. Chem. Soc.*, 2012, **134**, 12508–12515.
16 D. Laurencin, Y. Li, M. J. Duer, D. Iuga, C. Gervais and C. Bonhomme, *Magn. Reson. Chem.*, 2021, **59**, 1048–1061.
17 F. Pourpoint, C. Gervais, L. Bonhomme-Coury, F. Mauri, B. Alonso and C. Bonhomme, *Comptes Rendus Chim.*, 2008, **11**, 398–406.
18 Z. Gan, I. Hung, X. Wang, J. Paulino, G. Wu, I. M. Litvak, P. L. Gor'kov, W. W. Brey, P. Lendi, J. L. Schiano, M. D. Bird, I. R. Dixon, J. Toth, G. S. Boebinger and T. A. Cross, *J. Magn. Reson.*, 2017, **284**, 125–136.
19 D. G. Cory and W. M. Ritchey, *J. Magn. Reson. 1969*, 1988, **80**, 128–132.
20 B. M. Fung, A. K. Khitrin and K. Ermolaev, *J. Magn. Reson.*, 2000, **142**, 97–101.
21 F. Mentink-Vigier, I. Marin-Montesinos, A. P. Jagtap, T. Halbritter, J. van Tol, S. Hediger, D. Lee, S. Th. Sigurdsson and G. De Paëpe, *J. Am. Chem. Soc.*, 2018, **140**, 11013–11019.
22 G. Teymoori, B. Pahari, B. Stevensson and M. Edén, *Chem. Phys. Lett.*, 2012, **547**, 103–109.
23 G. Teymoori, B. Pahari and M. Edén, *J. Magn. Reson.*, 2015, **261**, 205–220.
24 K. Märker, S. Paul, C. Fernández-de-Alba, D. Lee, J.-M. Mouesca, S. Hediger and G. D. Paëpe, *Chem. Sci.*, 2017, **8**, 974–987.
25 S. Paul, N. D. Kurur and P. K. Madhu, *J. Magn. Reson.*, 2010, **207**, 140–148.
26 C. Martineau, B. Bouchevreau, F. Taulelle, J. Trébosc, O. Lafon and J. P. Amoureux, *Phys. Chem. Chem. Phys.*, 2012, **14**, 7112–7119.
27 A. Brinkmann and A. P. M. Kentgens, *J. Am. Chem. Soc.*, 2006, **128**, 14758–14759.
28 A. P. M. Kentgens and R. Verhagen, *Chem. Phys. Lett.*, 1999, **300**, 435–443.
29 M. Goswami, P. J. M. Van Bentum and A. P. M. Kentgens, *J. Magn. Reson.*, 2012, **219**, 25–32.
30 J. J. Helmus and C. P. Jaroniec, *J. Biomol. NMR*, 2013, **55**, 355–367.
31 P. Virtanen, R. Gommers, T. E. Oliphant, M. Haberland, T. Reddy, D. Cournapeau, E. Burovski, P. Peterson, W. Weckesser, J. Bright, S. J. van der Walt, M. Brett, J. Wilson, K. J. Millman, N. Mayorov, A. R. J. Nelson, E. Jones, R. Kern, E. Larson, C. J. Carey, İ. Polat, Y. Feng, E. W. Moore, J.

VanderPlas, D. Laxalde, J. Perktold, R. Cimrman, I. Henriksen, E. A. Quintero, C. R. Harris, A. M. Archibald, A. H. Ribeiro, F. Pedregosa and P. van Mulbregt, *Nat. Methods*, 2020, **17**, 261–272.
32 W. Kolodziejski and J. Klinowski, *Chem. Rev.*, 2002, **102**, 613–628.
33 J. Vandevondele, M. Krack, F. Mohamed, M. Parrinello, T. Chassaing and J. Hutter, *Comput. Phys. Commun.*, 2005, **167**, 103–128.
34 S. Grimme, J. Antony, S. Ehrlich and H. Krieg, *J. Chem. Phys.*, 2010, **132**, 154104.
35 S. Goedecker, M. Teter and J. Hutter, *Phys. Rev. B - Condens. Matter Mater. Phys.*, 1996, **54**, 1703–1710.
36 J. VandeVondele and J. Hutter, *J. Chem. Phys.*, 2007, **127**, 114105.
37 S. Nosé, *J. Chem. Phys.*, 1984, **81**, 511–519.
38 P. Giannozzi, S. Baroni, N. Bonini, M. Calandra, R. Car, C. Cavazzoni, D. Ceresoli, G. L. Chiarotti, M. Cococcioni, I. Dabo, A. Dal Corso, S. De Gironcoli, S. Fabris, G. Fratesi, R. Gebauer, U. Gerstmann, C. Gougoussis, A. Kokalj, M. Lazzeri, L. Martin-Samos, N. Marzari, F. Mauri, R. Mazzarello, S. Paolini, A. Pasquarello, L. Paulatto, C. Sbraccia, S. Scandolo, G. Sclauzero, A. P. Seitsonen, A. Smogunov, P. Umari and R. M. Wentzcovitch, *J. Phys. Condens. Matter*, 2009, **21**, 395502.
39 J. P. Perdew, K. Burke and M. Ernzerhof, *Phys. Rev. Lett.*, 1996, **77**, 3865.
40 P. Pyykkö, *Mol. Phys.*, 2018, **116**, 1328–1338.
41 B. K. Sahoo, *Phys. Rev. - At. Mol. Opt. Phys.*, 2009, **80**, 012515.
42 K. M. N. Burgess, Y. Xu, M. C. Leclerc and D. L. Bryce, *Inorg. Chem.*, 2014, **53**, 552–561.
43 C. R. Harris, K. J. Millman, S. J. van der Walt, R. Gommers, P. Virtanen, D. Cournapeau, E. Wieser, J. Taylor, S. Berg, N. J. Smith, R. Kern, M. Picus, S. Hoyer, M. H. van Kerkwijk, M. Brett, A. Haldane, J. F. del Río, M. Wiebe, P. Peterson, P. Gérard-Marchant, K. Sheppard, T. Reddy, W. Weckesser, H. Abbasi, C. Gohlke and T. E. Oliphant, *Nature*, 2020, **585**, 357–362.
44 I. Goldberga, I. Hung, V. Sarou-Kanian, C. Gervais, Z. Gan, J. Novák-Špačková, T.-X. Métro, C. Leroy, D. Berthomieu, A. van der Lee, C. Bonhomme and D. Laurencin, *Inorg. Chem.,* 2024*, accepted* (doi:10.1021/acs.inorgchem.4c00300).
45 M. Profeta, M. Benoit, F. Mauri and C. J. Pickard, *J. Am. Chem. Soc.*, 2004, **126**, 12628–12635.
46 G. Wu, D. Rovnyak, P. C. Huang and R. G. Griffin, *Chem. Phys. Lett.*, 1997, **277**, 79–83.
47 F. Pourpoint, C. Gervais, L. Bonhomme-Coury, T. Azaïs, C. Coelho, F. Mauri, B. Alonso, F. Babonneau and C. Bonhomme, *Appl. Magn. Reson.*, 2007, **32**, 435–457.
48 S. E. Ashbrook and M. E. Smith, *Chem. Soc. Rev.*, 2006, **35**, 718–735.
49 C. Gervais, C. Coelho, T. Azaïs, J. Maquet, G. Laurent, F. Pourpoint, C. Bonhomme, P. Florian, B. Alonso, G. Guerrero, P. H. Mutin and F. Mauri, *J. Magn. Reson.*, 2007, **187**, 131–140.
50 C. H. Chen, I. Goldberga, P. Gaveau, S. Mittelette, J. Špačková, C. Mullen, I. Petit, T. X. Métro, B. Alonso, C. Gervais and D. Laurencin, *Magn. Reson. Chem.*, 2021, **59**, 975–990.
51 D. Laurencin and M. E. Smith, *Prog. Nucl. Magn. Reson. Spectrosc.*, 2013, **68**, 1–40.
52 M. Iijima, H. Tohda and Y. Moriwaki, *J. Cryst. Growth*, 1992, **116**, 319–326.
53 I. Goldberga, N. D. Jensen, C. Combes, F. Mentink-Vigier, X. Wang, I. Hung, Z. Gan, J. Trébosc, T.-X. Métro, C. Bonhomme, C. Gervais and D. Laurencin, *Faraday Discuss.*, 2023, **241**, 250–265.

# CHAPTER III

## Study of biominerals and bone *via* $^{1}H$-$^{31}P$ 2D CP-HETCOR NMR

## Summary

## I. Study of bone *via* 2D $^{1}H$-$^{31}P$ CP-HETCOR: existing methods and proposed improvements

Although the study of the OCP structure holds interest in its own right, we must focus back on our main subject, which is the comparative analysis of bone mineral in natural specimens *via* solid state NMR. This chapter will therefore present the different methods we have developed to study biological samples, and the results from our study of $LPA_1$ deficiency (Chapter I, section I.4) on bone mineral composition.

We have seen in Chapter I, section III.3, that bone mineral has a core-shell structure. It is composed of a carbonated, apatitic calcium phosphate core, and a hydrated, disordered surface, rich in hydrogen phosphates. The exact composition of the surface is still the source of much study and debate, with contradicting evidence likening it to OCP, ACP or DCPD. However, we know that there is a large amount of $HPO_4^{2-}$ sites at the surface (Figure 1), and that these sites can be distinguished via $^{1}H$-$^{31}P$ CP-HETCOR NMR.

Two studies have connected the linewidth of the $^{31}P$ signal of bone with osteoporosis and osteoarthritis.[1,2] This was explained by differences in the morphology of bone altering the NMR signal of bone mineral. Whether the changes concern *i)* the quantitative differences between surface and core signals or *ii)* changes to their composition, remains mostly unexplored. Because the differences between our samples are expected to be slight,[3] we wish to develop more robust methods for their qualitative and quantitative comparison.

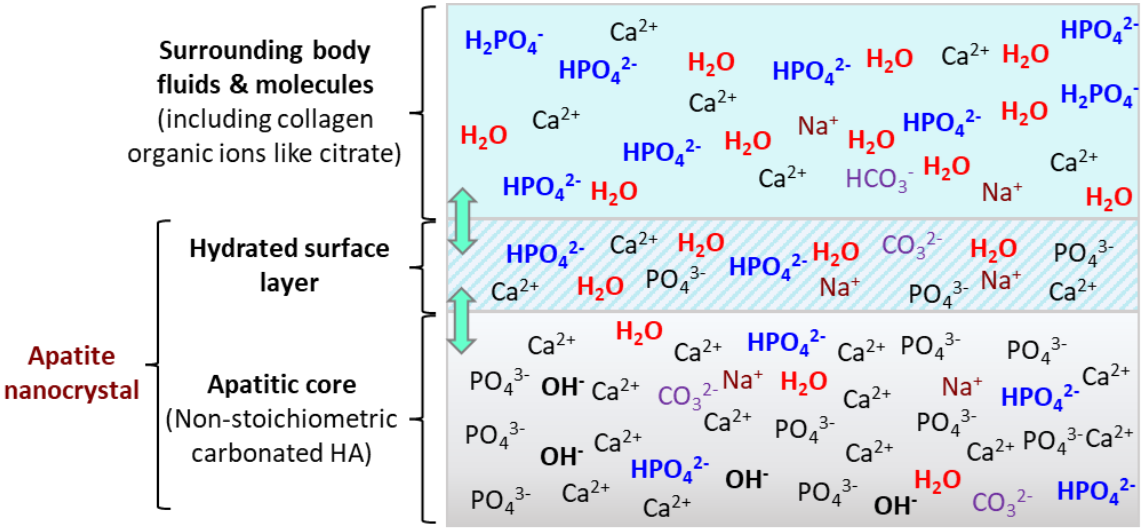


*Figure 1: Schematic representation of of the surface of an apatite nanocrystal in bone, showing the apatite core and hydrated surface layer, and including some of the main ions present in the different components. Adapted from Drouet* et al.[4]

## I.1. Quantification of core and surface signals in the mineral phase of bone

The use of $^{1}H$ – $^{31}P$ CP-HETCOR NMR for the study of bone mineral is three decades old, at the time of writing. To the best of my knowledge, the first study to effectively resolve the different proton environments of pristine bone mineral was published by Santos *et al.*[5] in 1994. Despite the low field strength (4.7 T) and low MAS rate (2.0-2.5 kHz), the team was able to obtain a decently resolved spectrum showing two resonances: a first peak around 0 ppm and a second wider one ranging from 3 ppm to 15 ppm in the $^{1}H$ dimension, both correlating with a signal centered at roughly 3 ppm on the $^{31}P$ dimension. The first signal was attributed to the $OH^-$ sites of the apatitic phase, and the second to $HPO_4^{2-}$ sites distributed in a disordered phase of bone mineral. For the first time, the two signals were no longer convoluted which raised a new question: is it possible to quantify the two sites to study the relative variation from one bone sample to the other?

While direct acquisition in $^{1}H$ NMR does not bring much information about the bone mineral due to the masking effect of the signal from the organic phase, $^{31}P$ NMR gives a signal exclusive to the mineral phase. However, since the linewidth of the $^{31}P$ Bloch Decay (BD) spectrum is caused by distributions of chemical shifts, no increase in field, MAS rate or $^{1}H$ decoupling field strength can narrow the peak beyond ≈ 2 ppm FWHM lineshape (see Miquel *et al.*, 1990).[6] As a matter of fact, BD MAS spectra of molar samples recorded at 16.4 T with high-power decoupling (not pictured) had a FWHM of 2.4 ppm. Therefore, it seems difficult for the core and surface sites to be resolved solely in the $^{31}P$ dimension, as further demonstrated below.

### I.1.1. Quantification from the deconvolution of $^{31}P$ spectra

As a first approximation, it is tempting to try to quantify the components of the $^{31}P$ BD spectrum of bone mineral, by performing a deconvolution of the signal. As seen before (Chapter I, section III.5), the two components corresponding to the core and surface signals of mineral platelets have different linewidths.[1,2,7] It seems sensible, then, to attempt to deconvolute the BD signal as the sum of two (or more) components, which would allow them to be quantified. For this, the two (or more) environments have to be precisely characterized in terms of $^{31}P$ position, peak width and lineshape of each of the contributions. Some studies relied on $T_1$ measurements to differentiate both components,[1] while others used comparisons of BD and CP spectra, assuming these methods favour the core and the surface,[7] respectively (Figure 2).

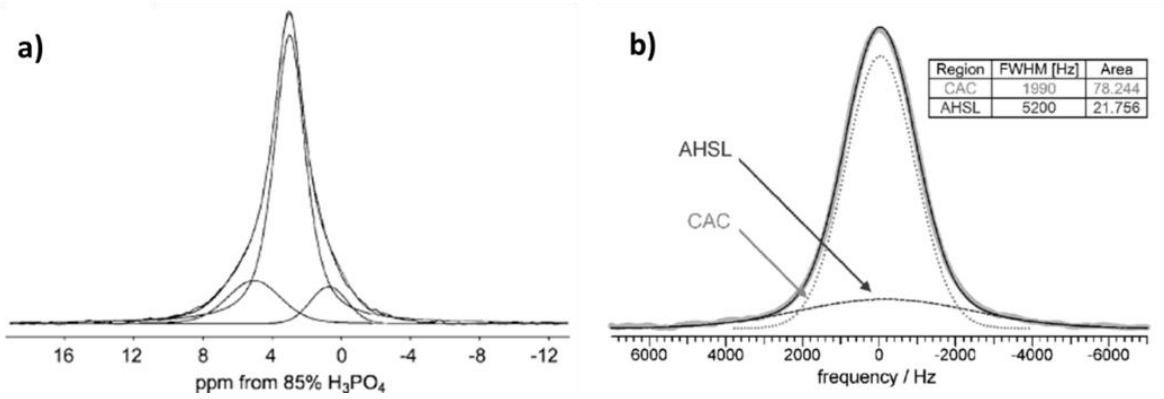


*Figure 2: Two decompositions of the $^{31}P$ MAS NMR spectra of biological apatites reported in the literature: a) human enamel BD spectrum ($B_0$ = 9.4 T, $\omega_r$ = 7.5 kHz),[7] b) human trabecular bone BD spectrum ($B_0$ = 4.7 T, static).[1] AHSL = amorphous hydrated surface layer, CAC = crystalline apatite core.*

Another possibility is to extract the different components peak widths from slices of a $^{1}H$ – $^{31}P$ CP-HETCOR spectrum. This has been reported in a 2019 analysis of bone mineral composition by Von Euw *et al.*[8] (Figure 3). In this contribution, a $^{31}P$ BD spectrum of bone is quantified using two component resonances, with the first assigned to apatitic $PO_4^{3-}$ sites and the second to non-apatitic $HPO_4^{2-}$ sites. The NMR parameters for those two components were determined from integrations of different regions of a CP-HETCOR spectrum. For this, the authors assumed that the apatitic core is represented by the low chemical shift correlation assigned to $OH^- \cdots PO_4^{3-}$ polarization transfers ($\delta_{iso}(^1H)$ between -2 to 2 ppm) and that the non-apatitic $HPO_4^{2-}$ sites correspond to the higher-frequency cross-peak ($\delta_{iso}(^1H)$ between 3 to 7 ppm).

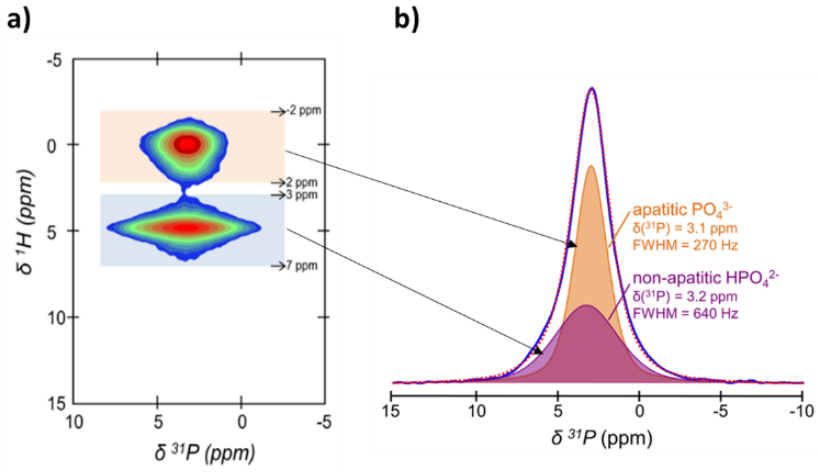


*Figure 3: a) CP-HETCOR spectrum of sheep bone, recorded by Von Euw* et al.,[8] *at $t_{cp}$ = 1.0 ms. b) Quantification of the apatitic $PO_4^{3-}$ and non-apatitic $HPO_4^{2-}$ sites from a BD spectrum of the same sample. The linewidth and position of the two peaks correspond to integrations over F1 of the CP-HETCOR spectrum in the range $\delta_{iso}(^1H)$ = [-2,2] ppm and [3,7] ppm respectively. $B_0$ = 7.04 T, $\nu_r$ = 14 kHz.*

However, we noticed that acquiring a CP-HETCOR spectrum at two different contact times on the same bone sample exhibited peaks of varying linewidths (Figure 4). This would imply that environments with different CP dynamics and different chemical shift distributions are overlapping at similar $^{31}$P chemical shifts. From this, we deduced that the description of the CP-HETCOR spectrum as being the result of two $^{31}$P distinct environments is oversimplified (see section V.4 for more details). Therefore, we cannot reliably decompose the $^{31}$P BD resonance simply through a sum of peaks extracted from the slices of a single contact time CP-HETCOR spectrum.

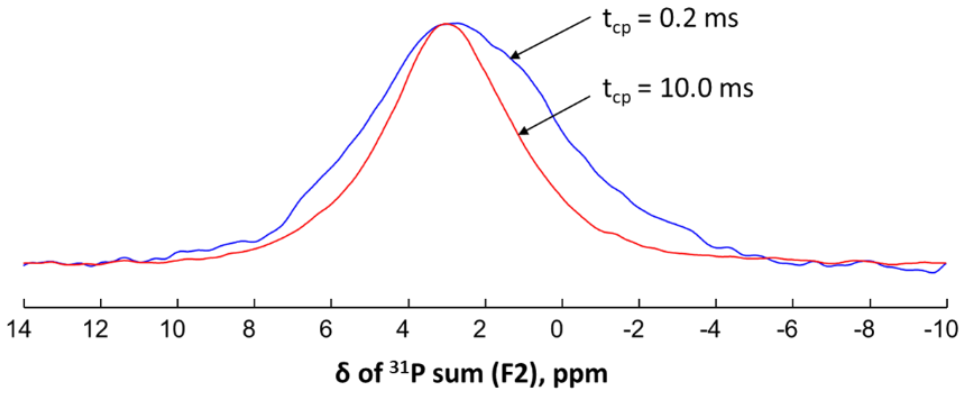


*Figure 4: $^{31}$P F2 sum of the surface signals (2.5 to 20.0 ppm) of the $^{1}$H-$^{31}$P CP-HETCOR spectra of a mouse bone sample at two different contact times, $t_{CP}$ = 0.2 ms and 10.0 ms. Note the differing linewidths for the two contact times. The intensities are normalized to match the maxima. $B_0$ = 7.04 T, $\nu_r$ = 14 kHz, ns = 16, RD = 2 s.*

### I.1.2. Quantification from deconvolution of $^{1}$H indirect dimension of CP HETCOR

Another method to quantify the core and surface components of bone mineral reported in various publications[2,9,10] is to study the indirectly reconstructed $^{1}$H spectrum of $^{1}$H – $^{31}$P CP-HETCOR experiment, usually obtained by summing the intensity of the points for a given row of the spectrum. The reconstructed $^{1}$H spectrum can then be decomposed into different core and surface resonances, which are quantified either by deconvolution (Figure 5) or simply by integrating the different regions. The advantage of this method is its simplicity: one must only record CP-HETCOR experiments and process the indirect dimension as if it was from a direct acquisition. This not only gives a relative quantification of the two environments *via* the $^{1}$H dimension, but also information about the CP dynamics for each.

However, the method also has its limitations. First, it requires a series of acquisitions at different contact times, since the observed magnetization is dependent on CP dynamics, which could vary from one sample to the next (and needs to be measured to compensate for its effects. Moreover, too mobile $^{1}$H species may be “invisible” due to inefficient polarization transfer to $^{31}$P nuclei. It

also relies on the assumption that the apatitic core of bone has no other $^{1}H$ resonance than its characteristic 0 ppm $OH^-$ signal. This is contradicted by in-depth studies of this $^{1}H$ signal.[11] Next, treating a 2D data set by simplifying it down to a single dimension causes a loss of information: we completely lose the additional data carried by the $^{31}P$ dimension ($^{31}P$ $\delta_{iso}$ and FWHM). Lastly, summing over an interval will either introduce noise from outside the signal or cut off the edges of the signal, losing information in either scenario. The resulting 1D spectrum will therefore always have added noise or lowered signal when compared to the initial 2D correlation map.

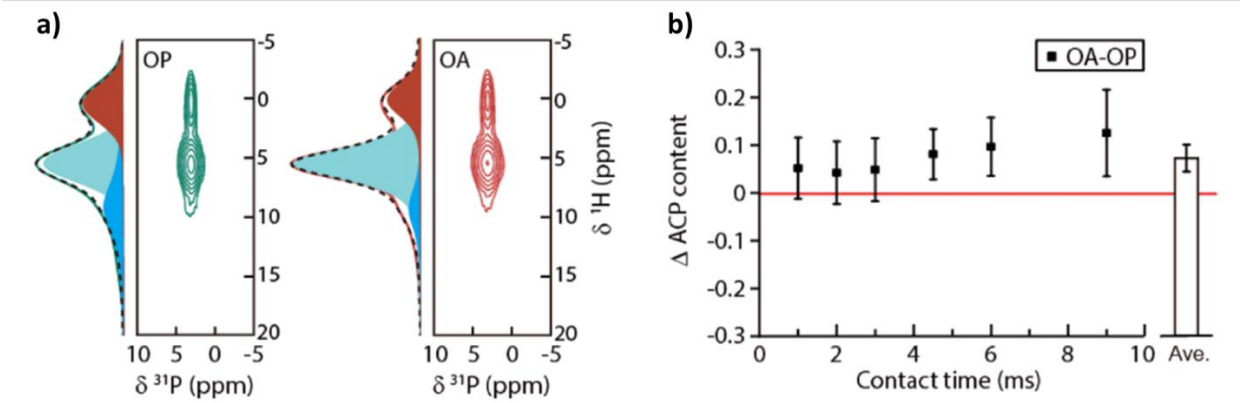


*Figure 5: Comparison of osteoporotic (OP) and osteoarthritic (OA) bones via the $^{1}H$ dimension of a $^{1}H$-$^{31}P$ CP-HETCOR spectrum by Zeng* et al.[2] *a) CP-HETCOR spectrum and decomposition along the $^{1}H$ dimension. b) Quantification based on the relative signal intensity of "ACP" (surface) and "HA" (core) environments.*

As a result, it is theoretically preferable to analyze the different regions directly from the 2D NMR spectrum (rather than use the projections). This is not a new approach, as it is often used in the field of metabolomics for the quantification of metabolites in extremely convoluted spectra.[12,13] In solids, bone mineral stands out as being a standalone case, where the presence of two extremely sensitive nuclei allows for the relatively fast acquisition of 2D spectra, but where the nucleus with a relatively more resolved spectrum ($^{1}H$) is impossible to study solely through direct acquisition (due to the presence of overlapping collagen resonances), while the other nucleus ($^{31}P$) lacks the resolution for a quantification through direct acquisition. The quantification should therefore be done based on a series of CP-HETCOR analyses, and, due to the limitations of 1D decomposition, should preferably be done directly on the 2D signal.

### I.2. From CP to quantitative analysis: the theory of cross-polarization dynamics

Before we discuss the quantification of CP-HETCOR spectra, the theory that links the signal intensity in a CP spectrum to the initial magnetization of the system needs to be recalled. Thankfully, since CP is one of the most common sequences in solid state NMR, the dynamics of

the spin-transfer are well documented. Kolodziejski *et al.*[14] have published a handy guide detailing the different models of cross-polarization dynamics, on which we will base our analysis.

### I.2.1. Cross-Polarization and Hartmann-Hahn matching condition

At the core of these measurements is the cross-polarization (CP) sequence. As previously reported (Chapter I, section IV.1.3), CP is a double-resonance experiment that relies on the continuous irradiation of two nuclei at matching radiofrequency fields,[15] allowing the polarization transfer from an abundant spin system (I) to a dilute spin system (S). The Hartmann-Hahn (HH) matching condition sets a relationship between the radiofrequencies of the two nuclei that must be satisfied for an optimal magnetization transfer: $\gamma_I B_{1I} = \gamma_S B_{1S}$, equivalent to $\omega_{1I} = \omega_{1S}$ ($\omega_{1I}$ and $\omega_{1S}$ corresponding to I and S irradiation frequencies, respectively).

In MAS, the dipolar coupling responsible for the polarization transfer becomes time-dependent. In practice, the polarization transfer still occurs.[16] Multiple possible matching conditions then arise under magic angle spinning conditions (Figure 6): $\gamma_I B_{1I} = \gamma_S B_{1S} \pm n\omega_r$ with n an integer and $\omega_r = 2\pi\nu_r$ with $\nu_r$ the rotation frequency of the sample.

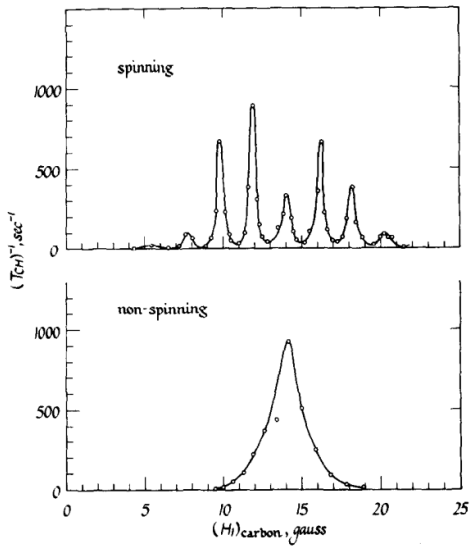


*Figure 6: Comparison of the rate of transfer of polarization in adamantane as a function of the $^{13}C$ RF field, from Stejskal* et al.*[16]*

These matching conditions are typically referred to by the value of n (usually n = -1, 0 or 1). Another common variation to the CP sequence is the addition of a variable-power ramp on the $^1H$ spin-lock power.[17] The ramp effectively sweeps through a range of radiofrequency fields on I, while the S spin-lock remains constant. This lowers the optimum efficiency of the CP slightly, and in return makes small deviations from the matching condition less impactful. In practice, because of field and radiofrequency inhomogeneity, ramped-CP has a similar or higher efficiency to square-CP, especially for off-resonance peaks.

There are therefore multiple possible matching conditions for a given radiofrequency field. The choice of matching condition has an important impact on polarization transfer dynamics. Detailing the origins of these varying efficiencies is beyond the scope of this study. We however examined the practical impact of different matching conditions on the CP dynamics of a synthetic sample (See section III.2.2).

### I.2.2. The I-S model

A CP experiment is not directly quantitative due to the varying rates of polarization transfer and relaxation between local environments in the structure. Yet, the intensity can be linked back to the initial magnetization using a theoretical model. The simplest model for CP dynamics, called the I-S model,[18] (Figure 7 and Figure 8) is the following: the polarization transfer is carried between $^{1}$H (I spin), which has a higher equilibrium magnetization, to $^{31}$P (S spin), which has a lower equilibrium magnetization. These different spin populations can be understood in terms of spin-temperature.[19] For a nucleus with a spin ½, the inverse spin temperature is given by the relationship[20] $\beta = (k_B T_s)^{-1}$ with $k_B$ the Boltzmann constant and $T_s$ the temperature of the system.

Each element of the system can be considered as its own reservoir of finite volume with a given initial temperature. At the start of the experiment, the $^{1}$H has a high inverse spin-temperature, whereas the $^{31}$P has a low inverse spin-temperature (because of the difference in gyromagnetic ratio). They are surrounded by a "spin lattice", which is described as a very-high inverse spin-temperature thermostat for the system.

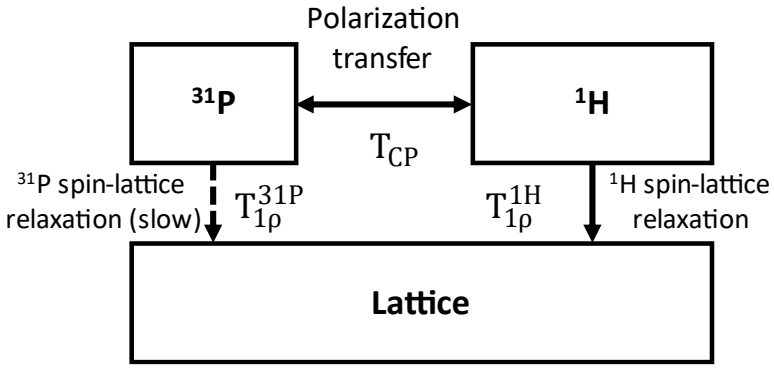


*Figure 7: Diagram showing the I-S model applied in this study. Adapted from Kolodziejski* et al.*[14]*

Once the cross-polarization sequence starts, the different reservoirs are put into contact, which equalizes the temperatures across the system and gradually cools them to the spin-temperature of the lattice. The rate of transfer from $^{1}$H to $^{31}$P is dictated by a CP rate constant $T_{cp}$, which is linked to the strength of the dipolar coupling between the two nuclei and local dynamics. Their interaction with the spin-lattice induces a progressive loss of magnetization with a relaxation time constant noted $T_{1\rho}^{1H}$ or $T_{1\rho}^{31P}$. The two inverse spin temperatures $\beta_{1H}$ and $\beta_{31P}$ are therefore subject to the differential equations:

$$\frac{d\beta_{1H}}{dt} = -\frac{\beta_{1H}-\beta_{31P}}{T_{CP}} - \frac{\beta_{1H}}{T_{1\rho}^{1H}} \qquad (1)$$

$$\frac{d\beta_{31P}}{dt} = -\frac{N_{1H}}{N_{31P}}\frac{\beta_{31P}-\beta_{1H}}{T_{CP}} - \frac{\beta_{1H}}{T_{1\rho}^{31P}} \qquad (2)$$

with $N_{31P}$ / $N_{1H}$ the relative spin populations involved in the transfer. The solution to these equations is complex, but can be simplified by the following assumptions: first, we can presuppose that the initial polarization of $^{1}$H is much greater than that of $^{31}$P, both because of the difference in gyromagnetic ratio but also the difference in their longitudinal relaxation $T_1$. By using a recovery delay much lower than the $T_1$ of the $^{31}$P isotope, $^{31}$P presaturation pulses and dummy scans, we ensure that the $^{31}$P magnetization has had minimal time to recover before the polarization transfer.

By making this assumption, the solution is reduced to:

$$I(t_{cp}) = I_0\left(1 + \frac{T_{CP}}{T_{1\rho}^{31P}} - \frac{T_{CP}}{T_{1\rho}^{1H}}\right)^{-1}\left[e^{-\frac{t_{cp}}{T_{1\rho}^{1H}}} - e^{-\left(\frac{t_{cp}}{T_{CP}}+\frac{t_{cp}}{T_{1\rho}^{31P}}\right)}\right] \qquad (3)$$

If $\frac{T_{CP}}{T_{1\rho}^{31P}} \approx 0$ (i.e. assuming that the weaker coupling of the $^{31}$P isotope to the spin-lattice makes it less susceptible to spin-lattice relaxation), we reduce the number of constants in the equation to three, which greatly simplifies the numerical analysis:

$$I(t_{cp}) = I_0\left(1 - \frac{T_{CP}}{T_{1\rho}^{1H}}\right)^{-1}\left[e^{-\frac{t_{cp}}{T_{1\rho}^{1H}}} - e^{-\frac{t_{cp}}{T_{CP}}}\right] \qquad (4)$$

meaning that the intensity of the cross-polarized signal is expected to depend solely on the two time-constants $T_{CP}$ and $T_{1\rho}^{1H}$, and on the intensity $I_0$, which is proportional to the equilibrium magnetization of the $^{31}$P nucleus. Therefore, knowing the value of $I_0$ directly gives us access to the quantification of the phosphorus nuclei of a given type in our sample, theoretically allowing us to extract quantitative information from a series of CP experiments. Note that this also relies on the assumption that $T_{CP}$ is shorter than $T_{1\rho}^{1H}$. In case of doubt, independent measurements of the two time-constants can be carried out using specialized sequences such as TORQUE.[21]

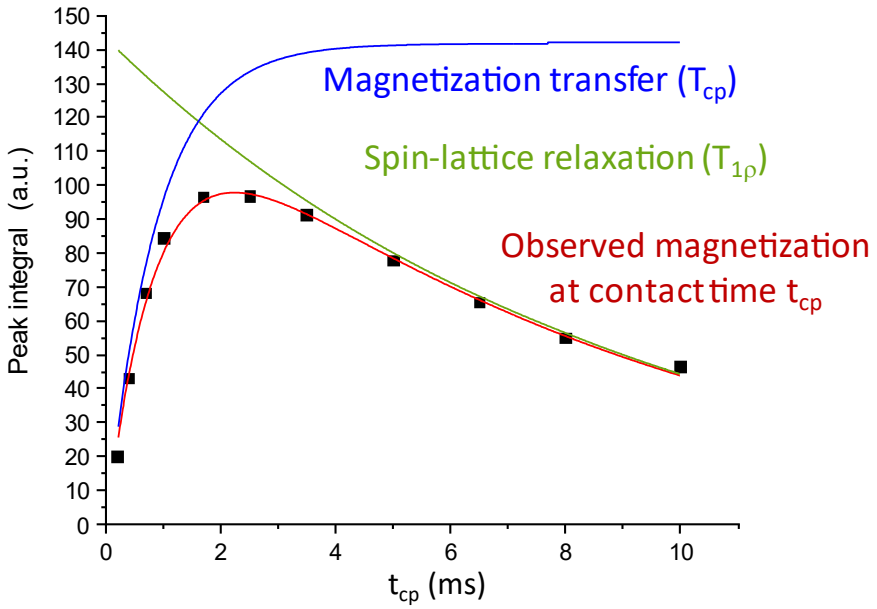


*Figure 8: Illustration of the signal intensity over the $t_{cp}$ of a variable contact-time CP experiment, as described by Eq. 4 (I-S model). The experimental data is taken from measurements of the intensity of a $H_2O \cdots (H)PO_4^{(2)3-}$ peak in a series of CP-HETCOR measurements of mouse bone (more details are given in section I.3.1).*

### I.2.3. Application to a model sample

In order to evaluate this model in the frame of calcium phosphates, we decided to first and foremost test the quantification of the different $^{31}P$ signals in OCP, i.e. the phase which we extensively studied in the previous chapter. The BD and CP spectra can be decomposed into five resonances (which correspond to six sites, with two overlapping at -0.4 ppm, as discussed in the previous chapter) (Figure 9). Fitting the lineshape of the experimental spectrum using DMfit[22] gives us an integral for each of the resonances.[23] The BD quantification is quite similar to what is expected based on the crystal structure, with a moderate error caused by the possible partial hydrolysis of the sample with time (creating an HAp impurity signal around 3 ppm). Note that in the previous chapter, this integration had been done on a newly synthesized sample and at a higher field, leading to values closer to the theoretically expected values, but CP dynamics at ambient temperature discussed in this section were not recorded on this sample.

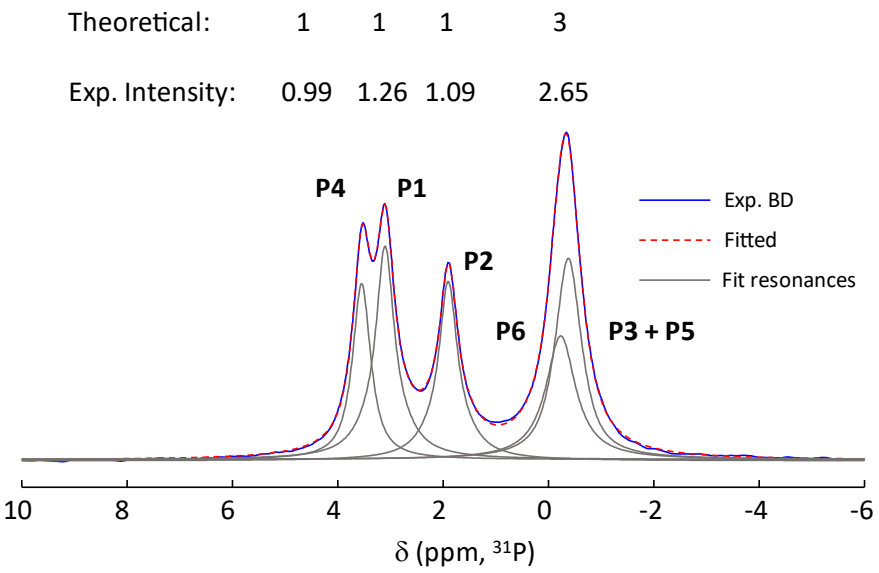


*Figure 9: $^{31}$P MAS Bloch Decay NMR spectrum of OCP ($B_0$ = 7.04 T, $\nu_r$ = 14 kHz) and its fitted resonances. A peak at 3 ppm, due to the presence of an HAp impurity, is superimposed with P1. The integration of the rotational bands was neglected as their intensity is below 1% that of the central signals.*

We expected to obtain the same set of $I_0$ values when applying the above method to a $^{1}$H – $^{31}$P variable contact time CP study of OCP. For this purpose, we have acquired six 1D CP experiments at increasing contact times: 0.2, 0.4, 0.8, 1.6, 3.2 and 6.4 ms (Figure 10). These spectra were acquired using an optimized CP sequence with an n = -1 HH condition and a 90.100 ramp.

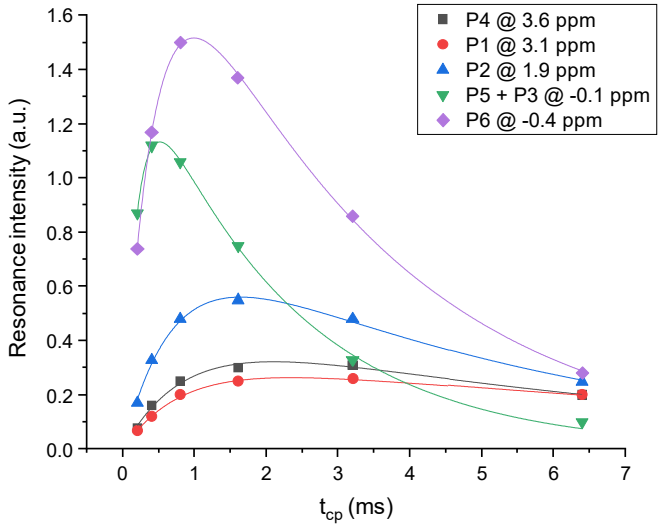


*Figure 10: 1D integrated intensities of the $^{31}$P resonances of OCP (Figure 9) in a variable contact time CPMAS experiment, depending on the contact time $t_{cp}$. The curves correspond to a fit based on Eq. 4, with the constants $I_0$, $T_{cp}$ and $T_{1\rho}^{1H}$ optimized to match experimental data.*

For each spectrum, we then had to adjust the intensities of the fit in DMfit, and plot the values as a function of the contact time used for the acquisition. This plot could then be fitted with OriginPro 2018 using the simplified expression seen above (Eq. 4, Table 1).

| **Resonance** | **P4** | **P1** | **P2** | **P3 + P5** | **P6** |
|---|---|---|---|---|---|
| **Expected intensity** | 1 | 1 | 1 | 2 | 1 |
| **$I_0$ (a.u.)** | 0.51 ± 0.05 | 0.38 ± 0.01 | 0.92 ± 0.05 | 1.71 ± 0.04 | 2.49 ± 0.04 |
| **$T_{CP}$ (ms)** | 0.87 ± 0.12 | 0.82 ± 0.05 | 0.72 ± 0.06 | 0.20 ± 0.01 | 0.44 ± 0.01 |
| **$T_{1\rho}^{1H}$ (ms)** | 7.3 ± 1.4 | 11.5 ± 1.3 | 5.0 ± 0.5 | 2.09 ± 0.01 | 2.99 ± 0.08 |
| **$R^2$ (COD)** | 0.989 | 0.998 | 0.994 | 0.999 | 0.999 |

*Table 1: CP dynamics parameters calculated from the variable contact time experiment, using Eq. 4 to model the expected intensity of the signals* (*Figure 10*)*. The error intervals correspond to the uncertainty during fitting, and do not take into account experimental errors.*

The evolution of the intensities over the contact time was in accordance with our expression, with an $R^2$ above 0.98 for all peaks. We could have expected to see a good agreement between the theoretically derived intensities from our experimental parameters, and those of the known OCP crystal structure. Rather, although the intensity over the contact time follows a bi-exponential curve, the $I_0$ value of the model does not correspond to the expected intensity of the different peaks. The $I_0$ of the low-frequency peaks is severely overestimated, whereas the high-frequency ones are underestimated. The large variations in $T_{1\rho}^{1H}$ are characteristic of a system with limited spin-diffusion, which is contrary to the hypotheses of the I-S model.

The use of alternate CP models, like the I-I*-S model, were attempted. This model describes the case where the magnetization of a distant spin-reservoir (for example, the protons of the hydrated interlayer) is transferred to the dilute spin S through a nearby proton I*.[14] The rate of the transfer between I and I* is limited by a spin-diffusion rate $T_d$. However, the application of this model significantly worsened the quality of the fit, while giving values of $I_0$ similar to those found through the application of the I-S model. This is unsurprising, given the small number of experiments (6), which is also be a limiting factor in CP-HETCOR 2D decompositions. We will come back to the application of this second model when observing biological samples.

At this stage, it therefore seems that the I-S model remains both the simplest model and that with the best predictive power for OCP, despite the discrepancies between $I_0$ and the expected spin-count $M_0$. OCP is not the only material to have encountered this issue. Studies in cements,[24] among others, have encountered similar difficulties when trying to match experimental and theoretical quantifications. We can try to understand the source of these issues by looking at the environment of the sites in the OCP crystal cell (Figure 11).

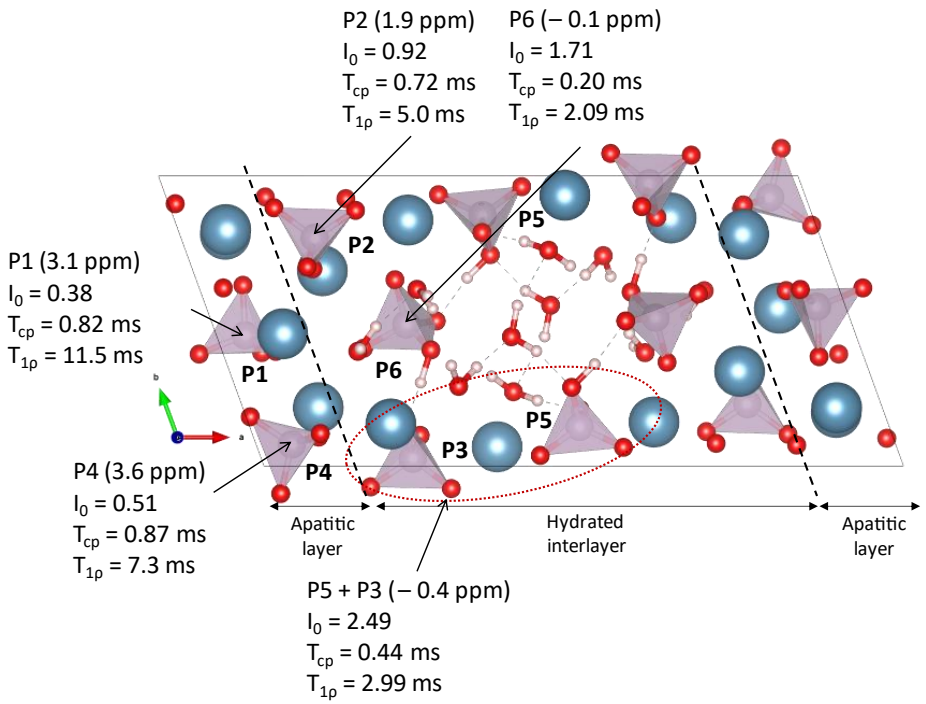


*Figure 11: Crystallographic structure of OCP, showing the six peaks assigned to their respective site according to the literature,[23] with their respective CP time constants and $I_0$ values, as extracted from the I-S model (Table 1).*

We see that the structure presents a variety of sites which are problematic in the two previously mentioned CP models. The sites P1, P4 and P2 are distant from the majority of the protons (located in the hydrated interlayer) and predominantly get their magnetization from a single water molecule, which is itself quite distant from the interlayer. This goes against the characterization of the phosphorus atom as a "dilute spin", as it is more abundant in the crystalline layer than the protons. This is in opposition to the P3, P5 and P6 sites, which exhibit a P-OH for P5 and P6 and are moreover all close to large cluster of water molecules, likely to be communicating through homonuclear $^{1}H$-$^{1}H$ spin-diffusion. The difference between the two regions is quite visible, as the P4 and P1 sites further from the interlayer are severely undercounted by $I_0$, whereas the P3, P5 and P6 sites which are close to the interlayer are overcounted.

We also considered the structural information that we may be able to gather from the characteristic $T_{cp}$ and $T_{1\rho}$ parameters. Unfortunately, because of the presence of mobility in OCP (see previous chapter), the $T_{cp}$ values could not be directly correlated with the $^{1}H$-$^{31}P$ dipolar coupling. However, we can see that there is still a significant correlation between the values of $T_{cp}$ and $T_{1\rho}$, and the distance of the phosphorus site to its nearest proton (Figure 12). The latter values seem therefore useful to glean more information from a peak than can be achieved from a simple 1D spectrum.

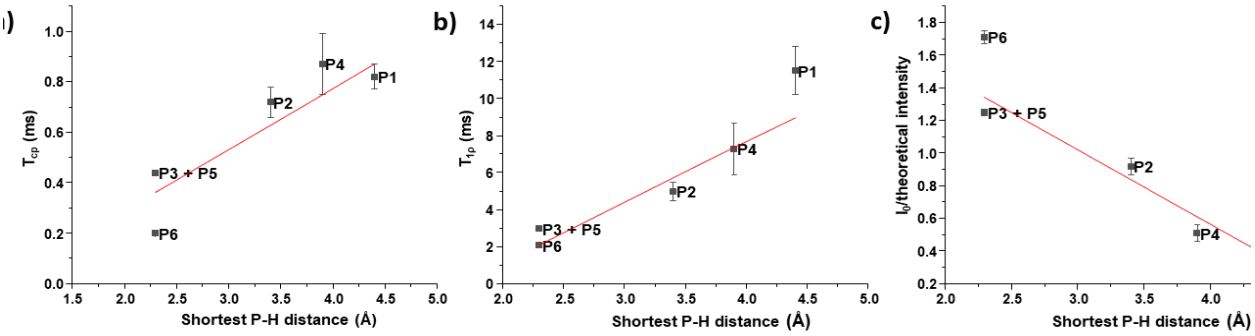


*Figure 12: Evolution of different parameters of the CP dynamics fit (Figure 7) over the shortest P-H distance for the five peaks of OCP observed in 1D $^{31}$P NMR. a) $T_{cp}$, b) $T_{1\rho}$, c) $I_0$ / theoretical intensity. The peaks P3 and P5 have similar P-H distances (2.2 vs 2.4 Å) and chemical shifts, and were considered indistinguishable for the purpose of these graphs (an averaged P-H distance of both sites was chosen). The red lines are not based on any predictive model and are meant to show broad trends in the data.*

In conclusion, while it is theoretically possible to quantify different sites *via* a variable $t_{CP}$ series of experiments, the method is not fully reliable and cannot give an accurate value for $I_0$ in some samples (possibly due to molecular dynamical effects or limited spin-diffusion). However, the values of $T_{cp}$ and $T_{1\rho}$ that are obtained from the analysis may be pertinent for the comparison of different sites. Despite the imperfection of the model, we will continue reporting the $I_0$, $T_{cp}$ and $T_{1\rho}$ values while making the assumption that they conserve the physical significance that they are usually given. This assumption is necessary, for example, when resolving overlapping sites based on their $T_{1\rho}$ measurements (see § VI.1.1.). We will therefore continue our analysis, keeping in mind the limitations of this method and the divergence from the theoretical model.

### I.3. Expansion to the analysis of 2D $^{1}$H-$^{31}$P CP-HETCOR spectra

As previously discussed, the 2D spectra obtained through $^{1}$H-$^{31}$P CP-HETCOR experiments are expected to contain much more information than the 1D spectra of bone mineral. However, reducing the spectra down to a single dimension, as is commonly done, removes the relevant data in the second dimension with no practical upside aside from simplicity. We would therefore want to decompose the 2D correlation maps directly for a more accurate estimation of their NMR parameters.

This can be done with commonly used NMR processing programs, such as DMfit[22] and ssNake.[25] However, these programs have characteristics that make them less suitable for our study. Firstly, to the best of my knowledge, neither program (in its directly downloadable version) allows for the fit parameters (peak position, peak width, etc.) to be bound within an interval. Without the ability to limit the range in which parameters are allowed to vary, we may end up with impossibly large or impossibly small fitted parameters. ssNake, for example, allows the Gaussian/Lorentzian ratio of pseudo-Voigt peaks to go below zero, giving rise to physically meaningless lineshapes.

This increases the risk of falling into a physically impossible local minimum during the fitting process (or of fitting the noise, baseline, etc.), which has to be manually reverted out in order to continue fitting. Another limitation is the type of algorithm used to solve the least-squares minimization problem. There are a variety of algorithms available to solve these non-linear minimization problems.[26] DMfit, as an example, uses a gradient-descent method, whereas ssNake gives the choice between two methods: the Powell and Nelder-Mead algorithms. From our tests, we noticed that some methods seem to find unsuitable local minima more often than others. Consequently, we chose the Trust Region Reflective algorithm rather than the Powell's dogleg method. Finding the optimal algorithm to fit multidimensional NMR spectra is outside the scope of this work. However, we note that despite the importance of lineshape fitting in solid state NMR, to the best of my knowledge, little published work has gone into finding the most reliable and user-friendly numerical methods to ensure the smooth decomposition of 2D spectra. Lastly, a practical consideration was the mixed use of Varian and Bruker NMR data in this study.

Because of these constraints and preferences, we chose to write a homemade script using the Python language. Python was chosen because the Nmrglue package[27] allows us to open data from Bruker and Varian systems with equal ease and transform it into multidimensional matrices that can be easily transformed, fitted and subsequently plotted with the popular NumPy,[28] Scipy[29] and MatplotLib[30] packages.

### I.3.1. Chemical environments in bone, fitting the $^1$H dimension

Before we begin decomposing the spectra, it is important to know how many different peaks we expect to observe in our spectrum. The $^1$H dimension of CP-HETCOR spectrum of bone (Figure 13) is clearly made up of two very distinct parts: a sharp peak with a $\delta_{iso}(^1H)$ at 0 ppm, and a broad peak (previously assigned to an amorphous component[2,8]) ranging from 3 to 16 ppm. The 0 ppm peak is sharp and resembles the $OH^-$ peak of crystalline apatite, and has therefore been assigned to correlation between the $OH^-$ sites of the crystalline core and their adjacent $PO_4^{3-}$. The broad signal is asymmetric in respect to the proton dimension: it has a maximum around 5.5 ppm (close to the chemical shift of weakly bound water), but also a large component at higher frequencies that can appear as a nearly resolved peak at low contact times. The peak centered at ~5.5 ppm has been shown to vary in intensity based on the hydration level of the bone,[31] but remains visible even after significant dessication.[32] The higher frequency component (centered at ~11 ppm) is commonly assigned to $HPO_4^{2-}$ sites in the disordered surface of bone mineral, as it is similar both in CP dynamics and $^1$H chemical shift to the $HPO_4^{2-}$ sites found in other calcium phosphates (DCPD, Monetite, OCP).[8] Consistently with the literature,[2,9] we can safely propose to decompose our $^1$H dimension into three broad components:

- a peak at 0 ppm originating from $OH^-$ sites in the apatitic core of the bone mineral. The corresponding correlation peak on the CP-HETCOR will be labelled $OH^- \cdots PO_4^{3-}$.

- a peak at ~5.5 ppm corresponding to a collection of variously-bound water molecules in the disordered surface shell. The related correlation peak on the CP-HETCOR will be labelled $H_2O \cdots (H)PO_4^{(2)3-}$ since both $HPO_4^{2-}$ and $PO_4^{3-}$ may be present.

- a broad peak at ~11 ppm originating from the protons of $HPO_4^{2-}$ sites, presumably arising mainly from the disordered shell at the surface of crystalline HAp platelets. This will be labelled $HPO_4^{2-}$.

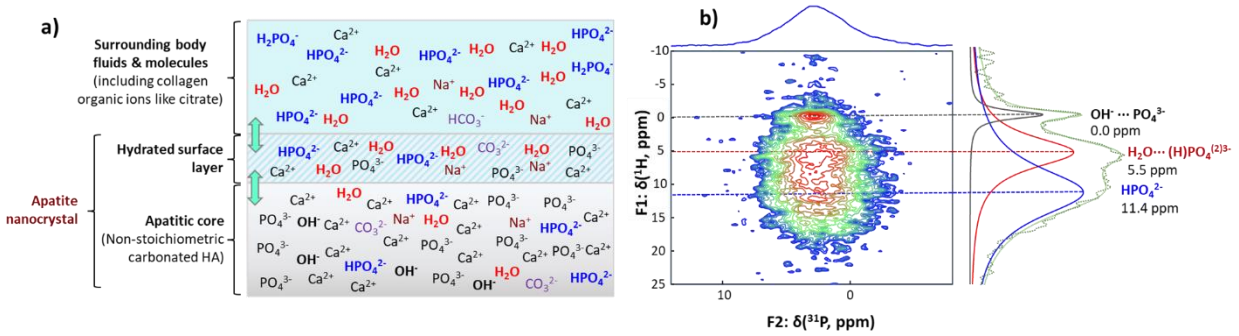


*Figure 13: a) Schematic representation of of the surface of an apatite nanocrystal in bone. b) Decomposition of the $^1H$ dimension of a CP-HETCOR spectrum of cortical femoral bone, recorded with $t_{cp}$ = 0.2 ms, considering three $^1H$ peaks, with their assignments ($OH^- \cdots PO_4^{3-}$ in black, $H_2O \cdots (H)PO_4^{(2)3-}$ in red and $HPO_4^{2-}$ in blue). $B_0$ = 7.04 T, $\nu_r$ = 14 kHz, ns = 16, RD = 2 s, td (F1) = 128, US (Uniform Sampling, Cf §III.1.1). $t_{exp}$ = 1h08*

Because of the relatively low magnetic field strength and rotation rate used in the majority of the work reported in this chapter ($B_0$ = 7.04 T, $\nu_r$ = 14 kHz), the surface sites are broadened by their $^1H$-$^1H$ dipolar coupling. As a result, some of the finer details of the $^1H$ dimension are lost when compared to a higher-resolution acquisition. This is visible when decomposing a CP-HETCOR experiment acquired at a higher field (14.1 T) and rotation rate ($\nu_r$ = 20 kHz) (Figure 14). This shows that bone mineral has a larger number of proton chemical environments than those described by our simplified model (Figure 1), as has been highlighted before.[8] Because the higher field strength magnets were in high demand in the labs where I performed my thesis, I conducted the majority of the study on the 7.04 T magnet of the LCMCP. The information yielded from higher field experiments will be discussed later on (See § IV), and we will see that information gathered at higher-fields can also be deduced from the 2D variable-$t_{cp}$ experiments at lower fields. Note that a possibility not explored in this study was the addition of Lee-Goldberg $^1H$ decoupling during the evolution time to increase F1 resolution, as it may alter the lineshape and quantifications.

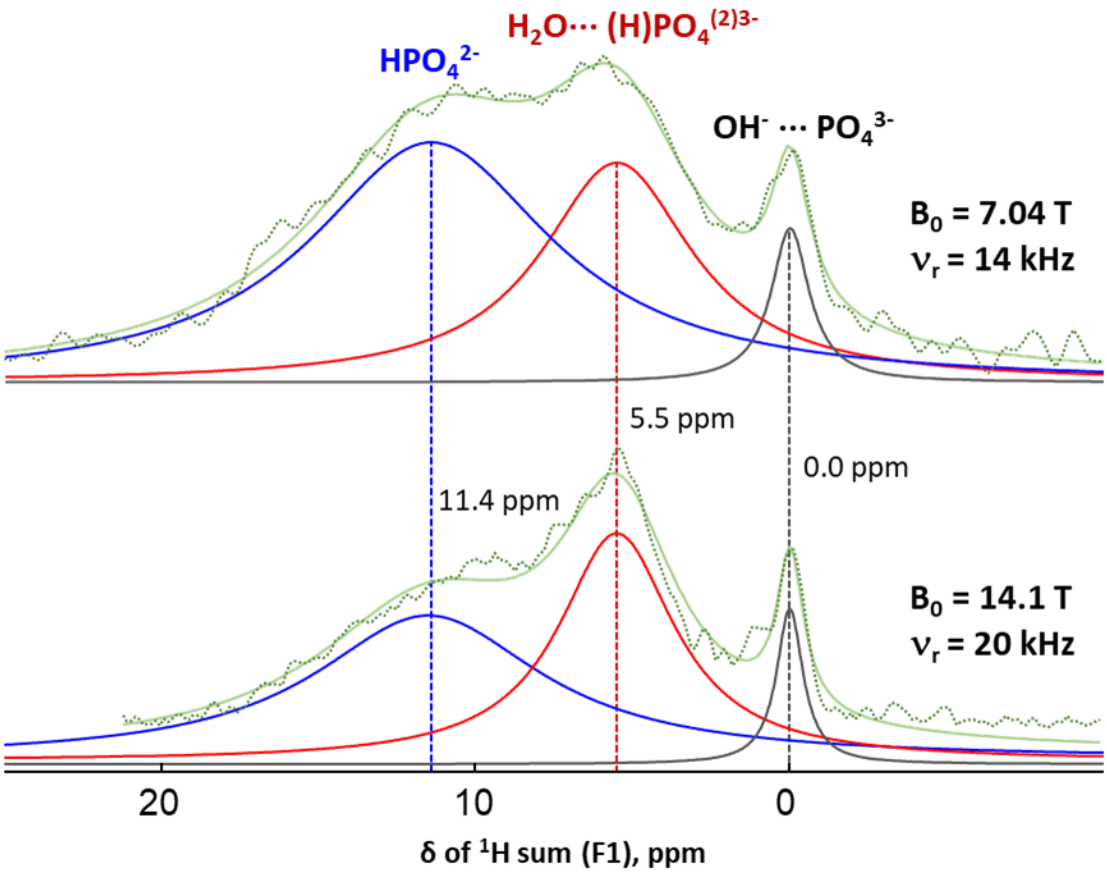


*Figure 14: Sum on the $^{1}H$ dimension of CP-HETCOR spectra of cortical femoral bone recorded with $t_{cp}$ = 0.2 ms, at two different magnetic fields. Note the differences between experimental and simulated lineshape are more visible at 14.1 T ($OH^{-} \cdots PO_4^{3-}$ in black, $H_2O \cdots (H)PO_4^{(2)3-}$ in red and $HPO_4^{2-}$ in blue). Top: $B_0$ = 7.04 T, $\nu_r$ = 14 kHz, ns = 16,* RD *= 2 s, td (F1) = 128, US, $t_{exp}$ = 1h. Bottom: 14.1 T, $\nu_r$ = 20 kHz, ns = 128,* RD *= 2 s, td (F1) = 84, US, $t_{exp}$ = 6 h.*

### I.3.2. Presentation of the homemade 2D fitting script and its operation

The purpose of the script is to be able to fit a series of CP-HETCOR spectra with a number of 2D peaks. Each peak is the product of two Pseudo-Voigt lineshapes, one in the direct dimension F2 ($^{31}P$ in our case) and another in the indirect dimension F1 ($^{1}H$ in our case). The script relies heavily on automation, running from input files described below.

#### *I.3.2.1 Input files*

Our usual 2D fitting procedure presented here relies on two Python scripts, called “2D fitting setup” and “2D fitting buildup”. For the sake of simplicity and ease of automation, the scripts have no graphical interface, and rely entirely on input and output files. Two files are required, which are shared between the two scripts: *readparam.txt* and *fitparam.txt*.

The *readparam.txt* file (Figure 15) contains information about the location and name of the CP-HETCOR experiments, as well as miscellaneous parameters (spectrum truncation, image export

format…). Aside from the location of the experiments and the name of the output file (fileloc and filename), we also need to point to a "setup" experiment which can be fitted in isolation to give an initial guess for the fitting routine, and the list of experiments recorded at different $t_{cp}$ (explist) alongside the contact times associated to each of these experiments (timelist). It also allows for the data to be sliced at the edges if the F2 spectral window is too large, in order to increase the efficiency of the fitting routine (truncystart and truncyend parameters). This works similarly to Topspin's STSR and STSI parameters, but uses values directly in ppm for ease of use. The Inkscapeloc parameter handles the integration of Inkscape within the fitting program, which serves to output visual representations of the fitting routines.

```
#file location (location of the folder containing the exp, with \\ at the end) :

fileloc =   C:\Users\Adam\Documents\NMR docs\Paris NMR\Paris NMR 2024.01.07 300 MHz\\

#file name (used for naming output files) :

filename    =   MOL1545pp_cpbuildup

#setup expno (expno for the peak fitting program) :

expno   =   300

#list of exp, ordered by increasing tcp :

explist =   [300,311,301,302,303,312,304,305,306,307,308,309,310]

#list tcp, in respective order :

timelist =  [0.2,0.3,0.4,0.7,1,1.3,1.7,2.5,3.5,5,6.5,8,10]

#truncx, truncy (removes data points from the edges of the 2D data) :

truncystart =   10
truncyend   =   -4

#Inkscapeloc (location of inscape.exe file, filename included) :

Inscapeloc  =   "C:\Program Files\Inkscape\bin\inkscape.exe"
```

*Figure 15: Example of readparam.txt input file.*

The other file, *fitparam.txt* (Table 2), contains the NMR parameters of the peaks, for the initial guess of the fitting routine. Each line beyond the first is a different peak with its own independent NMR parameters values. The program supports a theoretically unlimited number of peaks, although each additional peak will have an impact on the time-performance of the fitting algorithm. Each peak is characterized by an F2 $\delta_{iso}(^{31}P)$ and F1 $\delta_{iso}(^{1}H)$ (denoted Pos X and Pos Y, in ppm), an integral (amp, in a.u.), two peak widths (FWHM X and Y, in ppm) and two Gaussian/Lorentzian ratios (gl X and Y). Each of these values have an attached column (*) that dictates whether it is treated as a constant (* = 0) or a variable (* ≠ 0) during the fitting routine. The variables for the $\delta_{iso}$ and FWHM (Full Width at Half Maximum) also allow the values to be restricted to an inclusive interval (columns min and max). The program will return an error if the values for $\delta_{iso}$ and FWHM are outside the given interval (e.g. "X2 is impossible").

| Peak | Pos(X) | | | Pos(Y) | | | Amp | FWHM(X) | | | FWHM(Y) | | | gl(X) | gl(Y) |
|---|---|---|---|---|---|---|---|---|---|---|---|---|---|---|---|
| n | min | δ $^{31}$P (ppm) | max | min | δ $^{1}$H (ppm) | max | | min | FWHM $^{31}$P (ppm) | max | Min | FWHM $^{1}$H (ppm) | max | | |
| 1 | 0.1 | 3.0* | 6.0 | -0.2 | 0.0* | 1.0 | 1.0* | 1.5 | 3.0* | 3.5 | 0.0 | 1.0* | 3.0 | 0.3 | 0.2 |
| 2 | 0.1 | 3.0* | 6.0 | 4.9 | 5.0* | 7.5 | 1.0* | 1.5 | 5.0* | 10.0 | 0.0 | 6.0* | 8.0 | 0.4 | 0.0 |
| 3 | 0.1 | 3.0* | 6.0 | 7.5 | 11.0* | 15.0 | 1.0* | 1.5 | 6.0* | 10.0 | 8.0 | 10.0* | 20.0 | 0.6 | 0.0 |

*Table 2: Initial fit parameters for the series 1, from the fitparam.txt file. Pos = $\delta_{iso}$ (ppm), FWHM = full width at half maximum (ppm), Amp = peak integral (a.u.), gl = Gaussian/Lorentzian ratio. X = F2 dimension ($^{31}$P), Y = F1 dimension ($^{1}$H). * denotes parameters which are varied during the fit. n enumerates the peaks.*

### *I.3.2.2 "2D Setup" routine and output files*

In the "2D fitting setup" routine, the script reads its data from the address *fileloc\expno\pdata\1*, with *fileloc* and *expno* read from *readparm.txt* (Figure 15). It then takes the fitting parameters and constants from *fitparam.txt* (Table 2) and calculates an initial simulated lineshape. The lineshape is a three-dimensional matrix, which is then plotted alongside the experimental data (Figure 16). This is displayed in a new pop-up window.

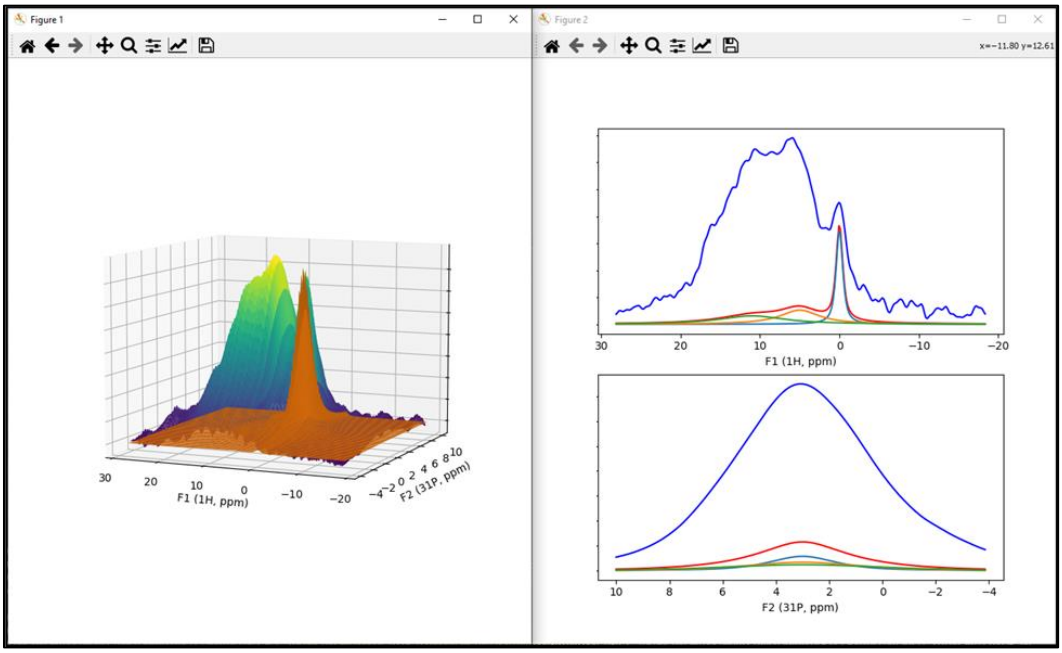


*Figure 16: First graphical display of the "2D fitting setup" script. The left window shows a 3D representation of the experimental data (blue-yellow) and the initial guess (orange). Right are projections (summed) of the data along the F1 (top) and F2 (bottom) dimensions (blue), together with the initial guess (red) and its individual components ($OH^- \cdots PO_4^{3-}$ in green, $H_2O \cdots (H)PO_4^{(2)3-}$ in orange, $HPO_4^{2-}$ in light blue) of the initial guess. The $^{1}$H-$^{31}$P CP-HETCOR spectrum being fitted is that of a healthy mouse molar, recorded with a 0.2 ms contact time ($B_0$ = 7.04 T, $\nu_r$ = 14 kHz, RD = 2 s, TD (F1) = 128, ns = 64).*

The program then starts fitting the variables to match the experimental data (using the Trust Region Reflective algorithm), after which a new display window opens with a plot of the new simulated lineshape (Figure 17). Once this window is closed, the files *fitparam.txt* and *setup_output.txt* are overwritten with new parameters (Figure 18). To avoid the multiplication of output files, it is not currently possible to revert the changes to *fitparam.txt*. It is therefore advised that the user open it with Notepad++, which allows for old files to be kept in memory after they have been overwritten.

The fitting process in the illustrations is that of a CP-HETCOR spectrum of a ground mouse molar. This example has a reduced spectral window in F2 (for illustrative purposes). The experimental data showcased contains 50k points of data. The fourteen variables are optimized within half a second to $R^2 > 0.98$. This runtime, however, grows exponentially with the number of variables.

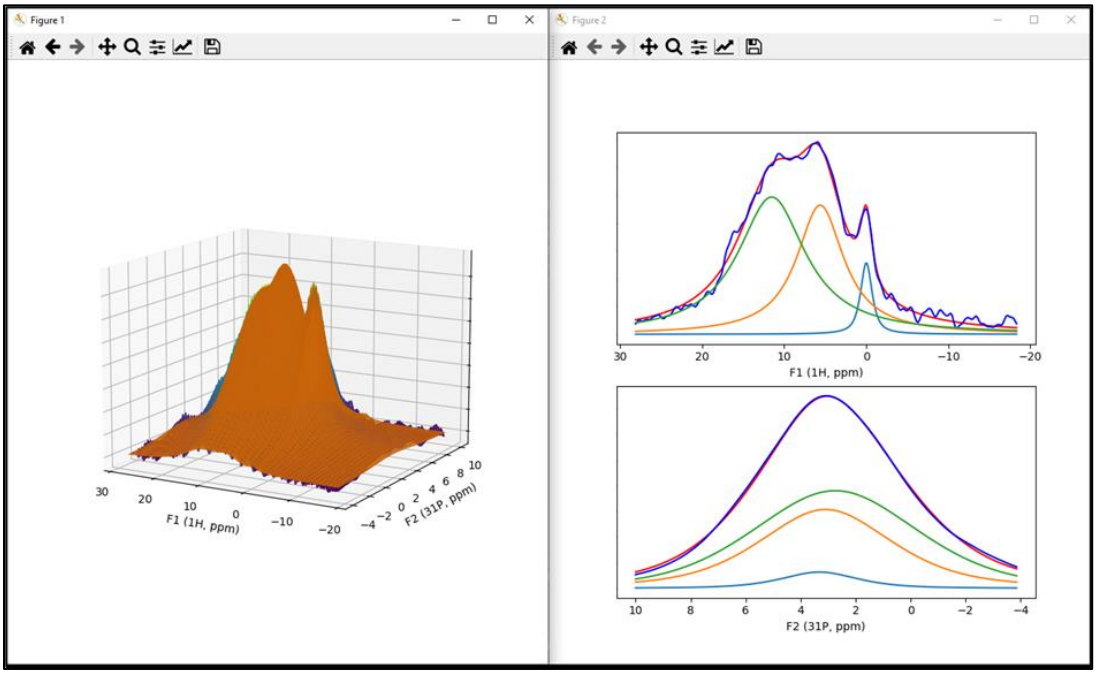


*Figure 17: Second display of the "2D fitting setup" script, showing the simulated lineshape after fitting (orange surface, red curve) proposed to match the experimental spectrum for Figure 16. Right are projections (summed) of the data along the F1 (top) and F2 (bottom) dimensions (blue), together with the initial guess (red) and its individual components ($OH^-$ ⋯ $PO_4^{3-}$ in green, $H_2O$ ⋯ $(H)PO_4^{(2)3-}$ in orange, $HPO_4^{2-}$ in light blue).*

*fitparam* before the fitting routine

| n | [min | Pos(X) | max] | * | [min | Pos(Y) | max] | * | Amp | * | [min | FWHM(X) | max] | * |
|---|---|---|---|---|---|---|---|---|---|---|---|---|---|---|
| 1 | 0.10 | 3.0 | 6.01 | 1 | -0.20 | 0.00 | 1.00 | 1 | 1.0 | 1 | 1.50 | 2.50 | 3.50 | 1 |
| 2 | 0.10 | 3.0 | 6.01 | 1 | 4.50 | 5.00 | 7.50 | 1 | 1.0 | 1 | 1.50 | 5.00 | 10.0 | 1 |
| 3 | 0.10 | 3.0 | 6.01 | 1 | 7.50 | 11.00 | 15.0 | 1 | 1.0 | 1 | 1.50 | 6.00 | 10.0 | 1 |

*fitparam* after the fitting routine

| n | [min | Pos(X) | max] | * | [min | Pos(Y) | max] | * | Amp | * | [min | FWHM(X) | max] | * |
|---|---|---|---|---|---|---|---|---|---|---|---|---|---|---|
| 1 | 0.10 | 3.2735 | 6.01 | 1 | -0.20 | 0.1031 | 1.00 | 1 | 21.09 | 1 | 1.50 | 2.2114 | 3.50 | 1 |
| 2 | 0.10 | 3.1406 | 6.01 | 1 | 4.50 | 5.9174 | 7.50 | 1 | 151.7 | 1 | 1.50 | 5.0463 | 10.0 | 1 |
| 3 | 0.10 | 2.7434 | 6.01 | 1 | 7.50 | 12.306 | 15.0 | 1 | 81.90 | 1 | 1.50 | 5.9182 | 10.0 | 1 |

Fit parameters and error bars reported in *setup_output.txt*

```
PosX1    3.0  ->      3.273   ± 0.001
PosY1    0.0  ->      0.103   ± 0.000
Amp1     1.0  ->      21.09   ± 0.033
StdevX1  2.5  ->      2.211   ± 0.002
StdevY1  1.5  ->      1.248   ± 0.001
PosX2    3.0  ->      3.140   ± 0.001
PosY2    5.0  ->      5.917   ± 0.003
Amp2     1.0  ->      151.7   ± 0.345
StdevX2  5.0  ->      5.046   ± 0.003
StdevY2  6.0  ->      6.820   ± 0.010
PosX3    3.0  ->      2.743   ± 0.003
PosY3    11.0 ->      12.30   ± 0.010
Amp3     1.0  ->      81.90   ± 0.339
StdevX3  6.0  ->      5.918   ± 0.008
StdevY3  9.5  ->      8.480   ± 0.023
R²   0.99182677
```

*Figure 18: Changes to fitparam.txt and new setup_output.txt output obtained after running the fitting routine.*

#### *I.3.2.3 Variable contact-time fitting routine: "2D fitting buildup" routine*

The second script, "2D fitting buildup", runs the exact same routine as the "setup" script, but on series of variable contact time experiments. The experiment numbers are given in the "explist" line of the *readparam.txt* file (Figure 15), and the contact times for each experiment are given in the "timelist" line. Here, we are fitting thirteen experiments with contact times ranging from 0.2 ms to 10 ms. Note that the experiments are scaled by their number of scans, allowing comparison between 2D experiments with different total numbers of scans. The fitting routine then individually calculates an optimized set of fit parameters for each experiment. The fits can then be visualized, either as 3D plots or projections of the simulated and experimental data (Figure 19). Similarly to the "setup" script, one may freely choose which parameters to set as variables. In the following discussion, three different sets of variables used to fit our example data are shown:

- Series 1: the position and width of the peaks in either dimension are set as variables.
- Series 2: only the amplitude varies the contact time over time.
- Series 3: the position and amplitudes of the peaks in both dimensions are variable, as well as the peaks' width in the F2 dimension. The peaks' width of $HPO_4^{2-}$ in the F1 dimension is fixed.

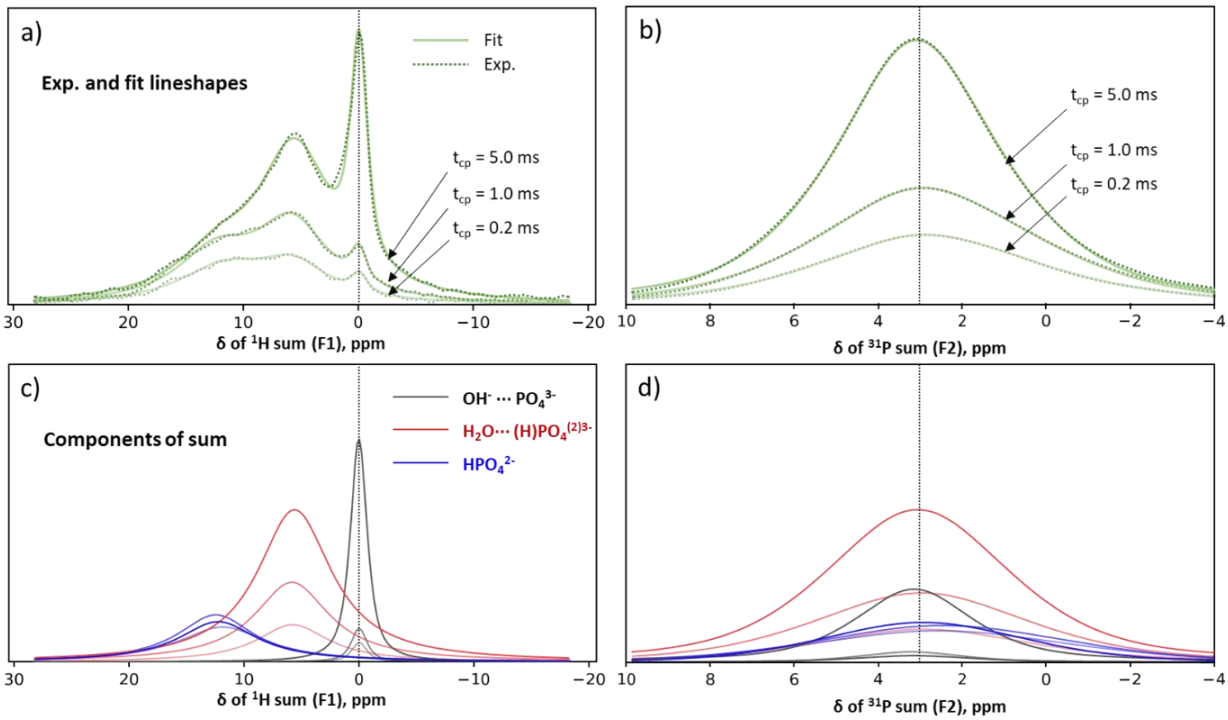


*Figure 19: a) Projections of the simulated and experimental spectra of a healthy mouse molar at three different contact times (0.2, 1.0 and 5.0 ms), summed along the F2 dimension. b) idem, summed along the F1 dimension. c) and d) Detail of the three components of the simulated spectrum, for each of the contact times ($OH^- \cdots PO_4^{3-}$ in black, $H_2O \cdots (H)PO_4^{(2)3-}$ in red and $HPO_4^{2-}$ in blue). Two vertical dotted lines are added as visual guides at 3.0 ppm ($^{31}$P) and 0.0 ppm ($^{1}$H).*

These files are automatically saved to the folder containing the experiments. A report is then given, summarizing the fitted values for each variable at each contact time, the estimated error intervals for each reported value and the overall $R^2$ value of the fit.

### I.3.3. Comparison with 1D fitting, impact of the method

We can evaluate the validity of our 2D fitting method by comparing it with a 1D fit of the same experiment using DMfit, using for example the 0.2 ms $t_{CP}$ CP-HETCOR spectrum of a healthy mouse molar (Figure 20). Here, the 1D sum of the F1 dimension is fitted using the same initial parameters we previously used for our 2D fit (Figure 16 to Figure 19). In both cases, all parameters aside from the g/l ratio of the peaks are set as variables. We observe that 2D fitting (Figure 20a) leads to very similar parameters to the fitting of the 1D sum (Figure 20b). The small differences are indicative of information contained on the F2 dimension that is only taken into account by fitting in 2D. As a side-note, it should be mentioned that doing a 1D fit of the F1 sum using our script yields the exact same values as those of DMfit. However, trying to fit the sum of the F2 dimension with 3 components directly in 1D gives some unrealistic $^{31}$P peak positions around 6 ppm as shown in Figure 20d. The lack of resolution of the $^{31}$P 1D spectrum obscures any information about the different chemical environments. In comparison, our method allows for the decomposition of the $^{31}$P dimension into three component peaks, with parameters for each

environment that are consistent with those observed directly on slices of the 2D spectrum. Interestingly for us, the slight differences in $^{31}P$ chemical shift between the three environments become immediately apparent.

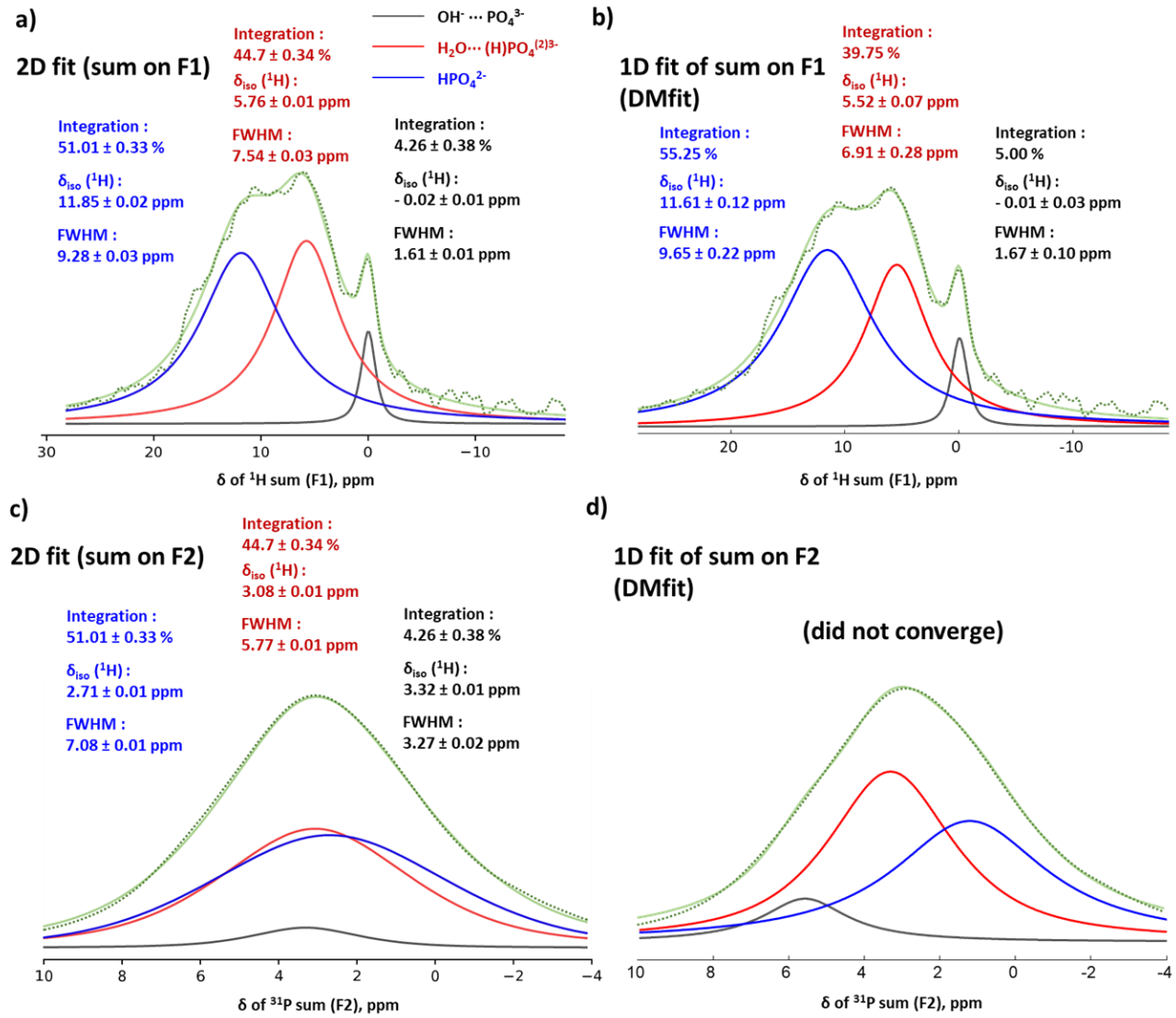


*Figure 20: Fit of the CP-HETCOR spectrum of a healthy mouse molar (recorded at $t_{CP}$ = 0.2 ms), using two different methods: a 2D fit of the data using our custom script (a,c), and a 1D fit of the projections in F1 and F2 using DMfit (b, d). In the first case (2D fit, left), only the result of the fitting process on the sum of the F1 and F2 projections is shown, for comparison purposes with the second case (1D fit, right).($OH^- \cdots PO_4^{3-}$ in black, $H_2O \cdots (H)PO_4^{(2)3-}$ in red and $HPO_4^{2-}$ in blue)*

### *I.3.3.1 Study of the CP dynamics of the different chemical environments*

Having developed tools for the fitting of the CP HETCOR data, the question that arises, then, is whether we are able to study the CP dynamics of a sample using this 2D fitting method. Using our 2D fit (Figure 20 a and c), we can plot the integral of each component over the contact time. We obtain a CP buildup curve, as shown in Figure 21.

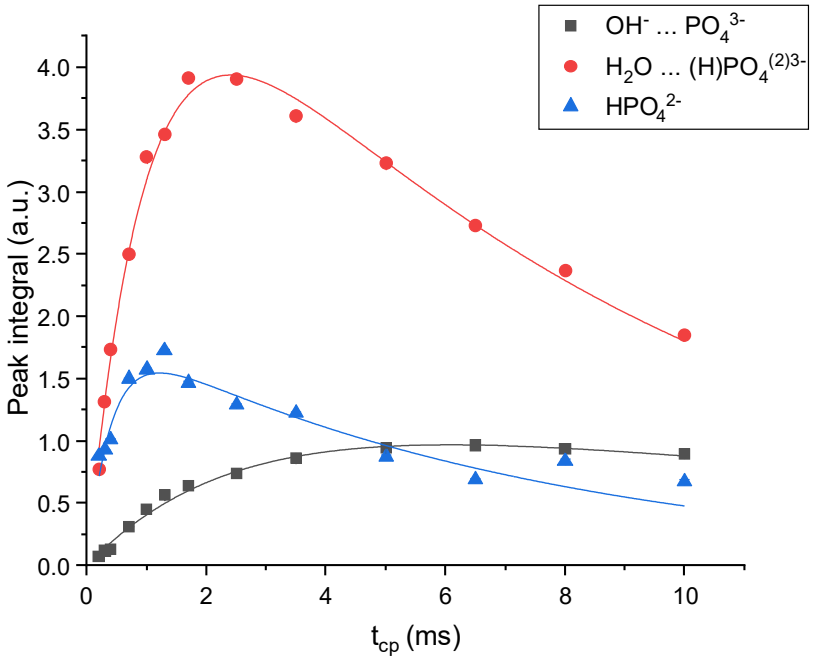


*Figure 21: Evolution of the integral of the three components of the CP-HETCOR spectra of a mouse molar (Figure 16 and Figure 22) over the contact time, obtained via the 2D fitting routine described above (Series 1). The error bars on the peak integrals are <1% of the value. Each data point represents a single CP-HETCOR experiment.*

The variation in the intensity over the contact time, as with the OCP example earlier, broadly follows a bi-exponential curve. We can therefore approximate its time-evolution with Eq. (4) (as it is the simplest model that adequately fits our experimental data). The values of the fitting parameters are given in Table 3.

| **Component** | **$OH^- \cdots PO_4^{3-}$** | **$H_2O \cdots (H)PO_4^{(2)3-}$** | **$HPO_4^{2-}$** |
|---|---|---|---|
| **$I_0$ (a.u.)** | 1.3 ± 0.3 | 5.3 ± 0.2 | 1.8 ± 0.1 |
| **$T_{CP}$ (ms)** | 2.6 ± 0.7 | 0.99 ± 0.07 | 0.39 ± 0.05 |
| **$T_{1\rho}^{1H}$ (ms)** | 19 ± 13 | 8.4 ± 0.9 | 7.1 ± 1.3 |
| **$R^2$** | 0.99 | 0.99 | 0.85 |

*Table 3: Fitted parameters of the evolution of CP-HETCOR peak integrals vs contact time (Figure 21) from the application of the I-S model (Eq. 4) to our example mouse molar.*

As expected, the sites with the shortest expected H-P distance (i.e. $HPO_4^{2-}$ ions) have a shorter $T_{cp}$, as their dipolar coupling which dictates the dynamics of the polarization transfer, increases with the inverse of the H-P distance. The more crystalline and less protonated environment of the $OH^-$ sites is also reflected by a longer $T_{1\rho}$ than the $H_2O$ and $HPO_4^{2-}$ sites. This shows the weaker interaction of the $OH^-$ site of the apatitic core with nearby $^{31}P$ spins. We also note that the latter fitted $T_{1\rho}$ has a much large error interval (19 ± 13 ms). This is due to the relaxation time-constant being longer than the $t_{cp}$ of the spectra recorded in this study. As the longest $t_{cp}$ is 10 ms for this

series, and the $T_{1\rho}$ is roughly 20 ms, the relaxation has a weak effect on the intensity of the $OH^-$ site. Therefore, the $T_{1\rho}$ of the $OH^-$ site cannot be measured with precision, unless we record experiments with much longer contact times, which is unreasonable with our current experimental setup. Indeed, high-power CP with contact times above 15 ms can damage standard NMR probes, especially when using a relatively short recycle delay of 2 s, and heteronuclear $^1H$ decoupling during the acquisition.

#### *I.3.3.2 Application of the I*-I-S model of spin-diffusion*

One oddity we observe in these data is the possible presence of weak intensity oscillations of the $HPO_4^{2-}$ correlation peak over the contact time (more distinctly visible in later experiments). This is in line with observations from previous 1D studies,[33] which have shown that the intensity of bone CP signal over contact time shows periodic oscillations that are characteristic of an I*-I-S model of polarization transfer. This model takes into account the limited rate of spin-diffusion between strongly coupled spins I (for example, the proton of an $HPO_4^{2-}$ site) and the magnetization reservoir I* (distant protons). This oscillation was observed in certain samples of our study, and may be visible here in the case of the $HPO_4^{2-}$ sites of the model (slightly higher intensity of $HPO_4^{2-}$ signal at $t_{CP}$ = 1.7 ms on Figure 21). In this case, the intensity can be approximated with the expression:

$$I(t_{cp}) = I_0\, e^{-\frac{t_{cp}}{T_{1\rho}^{1H}}}\left[1 - \frac{1}{2}e^{-\frac{t_{cp}}{T_d}} - \frac{1}{2}e^{-\frac{3t_{cp}}{2T_d}}\cos\left(\frac{bt}{2}\right)\right] \quad (5)$$

with $T_d$ the spin-diffusion time constant between I* and I, and b the dipolar coupling between I and S (in our case, the $^1H$ and $^{31}P$ sites involved in the direct cross-polarization). These oscillations are only visible in the case where the dipolar couplings are relatively uniform throughout the sample. If there is a large distribution of dipolar couplings, as may occur in biological samples, we instead observe a dampened buildup with an expression as follows:

$$I(t_{cp}) = I_0\, e^{-\frac{t_{cp}}{T_{1\rho}^{1H}}}\left[1 - \frac{1}{2}e^{-\frac{t_{cp}}{T_d}} - \frac{1}{2}e^{-\frac{3t_{cp}}{2T_d}}e^{-\frac{{t_{cp}}^2}{2{T_2}^2}}\right] \quad (6)$$

with $T_2$ the average of the inverse of *b* (the dipolar coupling between I and S).

Fitting the data from the example molar with Eq. 5 gives the parameters summarized in Table 4.

| Component | $OH^- \cdots PO_4^{3-}$ | $H_2O \cdots (H)PO_4^{(2)3-}$ | $HPO_4^{2-}$ |
|---|---|---|---|
| $I_0$ (a.u.) | 1.3 ± 0.4 | 5.4 ± 0.1 | 1.58 ± 0.06 |
| $T_d$ (ms) | 4 ± 1 | 1.60 ± 0.06 | 0.45 ± 0.07 |
| $T_{1\rho}^{1H}$ (ms) | 31 ± 32 | 10.3 ± 0.3 | 9.1 ± 0.7 |
| *b* (kHz) | 0.5 ± 0.7 | 2.0 ± 0.1 | 3.1 ± 4.4 |
| $R^2$ (COD) | 0.99 | 0.99 | 0.97 |

*Table 4: Fitted values of the evolution of CP-HETCOR peak integrals vs contact time (Figure 21) of the example mouse molar using the I*-I-S model (Eq. 5).*

Unfortunately, the very weak oscillations of the different peaks mean that it is impossible in this case to get a truly accurate value of the dipolar coupling *b* using Eq. 5. We can however note that these approximate values are quite similar to the theoretical $^1H$-$^{31}P$ couplings in model crystalline calcium phosphates. In HAp, the $^1H$-$^{31}P$ dipolar coupling between the $OH^-$ protons and the phosphates is 0.8 kHz. In OCP, the average calculated coupling between the protons of the water molecules and the phosphorus sites is 2.2 kHz. Lastly, the H-P averaged distance in the $HPO_4^{2-}$ sites of OCP gives a dipolar coupling of 4.4 kHz. The value of *b* that we obtain using this model is therefore somewhat indicative of the H-P expected distances in the different phases. The accuracy, however, is limited by the relative weakness of the observable oscillations: this may be indicative of a distribution of dipolar couplings, which causes an overlap and interference between different oscillations. The same effect may be caused by dynamical effects. Therefore, the data was subsequently fitted with Eq. 6, leading to the parameters summarized in Table 5.

| Component | $OH^- \cdots PO_4^{3-}$ | $H_2O \cdots (H)PO_4^{(2)3-}$ | $HPO_4^{2-}$ |
|---|---|---|---|
| $I_0$ (a.u.) | 1.2 ± 0.1 | 5.7 ± 0.2 | 2.0 ± 0.2 |
| $T_d$ (ms) | 5 ± 1 | 1.5 ± 0.1 | 0.52 ± 0.08 |
| $T_{1\rho}^{1H}$ (ms) | 55 ± 24 | 8.9 ± 0.6 | 7.1 ± 1.3 |
| $1/T_2$ (kHz) | 1.0 ± 0.1 | 1.0 ± 0.2 | 0 |
| $R^2$ (COD) | 0.99 | 0.99 | 0.88 |

*Table 5: Fitted values of the evolution of CP-HETCOR peak integrals vs contact time, of the example mouse molar (Figure 21), using the I*-I-S model with a distribution of dipolar couplings (Eq. 6)*

This model however fails to accurately describe our data, with a worse fit of the experimental data than the previous I-I*-S model for the $HPO_4^{2-}$ component in addition to unrealistic average dipolar H-P coupling $1/T_2$ for all sites. We nonetheless note that $I_0$ values vary only moderately from one model to the next, and that $T_{cp}/T_d$ and $T_{1\rho}$ values are rather consistent for the different fits (see Tables 3 to 5). We therefore decided to continue using the I-S model, as it is the simplest model that accurately describes the variation of the observed intensities over the contact time. We must however note that this is not indicative of the mechanism of polarization transfer in the sample, which may not be accurately described by either the I-S or the two I*-I-S models.

Despite these limitations, the obtained time-constants with I-S model still serve to characterize the three different environments observed in our signal. The $OH^-$ resonance, expected to originate from the crystalline core, has the slowest dynamics (both $T_{cp}$ and $T_{1\rho}$), characteristic of its distance to the $PO_4^{3-}$ sites in apatite and to the weak interactions with the spin-lattice due to its isolation in the $OH^-$ columns. The high-chemical shift sites of bone mineral ($HPO_4^{2-}$ ions and $H_2O\cdots$ $(H)PO_4^{(2)3-}$ sites) have much shorter $T_{cp}$ and $T_{1\rho}$ times, which is coherent with the short H-P distance and with the hydrated and disordered environment. The protons of the water molecules around 5 ppm have a much longer $T_{cp}$ but a similar $T_{1\rho}$, which indicates that they interact similarly with the spin-lattice, but sit much further from phosphorus sites.

#### *I.3.3.3 Choice of fitting parameters and flexibility of the method*

In this example, we have chosen to fit the 2D spectrum with three peaks of varying amplitude, position and width in all three dimensions. It may be argued that a CP-buildup of a peak with changing parameters over the contact time has no physical significance. Yet, the variation of the $\delta_{iso}$ and FWHM ($^{31}P$) parameters over the contact time shows that this is necessary to account for the entirety of the signal using three components (Figure 22), as the $^{31}P$ position of the different maxima and peak width vary significantly depending on the contact time of the CP-HETCOR experiment. This is also reflected in the variation of the fitted parameters over time.

As shown in Figure 22, we clearly see that the correlation we assigned to the $OH^-$ - $PO_4^{3-}$ transfers in the crystalline core shows very little change in position and peak width over the contact time (black squares), whereas the other two correlation peaks show a clear trend in the evolution of the $\delta_{iso}$ and FWHM ($^{31}P$) parameters over the contact time (red and blue symbols). These changes accurately track evolutions of the $^{31}P$ peak maxima measured on slices of the two correlation maps. We will attempt to explain these differences in observed NMR parameters later, with results from a variety of samples. For now, we note that there are probably more underlying resonances in this signal than have been reported here and in the literature. The fact that these resonances have different CP dynamics likely causes them to contribute differently to the observed $\delta_{iso}$ and FWHM of the overall signal, depending on the contact time.

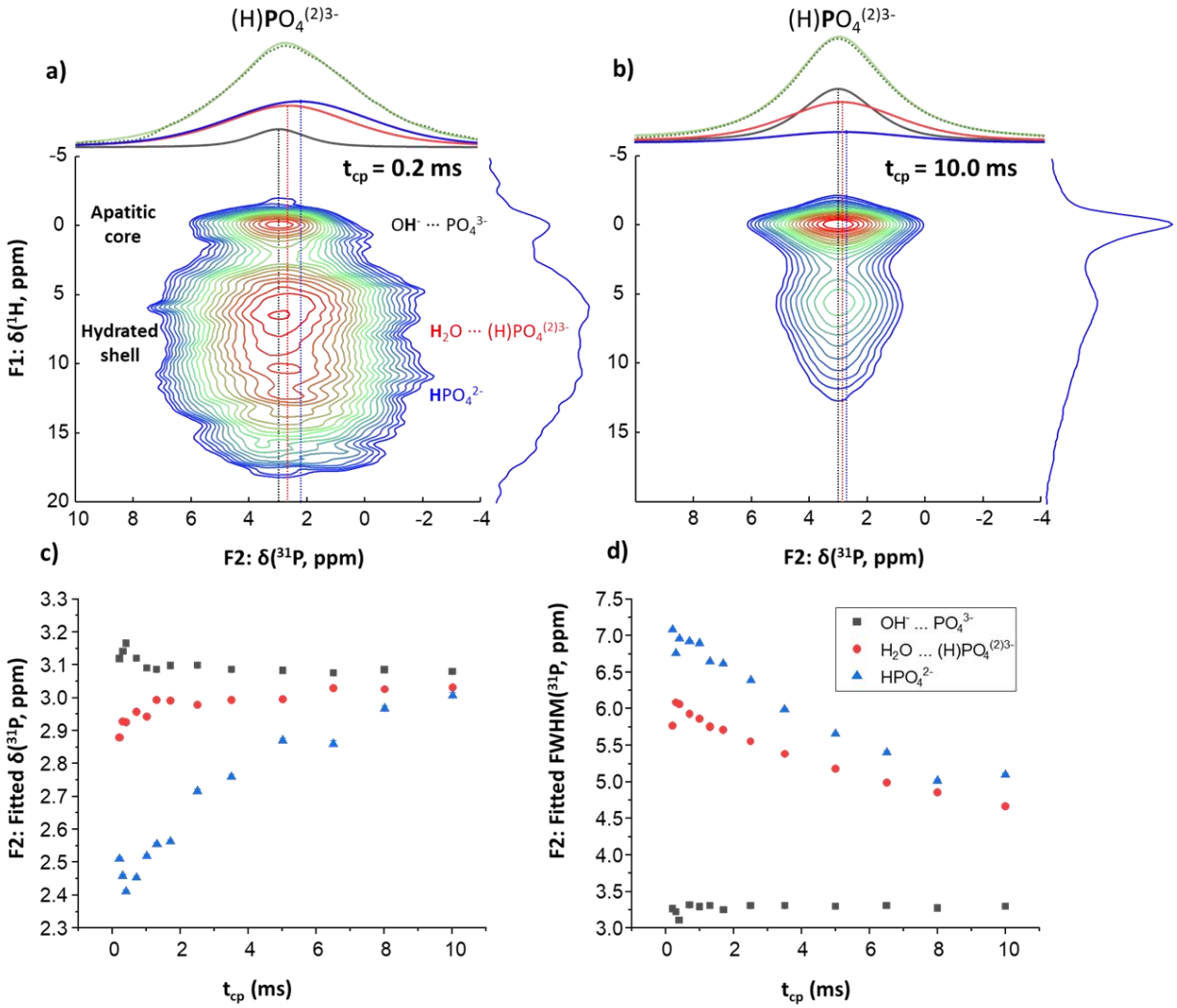


*Figure 22: a,b) : $^{1}H$-$^{31}P$ CP-HETCOR spectra of the example mouse molar at $t_{CP}$ = 0.2 ms and 10.0 ms, respectively ($B_0$ = 7.04 T, $\nu_r$ = 14 kHz, RD = 2 s, TD (F1) = 128, ns = 64, 32). Note the difference in the $^{31}P$ chemical shift of the correlations at $t_{CP}$ = 0.2 ms, less prominent at $t_{CP}$ =10.0 ms. c, d) Evolution of the $^{31}P$ fit parameters over the CP-HETCOR series.*

To illustrate this, we studied how the 2D fitting routine works when fitting the signal with frozen peaks (the amplitude is the only variable parameter for these peaks). For this, we "setup" the series with an intermediate contact time experiment ($t_{cp}$ = 5.0 ms), and then used the fitted $\delta_{iso}$ and FWHM values as constants over the series. Consequently, the only variable adjusted during the buildup was the amplitude of the three components. Below, we call this method of fitting "Series 2".

| Peak | Pos(X) | | | Pos(Y) | | | Amp | FWHM(X) | | | FWHM(Y) | | | gl(X) | gl(Y) |
|---|---|---|---|---|---|---|---|---|---|---|---|---|---|---|---|
| n | min | δ $^{31}$P (ppm) | max | min | δ $^{1}$H (ppm) | max | | min | FWHM $^{31}$P (ppm) | max | Min | FWHM $^{1}$H (ppm) | max | | |
| **1** | 0.1 | 3.07 | 6.0 | -0.2 | -0.0 | 1.0 | 1.0* | 1.5 | 3.3 | 3.5 | 0.0 | 1.74 | 3.0 | 0.3 | 0.2 |
| **2** | 0.1 | 2.99 | 6.0 | 4.9 | 5.53 | 7.5 | 1.0* | 1.5 | 5.1 | 10.0 | 0.0 | 7.85 | 8.0 | 0.4 | 0.0 |
| **3** | 0.1 | 2.86 | 6.0 | 0.0 | 12.1 | 15.0 | 1.0* | 1.5 | 5.6 | 10.0 | 8.0 | 8.32 | 20.0 | 0.6 | 0.0 |

*Table 6: Initial fitting parameters based on the $t_{cp}$ = 5.0 ms $^{1}$H-$^{31}$P CP-HETCOR spectra of the example mouse molar sample (Fitting Series 2).*

| Component | **$OH^{-}$ ⋯ $PO_4^{3-}$** | **$H_2O$ ⋯ $(H)PO_4^{(2)3-}$** | **$HPO_4^{2-}$** |
|---|---|---|---|
| $I_0$ (a.u.) | 1.3 ± 0.2 (1.3) | 5.1 ± 0.2 (5.3) | 1.5 ± 0.1 (1.8) |
| $T_{CP}$ (ms) | 2.7 ± 0.5 (2.6) | 1.03 ± 0.06 (0.99) | 0.33 ± 0.02 (0.39) |
| $T_{1\rho}^{1H}$ (ms) | 23 ± 11 (19) | 9.4 ± 0.8 (8.4) | 9.1 ± 0.6 (7.1) |
| $R^2$ (COD) | 0.99 (0.99) | 0.99 (0.99) | 0.97 (0.85) |

*Table 7: Fitted parameters of the CP-buildup fit of Series 2 for the $^{1}$H-$^{31}$P CP-HETCOR spectra of the example mouse molar, with $t_{CP}$ ranging from 0.2 to 10.0 ms. The values obtained with frozen peaks of varying intensity (Fitting with Series 1 procedure) are in parentheses for comparison.*

Fitting the series with frozen peaks, as could be expected, gives a worse fit of the individual correlation maps, more significantly at low contact-time experiments (Figure 23, insets). From the projections, we were able to see that the $^{31}$P peak width of the signal is significantly underestimated for low contact times. However, we also see a significant decrease in the uncertainty interval between Series 1 (Table 5) and Series 2 method (Table 7) for the CP dynamic parameters. This may indicate that there was a significant amount of overfitting in the initial series, possibly due to having variables that did not significantly improve the quality of the fit but that introduced a source of uncertainty in the measurements of the integrations.

Thanks to the flexibility and speed of our fitting routine, we are able to individually fix or vary the parameters to understand whether they have a significant effect on the quality of the fit. From this, we were able to determine that the FWHM of the $HPO_4^{2-}$ peak in the $^{1}$H dimension can be considered constant without significantly affecting the quality of the fit (Figure 23, blue *vs* red symbols). We were also able to determine that varying the g/l ratios has no visible impact on the fit, as they are nearly constant over the different contact times. Therefore, we can propose an "optimized" fitting process, where the $^{1}$H of $HPO_4^{2-}$ FWHM is fixed to an average value obtained from the first series (= 9.7 ppm). Below, we call this optimized fitting routine "series 3".

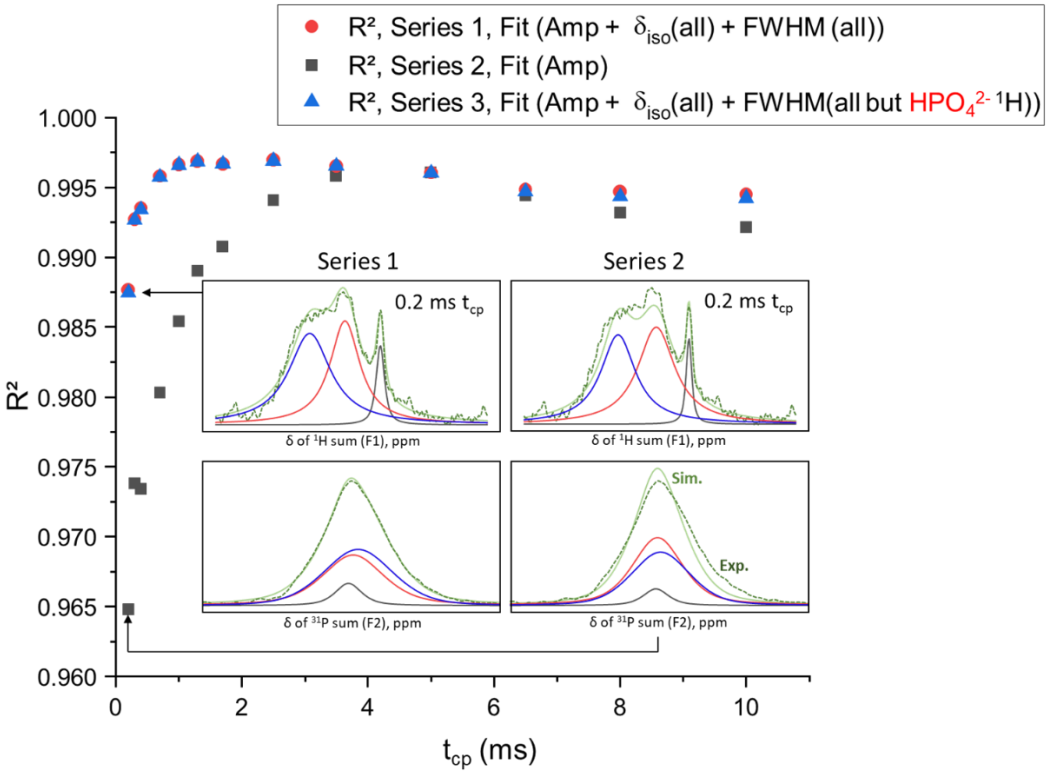


*Figure 23: Comparison of the R² parameter describing the average differences between the experimental spectra and simulated lineshape at the different contact times, for all three series corresponding to the $^{1}H$-$^{31}P$ CP-HETCOR spectra of the example mouse molar. Note that the R² is expected to decrease at low and high contact times due to a lower signal/noise ratio. The inset corresponds to the projected sums in F1 and F2 of the $t_{cp}$ = 0.2 ms fit for fitting series 1 and 2. ($OH^{-} \cdots PO_4^{3-}$ in black, $H_2O \cdots (H)PO_4^{(2)3-}$ in red and $HPO_4^{2-}$ in blue).*

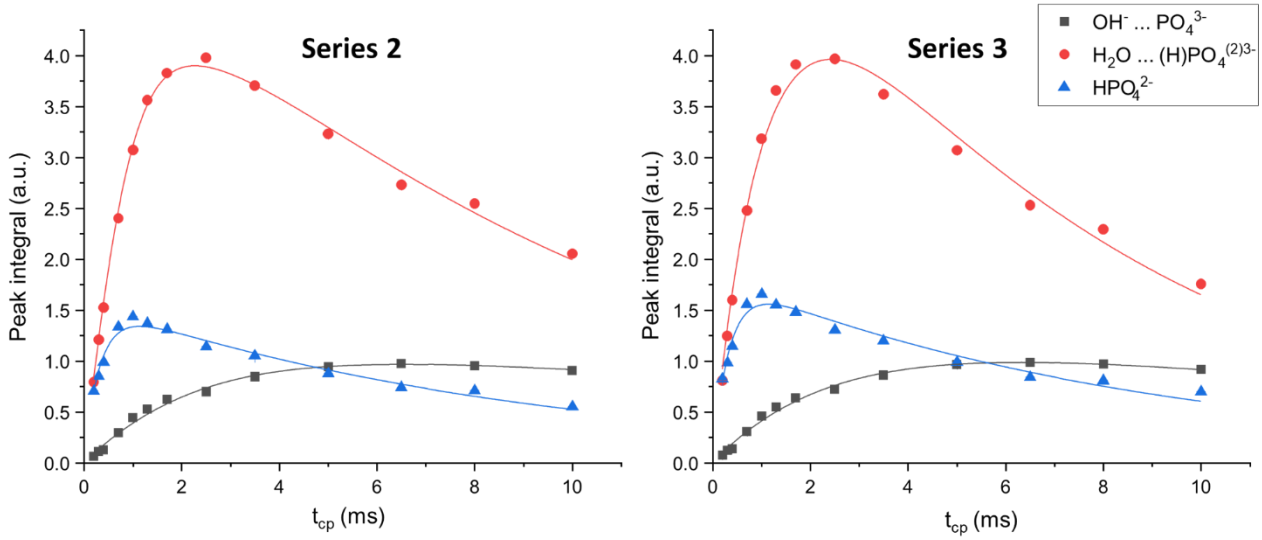


*Figure 24: Evolution of the integral of the three components of example mouse molar over the contact time, for the "series 2" and "series 3" fitting routines.*

| Component | $OH^- \cdots PO_4^{3-}$ | $H_2O \cdots (H)PO_4^{(2)3-}$ | $HPO_4^{2-}$ |
|---|---|---|---|
| $I_0$ (a.u.) | 1.3 ± 0.2 (1.3/1.3) | 5.5 ± 0.3 (5.3/5.1) | 1.8 ± 0.1 (1.8/1.5) |
| $T_{CP}$ (ms) | 2.6 ± 0.6 (2.6/2.7) | 1.08 ± 0.08 (0.99/1.03) | 0.34 ± 0.03 (0.39/0.33) |
| $T_{1\rho}^{1H}$ (ms) | 23 ± 15 (19/23) | 7.3 ± 0.7 (8.4/9.4) | 8.9 ± 0.9 (7.1/9.1) |
| $R^2$ | 0.99 (0.99/0.99) | 0.99 (0.99/0.99) | 0.95 (0.85/0.97) |

*Table 8: Parameters of the CP-buildup obtained on the example mouse molar (Figure 24) with fitting Series 3, with a fixed $HPO_4^{2-}$ peak width in the $^1H$ dimension. The values in parenthesis correspond to the average ones extracted from the fitting Series 1/ Series 2.*

Although we are fitting the experiments with different methods in series 1, 2 and 3, this only has a moderate impact on our measurements of the CP dynamics parameters. Moving forwards, we will use the same method to minimize the difference between experimental data and fit, while minimizing overfitting. It consists in fixing $^1H$ FWHM for $HPO_4^{2-}$ peak to a weighted average value from Series 1, and fitting the position and intensities of the peaks in both dimensions, as well as $^{31}P$ and remaining $^1H$ FWHM (Series 3).

We conclude that this 2D fitting method is adequate for the analysis of CP-HETCOR spectra, giving us an accurate estimate of NMR parameters in both the direct and indirect dimensions simultaneously. Because the script entirely automates this process, it enables investigation of a large number of samples. We will later prove that the ability to easily select the parameters of the fit over a series was essential to gather the results presented in this study. We therefore have a reliable method for the analysis of variable contact times CP-HETCOR spectra, especially over large series of samples and experiments. Let us continue by presenting the samples we have analyzed in this study.

## II. Natural and synthetic apatites samples studied here by 2D CP-HETCOR

### II.1. Synthetic biomimetic apatites

Because of the complexity of bone, researchers often use a variety of model samples and in particular biomimetic apatites as a stand-in for bone mineral in a variety of contexts. They are used in the study of new implants,[34] biomineralization processes[35] and NMR investigations relying on the absence of proton signals from the organic phase,[32] just to name a few examples. Therefore, a variety of protocols exist for the synthesis of biomimetic apatites. In this study, we preferred those that are well-understood, experimentally simple to perform, and give a variety of well-characterized apatites.

In their 2012 publication,[36] C. Rey, C. Drouet *et al.* devised a number of protocols and characterized in detail the effects of different variables on the synthesis of biomimetic apatites. The initial protocol involved the rapid mixing of two solutions at room temperature (RT): an aqueous $Ca^{2+}$ solution with a concentration of 0.3 M, and an aqueous $HPO_4^{2-}$ solution with a concentration of 0.6 M. The reaction was then rapidly agitated for five minutes. The mixing and stirring of the highly concentrated solution caused the rapid precipitation of a large number of

seeding nanocrystals. Once the crystals were formed, the stirring was stopped and the solution was left to rest in a furnace at physiological temperature. This caused the existing seeds to mature and crystallize further. It was proven in the study that the maturation time (ranging from 20 minutes from 20 days) and temperature (from RT to 100°C) determine both the final stoichiometry and size of the crystals. Lower temperatures and shorter maturation times made the crystals smaller, less stoichiometric and increased their $HPO_4^{2-}$ content. A maturation time of at least a day was required to achieve a non-negligible $OH^-$ content in the mineral, which implied that shorter durations mostly yielded a more disordered calcium phosphate material. Similarly, the Ca/P ratio at 15 hours of maturation was 1.38 ± 0.4, and increased to 1.45 ± 0.4 at a day of maturation. To achieve a Ca/P in line with those reported for bone in the literature,[8] we therefore should have a maturation time of 15 hours to a day. Because it was reported that the hydrated surface could be denatured by drying (and yet, wet samples are problematic for ssNMR experiments), the samples were freeze-dried and immediately stored in a -20°C freezer. Note also that the solvents were not degassed before the synthesis, which added a small amount of carbonation to the apatite.

### II.1.1. Synthesis protocols for apatites

- ***Synthesis protocol of biomimetic apatites (HA_BM, CHA_BM and HA_NA)***

The synthesis protocol for our standard biomimetic apatite (HA_BM) is the following. Two solutions, A and B, are prepared right before the synthesis, with the specifications reported in Table 9.

| Sol. | Reagent | M (g/mol) | n (mmol) | C (M) | V (mL) | m (g) |
|---|---|---|---|---|---|---|
| A | $(NH_4)_2HPO_4$ | 236.15 | 60.6 | 0.606 | 100 | 8.00 |
| B | $Ca(NO_3)\cdot 4H_2O$ | 132.06 | 13.0 | 0.260 | 50 | 3.07 |

*Table 9: Reagents used for the synthesis of HA_BM.*

Solution A is added to a 600 mL round-bottom flask and stirred. Solution B is then rapidly added to solution A, after which the flask is sealed with a stopper. Rapidly after the addition, the solution turns white and opaque. The reaction medium is left to stir 5 minutes, after which the flask is transferred to a furnace set to 37°C. The solution is left to mature for 24 hours, after which it is filtered on a Büchner funnel under a weak vacuum. The damp powder (forming dense white plates) is then collected and freeze-dried overnight (15-18 hours depending on the synthesis). The dry powder is then separated on a 125 µm, steel-meshed sieve. The sieved product is stored in a −20°C freezer until use.

The resulting solid is a brightly white fine powder. The synthesis was repeated thrice, with the first one with a lower yield due to subpar filtering. Indeed, a fritted funnel was used, which immediately became clogged with powder, eventually wasting some product. The second and third syntheses, using a Büchner funnel, yielded 1.09 g and 1.10 g of sieved powder, respectively. The pH of the supernatant was estimated at 7.5 using a Litmus paper.

In the spirit of Prof. Rey's study, we also synthesized two variants of the biomimetic apatite. The first, CHA_BM, incorporates a larger number of carbonate ions together with some sodium substitution ions, by adding sodium carbonate into solution A (Table 10). The second, HA_NA, replaces the ammonium hydrogen phosphate with sodium hydrogen phosphate in order to introduce sodium substitutions in great amount (Table 11).

Observations during the synthesis of CHA_BM were identical to that of HA_BM, aside from the powder having a coarser aspect in the end. The protocol yielded 1.05 g of dry, sieved product.

| Sol. | Reagent | M (g/mol) | n (mmol) | C (M) | V (mL) | m (g) |
|---|---|---|---|---|---|---|
| A | $(NH_4)_2HPO_4$ | 236.15 | 60.6 | 0.606 | 100 | 8.00 |
| | $NaHCO_3$ | 84.01 | 71.4 | 0.714 | | 6.00 |
| B | $Ca(NO_3)\cdot 4H_2O$ | 132.06 | 13.0 | 0.260 | 50 | 3.07 |

*Table 10: Reagents used for the synthesis of CHA_BM*.

The synthesis of HA_NA was found to be more experimentally challenging due to the lower solubility of $Na_2HPO_4$ compared to its ammonium counterpart (77 g/L vs 575 g/L at 10°C). The solution had to be stirred for 15 min to fully dissolve the precursor. The fact that the mildly basic solution was exposed to air for a longer time may have increased the carbonation of the solution. The yield of the synthesis was also much lower, namely 0.76 g of unsieved product (compared to 1.22/1.50/1.19 g for the previous syntheses). The sieved yield was even lower, at 0.30 g. This lower yield was not mentioned in C. Rey *et al*. study,[36] and has no apparent cause aside from (perhaps) a slower crystal growth of the substituted apatite. The resulting powder was also much slower to dry, being damp after an overnight lyophilization, requiring a full 48 hours to match the appearance and ATR-IR water signature of the other powders. It was also generally coarser and difficult to handle, with a tendency to stick to surfaces.

| Sol. | Reagent | M (g/mol) | n (mmol) | C (M) | V (mL) | m (g) |
|---|---|---|---|---|---|---|
| A | $Na_2HPO_4$ | 141.96 | 60.6 | 0.606 | 100 | 8.61 |
| B | $Ca(NO_3)\cdot 4H_2O$ | 132.06 | 13.0 | 0.260 | 50 | 3.07 |

*Table 11: Reagents used for the synthesis of HA_NA.*

• ***Synthesis protocol of crystalline stoichiometric apatite (HA_CR)***

Aside from the biomimetic apatites, a crystalline, stoichiometric hydroxyapatite (HA_CR) was synthesized using a slow aqueous precipitation at high temperature, under basic conditions, using the reagents reported in Table 12.

| Sol. | Reagent | M (g/mol) | n (mmol) | C (M) | V (mL) | m (g) |
|---|---|---|---|---|---|---|
| A | $(NH_4)_2HPO_4$ | 246.15 | 10.0 | 0.20 | 50 | 2.36 |
| B | $Ca(NO_3)\cdot 4H_2O$ | 132.06 | 6.0 | 0.12 | 50 | 0.79 |

*Table 12: Reagents used for the synthesis of HA_CR*.

Here, the pH of the aqueous solution of $Ca(NO_3)\cdot 4H_2O$ is first adjusted to 10 by adding a 1M solution of $NH_4OH$. The solution is then stirred (300 rpm) under an Argon flow at 80°C, in a tri-neck round-bottom flask with a water-cooled condenser. The aqueous solution of $(NH_4)_2HPO_4$, the pH of which was also set to 10 using a 30% w/w $NH_4OH$ solution, is then added dropwise over an hour using an addition funnel. A white precipitate appears from the first drop. Once the addition is complete, the solution is left to stir for three more hours, under Argon. The product is then separated on a Büchner funnel. It is then dried in air, at 80°C overnight. The resulting solid is a moderately fine white powder (m = 0.98 g, *c.a.* 97% yield).

### II.1.2. Characterization of the synthetic apatites

Synthetic apatites were characterized via TEM microscopy, ATR-IR spectroscopy, pXRD measurements and $^{1}H$, $^{31}P$ and $^{13}C$ MAS NMR experiments.

The IR measurements were performed on a Perkin-Elmer Spectrum 2 FT-IR instrument, using the Attenuated Total Reflectance (ATR) mode. The pXRD patterns were recorded on an X'Pert MPD diffractometer using $CuK_{\alpha 1}$ radiation, with a voltage of 40 kV and a current of 25 mA, on a glassy planar sample holder. The patterns were recorded with $2\theta$ ranging starting at 3° up to 60° of deflection, with a step size of 0.017° and an acquisition time ranging from 10 minutes to 45 minutes. The TEM (Transmission Electron Microscopy) images were recorded on a JEOL 1400 Flash instrument. The sample was deposited on a double-sided conducting plate as a dispersion. The dispersion was formed by sonicating 1 mg of solid into 1 mL of 50/50 v. EtOH/$H_2O$ solution, of which a single droplet was laid on the plate that was then left to dry in air.

A cursory look at the TEM images for the four samples shows notable differences in size and morphology (*Figure 25*). Unsurprisingly,[36] the biomimetic apatites are much smaller than the crystalline HA_CR, in part due to the lower synthesis temperature and the difference in pH during precipitation. Less expected, the HA_NA crystallites appear here as much larger than the two other biomimetic samples. They all share a needle-like shape, with different levels of elongation. The HA_NA and HA_CR crystals appear extremely elongated, where the CHA_BM are more ovoid. The biomimetic samples appear to have a more homogeneous size distribution, with the typical crystal of HA_BM being apparently around 50 nm, CHA_BM 30 nm and HA_NA over 100 nm. The HA_CR crystals appear to be less uniform in size, and it is difficult to say whether we are looking

at self-assembled clumps of small crystals or if the crystals are micrometric with an irregular surface.

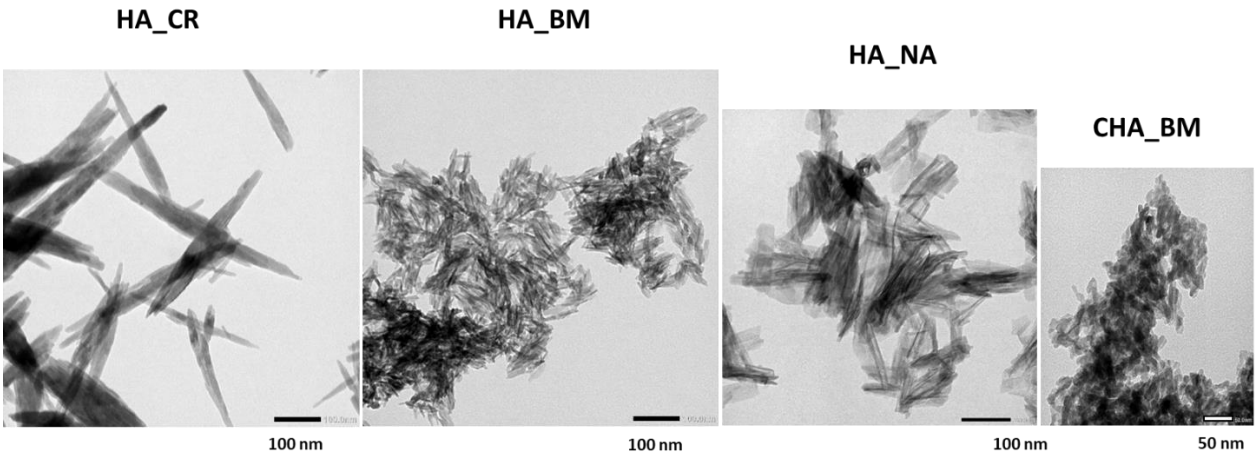


*Figure 25: Selected TEM images of the four samples of apatite. The images have been selected as being representative of the samples they depict. The images are scaled identically. Note that some of the renderings have had their brightness uniformly increased.*

These differences in crystal morphology are linked to the differences in composition between the apatites (and also in synthetic conditions, for the HA_CR phase). This is most visible in IR-ATR spectroscopy (Figure 26) where the characteristic signals of the carbonates vary significantly from one sample to the next. The CHA sample shows heavy carbonation[37] while HA_BM only shows very weak carbonation, with a broad weak peak centered at 1446 $cm^{-1}$. The HA_CR shows a slightly more pronounced 1415 $cm^{-1}$ peak, suggesting a different carbonation scheme in the latter sample (possibly due to the difference in synthetic procedure). No strong conclusion can be made on whether we have a predominant A or B-type substitution (Chapter I, section II.2) when looking at these bands, as assignments of IR spectra in the carbonate $\nu_3$ stretching regions have been shown to be ambiguous.[37] Moreover, because of the small size of the particles, it is possible that surface-adsorbed carbonates or disordered impurities are contributing to these resonances.

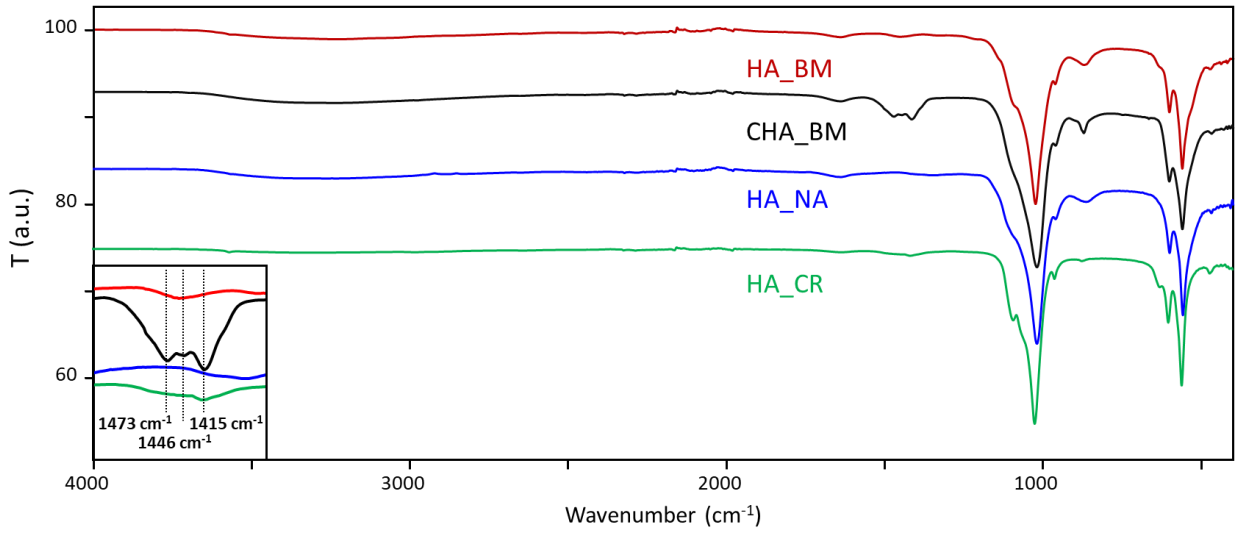


*Figure 26: IR-ATR spectra of the dry powders of biomimetic apatites (HA_BM, CHA_BM and HA_NA), in comparison to the more stoichiometric phase (HA_CR). The inset shows the characteristic signals of the carbonates.*

Interestingly, the differences in composition and crystal size are also partly reflected by pXRD patterns (Figure 27). Here, we observe that only HA_CR stands out due to its much narrower diffraction peaks. This suggests either larger coherence domains and/or lower degree of chemical disorder. of the sample compared to the biomimetic apatites.

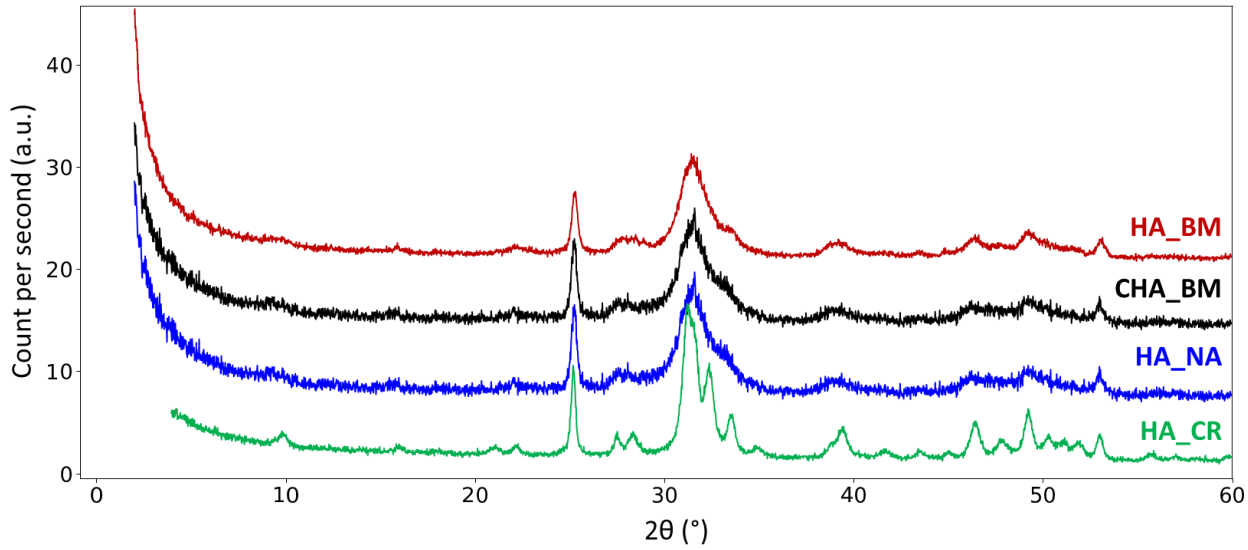


*Figure 27: Comparison of the pXRD patterns of the synthetic apatites, showing the much narrower diffraction peaks of the non-biomimetic HA_CR sample.*

The presence of A and B type carbonation in CHA_BM could be studied in more detail via $^{13}C$ NMR. Using a $^{1}H$–$^{13}C$ CP MAS sequence on a 7.04 T spectrometer equipped with a double resonance 4 mm probe spinning at 14 kHz, we were able to detect a $^{13}C$ NMR signal corresponding to carbonate substitutions in CHA_BM. This broad $^{13}C$ resonance was compared to a reference apatite which had been prepared with $^{13}C$-enriched carbonate substitutions[38] in both A and B positions (Figure 28).

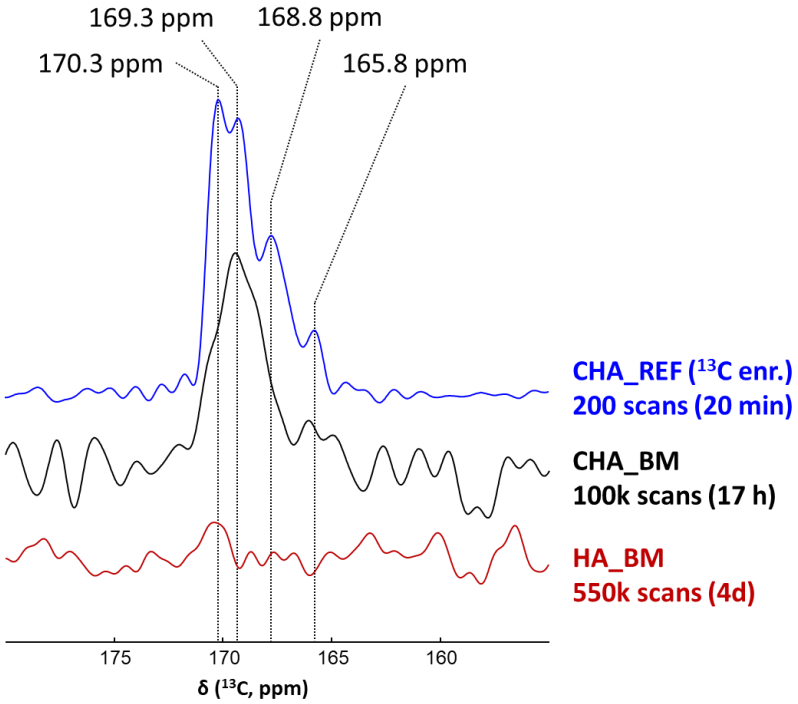


*Figure 28: $^{1}H$ - $^{13}C$ CPMAS NMR spectra of a $^{13}C$-enriched carbonated hydroxyapatite[38] and two non-labeled biomimetic samples prepared as part of this thesis. $B_0$ = 7.04 T, $t_{cp}$ = 6.0 ms, $\nu_r$ = 5 kHz, RD = 2 s (CHA_BM), 5 s (CHA_REF), 0.6 s (HA_BM).*

CHA_BM shows a broad $^{13}C$ resonance spanning from 171 ppm to 167 ppm (and possibility extending to 165 ppm, barely above the noise level) with a maximum around 169.3 ppm. The HA_BM sample, despite a large number of scans, does not show a signal above the noise level in these measurement conditions. Although the chemical shift of the carbonate sites of apatite can vary significantly from one sample to the next,[39,40] some resonances assignments could be proposed on the basis of 2D experiment and DFT modeling[40] but is beyond the scope of this study.

The following can therefore be said about our samples: the three biomimetic apatites share a relatively similar synthetic protocol. Changing the precursors had a significant impact on the final product, providing a set of model samples containing different types of substitutions ($Na^+$, $CO_3^{2-}$) present in bone which will be useful for the development of the 2D fitting method and comparison with bone results.

## II.2. Mice bone and teeth

The aim of this part of the study was to determine whether the absence of the $LPA_1$ receptor has an influence on the composition and/or structural organization of bone mineral. For this, a number of bone samples from $LPA_1$ deficient and wildtype mice were analyzed.

The samples were sent by our ANR-collaborators in Toulouse. They originated from frozen mice, and were comparable to those analyzed in the previously discussed study by Gennero *et al*.[3] They corresponded to mice's femoral cortical bones, molars and incisors. For femoral samples, the cortical bone was manually separated from the trabecular bone. The samples were extracted from the frozen specimen, then washed with water and conserved overnight in a 4°C refrigerator. The next day, the samples were sterilized with 3% w/w $H_2O_2$, then washed again with water. The bone fragment was packed still humid into an Eppendorf with a humid paper ball (not in contact) to maintain the humidity inside the tube. The products were cooled during shipping using an insulated box with an ice pack, which was still partially frozen upon arrival. Afterwards, they were stored in a -20° freezer until our analysis.

The biological samples were taken out of the freezer shortly before the NMR analysis. Once thawed (15 minutes out of the freezer), they were gently ground into large fragments with an agate mortar and pestle. The fragments were then packed into a 4 mm CRAMPS rotor, held in place with a PTFE insert. The choice of the CRAMPS rotor was necessary to compensate for the various masses of sample, which can take up (visually) anywhere from a $10^{th}$ to the $3^{rd}$ of the total volume of a standard 4 mm Bruker rotor. The grinding and packing process was done as rapidly as possible, with a usual time of 30 minutes between thawing and packing. The rotors were then inserted into the NMR spectrometer and spun to 14 kHz.

To help characterize the phenotype of $LPA_1$ deficient mice, 11 bone samples were analyzed using our variable-$t_{cp}$ CP-HETCOR experiments. The samples are referred to by their type, specimen number, genotype, and sex :

- Type of sample: incisors (IN), molars (MOL) and femoral cortical bone (FCM).
- Specimen reference number: 1 to 4 digit number
- Genotype: +/+ (= wild-type – WT: no genetic modification), or -/- (= knock out _ KO: with LPA1 deficiency)
- Sex : ♂ = male; ♀ = female

As an example, "MOL1545 +/+ ♂" denotes a molar sample of a male (♂) specimen numbered 1545 with a $LPA_1^{+/+}$ wild type (WT) genotype (namely genetically unmodified). The −/− symbol denotes $LPA_1$ knock-out (KO) mice for which a targeted deletion of $LPA_1$ receptor was achieved.

The list of samples we compared using a variable-$t_{cp}$ CP-HETCOR experiment is as follows:

| Sample | Age (months) | Mass (mg) |
|---|---|---|
| FCM 7 +/+ ♂ | 10 | 37.8 |
| FCM 89 -/- ♀ | 10 | 18.7 |
| FCM 99 +/+ ♂ | 10 | 7.7 |
| FCM 114 +/+ ♂ | 10 | 10.9 |
| FCM 120 -/- ♀ | 10 | 5.5 |
| FCM 190 -/- ♂ | 10 | 11.5 |
| FCM 1545 +/+ ♂ | 10 | 19.0 |
| MOL 1545 +/+ ♂ | 10 | 18.5 |
| IN 1545 +/+ ♂ | 10 | 48.6 |
| FCM1550 -/- ♂ | 10 | 16.0 |
| FCM 1549 +/+ ♂ | 4 | 5.8 |

*Table 13: List of samples included in our comparative study of bone/dental tissues. The mass values correspond to weight of samples in the rotors.*

Note that these are not the only samples that were analyzed in our study, as other samples were used early-on before the protocol for the CP-HETCOR analysis was established. For the sake of consistency, these will be kept out of the comparative analysis. The $I_0$ reported later in the manuscript are normalized by the sum of $I_0$ for all three components in the sample.

## III. 2D acquisition protocol

Just like for a series of 1D acquisitions, a series of 2D CP-HETCOR spectra has to be thoroughly optimized to minimize the experimental time and maximize the quality of the results (signal/noise ratio, resolution). For this reason, we have first analyzed the samples under a number of different test-acquisition conditions in order to optimize later experiments.

### III.1. Non-Uniform Sampling (NUS)

Fundamentally, Fourier-transform NMR spectroscopy relies on our ability to record the free induction decay (FID) of a nucleus precessing out of equilibrium. To discriminate the frequencies composing the FID, we need to observe the oscillation of the magnetization over time. Like any physical measurement, we are unable to measure continuously and must make a series of discrete acquisitions. This is done by using an analog-to-digital converter (ADC), which transforms the analog signal of the coil into a digital reading at a fixed frequency. With the fast Fourier transform algorithm, we can rapidly process these measurements to turn our time-domain data into its representation in the frequency-domain.

The number of data points in the resulting FT spectrum depends on the number of discrete acquisitions made during the length of the FID. In parallel, the range of frequencies that can be distinguished using this method in inversely proportional to the time between two measurements. NMR spectroscopists must therefore choose how to sample their FID carefully.

For this, they must record the FID in its entire length, with a sufficient number of points to have the required spectral resolution and a sufficiently small dwell-time to cover the interval of frequencies they are interested in. Adding unnecessary points to the FID increases the space required to store the experiment, and increases the processing time. However, computers have become sufficiently fast and storage sufficiently cheap and available, that one can afford to the luxury of oversampling their FIDs without experiencing any drawback.

This changes drastically when recording a two-dimensional experiment. In the indirect dimension (F1), instead of sampling the indirect FID using a converter, we transfer the magnetization of the nucleus at different points in time using a variable delay in the pulse sequence. Let us take the example of a $^{1}$H-$^{31}$P CP-HETCOR sequence: we wish to record the FID of the proton nucleus indirectly through $^{31}$P measurements. For this, we can introduce an "evolution delay" $t_1$ between the excitation of the $^{1}$H and the magnetization transfer. If the delay is zero, we effectively record a regular CP experiment. But if we increase the delay, the resulting $^{31}$P NMR spectrum will be modulated by the amplitude of the proton magnetization after a free induction decay of $t_1$. Therefore, by varying $t_1$, we can measure the FID of the $^{1}$H at different points in time. This is the basis of multidimensional NMR,[41] a ubiquitous and necessary tool for all kinds of high-resolution NMR studies. However, this method has a tradeoff: for every point of the FID we wish to sample, we have to record a 1D spectrum. This makes the recording of a 2D spectrum time-consuming, as we need a relatively large number of points to get an accurate representation of the FID in the indirect dimension.

Recording a high-quality 2D spectrum therefore requires a good understanding of the NMR properties of our sample and possibly a certain amount of trial and error. Underestimating the length of the FID leads to a truncated recording of the indirect dimension, causing a loss of resolution and the appearance of "wiggles" that distort the signal around the truncated peak. Due to software limitations, it is usually not possible to lengthen the acquisition of the indirect dimension once the 2D experiment has been started, and the whole experiment must be restarted from the first slice when the indirect dimension is incorrectly sized. To avoid this, we may be tempted to increase the dwell time to lengthen the acquisition without impacting the experimental time. However, the width of the spectral window is equal to the inverse of the dwell time. A signal that falls outside of this window will be "folded back" into the window, resulting in an unreadable signal (note that by selecting a dwell time as multiple of the rotor period, we can fold the rotation bands back onto the isotropic signal, and therefore let them fall outside the spectral window without issue). Lastly, we can increase the number of transients recorded in the indirect dimension without increasing the dwell time, but this results in a longer experimental time. This can be compensated by reducing the number of scans accumulated for each 1D slice, at the cost of the signal/noise ratio.

As a result, recording a multidimensional experiment requires a number of compromises. We wish to acquire large series of 2D spectra over numerous samples, which is putting an extreme strain on our experimental time. Therefore, any method to reduce the experimental time without altering the overall lineshape or quantitativity should be considered. This is why we chose to explore non-uniform sampling (NUS) for the acquisitions in the indirect dimension.

### III.1.1. The principle of NUS

Non-uniform sampling is an alternative method for sampling the indirectly acquired FID. During a uniformly sampled (US) acquisition, the evolution delay is incremented by a constant value. However, not all points of the FID are required to reconstruct it accurately. Although the first points of an FID give the highest signal/noise and are essential to observe rapidly decaying signals, the later points have a low signal/noise but are necessary to determine the lineshape and frequency of slow decaying signals. Spectroscopists have therefore developed alternative methods to reconstruct the FID from incomplete recordings, in order to focus on a larger proportion of transients at the beginning of the FID, where the signal/noise ratio is best (Figure 29).

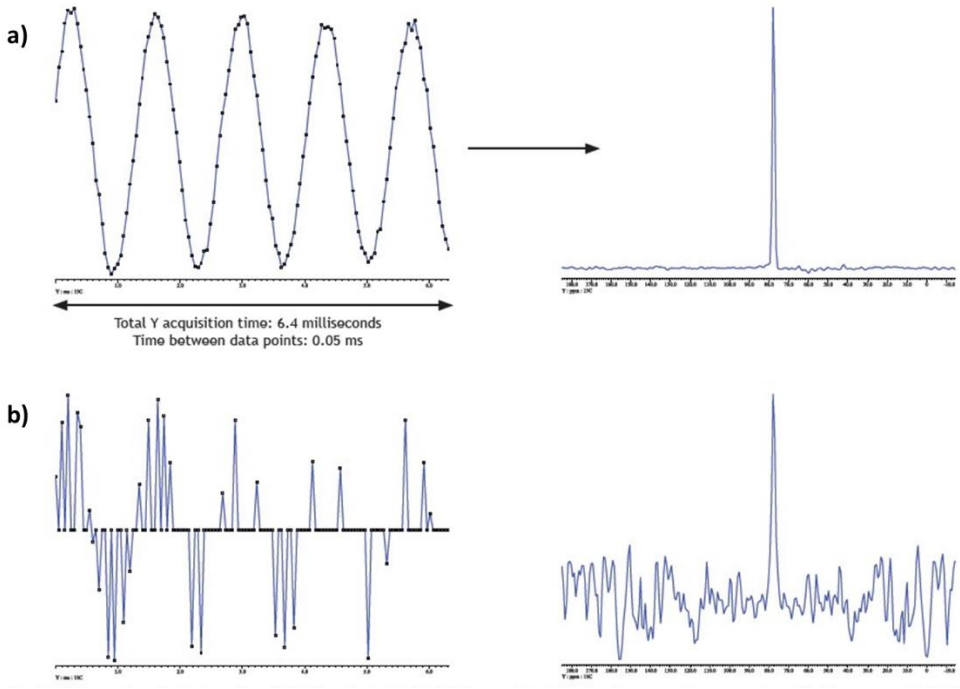


*Figure 29: illustration of the difference between uniform (a) and non-uniform (b) sampling.*[42]

A number of different recording and reconstruction schemes have been proposed over the years.[43,44] Thankfully for us, comparative studies of different NUS schemes already exist.[45] Notably, Dr Guillaume Laurent's thesis[46] provides a helpful guide to the effect of different sampling schemes and algorithms on the CP-HETCOR signal of apatites (Figure 30). Using a 25%

sampled Poisson distribution of the evolution times and the IRLS algorithm[47,48] with a virtual-echo for the reconstruction of the FID, he was able to accurately reconstruct an indirect FID with a quarter of the sampling of a uniformly-sampled (US) control. The best reconstructed FID (orange line) shows a superior signal/noise ratio and conserves finer details (like the 167 ppm shoulder, green circle), with only a quarter of the acquisition time. This immense time gain comes at the cost of signal. However, it is estimated that optimized NUS acquisitions can potentially reach the same signal/time ratio as a US acquisition in a third of the acquisition time.[44]

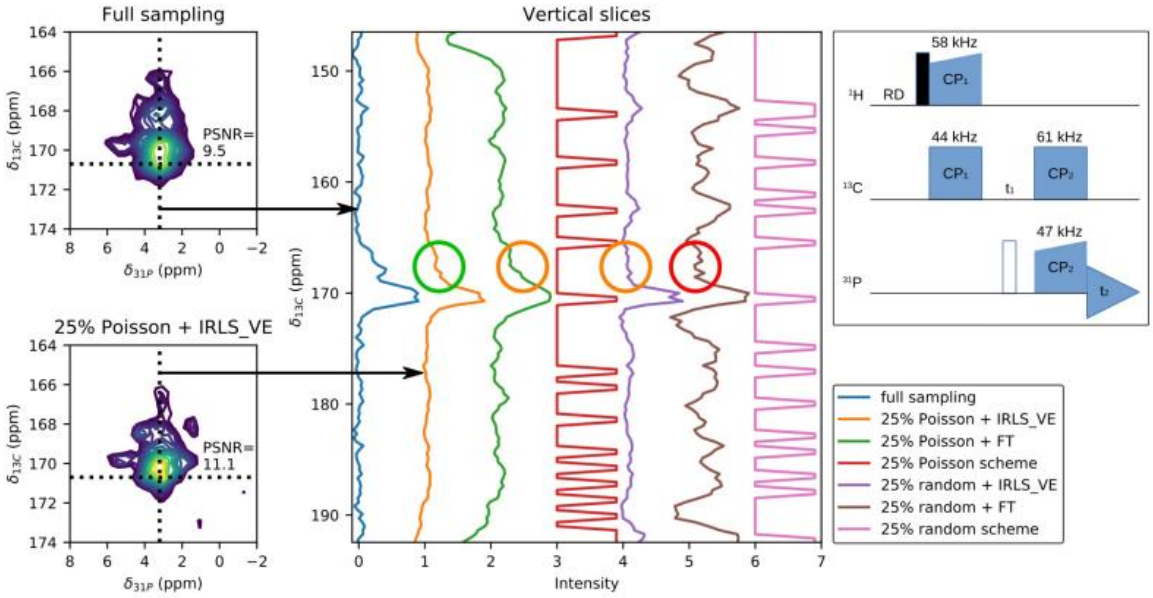


*Figure 30: Comparison of different sampling and reconstruction schemes in a {$^{1}$H}-$^{13}$C – $^{31}$P CP-HETCOR experiment on synthetic $^{13}$C-enriched carbonated apatites, as reported by Dr G. Laurent in his thesis.[46] The circled area highlights a shoulder which was used to establish the best processing method for NUS spectra in apatites. The number of scans per transient is the same in all cases, giving the NUS schemes an experimental time four times faster than the fully-sampled spectrum.*

As part of the present work, we tested the validity of the NUS method on our samples by recording two series of experiments on our example mouse molar: a non-uniformely sampled and a uniformely sampled set of variable contact times CP-HETCOR experiments. The sampling scheme used was a customized Poisson distribution, with 31 fully-sampled slices followed by 31 randomly-sampled slices. The start of the FID (t < 2.2 ms) is 100% sampled, and the later part (2.2 ms < t < 36.6 ms) is 6.5% sampled, in order to reconstruct an FID of 512 slices. This gives our sampling scheme a total sparcity of 12.5%, making it eight times faster than an equivalent US acquisition.

It is difficult to fairly compare US and NUS acquisitions, as an optimized NUS scheme will typically probe a time-domain that is longer than an optimized US scheme. On the other hand, the US acquisition will likely be severely truncated at an equal number of transients. We have conducted

multiple experiments for the comparison of US and NUS acquisitions, showing that a spectrum of comparable quality can be acquired in a much shorter time using NUS, at the cost of minor distortions of the lineshape (Figure 31). One visible impact of the NUS method is the non-uniformely distributed noise. This distribution is dependent on the processing algorithm. It causes the noise to be greater in regions adjacent to the signal, and lesser on the signal itself. This makes normal measurements of signal/noise ratio unreliable, and introduces new challenges for some of our point-by-point processing methods (§ 0). However, for the purpose of 2D fitting, the relatively small intensity of the NUS noise has relatively little impact on the fitting, as will be demonstrated in the next section.

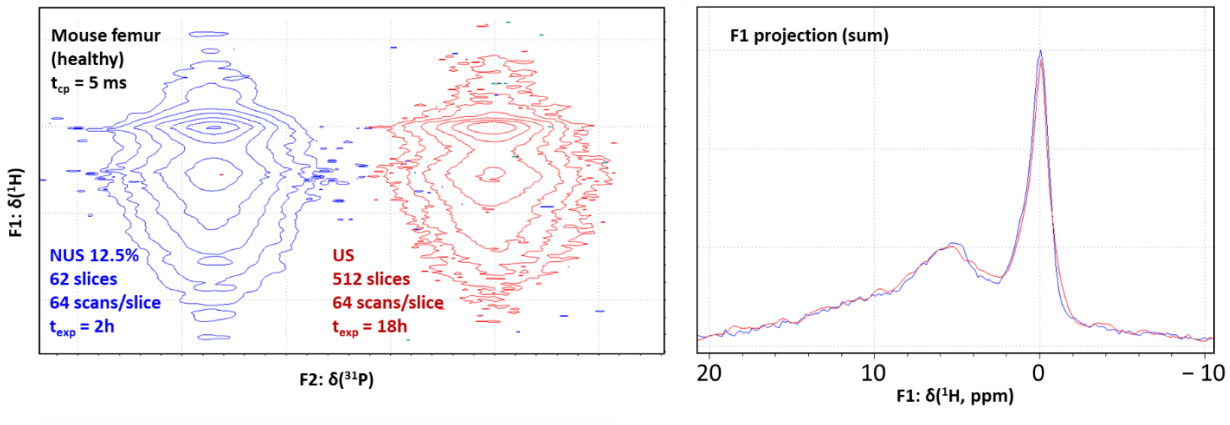


*Figure 31: Comparison of a US (blue) and NUS (red) $^{1}H$-$^{31}P$ CP-HETCOR acquisition of equal time-domain (TD = 36.6 ms) of an example mouse femur sample ($B_0$ = 7.04 T, $t_{cp}$ = 5.0 ms, $\nu_r$ = 14 kHz, RD = 2 s). The US acquisition has 512 slices of 64 scans each; the NUS acquisition has 62 slices of 64 scans each (12.5% sparcity). The NUS acquisition is therefore 8 times shorter. The NUS FID was reconstructed using an IRLS algorithm with a Virtual Echo. The 2 spectra have identical processing parameters (F1 lb = 50 Hz, SI = 256).*

### III.1.2. Impact of NUS on 2D fitting parameters

To judge the impact of the newly introduced NUS acquisition on the 2D fitting routine, we have recorded a series of CP-HETCOR experiments on our example mouse molar with variable contact times, in optimized conditions for both types of acquisition. Here, the US recording was done with the minimal number of slices (128) required to acquire the F1 FID with minimal truncation. The NUS was recorded as previously described with 62 slices and 12.5% sparcity. To give the two series a comparable acquisition time, the number of scans per slice for the NUS acquisition was doubled, leading to an identical quantity of scans per series. To maximize the signal/noise of low contact time experiments, additional scans have been added in both cases (ns×2 for $t_{cp}$ of 0.2 and 0.3 ms, ×1.5 for a 0.4 ms $t_{cp}$). Data recorded at $t_{cp}$ = 0.2 ms with equal experimental times are shown in Figure 32.

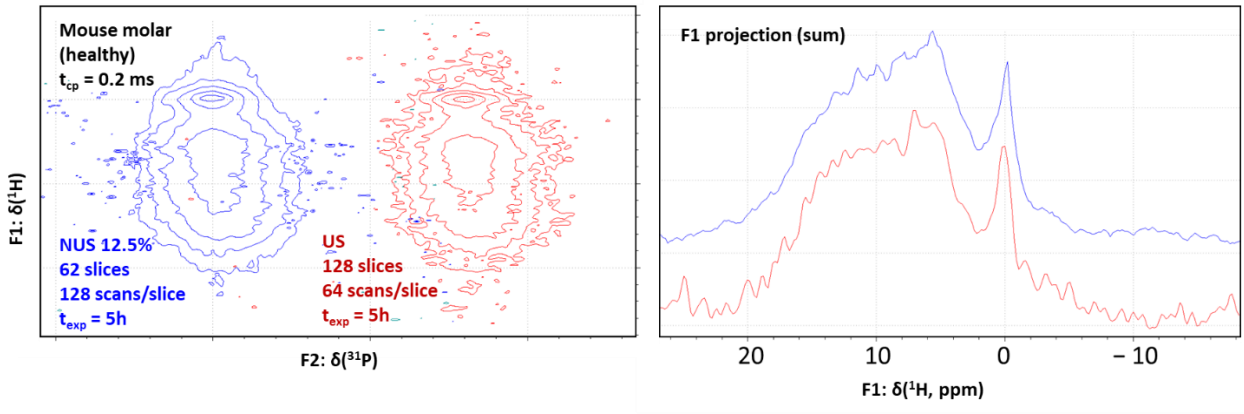


*Figure 32: Comparison of US and NUS CP-HETCOR experiments on an example mouse molar at identical contact times and experimental times ($B_0$ = 7.04 T, $t_{cp}$ = 0.2 ms, $\nu_r$ = 14 kHz, RD = 2 s), showing the much higher noise of the US experiment.*

The impact of the NUS on the signal/noise ratio of the spectrum is evident from a comparison of two spectra at the same contact time: although the experimental time is slightly lower for the NUS acquisition, the contours of the signal show much more distortion from the noise with US than with NUS (Figure 32). A comparison of the fitted CP parameters was then performed (Table 14).

**US:**

| Component | $OH^- \cdots PO_4^{3-}$ | $H_2O \cdots (H)PO_4^{(2)3-}$ | $HPO_4^{2-}$ |
|---|---|---|---|
| $I_0$ (a.u.) | 1.3 ± 0.2 | 5.5 ± 0.3 | 1.8 ± 0.1 |
| $T_{CP}$ (ms) | 2.6 ± 0.6 | 1.08 ± 0.08 | 0.34 ± 0.03 |
| $T_{1\rho}^{1H}$ (ms) | 23 ± 15 | 7.3 ± 0.7 | 8.9 ± 0.9 |
| $R^2$ (COD) | 0.99 | 0.99 | 0.95 |

**NUS:**

| Component | $OH^- \cdots PO_4^{3-}$ | $H_2O \cdots (H)PO_4^{(2)3-}$ | $HPO_4^{2-}$ |
|---|---|---|---|
| $I_0$ (a.u.) | 1.2 ± 0.1 | 5.3 ± 0.3 | 1.75 ± 0.06 |
| $T_{CP}$ (ms) | 2.2 ± 0.3 | 1.00 ± 0.07 | 0.32 ± 0.03 |
| $T_{1\rho}^{1H}$ (ms) | 32 ± 17 | 7.8 ± 0.6 | 9.2 ± 0.7 |
| $R^2$ (COD) | 0.99 | 0.99 | 0.95 |

*Table 14: Fitted parameters of the evolution of the CP-HETCOR peak integrals vs contact time with US or NUS from the application of the I-S model (Eq. 4) to our example mouse molar (Figure 32), with initial fitting parameters from the Series 3.*

As seen in the values of Table 14, the addition of NUS has relatively little impact on the fit parameters. It would appear that the $T_{cp}$ times for the NUS buildup are slightly longer, although

this may be due to the dehydration of the sample inside the rotor (as two days of acquisition separate the two series). More importantly, the calculated $I_0$ are very similar in both cases, which shows that the $I_0$ values are mostly independent of the F1 sampling method and the measured $T_{cp}$ and $T_{1\rho}$ values. Similarly, the information gathered about the position and width of the peaks is similar between US and NUS experiments.

## III.2. Choice of experimental parameters for the variable-$t_{cp}$ CP-HETCOR experiment

### III.2.1. Recycle delays and contact times

The acquisition of 2D spectra is a lengthy process since even with a good signal/noise ratio, a minimal number of scans is required. To avoid artefacting and phasing issues, we must fully cycle the phase for each slice (in the case of our CP-HETCOR sequence, this requires 16 scans). This is then multiplied by the total number of slices, 62 in the case of our NUS sampling sequence. This gives us a required minimum of 992 scans, which is multiplied by the recycle delay. Because we want quantitative information about our samples, we choose a recycle delay greater than 4 times the slowest $^1H$ $T_1$ relaxation constant, which equals to a 98% recovery of the magnetization, and a 2% quantitative error from variations in $T_1$. Because of the 1H contribution of the organic phase, we cannot measure the $^1H$ $T_1$ directly using a saturation recovery experiment. However, we can measure it indirectly by transferring the magnetization to the $^{31}P$ nuclei. This indirect CP-saturation-recovery experiment gave us a $^1H$ $T_1$ time values of 0.55 s for studying the mineral component in multiple bone samples, and our recycle delay was consequently set at 2 s for all samples.

Consequently, the shortest experiment we could record was half an hour long. Practically, biological samples required a significantly higher number of scans to achieve a good signal/noise ratio, leading to experiments generally ranging from one to five hours. This severely limits the number of experiments we are able to record in a reasonable timeframe. We therefore needed to select a limited set of contact times which can give us good measurements of the CP dynamics for all samples.

In order to precisely determine $T_{cp}$ and $T_{1\rho}$ for all sites, we needed to acquire a number of experiments with contact times lower than their $T_{cp}$ and a number with contact times greater than their $T_{1\rho}$ in order to get accurate estimates of both values. As seen in the values presented above (Table 14), this is problematic when measuring the $T_{1\rho}$ values for the $OH^- \cdots PO_4^{3-}$ peak, as the value is much greater than the longest contact time we have recorded < 20 ms. We could have chosen to bypass this limitation, as neglecting the $OH^- \cdots PO_4^{3-}$ $T_{1\rho}$ relaxation only has a very small influence on the calculated $I_0$ (< 5%). Thus, we instead chose to acquire more points at lower contact times.

Because of the short $T_{cp}$ value of the $HPO_4^{2-}$ correlation peak (~0.3 ms at the shortest), we also needed a number of high-quality spectra at very short contact times to accurately measure its dynamics. This induced a new difficulty: the signal of the CP-HETCOR experiment at low contact times is extremely weak. As the $HPO_4^{2-}$ signal only accounts for a small part of the total signal, and given that it is the broadest peak in both dimensions, it has a lower maximum than the other peaks. This made it susceptible to being overtaken by noise in smaller samples. As a measure of comparison, the signal/noise ratio of the first slice of a 2D CP-HETCOR spectrum on a 5.8 mg sample is 23.5 with 256 scans at $t_{cp}$ = 0.2 ms, whereas we achieve a signal/noise ratio of 60.5 with 96 scans at $t_{cp}$ = 10 ms (Figure 33). For practical purposes, we found that contact times lower than 0.2 ms did not produce a reasonable signal/noise ratio.

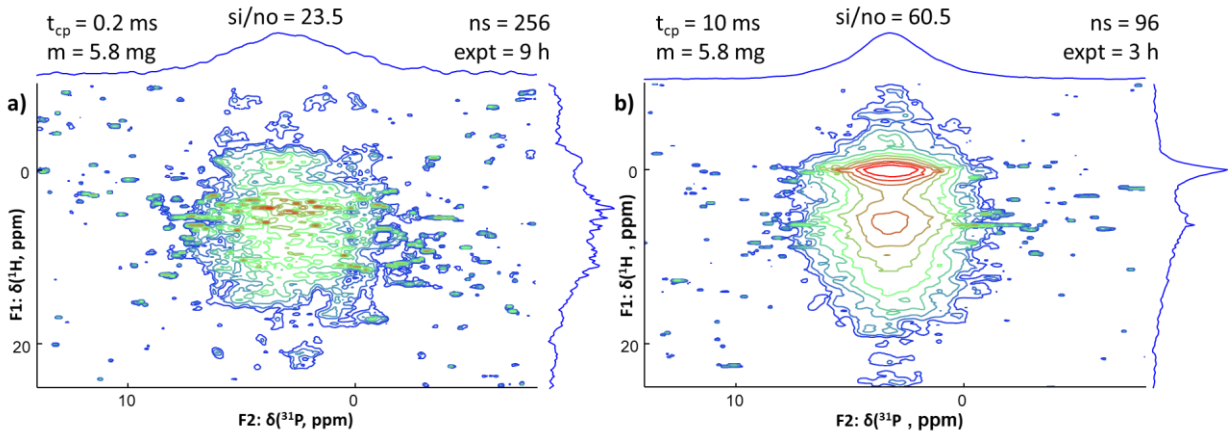


*Figure 33: CP-HETCOR spectra of a 5.8 mg mouse femur sample at contact times of a) 0.2 ms and b) 10 ms. The signal/noise ratio was measured using Topspin's "sino" tool on the first slice of each 2D. $B_0$ = 7.04 T, $\nu_r$ = 14 kHz, RD = 2 s td (F1) = 62, NUS, HH n = -1, ramp.90.100.*

Based on the above, we therefore started the variable $t_{cp}$ series with an initial value of 0.2 ms, and incremented it up to 10 ms in increasing intervals. The $t_{cp}$ series for most analyses was the following:

$t_{cp}$ = [0.2 ms, 0.3 ms, 0.4 ms, 0.7 ms, 1.0 ms, 1.3 ms, 1.7 ms, 2.5 ms, 3.5 ms, 5.0 ms, 6.5 ms, 8.0 ms, 10.0 ms].

This will be considered the standard for all samples, and we will only mention deviations from this pattern from now-on. Note that these experiments were not run in increasing order of $t_{cp}$ to minimize the effects of sample dehydration on the observed values (typically, $t_{cp}$ = 0.3 ms and 1.3 ms points were recorded at the end of the series).

### III.2.2. Hartmann-Hahn conditions

Experiments were first carried out on the synthetic sample CHA_BM, with a fixed $^{1}H$ radiofrequency field of $\omega_{1H}$ = 62.5 kHz (corresponding to a 90° pulse of 4 µs). A corresponding $^{31}P$ radiofrequency field of the same frequency was applied and optimized to find the n = 0 HH matching condition. The HH = -1, +1 conditions were optimized by varing the power of the $^{31}P$ radiofrequency field up and down until two maxima were found. The conditions -1 and +1 with a 90.100 ramp were found to both give a similar amount of signal when optimized. A square spinlock gave a similar signal, with a slightly more precise matching condition.

Three series of experiments were acquired (Figure 34). The first had the matching condition n = -1 ($\omega_{rf,31P}$ = 48.5 kHz) and a 90.100 ramp as the proton spinlock (the $^{1}H$ irradiation starts at 90% of the indicated power and builds up linearly to 100% over the contact time). The second had the matching condition n = +1 ($\omega_{rf,31P}$ = 76.5 kHz) and an identical ramp. The third had the matching condition n = +1 ($\omega_{rf,31P}$ = 76.5 kHz) and a constant spinlock power ("square" CP pulse). We did not investigate the efficiency of the n = 0 HH condition as its intensity was significantly weaker than that of the other conditions for $t_{cp}$ = 1 ms, evidencing slower CP transfer that would render it unsuitable for our study.

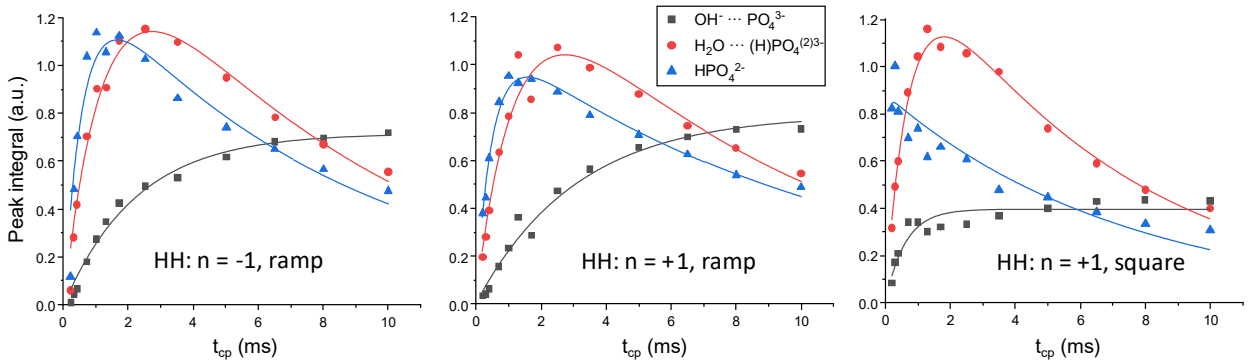


Figure 34: CP-buildup of the CHA_BM CP-HETCOR correlation peaks, recorded using different HH matching conditions and spin-lock pulse shapes. All series have identical acquisition and processing parameters aside from the differing CP conditions mentioned above ($B_0$ = 7.04T, $\nu_r$ = 14 kHz, RD = 2.8 s, $t_{exp}$ = 15h per series). See Table 18 for initial fitting parameters (Series 3 with Eq. 4). Attempts to fit the data using the I*-I-S model were unsuccessful on all three series.

For the n = +1 HH condition with a 90.100 ramp, the CP dynamics parameters were the following (Table 15).

| **Component** | **$OH^- \cdots PO_4^{3-}$** | **$H_2O \cdots (H)PO_4^{(2)3-}$** | **$HPO_4^{2-}$** |
|---|---|---|---|
| **$I_0$ (a.u.)** | 0.79 ± 0.05 | 1.44 ± 0.17 | 1.10 ± 0.04 |
| **$T_{CP}$ (ms)** | 3.08 ± 0.40 | 1.21 ± 0.20 | 0.49 ± 0.04 |
| **$T_{1\rho}^{1H}$ (ms)** | >> 10 ms | 8.40 ± 2.04 | 10.60 ± 1.30 |
| **$R^2$ (COD)** | 0.98 | 0.97 | 0.98 |

*Table 15: Fitting parameters of CP-HETCOR peak integrals of the CHA_BM sample at HH matching condition n = +1 recorded with a 90.100 ramp, on the basis of the I-S model.*

For the n = -1 HH condition with a 90.100 ramp, we obtained the values reported in Table 16.

| **Component** | **$OH^- \cdots PO_4^{3-}$** | **$H_2O \cdots (H)PO_4^{(2)3-}$** | **$HPO_4^{2-}$** |
|---|---|---|---|
| **$I_0$ (a.u.)** | 0.72 ± 0.02 | 1.64 ± 0.17 | 1.35 ± 0.12 |
| **$T_{CP}$ (ms)** | 2.25 ± 0.20 | 1.27 ± 0.21 | 0.57 ± 0.12 |
| **$T_{1\rho}^{1H}$ (ms)** | >> 10 ms | 7.43 ± 1.42 | 8.06 ± 1.64 |
| **$R^2$ (COD)** | 0.98 | 0.96 | 0.87 |

*Table 16: Fitting parameters of CP-HETCOR peak integrals of the CHA_BM sample at HH matching condition n = -1 recorded with a 90.100 ramp, on the basis of the I-S model. *Fit did not converge*

Lastly, for the n = +1 HH condition with a "square" spinlock, the CP dynamics parameters were the following (Table 17).

| **Component** | **$OH^- \cdots PO_4^{3-}$** | **$H_2O \cdots (H)PO_4^{(2)3-}$** | **$HPO_4^{2-}$** |
|---|---|---|---|
| **$I_0$ (a.u.)** | 0.39 ± 0.02 | 1.49 ± 0.06 | 0.88 ± 0.03 |
| **$T_{CP}$ (ms)** | 0.60 ± 0.08 | 0.74 ± 0.05 | << 0.2 ms |
| **$T_{1\rho}^{1H}$ (ms)** | >> 10 ms | 6.40 ± 0.48 | 7.31 ± 1.14 |
| **$R^2$ (COD)** | 0.99 | 0.91 | 0.86 |

*Table 17: Fitted parameters of CP-HETCOR peak integrals of the CHA_BM sample at HH matching condition n = +1 recorded with a square spinlock, on the basis of the I-S model.*

Here, the CP dynamics of the square spinlock are problematic: despite an overall lower intensity for all peaks, the CP buildup of the $HPO_4^{2-}$ signal is much too short to be measured using our $t_{cp}$ list. The signal instead seems to reach its greatest intensity at 0.2 ms. This is a problem for the determination of $I_0$, as varying the $T_{cp}$ value in the [0.05 ms; 0.1 ms] interval (plausible values given the appearance of the fit) changes the $I_0$ by over 10%. On the other hand, the signal from the $OH^-$ proton does not reach a clear plateau, with a relatively short initial $T_{cp}$ rate followed by a slow increase over longer contact times. This may explain the underestimated value of $I_0$ when compared to the other two series.

In conclusion, the choice of HH matching condition has its importance when trying to measure CP dynamics from integrations of the 2D maps, as the matching condition can either significantly shorter or lengthen the dynamics. Given that we would preferably want our apatite and bone mineral samples to have $T_{cp}$ time constants that fall in the range of the contact times we measure, the HH condition must therefore be chosen to adapt to the dynamics of the samples we study. Because the n = -1 condition was found to be suitable for the study and requires lower power radiofrequency fields, it was chosen for their study. This, however, is another indication that polarization transfers in variable-$t_{cp}$ experiments do not follow a standard model in biominerals, and that the values of $I_0$ can at best lead to a relative quantification for samples recorded in the exact same conditions. It also highlights the importance of reporting the exact CP conditions (shape, $\omega_{B1,I}$, $\omega_{B1,S}$) when publishing information about CP dynamics. Note that all the data presented in section IV. below used the HH -1 ramped CP conditions, unless specified ($\omega_{rf,1H}$ = 62.5 kHz, $\omega_{rf,31P}$ = 48.5 kHz, ramp 90.100).

Thankfully for us, the other information about the signal (evolution of the position and width of the peaks over the contact time) was not significantly altered by the change of CP conditions (*Figure 35*). Note that variations observed at very low contact times (especially at $t_{CP}$ = 0.2 ms) are not significant due to low signal/noise ratio. Here, we observed that the $^{31}P$ positions of the cross-peaks vary consistently over the contact time. We will discuss the possible causes of this in more detail in the following sections. We however note for the purpose of these comparisons that the significantly shorter $T_{cp}$ of the square HH +1 matching condition had an impact on the initial slope of the parameters. This is especially visible for the $HPO_4^{2-}$ peak, for which the $\delta_{iso}(^{31}P)$ increased by 0.45 ppm in the first 2 ms, compared to the other conditions where it increased only by 0.15 ppm. This indicates that the underlying mechanism that explains these evolutions in lineshape are tightly intertwined with the CP dynamics of our sample.

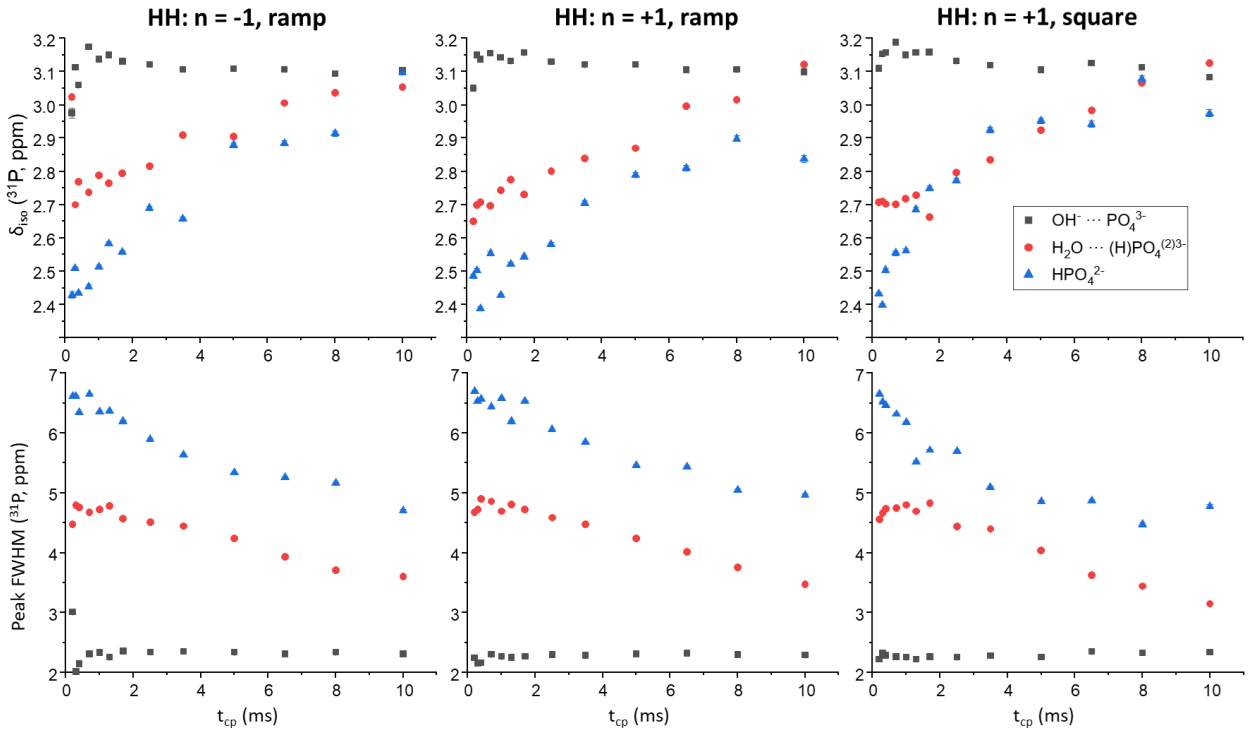


*Figure 35: Evolution of the $^{31}P$ parameters ($\delta_{iso}$ and FWHM) of the different environments in CHA_BM as a function of $t_{cp}$, for different HH conditions, obtained by fitting a series of CP-HETCOR experiments ($B_0$ = 7.04T, $\nu_r$ = 14 kHz, RD = 2.8 s, $t_{exp}$ = 15h per series). See Table 18 for initial fitting parameters.*

### III.2.3. Phasing and processing

An important factor to reliably fit the spectra in 2D is to ensure a stable baseline and stable phasing throughout the experiment series. It was observed that small changes in the phasing of the CP-HETCOR spectra could have an outsized impact on the extracted buildup parameters. For this reason, all experimental parameters were chosen to ensure the reproducibility of the probe tuning and matching conditions which can influence the phasing.

Firstly, the acquisitions were made with a moderate heteronuclear decoupling radiofrequency field (62.5 kHz spinal-64), as higher $^{1}$H powers can have a destabilizing effect on the probe tuning. The variable-temperature unit was not used to avoid experimental complexity. The tuning was done in a reproducible manner, first matching and tuning the $^{31}$P channel (in the high to low frequency direction), then matching and tuning the $^{1}$H channel in the same manner. With all of those precautions in place, the phasing of different CP-HETCOR spectra was found to be extremely stable, keeping a consistent value over a week of acquisition. This way, the "correct" phase could be established on a CP spectrum with a large amount of signal ($t_{cp}$ = 5 ms), then applied throughout the CP-HETCOR series. No additional 1$^{st}$ order phasing was needed on any slice of the 2D experiment, nor was any additional phasing needed in the F1 dimension.

### III.2.4. Other acquisition parameters and referencing

The initial $^{1}$H 90° "read" pulse was 4 µs long, which corresponds to a radiofrequency of 62.5 kHz. A presaturation pulse train was added on the $^{31}$P channel, which consisted of an initial 90° pulse (4 µs, 62.5 kHz) followed by a precession period of 20 ms, repeated 20 times over. After the CP contact pulse, the pre-scan delay was set to 5.0 µs, which was found sufficient to remove ringing from the FID without distorting the baseline. The digitization mode chosen in Topspin was baseopt, although under modes were not found to influence the acquisition. A 62.5 kHz spinal-64 heteronuclear decoupling sequence is applied to the $^{1}$H dimension during the 21 ms $^{31}$P acquisition. The acquisition mode for the F1 dimension was States-TPPI.

The $^{31}$P dimension was referenced to an 85% $H_3PO_4$ solution, set to 0.0 ppm. The $^{1}$H dimension was referenced to adamantane, setting the signal to 1.75 ppm or indirectly with the OH signal of HAp (at 0.0 ppm).

## IV. Analysis of model samples by 2D CP-HETCOR

Variable-$t_{cp}$ CP-HETCOR spectra were recorded for the three model samples HA_BM, CHA_BM and HA_NA. The three series were fitted using the previously described "Series 3" method: peak positions, amplitudes, and $^{31}P$ FWHM were variable, while $^{1}H$ FWHM of $HPO_4^{2-}$ and g/l ratios were set based on averaged values over the series.

The initial fit parameters chosen for all synthetic samples (on the basis of a preliminary fit using the Series 1 method) were the following:

| Peak | Pos(X) | | | Pos(Y) | | | Amp | FWHM(X) | | | FWHM(Y) | | | gl(X) | gl(Y) |
|---|---|---|---|---|---|---|---|---|---|---|---|---|---|---|---|
| n | min | δ $^{31}P$ (ppm) | max | min | δ $^{1}H$ (ppm) | max | | min | FWHM $^{31}P$ (ppm) | max | min | FWHM $^{1}H$ (ppm) | max | | |
| **1** | 0.1 | 3.0* | 6.0 | -0.2 | 0.00* | 1.0 | 1.0* | 0.5 | 3.0* | 3.5 | 0.0 | 1.0* | 3.0 | 0.5 | 0.2 |
| **2** | 0.1 | 3.0* | 6.0 | 4.9 | 5.50* | 7.5 | 1.0* | 1.5 | 5.5* | 10.0 | 0.0 | 4.2* | 8.0 | 0.5 | 0.0 |
| **3** | 0.1 | 3.0* | 6.0 | 7.5 | 12.9 | 15.0 | 1.0* | 1.5 | 6.0* | 10.0 | 8.0 | 9.7 | 20.0 | 1.0 | 0.0 |

*Table 18: Initial parameters for the fitting of the three CP-HETCOR series (Figure 36) of synthetic HA samples, following the Series 3 method. The $^{1}H$ position* and FWHM *of the $HPO_4^{2-}$ peak was fixed in this comparison.*

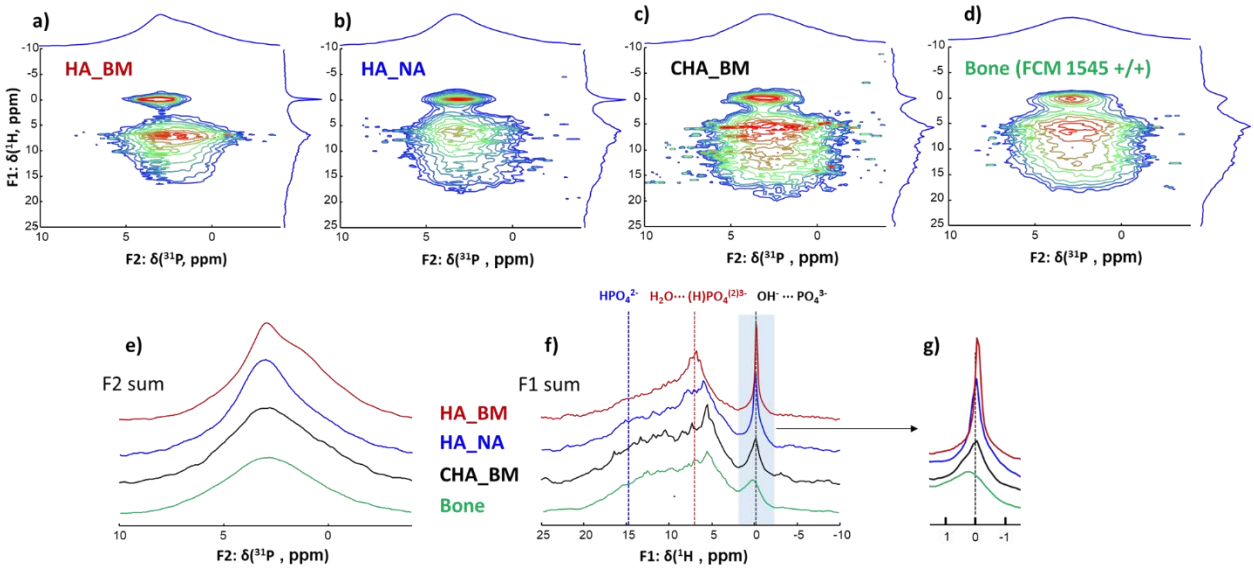


*Figure 36: Top: comparison of the CP-HETCOR signal at $t_{cp}$ = 0.2 ms of four samples: a) HA_BM, b) HA_NA c) CHA_BM d) mouse cortical bone FCM 1545 +/+. $B_0$ = 7.04 T, $\nu_r$ = 14 kHz, TD (F1) = 62, NUS. HA_BM: ns=16, RD=2.5 s. HA_NA: ns=32, RD=2.0 s. CHA_BM: ns=64, RD=2.8 s. FCM 1545 +/+: ns = 64, D1 = 2.0 s. Bottom: comparison of the e) F2 and f) F1 sums for these three phases, with g) a highlight on the 0 ppm peak of the F1 sum. All acquisitions used identical processing (with contour levels incremented by a fixed percentage of the maximum intensity) and acquisition parameters (aside from the ones listed above).*

Comparing the CP-HETCOR spectra at a given contact time (Figure 36), we can already observe significant differences between the samples. All fours samples have a strongly asymmetrical $^{31}P$ peak, with a maximum around 3.0-3.1 ppm. The asymmetry is nonetheless different in the four cases (Figure 36-d). HA_BM shows a narrow peak at the maximum with a broad shoulder at ~2 ppm. CHA_BM and bone sample, in contrast, have a broader resonance with no distinct shoulder, but still show a significant misalignment between the maxima and the center of gravity of the peak. This is explained when looking at the CP-HETCOR correlation maps, where we observe an $OH^-$ resonance which is much narrower in both dimensions for HA_BM and a significant difference in chemical shift between the $^{31}P$ signals correlating with the $OH^-$ peak and the other "surface" $^1H$ sites ($H_2O$ and $HPO_4^{2-}$), when compared to the other two samples. The $H_2O \cdots (H)PO_4^{(2)3-}$ correlation peak is also of interest, with a higher frequency $^1H$ maximum for HA_BM (7.1 ppm) than for HA_NA (6.2 ppm) and CHA_BM (5.6 ppm). However, as shown previously, the peak positions can vary with $t_{CP}$ (Figure 35), because a peak can actually be the superposition of two components with different CP dynamics. This point will be further discussed later.

### IV.1. CP buildup parameters

For better comparison of the 3 synthetic samples, it is therefore best to look directly at the fitted parameters of the variable-$t_{cp}$ 2D fit of CP-HETCOR spectra of all three sites (Figure 37), after having started from the initial parameters listed above (Table 18). Note that the $HPO_4^{2-}$ peak had its position fixed due to a high uncertainty in the case of HA_BM at high contact times. This fortunately had little effect on the other parameters of the series, as the $^1H$ position of the $HPO_4^{2-}$ peak had very small changes (0.2 ppm) when left as a variable.

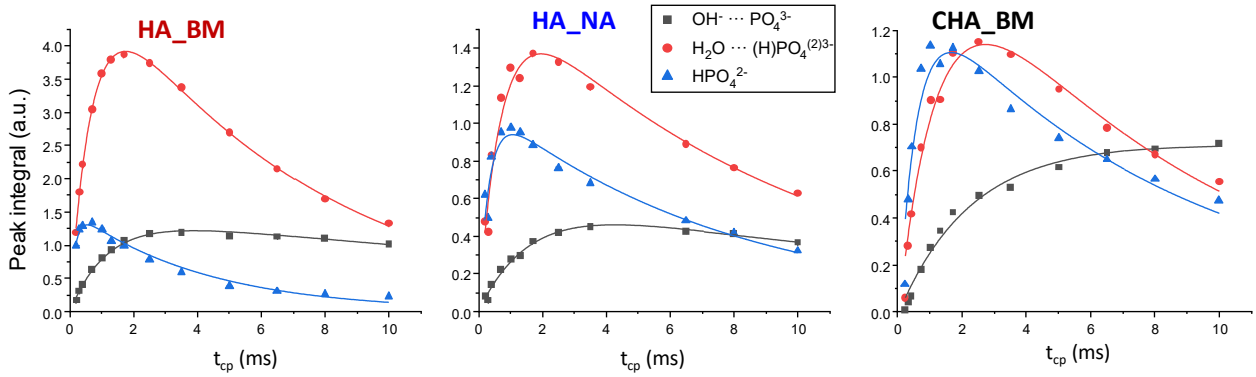


*Figure 37: Intensity of the $^1H$-$^{31}P$ CP-HETCOR correlation peaks over the contact time for all three synthetic samples. Initial fitting parameters in Table 18, using the method from Series 3. Note that HA_NA is missing its $t_{cp}$ = 5.0 ms data-points, due to an unreadable acquisition file.*

Observing the amplitude of the different peaks over the contact time yields a few interesting observations. First, the HA_NA and HA_BM curves can be fitted with the double-exponential expression of the I-S model satisfyingly, although they exhibit somewhat different CP dynamics (Figure 37, Table 19). Their $T_{CP}$ values systematically decrease in the order $HPO_4^{2-} < H_2O \cdots (H)PO_4^{(2)3-} < OH^- \cdots PO_4^{3-}$, consistently with expected decreasing H-P distances and decreasing $^1H$-

$^{31}$P dipolar couplings. In addition, the longer $T_{1\rho}^{1H}$ values of $OH^- \cdots PO_4^{3-}$ may reflect the weaker spin-lattice interaction in its apatitic environment.

| HA_BM | | | |
|---|---|---|---|
| **Component** | **$OH^- \cdots PO_4^{3-}$** | **$H_2O \cdots (H)PO_4^{(2)3-}$** | **$HPO_4^{2-}$** |
| **$I_0$ (a.u.)** | 1.40 ± 0.08 | 5.07 ± 0.10 | 1.49 ± 0.06 |
| **$I_0$ (% of total)** | 14.8 ± 0.6 % | 65.9 ± 2.1 % | 19.3 ± 0.9 % |
| **$T_{CP}$ (ms)** | 0.90 ± 0.07 | 0.69 ± 0.02 | 0.16 ± 0.02 |
| **$T_{1\rho}^{1H}$ (ms)** | >> 10 ms | 6.79 ± 0.22 | 4.16 ± 0.29 |
| **$R^2$ (COD)** | 0.99 | 0.99 | 0.99 |

| HA_NA | | | |
|---|---|---|---|
| **Component** | **$OH^- \cdots PO_4^{3-}$** | **$H_2O \cdots (H)PO_4^{(2)3-}$** | **$HPO_4^{2-}$** |
| **$I_0$ (a.u.)** | 0.42 ± 0.01 | 1.70 ± 0.13 | 1.10 ± 0.04 |
| **$I_0$ (% of total)** | 13.1 ± 0.9 % | 52.8 ± 5.0 % | 34.1 ± 2.3 % |
| **$T_{CP}$ (ms)** | 1.00 ± 0.10 | 0.69 ± 0.09 | 0.32 ± 0.02 |
| **$T_{1\rho}^{1H}$ (ms)** | >> 10 ms | 9.13 ± 1.41 | 7.62 ± 0.60 |
| **$R^2$ (COD)** | 0.97 | 0.96 | 0.97 |

| CHA_BM | | | |
|---|---|---|---|
| **Component** | **$OH^- \cdots PO_4^{3-}$** | **$H_2O \cdots (H)PO_4^{(2)3-}$** | **$HPO_4^{2-}$** |
| **$I_0$ (a.u.)** | 0.72 ± 0.02 | 1.64 ± 0.17 | 1.35 ± 0.12 |
| **$I_0$ (% of total)** | 19.3 ± 1.8 % | 44.2 ± 6.0 % | 36.5 ± 4.6 % |
| **$T_{CP}$ (ms)** | 2.25 ± 0.20 | 1.27 ± 0.21 | 0.57 ± 0.12 |
| **$T_{1\rho}^{1H}$ (ms)** | >> 10 ms | 7.43 ± 1.42 | 8.06 ± 1.64 |
| **$R^2$ (COD)** | 0.98 | 0.96 | 0.87 |

*Table 19: Fitting parameters of CP buildups (Figure 37) of the three synthetic samples, on the basis of the I-S model (Series 3). *Fit did not converge, uncertainty greater than the fitted values*.

An interesting observation can be made when measuring the intensities as a percentage of the total CP signal. The proportion of the signal attributable to the $OH^-$ resonance in HA_BM, CHA_BM and HA_NA are roughly similar relative to the "surface" signal. However, the higher percentage in CHA_BM is puzzling given the B-type substitutions that should lower the $OH^-$ content relative to the other samples. Given the limitations we have found on the accuracy of the CP buildup curves, we should not try to interpret this data any further.

## IV.2. Peak positions and widths

The analysis of the fitted peak positions and widths in the $^{31}P$ dimension shows puzzling differences between the samples (Figure 38). Given the typical description of biomimetic apatite nanocrystals (core-shell model with a hydrated surface, see Figure 1), we would expect to see two main $^{31}P$ contributions (one for the core, and one for the surface). More specifically, the protonated species of the hydrated surface (e.g. $HPO_4^{2-}$, $H_2O$) should correlate with the $^{31}P$ sites of the surface, and the core $OH^-$ with the $PO_4^{3-}$ ions of the crystalline core. Instead, we see a significant variation in the $^{31}P$ position of all three signals from one sample to the next.

For the $OH^- \cdots PO_4^{3-}$ cross-peaks (black squares in Figure 38), a nearly constant $^{31}P$ chemical shift and peak width is observed, regardless of the $t_{CP}$ value. The peak width of this correlation increases from the least substituted apatite (HA_BM) to the most substituted ones (HA_NA and CHA_BM), in line with a larger variety of local environments for the $OH^-$ groups, as $Na^+$ and $CO_3^{2-}$ ions enter the HA lattice.

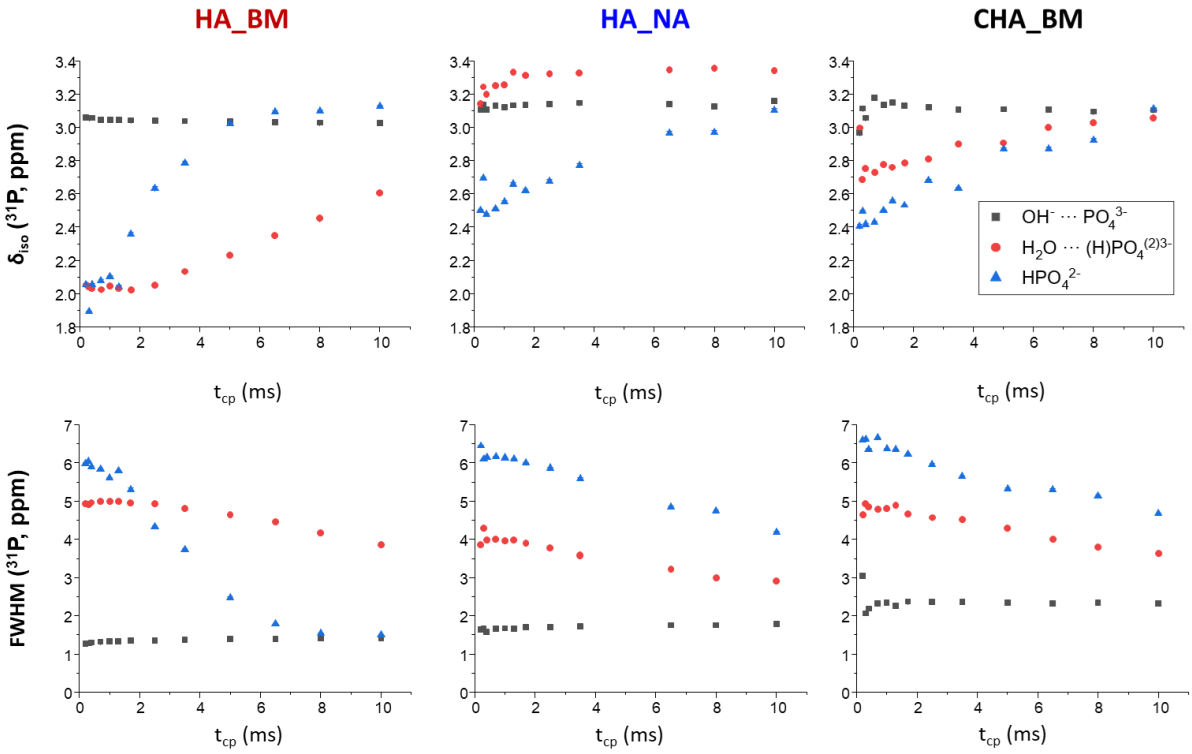


*Figure 38: Evolution of the $^{31}P$ fitting parameters (namely position and FWHM) over the contact time for all three synthetic samples. The CP-dynamics parameters are given in Table 19, experimental parameters as in Figure 36. Note the strong variations between samples in the relative $\delta_{iso}(^{31}P)$ of the signals.*

The $HPO_4^{2-}$ correlations (blue triangles in Figure 38) show a smaller $\delta_{iso}(^{31}P)$ at low contact times (~2.0 ppm for HA_BM, and ~2.5 ppm for HA_NA and CHA_BM) which increases gradually with the contact time to *ca.* 3.0 ppm. This implies that there are at least two types of $HPO_4^{2-}$ chemical environments, leading to at least two different possible chemical shift values. Given that the low $\delta_{iso}(^{31}P)$ environment is more intense at low contact times and the high-frequency $HPO_4^{2-}$ $\delta_{iso}(^{31}P)$ is predominant at high contact times, this indicates that there is a difference in CP dynamics between the two.

The most puzzling aspect of the peak positions is the $\delta_{iso}(^{31}P)$ evolution of the $H_2O$ ··· $(H)PO_4^{(2)3-}$ signal (red circles in Figure 38). Below, we will refer to it as the $H_2O$ cross-correlation/peak for the sake of simplicity. In the HA_BM sample, it starts at a chemical shift of 2.0 ppm at low contact times, and increases slowly with increasing contact times, up to 2.6 ppm (although the trend line suggests it may continue to increase past 10 ms of $t_{cp}$). To explain the behavior of this cross-peak, we have looked in closer detail at the CP-HETCOR signal. In particular, we have studied the changes to the $H_2O$ cross-peak lineshape over the contact time (Figure 39).

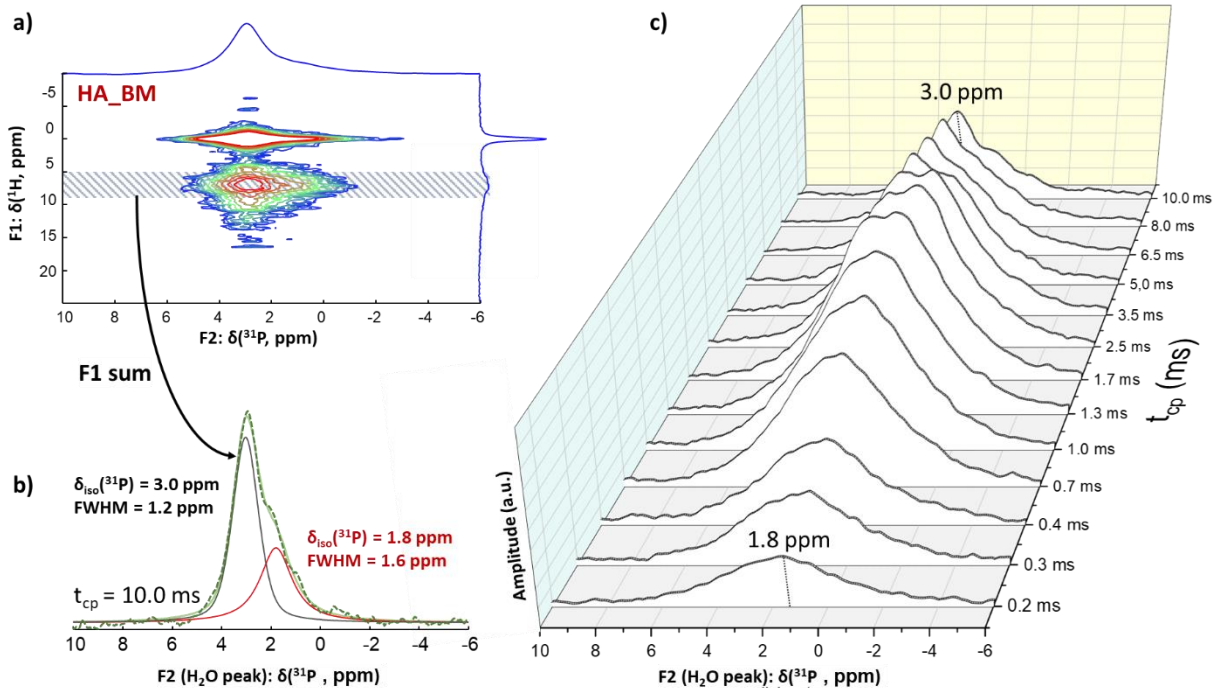


*Figure 39: a) CP-HETCOR of HA_BM at $t_{cp}$ = 10.0 ms. b) Sum of the 5.0 – 9.0 ppm (F1) area onto the F2 dimension, with a decomposition by two Gaussian peaks (DMfit). c) Comparison of the $H_2O$··· $(H)PO_4^{(2)3-}$ signal projection onto F2 of the CP-HETCOR experiments for HA_BM at different contact times. The $H_2O$ cross-peak was obtained by summing the F2 slices over the F1 dimension, from 5.0 ppm to 9.0 ppm. To avoid the appearance of non-uniform noise, this series was recorded using a US scheme (TD = 450, AQ = 16 ms). $B_0$ = 7.04T, $\nu_r$ = 14 kHz, ns = 8, RD = 2.5 s, $t_{exp}$ = 32h). The partial phase cycling of the series of experiments gave a non-zero baseline, but otherwise had no impact on the lineshape or phasing when compared to the NUS series.*

Here, for HA_BM (and only this sample), we see that different resonances can be observed depending on the $t_{cp}$. At $t_{cp}$ = 3.5 ms, two $^{31}P$ maxima of nearly equal intensity are very clearly visible. The first, wider peak, is predominant at low contact time, and is centered at $\delta_{iso}(^{31}P) \approx 1.8$ ppm. The second narrower resonance becomes more intense at contact times above 5 ms, and has a $^{31}P$ chemical shift of 3.0 ppm. The presence of at least two resonances with different chemical shifts that explain the evolutions seen in Figure 38, both the increasing $\delta_{iso}$ and decreasing FWHM over $t_{cp}$. A similar finding can be made concerning the $HPO_4^{2-}$ correlation peak (not pictured here), with a $^{31}P$ lineshape that can be decomposed into a 1.5 ppm shoulder (favored at short $t_{cp}$) and a sharper 3.0 ppm resonance. This is not, however, the case of the $OH^-$ cross-peak, which is relatively constant in width and position in the $^{31}P$ dimension, regardless of the $t_{cp}$ value. We will discuss the implications of this finding later on, and will first attempt to explain the parameters of the other series.

In contrast with HA_BM, HA_NA and CHA_BM do not have the same resolution in the $^{31}P$ dimension that HA_BM has, both due to a higher level of substitution (leading to a larger diversity of $^{31}P$ local environments), and a smaller range of chemical shifts for the $^{31}P$ NMR maxima. As a result, we do not see any resolved individual peaks when studying slices of each of the correlations, but rather broad asymmetric shoulders.

A very unexpected result for these synthetic samples is the $H_2O$ cross- peak position of HA_NA on the $^{31}P$ dimension, sitting between 3.0 ppm at short contact times and 3.3 ppm at long contact times, i.e. at values much higher than for the other two samples. Additionally, the $R^2$ value of HA_NA was below 0.9 at low contact times, implying an issue in the fit. To understand the origin of this higher-frequency peak, we plotted the difference between the simulated and experimental lineshapes (Figure 40). We noticed that HA_NA, unlike the other two samples, does not have a visually matching fit of the $^{31}P$ dimension of the 2D. The difference may therefore highlight hidden components that are not correctly described by the three-component model of apatite we have been using. From this difference, we can see a new resonance appear in negative, centered at $\delta_{iso}(^{31}P)$ = 3.5 ppm and $\delta_{iso}(^{1}H)$ = 0.0 ppm. It is broader than the $OH^-$ cross-correlation in both dimensions. Note that this new resonance cannot be eliminated by varying the g/l ratio of the $OH^-$ correlation in either dimension. Adding a new resonance to our model increases the $R^2$ of the $t_{cp}$ = 3.5 ms fit from 0.976 to 0.988. This places the new peak at [3.3 ppm; -0.2 ppm] with widths of [2.8 ppm; 2.4 ppm] in the F2 and F1 dimensions respectively. Compared to the $OH^-$ - $PO_4^{3-}$ resonance, with its $\delta_{iso}$ of [3.1 ppm; 0.0 ppm] and its width of [1.6 ppm, 0.3 ppm], it is much broader in the F2 but especially F1 dimension. This could be the resonance of a different type of apatitic $OH^-$, presumably one that is close to an $Na^+$ substitution.

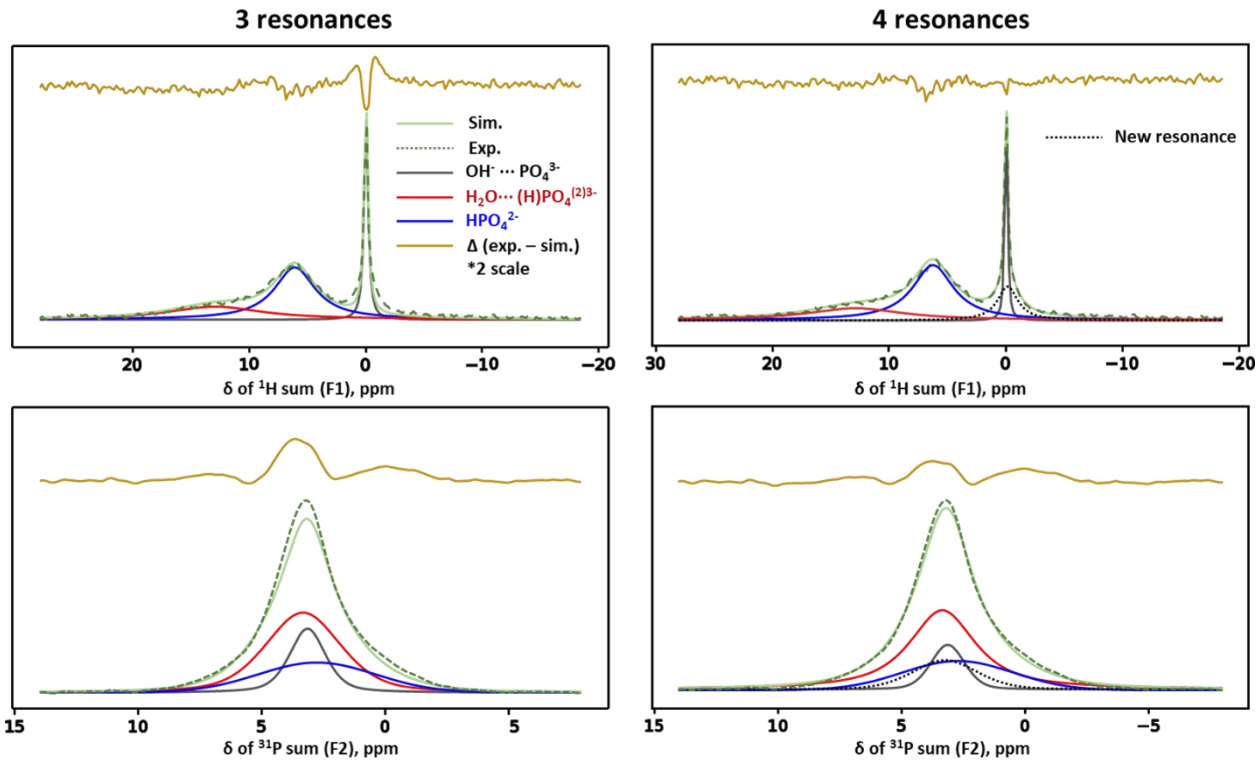


*Figure 40: $^{1}H$ (top) and $^{31}P$ (bottom) projections of the 2D fitting of the $t_{cp}$ = 3.5 ms CP-HETCOR spectrum of HA_NA. The golden line (scaled by a factor of 2) represents the difference between experimental data (dashed green line) and simulated lineshape (solid lines).*

Let us finish with the analysis of the CHA_BM sample (Figure 38, right). We remind the reader that this carbonated apatite is also expected to have some sodium content,[49] due to the use of $NaHCO_3$ as a carbonated precursor (although no explicit measurement was done on the sample). Here, we observe that both the $H_2O$ and $HPO_4^{2-}$ cross-peaks start at a lower $^{31}P$ chemical shift than the $OH^-$ one (2.7 and 2.4 ppm *vs.* 3.1 ppm respectively), but trend towards 3.1 ppm with increasing $t_{cp}$ (Figure 38). Like the other two samples, their $^{31}P$ FWHM decrease gradually from low to high $t_{cp}$, while the width of the $OH^-$ resonance stays unchanged regardless of the $t_{cp}$. In addition, note that the $^{1}H$ FWHM of the $OH^-$ resonance is much broader than that of the other two samples, at 1.0 ppm (compared to 0.35 and 0.40 ppm for HA_BM and HA_NM). These factors taken together seem indicative that CHA_BM apatite has a much more disordered core and surface due to the high degree of carbonate substitution.

Our analysis of the synthetic "model" phases has therefore shown that the 2D fitting of variable-$t_{cp}$ CP-HETCOR spectra potentially gives access to a wealth of structural information, even if the resolution of the spectra due to the relatively low field and spinning speed limits the depth of our analysis, especially in disordered samples like CHA_BM. Yet, we have to keep in mind that describing these spectra with three evolving (in chemical shift and width) components is a simplification of multiple underlying peaks.

In conclusion, the analysis of these model phases shows many features of synthetic HAps not evidenced in previous studies performed by $^{1}H$ and $^{31}P$ NMR. The choice of an automatic, homemade fitting script was found to be pertinent due to the speed and reproducibility of the fits. It would be possible to push this method much further, both with an increase in resolution and sensitivity, and with the addition of other nuclei and other analytical techniques. Some of these analyses will be explored later on in this chapter, while others remain beyond the scope of this study. Prime among the latter would be $^{23}Na$-$^{31}P$ and $^{13}C$-$^{31}P$ NMR correlation experiments,[50,51] which would help support some of the hypotheses detailed above (but may require a significant investment in spectrometer time). Before we stray too far from the original goal, let us focus back onto the analysis of bone mineral in $LPA_1$-/- mice animal models, using 2D $^{1}H$ – $^{31}P$ NMR.

# V. Study of biological materials

## V.1. "Fresh" and "dry" samples

An important question for the results analysis was whether the samples needed the same hydration state in order to be comparable. It would be extra-challenging if the hydration state could change the NMR characteristics and/or relative intensities of the peaks studied here, especially because even a small amount of grinding dries out part of the sample. Note that weighing rotors before and after NMR analysis suggested partial drying (-0.1 mg compared to an initial mass of 16.0 mg) inside the rotor during the analysis. Therefore, possible impact on the observed NMR parameters had to be tested.

Two series of experiments were acquired on the sample FCM1550 -/-: one in November 2022 on a "fresh" sample, ground and packed as described previously right after being thawed for the first time, and a second series in January 2023 on the "dry" sample, after the contents of the rotor had been emptied, placed back into an Eppendorf, frozen, thawed again and re-packed. In both cases, nine NUS CP-HETCOR experiments with 64 scans per slice, at contact times ranging from 0.2 ms to 10.0 ms (with the series [0.2, 0.4, 0.7, 1.7, 2.5, 3.5, 6.5, 8.0, 10.0 ms]) were recorded and analyzed in the same conditions. After the 2D fitting procedure described above was applied, the results we obtained were the following (Figure 41 and Table 20).

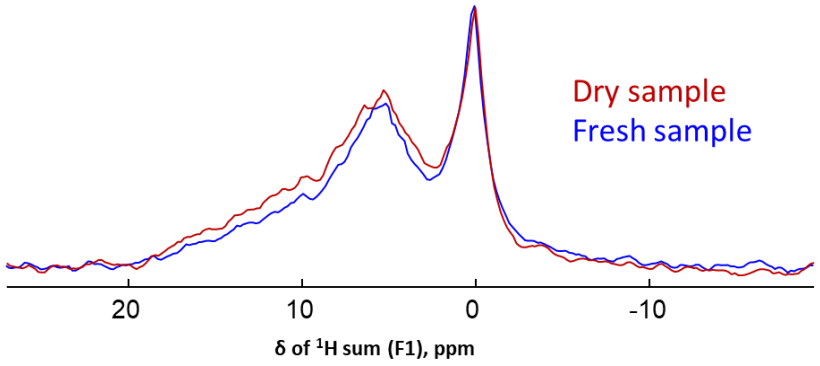


*Figure 41: F1 sum of the $t_{cp}$ = 3.5 ms CP-HETCOR spectra recorded for the "fresh" and "dry" FCM 1550 -/- ♂ sample. $B_0$ = 7.04T, $\nu_r$ = 14 kHz, ns = 8, RD = 2.0 s, $t_{exp}$ = 2 h. The spectra are unscaled. The mass of the sample was unchanged between acquisitions, with a ± 0.1 mg uncertainty.*

We observed that the drying of the sample has not significantly affected the position or width of the different peaks (see Figure 41 for the sum in the $^1$H dimension), but that it had a small impact on the CP dynamics for the sample, as shown in Table 20. The $T_{cp}$ values of the "fresh" sample were slightly longer than those of the dry sample, while their $T_{1\rho}$ are shorter. Nonetheless, variations were smaller compared to the range observed for apatitic model samples. Shorter $T_{CP}$ suggested higher dipolar couplings in the dry samples, consistently with a reduced mobility due to water loss. The small drying of the samples was not addressed as part of this work.

| FCM 1550 -/- ♂ "fresh" | | | |
|---|---|---|---|
| **Component** | **$OH^- \cdots PO_4^{3-}$** | **$H_2O \cdots (H)PO_4^{(2)3-}$** | **$HPO_4^{2-}$** |
| **$I_0$ (absolute)** | 3.5 ± 0.3 | 18.3 ± 1.6 | 11.0 ± 0.7 |
| **$I_0$ (% of total)** | 11.1 ± 1.1 % | 56.5 ± 4.4 % | 32.4 ± 2.1 % |
| **$T_{CP}$ (ms)** | 0.93 ± 0.30 | 0.78 ± 0.09 | 0.32 ± 0.03 |
| **$T_{1\rho}^{1H}$ (ms)** | >> 10 ms | 6.3 ± 0.6 | 5.2 ± 0.3 |
| **$R^2$ (COD)** | 0.85 | 0.98 | 0.99 |

| FCM 1550 -/- ♂ "dry" | | | |
|---|---|---|---|
| **Component** | **$OH^- \cdots PO_4^{3-}$** | **$H_2O \cdots (H)PO_4^{(2)3-}$** | **$HPO_4^{2-}$** |
| **$I_0$ (absolute)** | 3.8 ± 0.1 | 18.8 ± 0.8 | 11.0 ± 0.3 |
| **$I_0$ (% of total)** | 11.5 ± 0.4 % | 55.6 ± 3.0 % | 32.9 ± 1.5 % |
| **$T_{CP}$ (ms)** | 0.83 ± 0.04 | 0.67 ± 0.05 | 0.20 ± 0.02 |
| **(ms)** | >> 10 ms | 8.1 ± 0.8 | 5.3 ± 0.4 |
| **$R^2$ (COD)** | 0.98 | 0.99 | 0.98 |

*Table 20: Parameters of CP buildups, extracted from the fitting of the series of the CP-HETCOR experiments on the basis of the I-S model (Series 3) for the fresh and dry sample FCM1550 -/- m.*

## V.2. Processing

The data of all bone samples were processed identically using TopSpin (with lb = 50/50, si = 4k/256, constant F2 zero-order correction, no phasing on the F1 dimension, NUS processing as specified above). The 2D processing of the variable-$t_{cp}$ experiments proceeded as follows: using the same initial fitting parameters as the "Series 3" from the example buildup (Table 21), the CP-HETCOR series were then fitted automatically one after another.

| Peak | Pos(X) | | | Pos(Y) | | | Amp | FWHM(X) | | | FWHM(Y) | | | gl(X) | gl(Y) |
|---|---|---|---|---|---|---|---|---|---|---|---|---|---|---|---|
| n | min | δ $^{31}$P (ppm) | max | Min | δ $^{1}$H (ppm) | max | | min | FWHM $^{31}$P (ppm) | max | min | FWHM $^{1}$H (ppm) | max | | |
| **1** | 0.1 | 3.0* | 6.0 | -0.2 | 0.0* | 1.0 | 1.0* | 1.5 | 3.0* | 3.5 | 0.0 | 1.0* | 3.0 | 0.3 | 0.2 |
| **2** | 0.1 | 3.0* | 6.0 | 4.9 | 5.0* | 7.5 | 1.0* | 1.5 | 5.0* | 10.0 | 0.0 | 6.0* | 8.0 | 0.4 | 0.0 |
| **3** | 0.1 | 3.0* | 6.0 | 7.5 | 11.0* | 15.0 | 1.0* | 1.5 | 6.0* | 10.0 | 8.0 | 9.5 | 20.0 | 0.6 | 0.0 |

*Table 21: Initial fitting parameters for biological samples. * denotes a parameter that was treated as a variable.*

## V.3. CP dynamics and quantifications of the biological samples

Our script yielded fitted parameters for each spectrum of the series. The adequation of all fits was checked both visually and through the reported $R^2$ value. The intensities for each peak were then plotted and fitted over $t_{cp}$ using the I-S model of spin dynamics (Eq. 4). The corresponding CP dynamics parameters for all of the samples are summarized in Table 22. Note that FCM 120 -/-

was excluded from the study as its very small mass (5.5 mg) led to a very little signal, which proved to be too noisy to be reproducibly fit by the 2D fitting protocol, despite a relatively long acquisition time (three days).

| Component | $OH^- \cdots PO_4^{3-}$ | | | | $H_2O \cdots (H)PO_4^{(2)3-}$ | | | | $HPO_4^{2-}$ | | | |
|---|---|---|---|---|---|---|---|---|---|---|---|---|
| **Sample** | **$I_0$ (%)** | **$T_{cp}$ (ms)** | **$T_{1\rho}$ (ms)** | **$R^2$** | **$I_0$ (%)** | **$T_{cp}$ (ms)** | **$T_{1\rho}$ (ms)** | **$R^2$** | **$I_0$ (%)** | **$T_{cp}$ (ms)** | **$T_{1\rho}$ (ms)** | **$R^2$** |
| FCM 7 +/+ ♂ (fresh) | 12.2 ± 0.7 | 1.6 ± 0.1 | >> 10 | 0.99 | 57.2 ± 4.5 | 1.1 ± 0.1 | 9.5 ± 1.2 | 0.99 | 30.6 ± 2.3 | 0.40 ± 0.04 | 5.8 ± 0.9 | 0.94 |
| FCM 89 -/- ♀ (fresh) | 10.6 ± 0.8 | 2.3 ± 0.3 | >> 10 | 0.97 | 64.4 ± 1.8 | 2.0 ± 0.5 | 7.3 ± 2.7 | 0.98 | 24.9 ± 1.1 | 0.51 ± 0.08 | 7.4 ± 1.6 | 0.90 |
| FCM 99 +/+ ♂ (fresh) | 11.2 ± 0.8 | 0.9 ± 0.2 | >> 10 | 0.88 | 55.2 ± 4.4 | 0.60 ± 0.08 | 9.5 ± 1.3 | 0.96 | 33.6 ± 2.4 | 0.21 ± 0.03 | 7.6 ± 0.6 | 0.96 |
| FCM 114 +/+ ♂ (fresh) | 13.8 ± 0.6 | 1.5 ± 0.1 | >> 10 | 0.99 | 57.1 ± 2.9 | 1.1 ± 0.2 | 9.3 ± 2.4 | 0.96 | 29.2 ± 1.9 | 0.28 ± 0.03 | 7.6 ± 1.3 | 0.90 |
| FCM 190 -/- ♂ (dry) | 13.3 ± 0.6 | 0.85 ± 0.8 | >> 10 | 0.99 | 52.3 ± 3.4 | 0.71 ± 0.07 | 12.5 ± 1.9 | 0.98 | 34.5 ± 1.7 | 0.28 ± 0.02 | 7.1 ± 0.5 | 0.98 |
| FCM 1545 +/+ ♂ (dry) | 11.6 ± 1.3 | 1.0 ± 0.1 | >> 10 | 0.96 | 54.6 ± 8.6 | 0.8 ± 0.2 | 7.3 ± 1.7 | 0.98 | 33.9 ± 5.1 | 0.32 ± 0.07 | 5.2 ± 1.3 | 0.76 |
| FCM 1549 +/+ ♂ (fresh) | 14.5 ± 1.6 | 3.6 ± 0.4 | >> 10 | 0.98 | 57.4 ± 9.0 | 2.3 ± 0.4 | >> 10 | 0.99 | 28.2 ± 3.4 | 0.65 ± 0.08 | 9.9 ± 1.7 | 0.95 |
| FCM 1550 -/- ♂ (dry) | 11.5 ± 0.4 | 0.83 ± 0.04 | >> 10 | 0.99 | 55.6 ± 3.0 | 0.67 ± 0.05 | 8.1 ± 0.8 | 0.99 | 32.9 ± 1.5 | 0.20 ± 0.02 | 5.3 ± 0.4 | 0.94 |
| Mean ± σ (all bones) | 12.3 ± 1.3 | 1.6 ± 1.0 | >> 10 | 0.97 ± 0.03 | 56.7 ± 3.3 | 1.2 ± 0.6 | 9.1 ± 1.7 | 0.98 ± 0.01 | 30.9 ± 3.2 | 0.36 ± 0.15 | 7.0 ± 1.5 | 0.92 ± 0.06 |
| Mean ± σ (all +/+ bones) | 12.7 ± 1.3 | 1.7 ± 1.0 | >> 10 | 0.96 ± 0.04 | 56.3 ± 1.2 | 1.2 ± 0.6 | 8.9 ± 0.9 | 0.98 ± 0.01 | 31.7 ± 2.4 | 0.37 ± 0.15 | 7.4 ± 1.4 | 0.90 ± 0.07 |
| Mean ± σ (all -/- bones) | 11.8 ± 1.1 | 1.3 ± 0.6 | >> 10 | 0.98 ± 0.01 | 57.4 ± 5.1 | 1.1 ± 0.6 | 9.3 ± 2.3 | 0.98 ± 0.01 | 30.7 ± 4.2 | 0.33 ± 0.13 | 6.5 ± 0.9 | 0.94 ± 0.03 |
| MOL 1545 +/+ ♂ (fresh) | 16.0 ± 1.1 | 1.7 ± 0.2 | >> 10 | 0.96 | 55.4 ± 4.9 | 0.8 ± 0.1 | 9.9 ± 1.5 | 0.96 | 28.6 ± 2.3 | 0.25 ± 0.04 | 8.9 ± 1.3 | 0.87 |
| IN 1545 +/+ ♂ (fresh) | 12.9 ± 0.7 | 1.7 ± 0.1 | >> 10 | 0.98 | 53.5 ± 3.9 | 0.8 ± 0.1 | 6.6 ± 0.7 | 0.97 | 33.6 ± 1.6 | 0.25 ± 0.02 | 6.4 ± 0.3 | 0.98 |
| FCM 120 -/- ♀ | Did not converge (very low s/n) | | | | | | | | | | | |

*Table 22: CP dynamics parameters for all biological samples in this study, with CP-buildup curves fitted with the I-S model (Eq. 4). $I_0$ is expressed as the % of the sums of $I_0$ (with the error margin adjusted to reflect the error of the sum). Note that the fit of the molar sample was done using initial fitting parameters adjusted for bone samples, modifying slightly the measured CP dynamics compared to previously presented results. These values should be considered solely for comparisons to bone.*

The quantifications obtained for the different samples of the study are notably consistent (Figure 42). Given the natural variability of biological samples and the large variations in CP dynamics between the samples, we may expect a wide distribution of $I_0$. Yet for the different components, the standard deviation for the series is smaller than 10% of the mean. For the characteristic $OH^-$ ··· $PO_4^{3-}$ component, the normalized $I_0$ in bone samples (FCM) ranges from 10.6 ± 0.8 to 14.5 ± 1.6 %, with a mean of 12.3 ± 1.3 %. This is in contrast to a large variation in CP dynamics: for the same peak, the values of $T_{cp}$ range from 0.83 ± 0.04 ms (FCM 1550) up to 3.6 ± 0.4 ms (FCM1549), with a mean value of 1.6 ± 1.0 ms.

The value of $I_0$ for the $OH^-$ ··· $PO_4^{3-}$ component is also comparable to the values obtained for the biomimetic apatites (Table 19), for which the values were 14.8%, 13.1% and 19.3% for HA_BM, HA_NA and CHA_BM respectively. This consistency, as well as similarities in CP time constants, confirm the similarity of these samples to our bone.

Comparing the two groups against one another yields no significant difference between the bone mineral components of +/+ and -/- mice. From the perspective of these $^1H$-$^{31}P$ 2D NMR analyses, the bone minerals are therefore comparable in the two cases, down to an error margin of *ca.* 10% of the reported values.

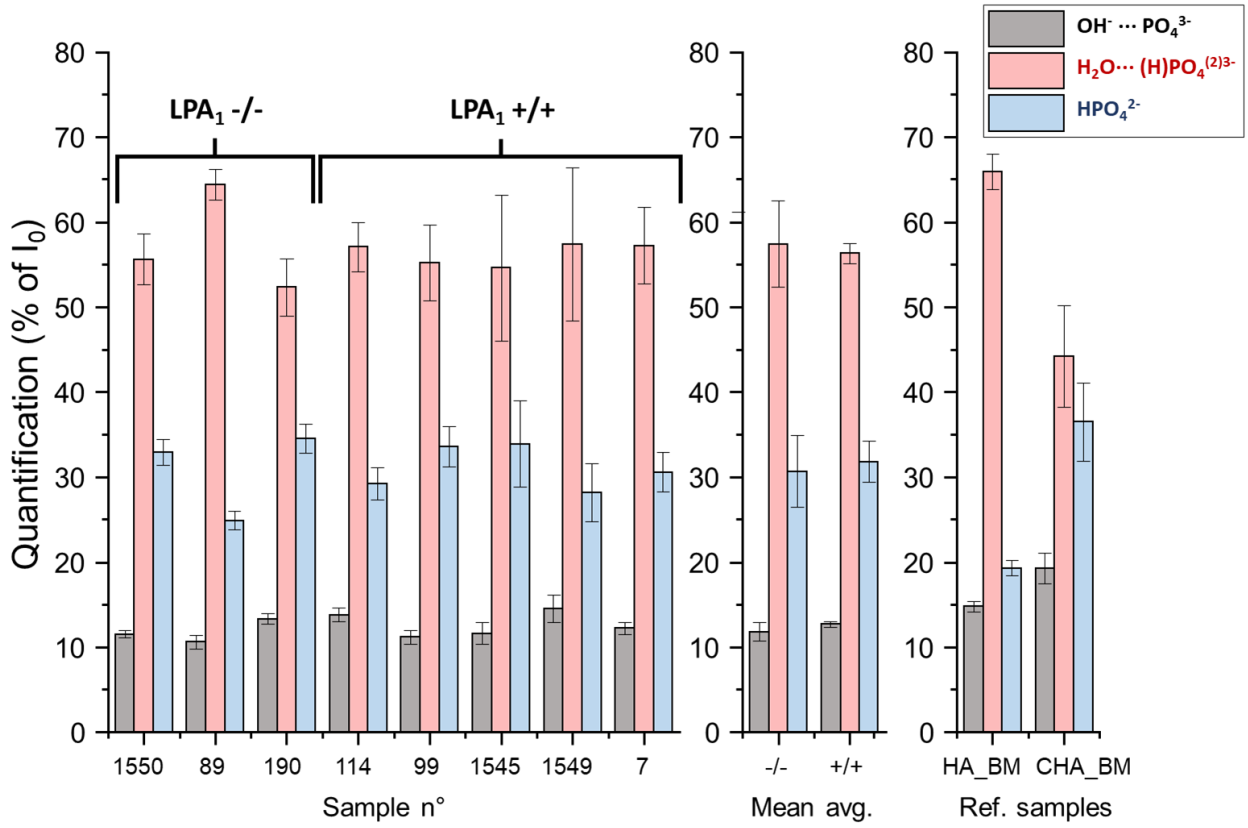


*Figure 42: Histogram showing the relative $I_0$ values (in %) for the different biological samples in this study and two synthetic models, expressed as a percentage of the sum of $I_0$ for the sample.*

### V.4. $^{31}$P Peak positions and widths

In the same manner as in Figure 38, we plotted the peak position (Figure 43) and peak width (Figure 44) of the different components in the F2 dimension. For the different bone samples, the evolution of the peak width with the contact time appears homogeneous. The $OH^-$ cross-peak has an initial $^{31}$P peak width of 2.5 ppm, which remains nearly constant with the different contact times (Figure 44, black squares). As with the synthetic samples, the $H_2O$ and $HPO_4^{2-}$ correlation cross-peaks are initially wider (~6.2 and ~5.2 ppm respectively), and become narrower with increasing contact times (Figure 44, red circles and blue triangles). The most striking aspect of this evolution is its near uniformity in all samples: the width of the $H_2O$ cross-peak was always found to be narrower in the $^{31}$P dimension than the $HPO_4^{2-}$ cross-peak, regardless of their relative $T_{cp}$ and $T_{1\rho}$ values.

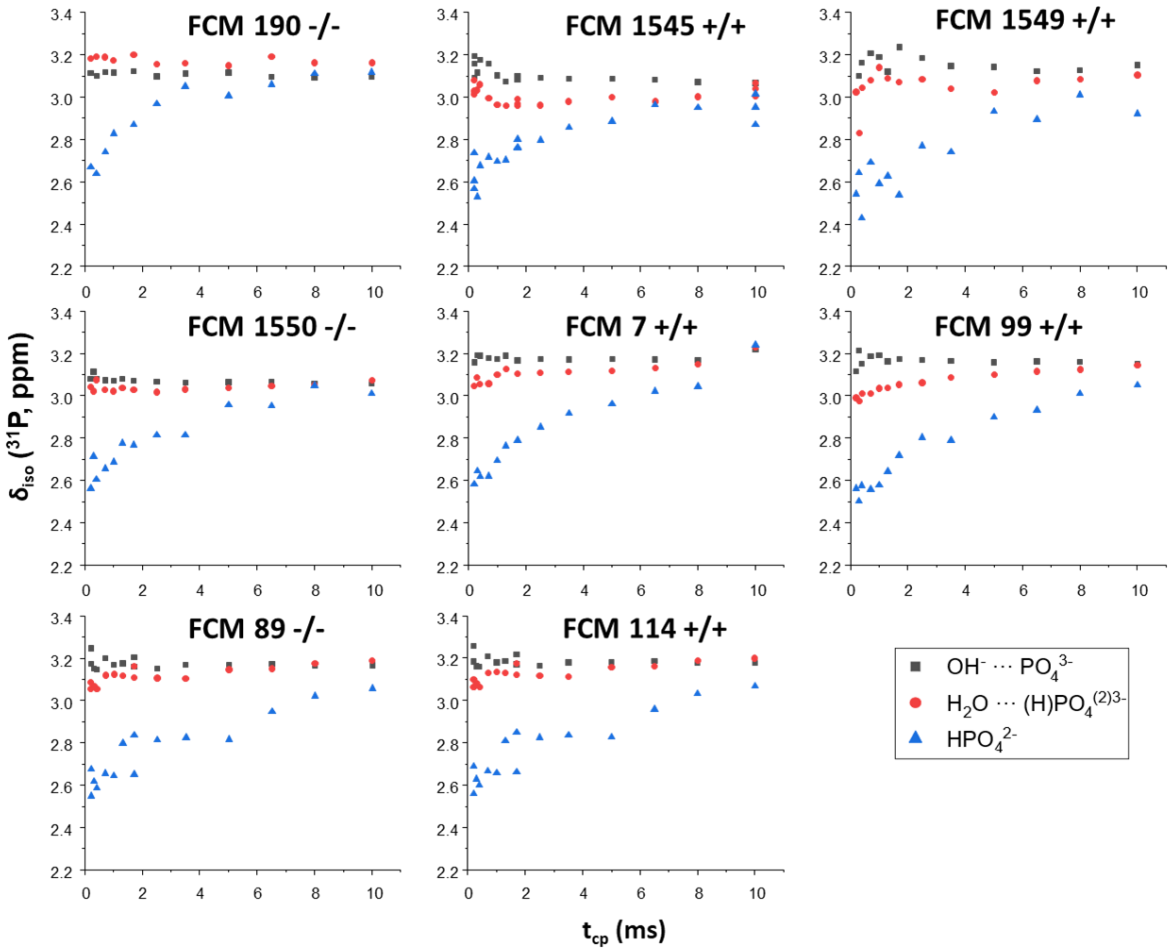


*Figure 43: $^{31}$P peak position at different contact times of the three components of the CP-HETCOR spectra for all bone samples (see for example Figure 45 for a representative 2D spectrum).*

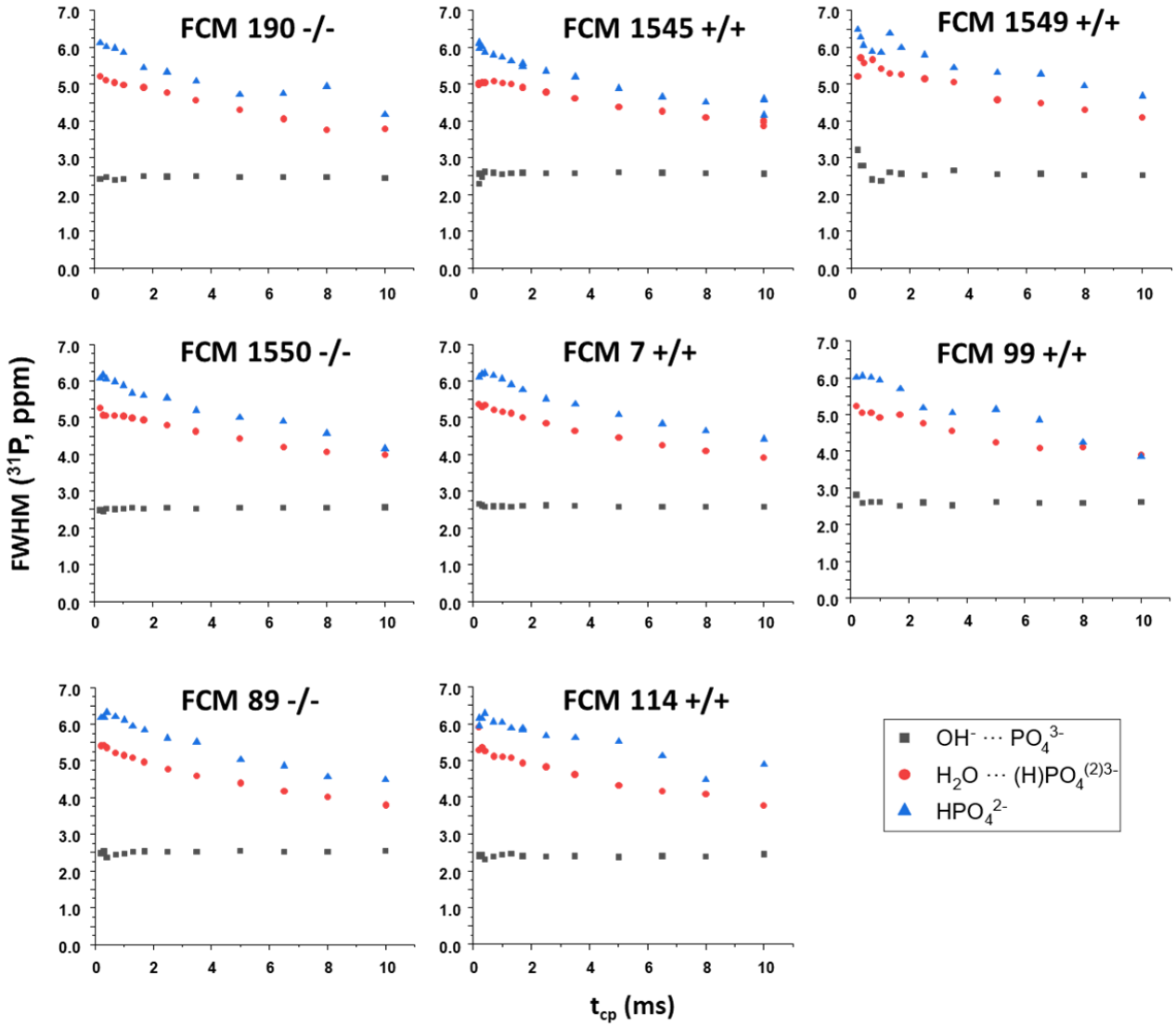


*Figure 44: $^{31}$P peak widths at different contact times of the three components of the CP-HETCOR spectra for all bone samples (see for example Figure 45 for a representative 2D spectrum).*

The $^{31}$P chemical shift data shows more variability between samples, although some features remain consistent from one to the next. As shown in Figure 43 (black squares), the $^{31}$P chemical shift related to the $OH^-$ cross-peak is stable with a chemical shift between 3.1 and 3.2 ppm, with some minor deviation at low chemical shift (ex: FCM1545 +/+) that can be explained by some minor phasing changes caused by measurement instabilities (manually correcting the phasing was found to cause more point-to-point discrepancies in the results). A common feature here is the gradual increase of the $HPO_4^{2-}$ $^{31}$P chemical shift from a low value of 2.6 ppm to a high one of 3.0-3.1 ppm (Figure 43, blue triangles). The $H_2O$ related cross-peak, in comparison, is more

inconsistent (Figure 43, red circles): in some samples (ex: FCM 99 +/+), it appears to have a $^{31}P$ chemical shift of ca. 3.0 ppm, lower than that of the $OH^-$ peak (3.2 ppm), which gradually increases over the contact time. In the FCM 190 -/- sample, however, the $H_2O$ related cross- peak appears to have a higher $^{31}P$ chemical shift than the $OH^-$ related cross- peak, which seems constant over the contact time (reminiscent of HA_NA). This difference is visible when taking a closer look at the FCM 190 CP-HETCOR correlation maps, and does not appear to be explainable by any particularity of the sample or experimental setup.

A new difficulty we encounter in interpreting these results is that it becomes difficult to tell what feature of a spectrum is causing differences in the F2 fitting data. For example, the $^{31}P$ chemical shift of the $H_2O$ related cross-peak is calculated to be roughly 0.15 ppm higher in FCM 190-/- than in FCM 1550-/- at all contact times. This is consistent when fitting the two experiments with different initial fitting parameters (Series 1, 3…), in different orders, or when using different processing parameters (with the F2 lb set to 100 or 50 Hz). Such differences are, however, essentially indistinguishable on spectra recorded at the same contact time (Figure 45). Indeed, aside from the difference in intensity of the $OH^-\cdots PO_4^{3-}$correlation (which is expected from the different quantifications), the difference in $^{31}P$ chemical shift of the components is almost invisible on the 2D correlation maps. This denotes the importance of developing alternative analysis methods (as developed in section VI) for the study of such CP-HETCOR maps, as there seems to still be information that we are not entirely able to extract from these spectra.

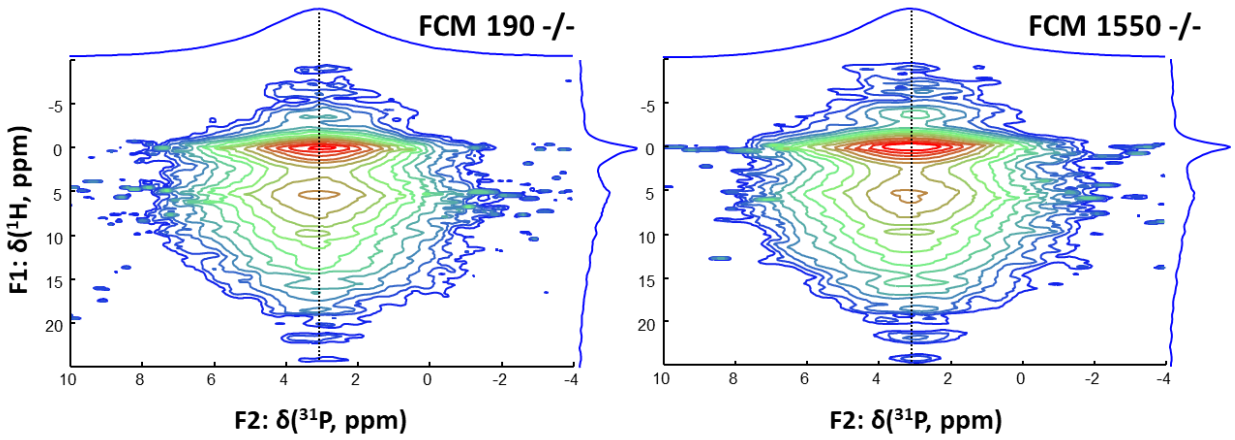


*Figure 45: CP-HETCOR spectra of FCM 190 -/- and FCM 1550 -/-, recorded at identical contact times ($t_{cp}$ = 6.5 ms; TD = 62 (NUS), $B_0$ = 7.04T, $\nu_r$ = 14 kHz, ns = 64, RD = 2 s, $t_{exp}$ = 2h).*

## V.5. $^{1}$H peak positions and widths

Similarly to the $^{31}$P dimension, no notable difference was seen in the $^{1}$H data of any one of the bone samples. We will only report below the data from two comparable bone samples with the highest signal/noise ratio, namely FCM 1550 -/- and FCM 1545 +/+ (Figure 46). In order to approximate an error margin for the data points, experiments at three contact times (0.2, 1.7, 10.0 ms) were each acquired three times over for FCM 1545 +/+. These were acquired out of order (chronologically) with the rest of the series.

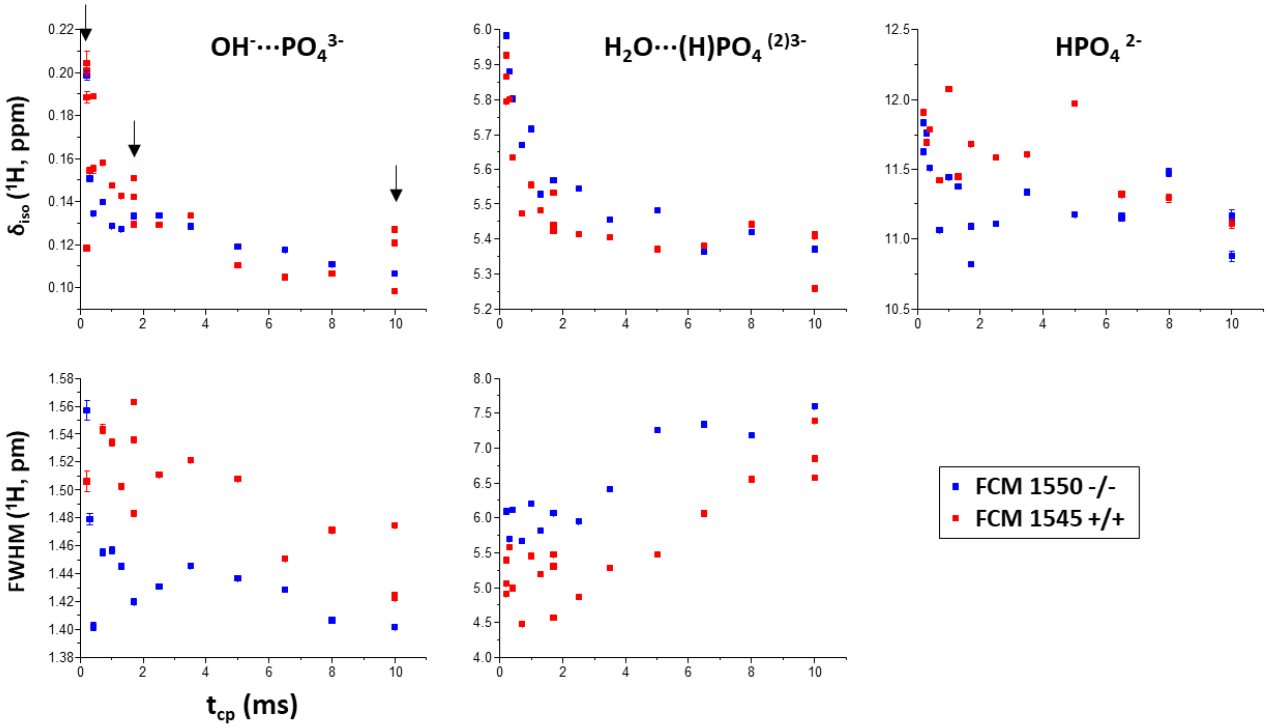


*Figure 46: $^{1}$H $\delta_{iso}$ and FWHM of the different resonances used in the 2D fitting routine, for the samples FCM 1550 -/- ♂ and FCM 1545 +/+ ♂. Note that for bone samples, the FWHM of the $HPO_4^{2-}$ resonance was fixed to 9.5 ppm. Note that three contact times (0.2, 1.7 and 10.0 ms) were acquired three times on FCM 1545 +/+, indicated by arrows on the first graph.*

As seen in Figure 46, the positions and linewidths of the cross peaks in the $^{1}$H dimension evolve along patterns that are relatively consistent between samples. Contrary to the $^{31}$P dimension, the $^{1}$H dimension shows a slight decrease in $\delta_{iso}$ and FWHM of the $OH^{-}\cdots PO_4^{3-}$ cross-peak with increasing contact times. In a similar manner, the $H_2O\cdots(H)PO_4^{(2)3-}$ correlation shows a decreasing $\delta_{iso}(^{1}H)$ with the contact time, associated with an increasing peak width. Lastly, the $HPO_4^{2-}$ $\delta_{iso}$ appears to decrease slightly with the contact time in the $^{1}$H dimension, although the trend is extremely weak. While these patterns are visible with samples available in "large quantities" such as FCM 1550 -/-and FCM 1545-/- (16.0 and 19.0 mg respectively), the higher noise level of other samples of the series make statistically significant comparisons between the different sample

types unfeasible. This reinforces the need for alternatives to the 2D fitting method for the comparison of these samples, and of comparisons at higher fields with higher signal/noise ratios.

In conclusion to this comparative analysis of $LPA_1$ -/- and $LPA_1$ +/+ bone samples, the variable-$t_{cp}$ experiments we conducted do not show significant differences in bone mineral, between mice with KO and WT bone phenotypes. In the initial study on these materials, ATR-IR analyses had shown that the proportion of mineral to organic phase were not significantly different between the two groups.[3] This, the authors concluded, was proof that the difference in bone quality reflected more differing levels of porosity inside of the bone, rather than a different chemical composition of the mineralized tissue (as seen in osteomalacia). Our study goes one step further, by showing that on the molecular level, the different local environments of bone mineral exist in similar ratios within the two types (Table 22). With an error margin of 10 % for all three components, the statistical strength of the result is greater than that obtained using the initial IR study. Our method therefore allows us to actually compare the composition of bone mineral, in relative terms. When compared to the other comparative analyses[1,2] of bone *via* solid state NMR, it has the advantage of providing a number of points of comparison between the samples ($^1$H quantification, $\delta_{iso}(^{31}P)$, FWHM ($^{31}$P)) which provides additional information about the underlying sites and disorder within the local environments of bone mineral.

Another interesting result from this study lies in the evolution of the peak width and position in the F2 ($^{31}$P) dimension (Figure 43, Figure 44). Because of the 2D fitting method, we are able to observe variations of NMR parameters in both dimensions. We revealed a significant shift in the phosphates $\delta_{iso}(^{31}P)$ correlating with the various $^1$H environments ($O\mathbf{H}^-$, $\mathbf{H}_2O$, $\mathbf{H}PO_4^{2-}$) at different contact times. From the earlier studies of model samples (Figure 39, Figure 40), we have seen evidence that this probably results from overlapping peaks with dissimilar CP dynamics.

One of the main limitations of the present work comes from the equipment used in this study. Because of the relatively low magnetic field strength (7.04 T) and MAS rotation rate (14 kHz), the $^1$H spectra we have analyzed are still broadened by residual dipolar couplings (Figure 14). Note that no Lee-Goldberg $^1$H decoupling was applied since this may alter the $^1$H lineshape and quantifications. This limits our ability to distinguish finer features of the spectra. Before we reach broader conclusions on the comparative analysis of bone, teeth and synthetic samples, in the next section, we will go over acquisitions done at higher fields that highlight the advantages of the higher resolution and signal. We will also review different methods for the analysis of these spectra.

## VI. Pushing 2D fitting further: variable-$t_{cp}$ CP-HETCOR at 14.1 T

$^{1}H$ – $^{31}P$ CP-HETCOR NMR experiments were also performed on a 14.1 T Varian VNMRS spectrometer using a 3.2 mm probe, spinning a zirconia rotor up to 20 kHz. Due to the limitations of the openVnmrJ software, NUS acquisitions could not be practically recorded, mandating the use of US. Three bone samples (which had already been analyzed and repacked) were analyzed: FCM 1545 +/+, FCM 1549 +/+ and FCM 1550 -/-. Unfortunately, the rotation of the samples was not optimal at the moment of the analyses: FCM 1549 had to be spun at 18 kHz instead of 20 kHz, as even several repackings and a layer of Teflon tape over the sample did not solve the instability issues encountered at higher rotation rates. A series of twelve CP-HETCOR experiments was recorded for each sample, with $t_{cp}$ values from 0.2 to 10.0 ms: [0.2, 0.3, 0.4, 0.7, 1.0, 1.7, 2.5, 3.5, 5.0, 6.5, 8.0, 10.0 ms]. In addition to the three bone samples, the CHA_BM sample was analyzed under similar conditions, with the addition of a spectrum at a contact time $t_{cp}$ = 1.3 ms. The recycle delays were set according to $T_1$ measurements *via* saturation-recovery experiments, with a recycle delay of 2.0 s for the bone samples, and of 3.5 s for CHA_BM. The length of the acquisition in the indirect dimension was set experimentally, with 84 slices for the bone samples and 90 for CHA_BM. The comparison of the spectra of CHA_BM at the 2 fields is shown in

Figure 47.

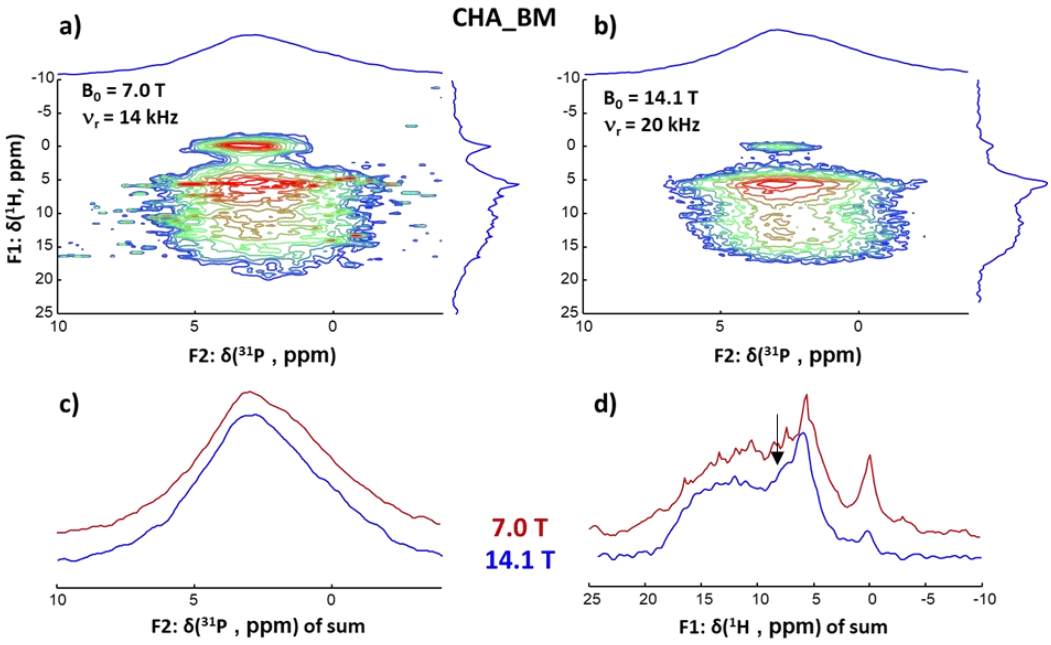


*Figure 47: Comparison of the $t_{cp}$ = 0.2 ms CP-HETCOR spectra of CHA_BM recorded a) on a $B_0$ = 7.04 T spectrometer ($\nu_r$ = 14 kHz, ns = 64, TD (F1) = 62 (NUS), RD = 2.8 s, $t_{exp}$ = 3 h). b) on a $B_0$ = 14.1 T spectrometer ($\nu_r$ = 20 kHz, ns = 48, TD (F1) = 90 (US), RD = 3.5 s, $t_{exp}$ = 4 h). c) Comparison of the sums over the F2 ($^{31}P$) dimension of the two spectra. d) Comparison of the sums over the F1 ($^{1}H$) dimension of the two spectra. Note the more obvious shoulder in the $H_2O$ region (6.5 ppm, arrow) at 14.1 T.*

The improvement in resolution and sensitivity makes it possible to distinguish new resonances that were not resolved at lower fields. A comparison of the two signals (Figure 47) shows that while no resolution gain can be achieved in the $^{31}P$ dimension due to a strong distribution of chemical shifts, the $^{1}H$ dimension shows slightly narrower peaks and the appearance of more obvious shoulders, particularly in the $H_2O$ region (around 6 ppm). This is problematic when attempting a 2D fit as described above: because of the larger number of resolved resonances, the number of parameters to be fitted simultaneously increases, along with the chances of overfitting. Our attempts to fit the sum over the F1 dimension of signals at various contact times showed that no less than six components were needed to match the experimental signal at longer contact times ($t_{cp}$ = 10.0 ms case illustrated in Figure 48). This prompted us to investigate new methods for the analysis of this signal, that could more efficiently distinguish these convoluted peaks.

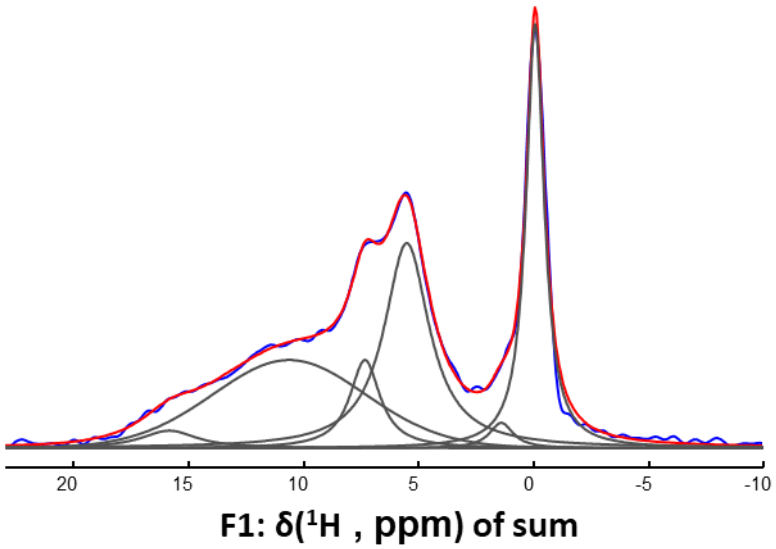


*Figure 48: Blue: Sum over the F1 ($^{1}H$) dimension of the CP-HETCOR signal of CHA-BM at $t_{cp}$ = 10.0 ms. Red: best fit using a sum of six Pseudo-Voigt peaks using DMfit. Grey: individual components of the lineshape. $B_0$ = 14.1 T, $\nu_r$ = 20 kHz, ns = 48, TD (F1) = 90 (US), RD = 3.5 s, $t_{exp}$ = 4 h.*

Up to this point, we have only analyzed our variable-$t_{cp}$ CP-HETCOR experiments using a single method: the successive 2D fitting of the individual spectra with three pseudo-Voigt peaks. This matches the experimental lineshape of most samples at low field, but the increased resolution at 14.1 T shows too many new resonances to fit accurately without distinguishing the underlying signals. However, increased signal opens up new possibilities for the analysis of the signal. We will present two new protocols in this section: the “point-by-point fitting” script and the “3D fitting” script.

### VI.1. "Point by point" fitting script

If two signals with significantly different CP dynamics are in close proximity on the CP-HETCOR spectrum (as seen with HA_BM, see Figure 39), it may be possible to discriminate them by $T_{cp}$ or $T_{1\rho}$ by measuring the CP dynamics for each point of the spectrum. For this purpose, this first script fits the intensity of each point of the CP-HETCOR spectrum over multiple contact times with the I-S model (Eq. 4). The values are then drawn onto a 2D color map (Figure 49).

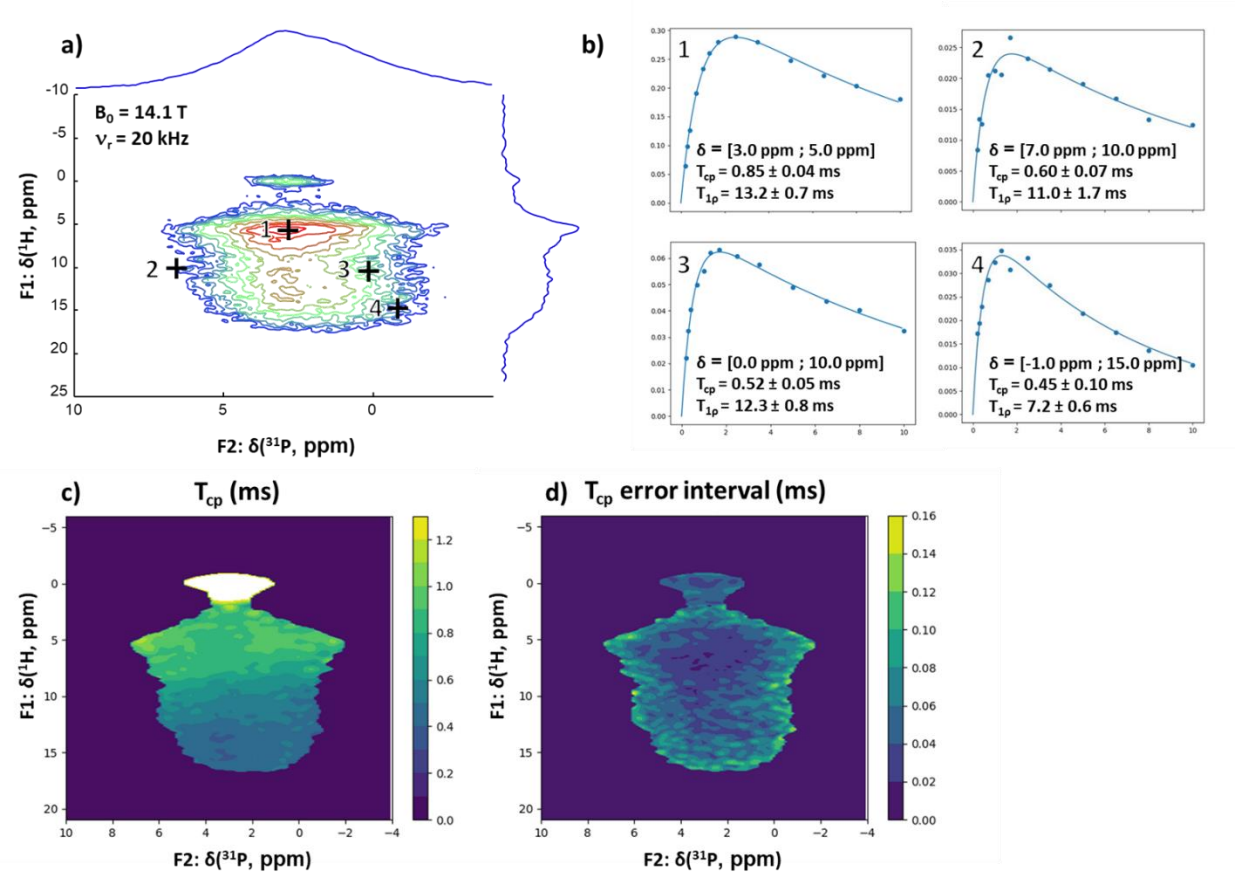


*Figure 49: Illustration of the "point by point" script: a) CP-HETCOR spectrum of CHA_BM at $t_{cp}$ = 0.2 ms ($B_0$ = 14.1 T, $\nu_r$ = 20 kHz, ns = 48, TD (F1) = 90 (US), RD = 3.5 s, $t_{exp}$ = 4 h). b) Fitting of the intensity of four example points of the spectrum at different contact times, using the I-S model. c) Color map of the fitted $T_{cp}$ values over the whole spectrum. d) Associated $T_{cp}$ error interval map.*

The operation of the script is straightforward: after locating the series from a *readparam.txt* file, it reads and stores in memory the intensity of the signal for each point of the spectrum. The points outside of the main signal are discarded (if their maximum is below 5% of the maximum of the series). The intensity is then fitted with a bi-exponential expression from the I-S model, and the fitted $T_{cp}$ and $T_{1\rho}$ are stored into a 2D matrix.

Because some resonances have $T_{1\rho}$ values that are too long to be accurately measured, the script may execute a second fit under the assumption of an infinite $T_{1\rho}$. If the error on $T_{1\rho}$ is greater than 30% of the fitted value, the script will attempt to fit it with a simplified I-S model that neglects the spin-lattice relaxation. If this does not improve the fit, the data is discarded and reported as a null value. $T_{CP}$ error interval corresponds to a 1σ confidence interval proposed by the fitting algorithm intensity at different contact times of individual points of the spectrum, using the I-S model.

The strength of this method is that it allows us to visualize differences in dynamics in different areas of the spectrum without any initial assumption about its underlying components (Figure 50).

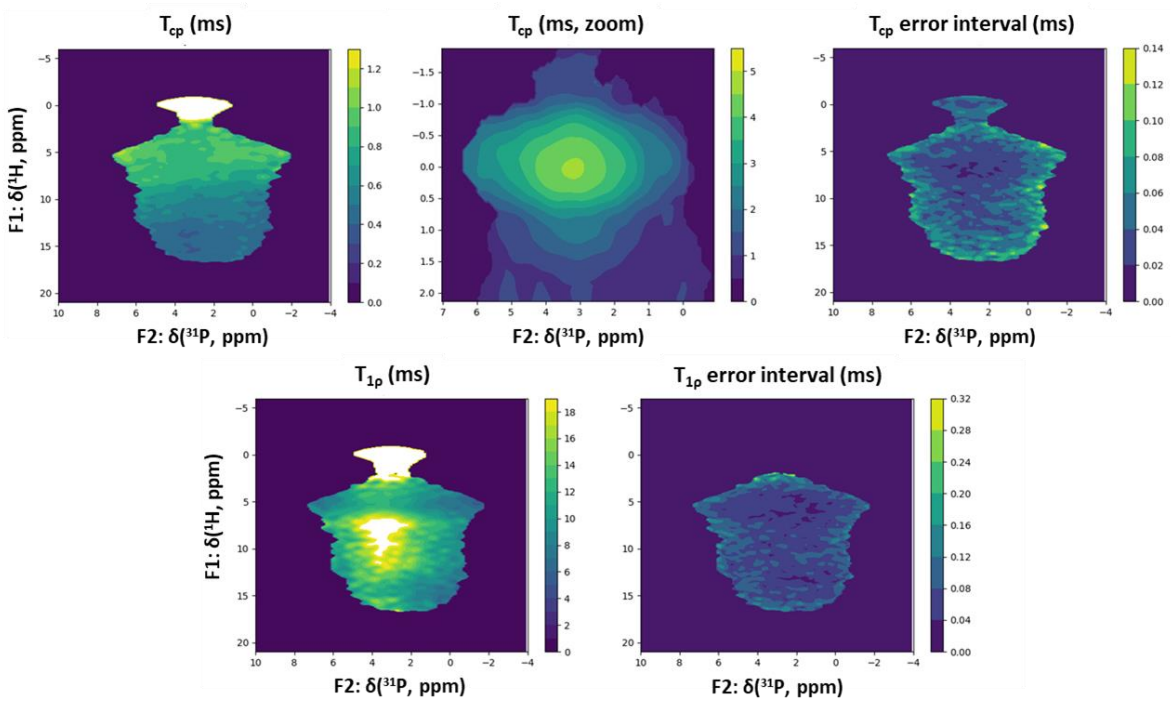


*Figure 50: Map of the "point by point" $T_{cp}$ and $T_{1\rho}$ values of CHA_BM. Two different color schemes were applied to the $T_{cp}$ map to highlight differences at short and long $T_{CP}$ values. ($B_0$ = 14.1 T, $\nu_r$ = 20 kHz)*

Analyzing these maps (Figure 50) reveals stunning contrasts between different regions of the spectrum. Predictably, the $T_{cp}$ of the apatitic $OH^-$ sites is much longer than for the other sites due to longer O**H**$^-$---**P**$O_4^{3-}$ distances and therefore smaller $^1$H-$^{31}$P dipolar coupling. The $H_2O$ and $HPO_4^{2-}$ regions show a gradual decrease of the $T_{cp}$ with increasing $^1$H chemical shift, which is expected given the shorter $T_{cp}$ values measured for $HPO_4^{2-}$ correlations (Table 19). The most surprising aspect of these maps is the strong contrasts in $T_{1\rho}$ values at different points of the signal (Figure 51). Specifically, at *ca.* 3.5 ppm in $^{31}$P and ranging from 6.5 to 12.0 ppm in $^1$H dimension, we observe an area of extremely long $T_{1\rho}$ values, which range from *ca.* 20 to 28 ms. Conversely, two

zones of smaller $T_{1\rho}$ are found at *ca*. 4.9 ppm and *ca*. 14.5 ppm in $^{1}H$ chemical shift, with the latter showing much shorter $T_{1\rho}$ values (*ca.* 8 ms) at lower $^{31}P$ chemical shifts (around 2 to 0 ppm).

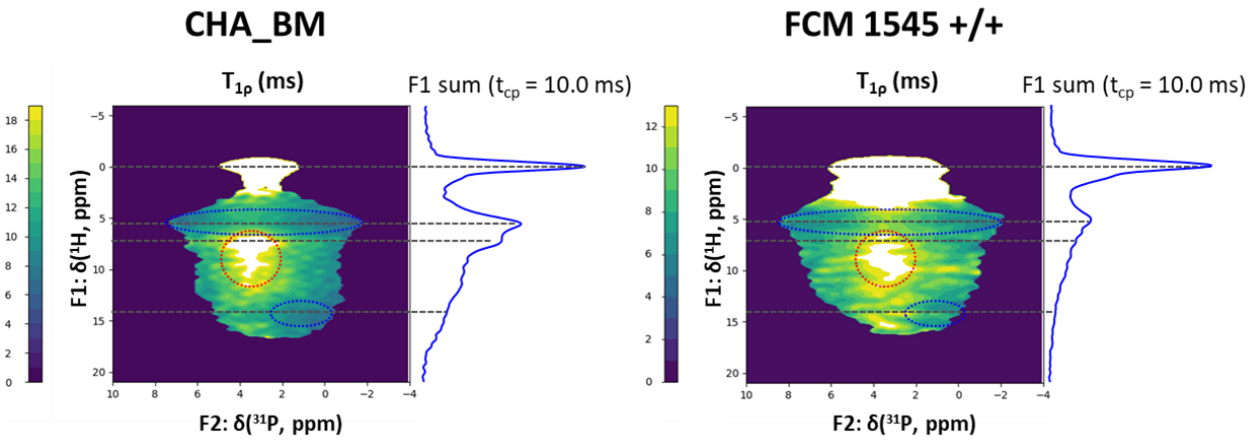


*Figure 51: $T_{1\rho}$ maps of the variable-$t_{cp}$ CP-HETCOR signal of CHA_BM and FCM 1545 +/+. An area of longer $T_{1\rho}$ is highlighted with a red circle and two of shorter $T_{1\rho}$ are highlighted in blue. To the right of the spectrum is the projection of the $^{1}H$ dimension at $t_{cp}$ = 10.0 ms (see Figure 48). Note the position of the red and blue circled areas in relation to the features of the $^{1}H$ spectrum. $B_0$ = 14.1 T, $\nu_r$ = 20 kHz*

We note that these features are not visible when observing slices of the spectrum at a single contact time, but show as shifting asymmetries and positions (~0.1 ppm) in peak maxima with increasing contact times.

The same analysis, when applied to bone samples, gives us an equivalent. For the sake of brevity, we will only depict the results for FCM 1545 +/+ at this magnetic field. The resulting maps (Figure 52) share a few notable commonalities with those of CHA_BM: the $T_{cp}$ map shows a similar gradient of $T_{cp}$ with shorter values at higher $^{1}H$ chemical shift. The $OH^{-}$ resonance shows shorter $T_{cp}$ near the center of the peak. The longest $T_{cp}$ values are found at a $\delta_{iso}(^{31}P)$ of 2.9 ppm (slightly different from the 3.2 ppm of CHA_BM). The areas of shorter $T_{1\rho}$ at $\delta_{iso}(^{1}H)$ of *ca*. 4.9 ppm and *ca*. 14.5 ppm also appear, as does the narrow area of longer $T_{1\rho}$ around 7.0 ppm. All these features are much less defined in the bone sample, possibly due to lower signal/noise ratio and the presence of broader resonances. We note that this analysis, when applied to the 7.04 T data (Figure 53), gave similar results but with much larger error margins and noise, given the lower signal/noise level. The higher field analysis is necessary in order to distinguish the boundaries of the different areas clearly.

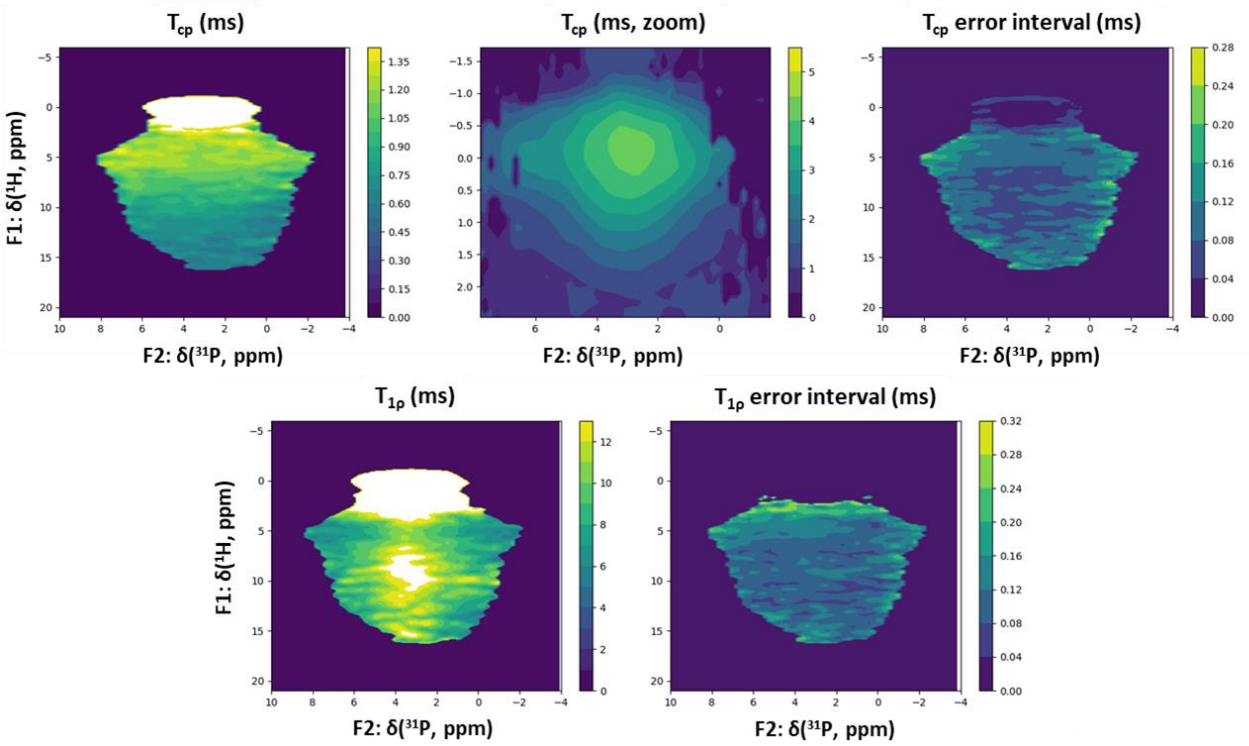


*Figure 52: Maps of the "point by point" $T_{cp}$ and $T_{1\rho}$ values of FCM 1545 +/+ ($B_0$ = 14.1 T, $\nu_r$ = 20 kHz).*

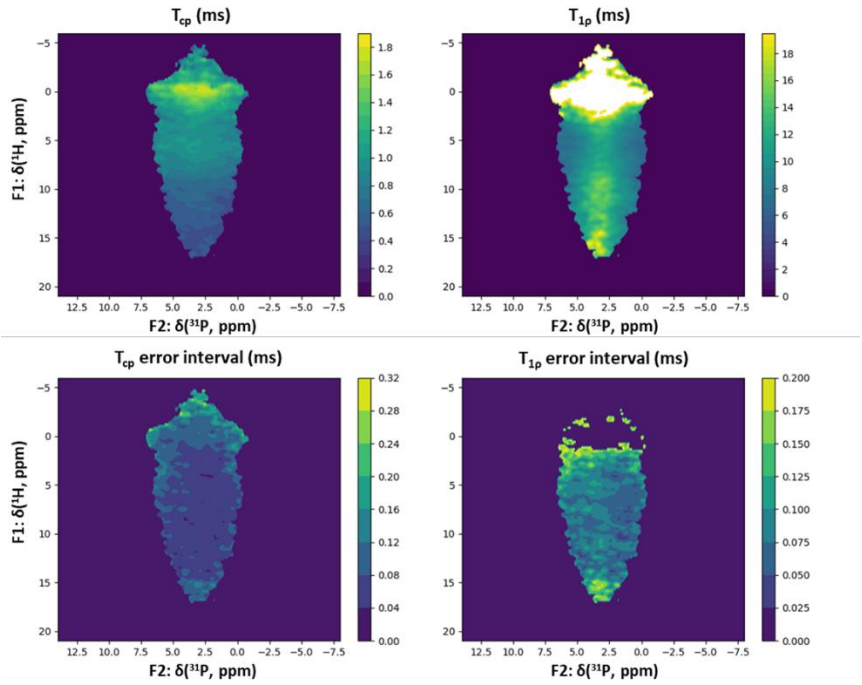


*Figure 53: Maps of the "point by point" $T_{cp}$ and $T_{1\rho}$ values of FCM 7 +/+, at $B_0$ = 7.04 T and $\nu_r$ = 14 kHz (US acquisitions).*

The fact that we can distinguish areas of contrasting $T_{cp}$ and $T_{1\rho}$ within a poorly resolved spectrum raises another question: is it possible to measure the NMR parameters of the underlying components of the signal on the basis of their $T_{cp}$ and $T_{1\rho}$ dynamics?

### VI.2. "3D fitting" script

The method is very similar to that of the 2D fitting script, both in input and output files. But the experimental data are no longer fitted at each contact time with different NMR parameters. Instead, they are fitted simultaneously with the same parameters, with amplitudes dictated by $T_{cp}$ and $T_{1\rho}$ variables. This, in theory, adds the contact time dynamics as a new parameter that the fitting routine can use to differentiate the peaks.

In practice, although the program has few differences with the earlier fitting routine, the addition of two new parameters ($T_{cp}$ and $T_{1\rho}$) and the simultaneous fitting of multiple spectra both slow the program down significantly. Whereas the 2D fitting routine needs a few seconds to fit a spectrum with three peaks, this new routine required upwards of fifteen minutes to fit a series of a dozen spectra, starting from a set of distant guesses. With six components, this process can take hours. Additionally, there is yet no command to stop an optimization in progress nor to estimate its duration. This makes the application of this method somewhat time-inefficient, although no attempt has been made to optimize the program. This also means that initial good guess about the underlying peaks is preferable, as this significantly speeds up the process of fitting the experimental data.

The best fit of CHA_BM using the 3D fitting script gave the following optimized solution while fitting every parameter simultaneously (Table 23 and Figure 54).

| **Tentative Assignment** | **n** | **$\delta_{iso}(^{31}P)$** | **$\delta_{iso}(^{1}H)$** | **$I_0$ (a.u.)** | **FWHM($^{31}$P)** | **FWHM($^{1}$H)** | **gl($^{31}$P)** | **gl($^{1}$H)** | **$T_{cp}$ (ms)** | **$T_{1\rho}$ (ms)** |
|---|---|---|---|---|---|---|---|---|---|---|
| Disordered $OH^-$ | 1 | 3.1 | -0.3 | 1.3 | 3.4 | 0.55 | 0.6 | 0.0 | 5.00 | >> 10 |
| Ordered $OH^-$ | 2 | 2.9 | 0.0 | 4.5 | 2.1 | 0.84 | 0.5 | 0.0 | 5.41 | >> 10 |
| Surface $H_2O$ | 3 | 2.5 | 5.4 | 8.8 | 5.6 | 1.73 | 1.0 | 0.0 | 1.03 | 6.44 |
| Structural $H_2O$ | 4 | 3.0 | 6.7 | 15.0 | 4.0 | 4.62 | 0.3 | 0.0 | 0.89 | 32.5 |
| Structural $HPO_4^{2-}$ | 5 | 2.4 | 11.4 | 9.4 | 6.4 | 5.19 | 1.0 | 0.0 | 0.46 | 11.2 |
| Surface $HPO_4^{2-}$ | 6 | 1.9 | 14.7 | 3.1 | 6.0 | 3.23 | 1.0 | 0.0 | 0.36 | 7.63 |

*Table 23: Optimized fitted parameters for CHA_BM using the 3D fitting method. Tentative assignment is discussed in the next section.*

Overall, this solution is slow to optimize, but gives an interesting estimation of the underlying signals (Table 23). It matches the signal well (Figure 54) with an $R^2$ of 0.994, showing a good match to the experimental data at all contact times. It also matches well (but not perfectly) with the data obtained from the $T_{cp}$ and $T_{1\rho}$ maps in Figure 50. The issue with this method is the strong potential for overfitting and the strong assumptions underlying the model (here, the presence of six peaks that all follow a biexponential CP dynamics curve).

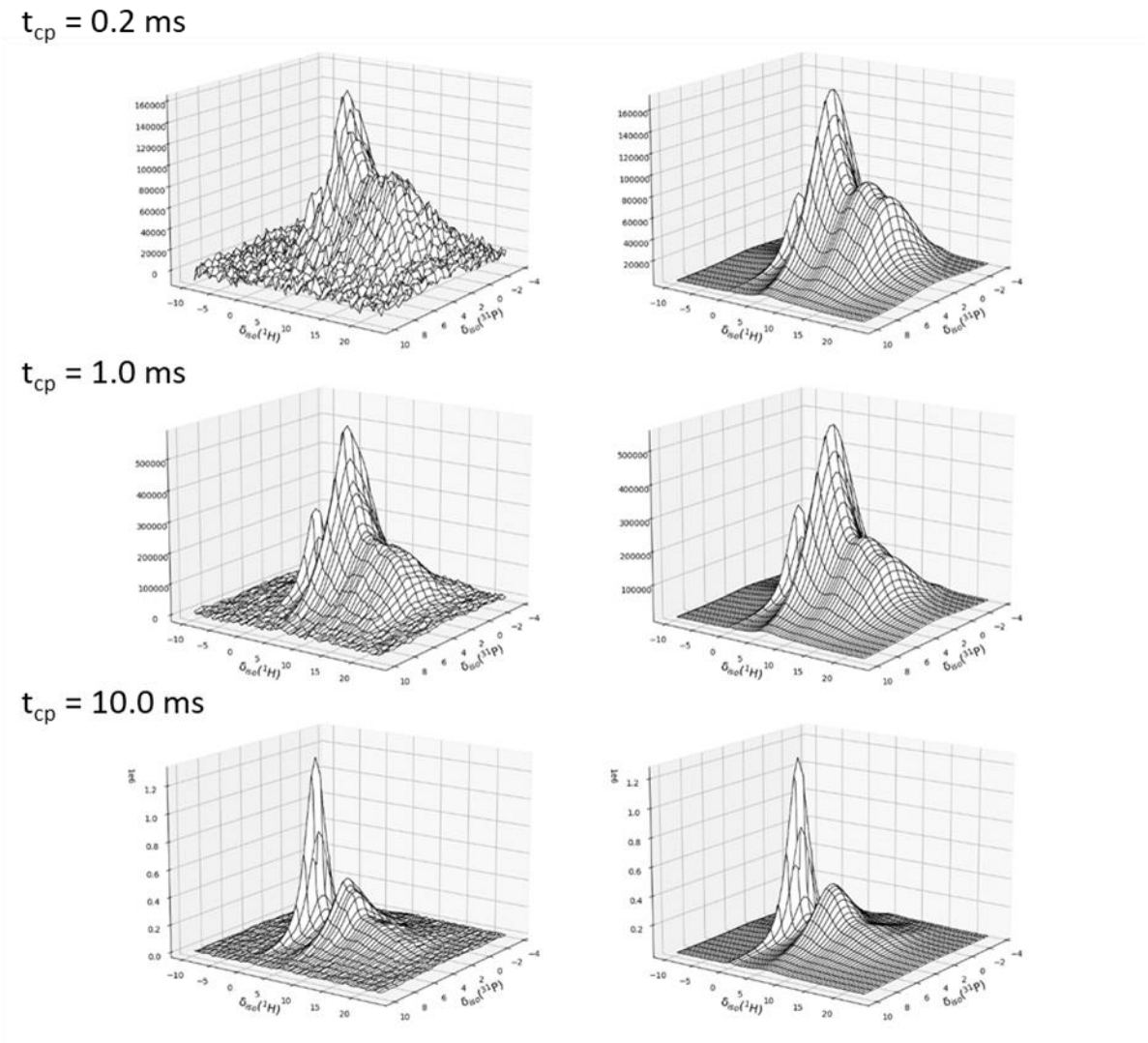


*Figure 54: Experimental (left) and simulated (right) signal using the 3D fitting method with the six peaks described in Table 23.*

## VII. Discussion: new insight into bone, teeth, and synthetic apatites.

We have presented experimental CP-HETCOR data gathered on multiple different biomimetic apatites and natural bone samples. During this process, we have come across multiple odd results that do not fit with the standard model for the composition of bone mineral. Unfortunately, due to time constraints, these results are for the moment fragmentary, and do not add up to a complete data set regarding our samples. Notably absent are higher-field data for two synthetic samples and teeth. However, we have sufficient data to hazard a guess as to their interpretation.

We have first shown that fitting a series of CP-HETCOR spectra at variable $t_{cp}$ could not be accurately described with the same three frozen peaks at all contact times. Because of the new 2D fitting method, it was found that the average $\delta_{iso}(^{31}P)$ of the signal increases with the contact

time, while the $^{31}P$ linewidth decreases with time. It was also found that this was only true for the $H_2O$ ⋯ $(H)PO_4^{-(2)3}$ and $HPO_4^{2-}$ cross-peaks, while the $OH^-$⋯ $PO_4^{3-}$ cross-peak remained unchanged. This led us to suspect the existence of multiple underlying components especially for the two former resonances. While the choice of three peaks with variable $\delta_{iso}$ and FWHM was made for the sake of simplicity and reproducibility, they do not represent a single chemical environment, but rather a collection of environments with close NMR characteristics (Figure 50 and Figure 52).

A closer look at the evolution of the linewidth with the contact time shows a similar trend for all samples, both biological and synthetic. The initial linewidth of both $H_2O$ and $HPO_4^{2-}$ peaks is somewhat similar for all apatitic samples, with the lowest value being FWHM($^{31}P$) = 4.0 ppm for the $H_2O$ peak of HA_NA and the highest at FWHM($^{31}P$) = 6.5 ppm for the $HPO_4^{2-}$ peak of bone mineral (Figure 38 and Figure 44). Over increasing contact times, the $^{31}P$ linewidth decreases to reach values between 5 and 3 ppm. This decrease is less pronounced in biological samples. We saw with the HA_BM example (Figure 39) that the decrease could be explained by the presence of two underlying components in the $H_2O$ signal. In this case, the first broad component, with $\delta_{iso}$($^{31}P$) = 1.8 ppm, closely matches the chemical shift of the $H_2O$ and $HPO_4^{2-}$ cross-peaks at low contact times. The second component has both the chemical shift and linewidth of the apatitic $OH^-$⋯$PO_4^{3-}$ cross-peak, which may indicate that this component comes from a similarly ordered environment than that of the apatitic signal.

One possible interpretation of the above data is the presence of at least two "types" of $H_2O$⋯$(H)PO_4^{-(2)3}$ and $HPO_4^{2-}$ signals in our samples, corresponding to different locations in the mineral. The first would originate from the amorphous surface shell as described in the literature, and we propose that the second originates from an apatitic environment. This would be consistent with repeated observations of structural water and hydrogen phosphates within crystalline apatites in the $^1H$ dimension, as well as with other analytical methods.[11,52,53]

This hypothesis may help explain other unexpected observations in this study. During the analysis of HA_NA, we showed the appearance of a fourth correlation which was indicative of an $OH^-$ site correlating with higher-frequency $\delta_{iso}$($^{31}P$) = 3.2 ppm of $PO_4^{3-}$ sites in a disordered environment (Figure 40). Because of the presence of sodium during the synthesis, we proposed that this signal corresponds to an $OH^-$ site in the vicinity of a $Na^+$ substitution. This could explain both the different $^{31}P$ chemical shift and the broader linewidth of the resonance. We can speculate that this could help to explain another unexpected feature: the differing $^{31}P$ chemical shift of the $H_2O$⋯$(H)PO_4^{-(2)3}$ resonance when compared to other apatitic samples (Figure 38). The $^{31}P$ chemical shift and linewidth of this signal at longer contact times also matches that of the "$OH^-$" site proposed to be close to $Na^+$. The environment of the slow-relaxing water in HA_NA could therefore also be in a substituted apatite environment.

Lastly, the presence of at least two types of $H_2O$⋯$(H)PO_4^{-(2)3}$ and $HPO_4^{2-}$ environments helps make sense of the point-by-point fitting of CHA_BM and bone samples (Figure 50, Figure 52). The $T_{1\rho}$

maps show strong contrasts at different points of the signal. Two areas of shorter $T_{1\rho}$ appear at 5.0 and 14.5 ppm in the $^{1}H$ dimension, with a stronger contrast at lower $^{31}P$ chemical shifts. This was also found to be applicable to the bone samples, which had a similar if broader $T_{cp}$ and $T_{1\rho}$ map compared to CHA_BM. The low $T_{1\rho}$ value in the $\delta_{iso}(^{1}H)$ = 5.0 ppm area can be explained by the presence of a signal originating from more mobile, weakly bound water molecules. The low $T_{1\rho}$ area at $\delta_{iso}(^{1}H)$ = 14.5 ppm may be caused by more mobile $HPO_4^{2-}$ sites. In contrast, the area of longer $T_{1\rho}$ was found *via* 3D fitting to have a $\delta_{iso}(^{31}P)$ of 3.3 ppm, similar to that of HA_NA.

It could be argued that the "apatitic" $H_2O$ and $HPO_4^{2-}$ resonances that we observe are the result of spin-diffusion from the surface to the core in our samples. We do not prefer this interpretation of the current data, as it is inconsistent with some of our observations:

- In HA_NA, the NMR parameters of "substituted" $OH^-$ sites and "unsubstituted" $OH^-$ sites do not tend to average out over long contact times, which would be expected given their theoretically close proximity.
- The HA_BM $HPO_4^{2-}$ correlation has faster changes in NMR parameters than the $H_2O$ correlation, indicating that the mechanism governing those two evolutions cannot rely on spin-diffusion from the surface to the core, which would have a common time constant.
- The NMR parameters of the $OH^-$ resonance are stable with $t_{cp}$ for all samples, indicating there is no evidence of spin-diffusion from the $OH^-$ to the other environments. Spin diffusion being a reciprocal phenomenon, it should tend to average the parameters in the sample, rather than trending towards the values of the core.

Therefore, it seems more likely to us that our observations most closely match the presence of multiple underlying sites, both in a disordered surface and in an apatitic environment.

In conclusion, these new observations strongly support the hypothesis that biomimetic apatites and bone mineral have at least two distinct sets of $H_2O$ and $HPO_4^{2-}$ signals: one originating from the disordered shell and the other from apatitic sites. More specifically, the new methods that are developed make use of both $^{1}H$ and $^{31}P$ dimensions simultaneously, and allow for robust comparisons between the local environments of synthetic and/or biological apatites. From this, we have observed both important contrasts in local environments between synthetic apatites synthesized using similar protocols (Figure 38) and an impressive consistency between samples of bone mineral from different specimen (Figure 43). The analyses of the $^{31}P$ NMR parameters also offers a new point of comparison between synthetic and biological. Although we are not yet at the level of fully resolving the underlying resonances of the bone $^{1}H$-$^{31}P$ CP-HETCOR NMR spectrum, the three complementary methods we have developed serve to get us a step closer to that point.

## VIII. Perspectives

The 2D study of the CP-HETCOR signal of apatite has grown in scope much beyond the initial objective, which was the relative quantification of the proton environments within bone mineral. We demonstrated that the signal was much more complex than initially proposed, and showed interesting features that required a variety of processing methods to fully unravel.

The quantification of the proton environments of bone is a mitigated success. Although we find similar values for a large number of bone samples (with an error margin *ca.* 10% for each component), the fact that the result differs based on the Hartmann-Hahn condition and on the physical state of the sample are not good indicators of the applicability to other models. The questionable validity of the underlying hypotheses of the I-S model are also a limiting factor.

It is clear that these methods could be applied in a systematic study of apatite and bone samples, possibly combined with smaller changes to the synthetic protocol of the model apatites in order to better understand the changes to the variables. With less time spent on methodological improvements, the use of spectrometer time could be more focused and a large number of samples could be analyzed in a few weeks (up to 5 samples per week appears to be the practical limit). Other possibilities not explored in this study were the addition of Lee-Goldberg $^{1}H$ decoupling during the evolution time to increase F1 resolution (although this may alter the lineshape and quantifications). Another option is the use of a Laplace transform on the variable-$t_{cp}$ data to resolve the different resonances in the time-domain. This transform would require a large number of experiments, possible only with high levels of signal. It would, however, open the possibility of using the $t_{cp}$ time-domain as a new dimension to resolve convoluted signals in CP-HETCOR experiments.

## IX. References


(1) Kaflak, A.; Chmielewski, D.; Kolodziejski, W. Solid-State NMR Study of Discrete Environments of Bone Mineral Nanoparticles Using Phosphorus-31 Relaxation. *Journal of Applied Biomedicine* **2016**, *14* (4), 321–330. https://doi.org/10.1016/j.jab.2016.07.001.

(2) Zeng, P.; Fu, Y.; Pang, Y.; He, T.; Wu, Y.; Tang, R.; Qin, A.; Kong, X. Solid-State Nuclear Magnetic Resonance Identifies Abnormal Calcium Phosphate Formation in Diseased Bones. *ACS Biomater. Sci. Eng.* **2021**, *7* (3), 1159–1168. https://doi.org/10.1021/acsbiomaterials.0c01559.

(3) Gennero, I.; Laurencin-Dalicieux, S.; Conte-Auriol, F.; Briand-Mésange, F.; Laurencin, D.; Rue, J.; Beton, N.; Malet, N.; Mus, M.; Tokumura, A.; Bourin, P.; Vico, L.; Brunel, G.; Oreffo, R. O. C.; Chun, J.; Salles, J. P. Absence of the Lysophosphatidic Acid Receptor $LPA_1$ Results in Abnormal Bone Development and Decreased Bone Mass. *Bone* **2011**, *49* (3), 395–403. https://doi.org/10.1016/j.bone.2011.04.018.

(4) Drouet, C.; Grossin, D.; Combes, C.; Sarda, S.; Cazalbou, S.; Rey, C. Apatites biomimétiques - Des biominéraux aux analogues de synthèse pour le biomédical. *Techniques de l'Ingénieur* **2018**, 1–28.

(5) Santos, R. A.; Wind, R. A.; Bronnimann, C. E. $^{1}$H CRAMPS and $^{1}$H-$^{31}$P HetCor Experiments on Bone, Bone Mineral, and Model Calcium Phosphate Phases. *Journal of Magnetic Resonance, Series B* **1994**, *105* (2), 183–187. https://doi.org/10.1006/jmrb.1994.1120.

(6) Miquel, J. L.; Facchini, L.; Legrand, A. P.; Marchandise, X.; Lecouffe, P.; Chanavaz, M.; Donazzan, M.; Rey, C.; Lernaitre, J. Characterisation and Conversion Study into Natural Living Bone of Calcium Phosphate Bioceramics by Solid State NMR Spectroscopy. *Clinical Materials* **1990**, *5* (2), 115–125. https://doi.org/10.1016/0267-6605(90)90011-J.

(7) Kolmas, J.; Ślósarczyk, A.; Wojtowicz, A.; Kolodziejski, W. Estimation of the Specific Surface Area of Apatites in Human Mineralized Tissues Using $^{31}$P MAS NMR. *Solid State Nuclear Magnetic Resonance* **2007**, *32* (2), 53–58. https://doi.org/10.1016/j.ssnmr.2007.08.001.

(8) Von Euw, S.; Wang, Y.; Laurent, G.; Drouet, C.; Babonneau, F.; Nassif, N.; Azaïs, T. Bone Mineral: New Insights into Its Chemical Composition. *Sci Rep* **2019**, *9* (1), 8456. https://doi.org/10.1038/s41598-019-44620-6.

(9) Nikel, O.; Laurencin, D.; McCallum, S. A.; Gundberg, C. M.; Vashishth, D. NMR Investigation of the Role of Osteocalcin and Osteopontin at the Organic–Inorganic Interface in Bone. *Langmuir* **2013**, *29* (45), 13873–13882. https://doi.org/10.1021/la403203w.

(10) Lin, K. S. K.; Tseng, Y.-H.; Mou, Y.; Hsu, Y.-C.; Yang, C.-M.; Chan, J. C. C. Mechanistic Study of Apatite Formation on Bioactive Glass Surface Using $^{31}$ P Solid-State NMR Spectroscopy. *Chem. Mater.* **2005**, *17* (17), 4493–4501. https://doi.org/10.1021/cm050654c.

(11) Duer, M. J. The Contribution of Solid-State NMR Spectroscopy to Understanding Biomineralization: Atomic and Molecular Structure of Bone. *Journal of Magnetic Resonance* **2015**, *253*, 98–110. https://doi.org/10.1016/j.jmr.2014.12.011.

(12) Gronwald, W.; Klein, M. S.; Kaspar, H.; Fagerer, S. R.; Nürnberger, N.; Dettmer, K.; Bertsch, T.; Oefner, P. J. Urinary Metabolite Quantification Employing 2D NMR Spectroscopy. *Anal. Chem.* **2008**, *80* (23), 9288–9297. https://doi.org/10.1021/ac801627c.

(13) Giraudeau, P. Quantitative 2D Liquid-State NMR. *Magnetic Resonance in Chemistry* **2014**, *52* (6), 259–272. https://doi.org/10.1002/mrc.4068.
(14) Kolodziejski, W.; Klinowski, J. Kinetics of Cross-Polarization in Solid-State NMR: A Guide for Chemists. *Chemical Reviews* **2002**, *102* (3), 613–628. https://doi.org/10.1021/cr000060n.
(15) Hartmann, S. R.; Hahn, E. L. Nuclear Double Resonance in the Rotating Frame. *Phys. Rev.* **1962**, *128* (5), 2042–2053. https://doi.org/10.1103/PhysRev.128.2042.
(16) Stejskal, E. O.; Schaefer, J.; Waugh, J. S. Magic-Angle Spinning and Polarization Transfer in Proton-Enhanced NMR. *Journal of Magnetic Resonance (1969)* **1977**, *28* (1), 105–112. https://doi.org/10.1016/0022-2364(77)90260-8.
(17) Metz, G.; Wu, X. L.; Smith, S. O. Ramped-Amplitude Cross Polarization in Magic-Angle-Spinning NMR. *Journal of Magnetic Resonance, Series A* **1994**, *110* (2), 219–227. https://doi.org/10.1006/jmra.1994.1208.
(18) Pines, A.; Gibby, M. G.; Waugh, J. S. Proton-enhanced NMR of Dilute Spins in Solids. *The Journal of Chemical Physics* **1973**, *59* (2), 569–590. https://doi.org/10.1063/1.1680061.
(19) Andrew, E. R. Spin Temperature and Nuclear Magnetic Resonance in Solids. *Phys. Bull.* **1971**, *22* (3), 161. https://doi.org/10.1088/0031-9112/22/3/030.
(20) Abragam, A.; Goldman, M. Principles of Dynamic Nuclear Polarisation. *Rep. Prog. Phys.* **1978**, *41* (3), 395. https://doi.org/10.1088/0034-4885/41/3/002.
(21) Klur, I.; Jacquinot, J.-F.; Brunet, F.; Charpentier, T.; Virlet, J.; Schneider, C.; Tekely, P. NMR Cross-Polarization When TIS>T1ρ; Examples from Silica Gel and Calcium Silicate Hydrates. *J. Phys. Chem. B* **2000**, *104* (44), 10162–10167. https://doi.org/10.1021/jp001342u.
(22) Massiot, D.; Fayon, F.; Capron, M.; King, I.; Le Calvé, S.; Alonso, B.; Durand, J.-O.; Bujoli, B.; Gan, Z.; Hoatson, G. Modelling One- and Two-Dimensional Solid-State NMR Spectra. *Magnetic Resonance in Chemistry* **2002**, *40* (1), 70–76. https://doi.org/10.1002/mrc.984.
(23) Davies, E.; Duer, M. J.; Ashbrook, S. E.; Griffin, J. M. Applications of NMR Crystallography to Problems in Biomineralization: Refinement of the Crystal Structure and 31P Solid-State NMR Spectral Assignment of Octacalcium Phosphate. *J. Am. Chem. Soc.* **2012**, *134* (30), 12508–12515. https://doi.org/10.1021/ja3017544.
(24) Skibsted, J.; Hjorth, L.; Jakobsen, H. J. Quantification of Thaumasite in Cementitious Materials by $^{29}$Si {$^{1}$H} Cross-Polarization Magic-Angle Spinning NMR Spectroscopy. *Advances in Cement Research*.
(25) Van Meerten, S. G. J.; Franssen, W. M. J.; Kentgens, A. P. M. ssNake: A Cross-Platform Open-Source NMR Data Processing and Fitting Application. *Journal of Magnetic Resonance* **2019**, *301*, 56–66. https://doi.org/10.1016/j.jmr.2019.02.006.
(26) Madsen, K.; Nielsen, H.; Tingleff, O. Methods for Non-Linear Least Squares Problems (2nd Ed.). **2004**, 60.
(27) Helmus, J. J.; Jaroniec, C. P. Nmrglue: An Open Source Python Package for the Analysis of Multidimensional NMR Data. *J Biomol NMR* **2013**, *55* (4), 355–367. https://doi.org/10.1007/s10858-013-9718-x.
(28) Harris, C. R.; Millman, K. J.; Van der Walt, S. J.; Gommers, R.; Virtanen, P.; Cournapeau, D.; Wieser, E.; Taylor, J.; Berg, S.; Smith, N. J.; Kern, R.; Picus, M.; Hoyer, S.; van Kerkwijk, M. H.; Brett, M.; Haldane, A.; del Río, J. F.; Wiebe, M.; Peterson, P.; Gérard-Marchant, P.;

Sheppard, K.; Reddy, T.; Weckesser, W.; Abbasi, H.; Gohlke, C.; Oliphant, T. E. Array Programming with NumPy. *Nature* **2020**, *585* (7825), 357–362. https://doi.org/10.1038/s41586-020-2649-2.

(29) Virtanen, P.; Gommers, R.; Oliphant, T. E.; Haberland, M.; Reddy, T.; Cournapeau, D.; Burovski, E.; Peterson, P.; Weckesser, W.; Bright, J.; van der Walt, S. J.; Brett, M.; Wilson, J.; Millman, K. J.; Mayorov, N.; Nelson, A. R. J.; Jones, E.; Kern, R.; Larson, E.; Carey, C. J.; Polat, İ.; Feng, Y.; Moore, E. W.; VanderPlas, J.; Laxalde, D.; Perktold, J.; Cimrman, R.; Henriksen, I.; Quintero, E. A.; Harris, C. R.; Archibald, A. M.; Ribeiro, A. H.; Pedregosa, F.; van Mulbregt, P. SciPy 1.0: Fundamental Algorithms for Scientific Computing in Python. *Nature Methods* **2020**, *17* (3), 261–272. https://doi.org/10.1038/s41592-019-0686-2.

(30) Hunter, J. D. Matplotlib: A 2D Graphics Environment. *Computing in Science & Engineering* **2007**, *9* (3), 90–95. https://doi.org/10.1109/MCSE.2007.55.

(31) Cho, G.; Wu, Y.; Ackerman, J. L. Detection of Hydroxyl Ions in Bone Mineral by Solid-State NMR Spectroscopy. *Science* **2003**, *300* (5622), 1123–1127. https://doi.org/10.1126/science.1078470.

(32) Wang, Y.; Von Euw, S.; Fernandes, F. M.; Cassaignon, S.; Selmane, M.; Laurent, G.; Pehau-Arnaudet, G.; Coelho, C.; Bonhomme-Coury, L.; Giraud-Guille, M.-M.; Babonneau, F.; Azaïs, T.; Nassif, N. Water-Mediated Structuring of Bone Apatite. *Nature Mater* **2013**, *12* (12), 1144–1153. https://doi.org/10.1038/nmat3787.

(33) Kaflak-Hachulska, A.; Samoson, A.; Kolodziejski, W. 1H MAS and 1H → 31P CP/MAS NMR Study of Human Bone Mineral. *Calcif Tissue Int* **2003**, *73* (5), 476–486. https://doi.org/10.1007/s00223-002-2111-5.

(34) Jonášová, L.; Müller, F. A.; Helebrant, A.; Strnad, J.; Greil, P. Biomimetic Apatite Formation on Chemically Treated Titanium. *Biomaterials* **2004**, *25* (7), 1187–1194. https://doi.org/10.1016/j.biomaterials.2003.08.009.

(35) Müller, F. A.; Müller, L.; Caillard, D.; Conforto, E. Preferred Growth Orientation of Biomimetic Apatite Crystals. *Journal of Crystal Growth* **2007**, *304* (2), 464–471. https://doi.org/10.1016/j.jcrysgro.2007.03.014.

(36) Vandecandelaere, N.; Rey, C.; Drouet, C. Biomimetic Apatite-Based Biomaterials: On the Critical Impact of Synthesis and Post-Synthesis Parameters. *J Mater Sci: Mater Med* **2012**, *23* (11), 2593–2606. https://doi.org/10.1007/s10856-012-4719-y.

(37) Ren, F.; Ding, Y.; Leng, Y. Infrared Spectroscopic Characterization of Carbonated Apatite: A Combined Experimental and Computational Study. *Journal of Biomedical Materials Research Part A* **2014**, *102* (2), 496–505. https://doi.org/10.1002/jbm.a.34720.

(38) Leroy, C.; Aussenac, F.; Bonhomme-Coury, L.; Osaka, A.; Hayakawa, S.; Babonneau, F.; Coelho-Diogo, C.; Bonhomme, C. Hydroxyapatites: Key Structural Questions and Answers from Dynamic Nuclear Polarization. *Anal. Chem.* **2017**, *89* (19), 10201–10207. https://doi.org/10.1021/acs.analchem.7b01332.

(39) Yoder, C. H.; Stepien, K. R.; Dudrick, R. N. The Distribution of Carbonate in Apatite: The Environment Model. *American Mineralogist* **2023**, *108* (6), 1072–1079. https://doi.org/10.2138/am-2022-8389.

(40) Su, Y.; Brigiano, F. S.; Petit, I.; Leroy, C.; Bonhomme, C.; Babonneau, F.; Tielens, F.; Gervais, C. Investigation of Carbonate Substitution in Hydroxyapatite by Combining Solid-

State NMR and DFT Calculations. *Chemistry–Methods* **2023**, *3* (11), e202300007. https://doi.org/10.1002/cmtd.202300007.
(41) Bodenhausen, G.; Freeman, R.; Morris, G. A.; Turner, D. L. NMR Spectra of Some Simple Spin Systems Studied by Two-Dimensional Fourier Transformation of Spin Echoes. *Journal of Magnetic Resonance (1969)* **1978**, *31* (1), 75–95. https://doi.org/10.1016/0022-2364(78)90172-5.
(42) *Non Uniform Sampling | NUS | 2D Correlation Experiments*. https://www.jeolusa.com/RESOURCES/Analytical-Instruments/Non-Uniform-Sampling-NUS (accessed 2024-06-17).
(43) Barna, J. C. J.; Laue, E. D.; Mayger, M. R.; Skilling, J.; Worrall, S. J. P. Exponential Sampling, an Alternative Method for Sampling in Two-Dimensional NMR Experiments. *Journal of Magnetic Resonance (1969)* **1987**, *73* (1), 69–77. https://doi.org/10.1016/0022-2364(87)90225-3.
(44) Hyberts, S. G.; Arthanari, H.; Wagner, G. Applications of Non-Uniform Sampling and Processing. In *Novel Sampling Approaches in Higher Dimensional NMR*; Billeter, M., Orekhov, V., Eds.; Springer: Berlin, Heidelberg, 2012; pp 125–148. https://doi.org/10.1007/128_2011_187.
(45) Linnet, T. E.; Teilum, K. Non-Uniform Sampling of NMR Relaxation Data. *J Biomol NMR* **2016**, *64* (2), 165–173. https://doi.org/10.1007/s10858-016-0020-6.
(46) Laurent, G. Increasing Solid-State NMR Sensitivity : Instrumentation, Fast Acquisitions and Signal Processing. phdthesis, Sorbonne Université, 2020. https://theses.hal.science/tel-03344148 (accessed 2024-06-17).
(47) Kazimierczuk, K.; Orekhov, V. Yu. Accelerated NMR Spectroscopy by Using Compressed Sensing. *Angewandte Chemie* **2011**, *123* (24), 5670–5673. https://doi.org/10.1002/ange.201100370.
(48) Holland, P. W.; Welsch, R. E. Robust Regression Using Iteratively Reweighted Least-Squares. *Communications in Statistics - Theory and Methods* **1977**, *6* (9), 813–827. https://doi.org/10.1080/03610927708827533.
(49) Laurencin, D.; Wong, A.; Chrzanowski, W.; Knowles, J. C.; Qiu, D.; Pickup, D. M.; Newport, R. J.; Gan, Z.; Duer, M. J.; Smith, M. E. Probing the Calcium and Sodium Local Environment in Bones and Teeth Using Multinuclear Solid State NMR and X-Ray Absorption Spectroscopy. *Phys. Chem. Chem. Phys.* **2010**, *12* (5), 1081–1091. https://doi.org/10.1039/B915708E.
(50) Mayen, L.; Jensen, N. D.; Laurencin, D.; Marsan, O.; Bonhomme, C.; Gervais, C.; Smith, M. E.; Coelho, C.; Laurent, G.; Trebosc, J.; Gan, Z.; Chen, K.; Rey, C.; Combes, C.; Soulié, J. A Soft-Chemistry Approach to the Synthesis of Amorphous Calcium Ortho/Pyrophosphate Biomaterials of Tunable Composition. *Acta Biomaterialia* **2020**, *103*, 333–345. https://doi.org/10.1016/j.actbio.2019.12.027.
(51) Yasar, O. F.; Liao, W.-C.; Mathew, R.; Yu, Y.; Stevensson, B.; Liu, Y.; Shen, Z.; Edén, M. The Carbonate and Sodium Environments in Precipitated and Biomimetic Calcium Hydroxy-Carbonate Apatite Contrasted with Bone Mineral: Structural Insights from Solid-State NMR. *J. Phys. Chem. C* **2021**, *125* (19), 10572–10592. https://doi.org/10.1021/acs.jpcc.0c11389.
(52) Heimann, R. B. *Calcium Phosphate: Structure, Synthesis, Properties, and Applications*, 1st Edition.; Nova Science Publishers Inc: New York, NY, 2013.

(53) Wilson, E. E.; Awonusi, A.; Morris, M. D.; Kohn, D. H.; Tecklenburg, M. M. J.; Beck, L. W. Three Structural Roles for Water in Bone Observed by Solid-State NMR. *Biophysical Journal* **2006**, *90* (10), 3722–3731. https://doi.org/10.1529/biophysj.105.070243.

# CHAPTER IV

## Observation of biominerals and bone *via* $^{1}H$-$^{43}Ca$ DNP-NMR

## Summary

## I. State of the art

As mentioned in section III.4.2 of the first chapter, $^{43}$Ca is an extremely insensitive nucleus. With a natural abundance of 0.135% and a gyromagnetic ratio 15 times lower than that of $^{1}$H, it sits at the edge of what can be reasonably observed using ordinary fields and probes.

One of the initial aims of this thesis was the observation of bone mineral using $^{43}$Ca NMR. Such spectra can be recorded using large-volume rotors and long acquisition times.[1,2] However, this gives a spectrum featuring a single unresolved peak, widened by second order quadrupolar broadening and chemical shift distributions. 2D experiments (MQ-MAS or $^{1}$H-$^{43}$Ca CP-HETCOR for instance) may help resolve resonances but would require faster spinning speeds than those generally accessible by large volume rotors, and even longer acquisition times.

As briefly explained in section IV.4 of chapter I, an increasing number of NMR spectroscopists have turned to DNP (Dynamic Nuclear Polarization) as a method for polarization enhancement. Despite the increased experimental difficulties inherent to DNP experiments (low temperature, choice of solvent composition and of radical for sample impregnation, etc…), the significant gain in signal justifies its use for low abundance nuclei. The technique has been successfully applied for the observation of the similarly insensitive $^{17}$O nucleus since 2012.[3–5]

The application of DNP to $^{43}$Ca NMR was first reported in 2017: Lee *et al.*[6] (including our ANR collaborators) demonstrated the applicability of $^{43}$Ca DNP for the study of apatites. In this study, a nanocrystalline, heat-treated, carbonated apatite (named CHAp_Ncomm in the rest of this chapter) was observed *via* $^{43}$Ca NMR using a CP transfer from hyperpolarized $^{1}$H to the $^{43}$Ca nuclei. The signal of the DNP-NMR experiment was significantly higher than that of a direct acquisition spectrum (Figure 1).

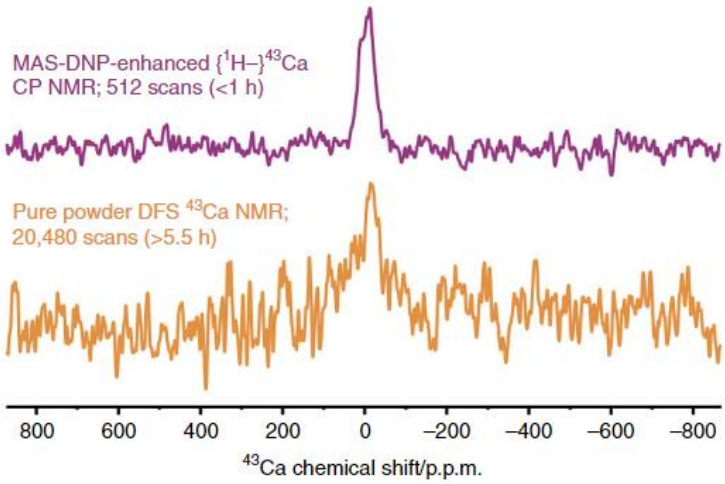


*Figure 1: Comparison of two $^{43}$Ca MAS NMR spectra, with and without DNP conditions recorded on a nanocrystalline carbonated HAp (CHAp_Ncomm). Top: $^{1}$H-$^{43}$Ca CPMAS experiment, with $t_{cp}$ = 5.0 ms, in DNP conditions. Bottom: pure powder direct acquisition DFS spectrum. $B_0$ = 9.4 T, $\nu_r$ = 8.5 kHz, T ≈ 100K. Spectra reproduced from the initial publication by Lee* et al.[6]

The gain in signal intensity was 35 compared to a non-impregnated sample recorded in the same conditions, leading to an estimated time save of three orders of magnitude when compared to a non-DNP experiment. This allowed the team to record a $^{1}H$ – $^{43}Ca$ CP-HETCOR NMR experiment in 15 hours (Figure 2).

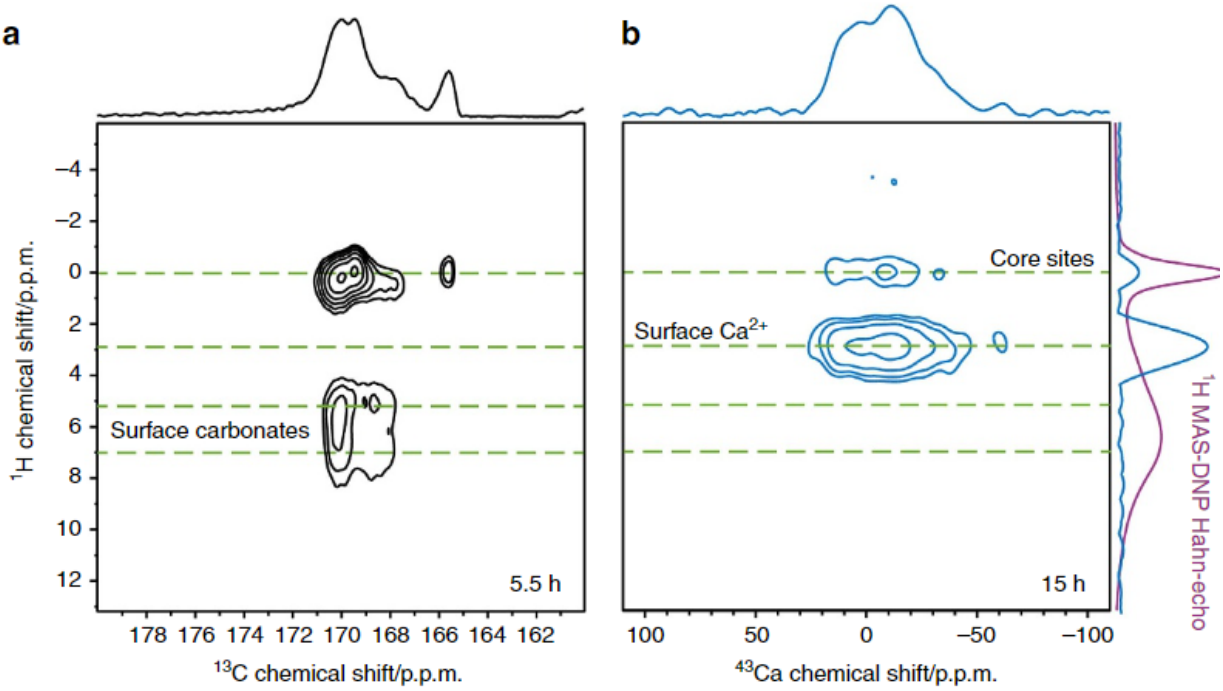


*Figure 2: $^{1}H$ – $^{43}Ca$ CP-HETCOR spectra recorded on a nanocrystalline carbonated HAp (CHAp_Ncomm) under DNP conditions. a) $t_{cp}$ = 7.0 ms, experimental time = 5.5 h. b) $t_{cp}$ = 3.0 ms, experimental time = 15 h. $B_0$ = 9.4 T, $\nu_r$ = 8.5 kHz, T ≈ 100K. Spectra reproduced from the initial publication by Lee* et al.[6]

This demonstrated the feasibility of natural-abundance 2D $^{1}H$-$^{43}Ca$ experiments in relatively short acquisition times, using the time-savings afforded by DNP enhancement. It should be noticed that a $^{43}Ca$ NMR study of complexes in a frozen solution was published very recently,[7] confirming the current interest in $^{43}Ca$ DNP-NMR.

A number of publications have used DNP-enhancement for the observation of bones and bone mineral.[8,9] They have focused on spin ½ nuclei present in bone, namely $^{13}C$, $^{15}N$ and $^{31}P$, allowing faster acquisitions of CPMAS and CP-HETCOR spectra. The reported signal enhancement for the $^{31}P$ signal in bone mineral by Azaïs et *al.*[9] is $\varepsilon_{on/off,31P}$ = 40.

All these results were encouraging and our objective was therefore to expand the previously study on apatites[6] to biological materials, and record natural-abundance $^{43}Ca$ DNP-NMR spectra of bone. Note that a DNP-enhanced $^{1}H$-$^{43}Ca$ CPMAS spectrum of mice teeth was recorded and published in the supplementary information of the Lee *et al.*[6] contribution (Figure 3). However, the experimental time was 38 hours for a signal which was only slightly above the noise level.

This may be attributed to the lack of optimization of the experimental conditions (no alternate DNP impregnation conditions were attempted on the mice teeth, for example). It however prefigured the fact that the optimal conditions for DNP-NMR may be different for biological samples than for synthetic apatites.

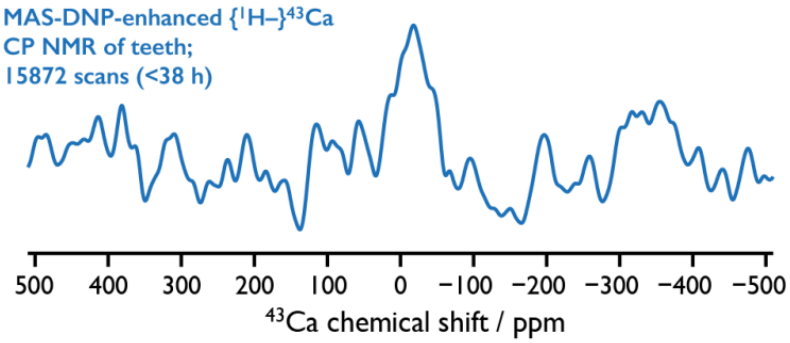


*Figure 3: DNP-enhanced $^{1}H$-$^{43}Ca$ CPMAS NMR of mice teeth. ($t_{cp}$ = 6 ms $B_0$ = 9.4 T, $\nu_r$ = 8.5 kHz, T ≈ 100K). Spectra reproduced from the initial publication by Lee* et al.[6]

After a presentation of the NMR set-up and samples preparation, the successive experimental improvements will be detailed before discussing the DNP-enhanced $^{1}H$-$^{43}Ca$ CPMAS spectra recorded on synthetic apatites and bone samples.

## II. Materials and methods

### II.1. DNP-enhanced NMR

The $^{1}H$ – $^{43}Ca$ CPMAS NMR experiments in DNP conditions were performed on a 9.4 T Avance III NMR spectrometer, operating at $^{1}H$ and $^{43}Ca$ Larmor frequencies of 400.00 and 26.93 MHz respectively, equipped with a 263 GHz gyrotron for microwave irradiation.

A low-temperature 3.2 mm probe in double resonance (HY) configuration in λ/4 $^{1}H$ transmission mode was used. An HY adaptor provided a bridge between the H and Y channels, while a 100-pF shunt capacitance was mounted in parallel to the Y capacitor, allowing to tune $\pm$ 0.5 MHz around the $^{43}Ca$ Frequency at 26.93 MHz. The samples were packed in $ZrO_2$ rotors of two types: 3.2 mm thin wall rotors (with a 2.6 mm internal radius and a 46 µL volume), and 3.2 mm regular wall rotors (with a 2.2 mm internal radius and a 32 µL volume), depending on the size of the samples and the availability of the rotors. They were spun to 8.5 kHz and cooled down to ≈ 100K. To avoid losing caps due to thermal contraction, the rotors were closed with a KEL-F cap wrapped in Teflon tape.

As demonstrated by Lee *et al.*,[10] $\varepsilon_{on/off}$ (or, the increase in signal observed when switching on the microwave irradiation) is not directly indicative of the actual increase in signal afforded by the DNP technique. This is caused by a range of factors (like changes in relaxation time constants, resolution, depolarizing effect of the radical, *etc…*) meaning that the real sensitivity gain factor is typically much lower than $\varepsilon_{on/off}$.

This is especially obvious in the analysis of CHA_Ncomm,[6] where the reported $\varepsilon_{on/off,1H}$ of 110 for the protons of the mineral only leads to an absolute sensitivity ratio (ASR) increase of 35. Note that ASR measures the increase in signal between an optimized, non-DNP experiment and an experiment in optimized DNP conditions. This is not easily measurable for $^{43}$Ca DNP experiments (compared to $^{31}$P for example), as natural-abundance $^{43}$Ca experiments are very lengthy.

Although ASR is a better metric of DNP enhancements than $\varepsilon_{on/off,}$ its reporting was not pratical in this configuration. It extremely lengthy to measure a high-quality $^{43}$Ca NMR spectrum for natural abundance samples, as signal with microwave irradiation only surpassed the noise level with optimized acquisitions of over an hour. For bone, the situation is even more problematic, as it is impossible to prepare an equivalent non-impregnated sample (as our samples are unique and dehydrate when packed), and the $^{43}$Ca spectra with DNP enhancement were too noisy to compare to a theoretical DFS acquisition. Consequently, our comparison of the DNP enhancement efficiency in this study was based on $^{1}$H signals that could be attributed to the apatitic $OH^-$ sites of samples. Because of the overlap of the DNP matrix $^{1}$H signals with this resonance, the $\varepsilon_{on/off,1H}$ was determined using a $T_{1\rho}^{1H}$ measurement experiment.[12] In this sequence, the $T_{1\rho}^{1H}$ filter eliminates part of the fast-relaxing matrix signal. We confirmed that the $\varepsilon_{on/off,1H}$ measured using this method was representative of the $^{1}$H polarization enhancement within the sample, as it was similar to the $\varepsilon_{on/off,31P}$ measured with a CPMAS experiment, using the same probe, in a $^{1}$H-$^{31}$P configuration. Using this same $T_{1\rho}^{1H}$ filter before a saturation-recovery experiment also allowed for measurements of the $T_1$ characteristic times of the mineral component of the biological samples.

The frequencies of both channels were referenced to the $^{1}$H signal of apatitic $OH^-$ groups ($\delta_{iso}$ ($^{1}$H) = 0.0 ppm). For this, the $^{43}$Ca frequency was set on the basis of the $^{1}$H frequency, in line with IUPAC recommendations,[11] using the expression for the reference $^{43}$Ca frequency $\nu_{43Ca} = \nu_{1H} \times \Xi_{43Ca}/100\%$, with $\Xi_{43Ca}$ equal to 6.730029%. Given the unsuitability of TMS and adamantane to low-temperature experiments, we used the $^{1}$H signal of the $OH^-$ of a crystalline apatite sample (which was referenced to adamantane at close to ambient temperature). No decoupling was applied on either channel during the 1D acquisitions.

## II.2. Sample preparation

A number of preliminary experiments were carried out on model crystalline and biomimetic apatite samples. Three of these samples are common to the last chapter namely HA_CR, CHA_BM and HA_BM (see chapter III, section II.1.2). A crystalline, $^{43}$Ca enriched apatite sample[13] named HA_ENR, was also used as a reference for $^{43}$Ca sequence optimizations. Moreover, biological samples similar to those presented in chapter III (section II.2) were sent by our ANR collaborators in Toulouse. They also originated from frozen mice and corresponded to male mice's femoral cortical bones with genotype: -/- (= knock out _ KO: with $LPA_1$ deficiency). The samples used in this study are summarized in Table 1.

The sample preparation protocol was found to be core to obtaining a high $\varepsilon_{on/off,1H}$ which is an essential first step for an efficient $^{1}$H to $^{43}$Ca polarization transfer. As reported by Azaïs et *al.*,[9] the $\varepsilon_{on/off,1H}$ value for a given sample increased if it was left to rest overnight after the impregnation with the DNP juice. Therefore, the preparation of a given sample was done at least a day before experimental observations, which was left overnight on the bench.

Two different dinitroxide radicals were investigated in the course of this study: AMUPol[14] and AsymPolPOK.[15] While AMUPol has proven to be highly efficient in a wide range of situations, the phosphate groups of the AsymPolPOK radical were expected to increase water solubility and decrease the possibility of radical dimerization, and also to favor binding at the surface of bone mineral.

| Sample | Polarizing agent | Solvent | $\varepsilon_{on/off,1H}$ | $T_{1,1H}$ (sample, s) |
|---|---|---|---|---|
| **HA_ENR (60% $^{43}$Ca enr.)** | AMUPol (old) | 60/30/10 $D_8$-Gly/$D_2O$/$H_2O$ | 11 | 5.7 |
| **HA_BM** | AMUPol 20 mM | 60/30/10 $D_8$-Gly/$D_2O$/$H_2O$ | 52 | 2.4 |
| | AMUPol 10 mM | 60/30/10 $D_8$-Gly/$D_2O$/$H_2O$ | 46 | 3.3 |
| | AsymPolPOK 10 mM | 60/30/10 $D_8$-Gly/$D_2O$/$H_2O$ | 50 | 1.1 |
| **CHA_BM** | AMUPol 10 mM | 60/30/10 $D_8$-Gly/$D_2O$/$H_2O$ | 110 | 5.6 |
| | AsymPolPOK 10 mM | 60/30/10 $D_8$-Gly/$D_2O$/$H_2O$ | 49 | 1.2 |
| **HA_CR** | AMUPol 10 mM | 60/30/10 $D_8$-Gly/$D_2O$/$H_2O$ | 130 | 5.1 |
| **FCM 84 -/-** ♂ | AsymPolPOK 25 mM | 60/30/10 $D_8$-Gly/$D_2O$/$H_2O$ | 32 | 0.8 |
| **FCM 86 -/-** ♂ | AsymPolPOK 10 mM | 60/40 $D_8$-Gly/$H_2O$ | 26 | 1.1 |
| **FCM 81 -/-** ♂ | AsymPolPOK 40 mM | 60/30/10 $D_8$-Gly/$D_2O$/$H_2O$ | 32 | 1.2 |

*Table 1: Samples observed in the $^{1}$H-$^{43}$Ca DNP experiments. $\varepsilon_{on/off,1H}$ and $T_1$ were measured on the $^{1}$H apatitic $OH^-$ peak of the NMR spectra.*

The biological samples were unthawed shortly (≈ 15-30 mins) before grinding. An agate mortar and pestle were then used to crush the sample into a very fine powder. The sample was then impregnated inside the mortar with the DNP juice, and stirred into a homogeneous, slightly damp

clump. The quantity of added solvent was determined empirically, with the objective of obtaining a uniformly damp solid which does not form a paste.

## III. Results

### III.1. Preliminary experiments on $^{1}$H to $^{43}$Ca polarization transfer

The initial $^{1}$H – $^{43}$Ca CPMAS NMR experiments on the $^{43}$Ca-enriched apatite (HA_ENR) had the aim of optimizing conditions for the $^{1}$H to $^{43}$Ca polarization transfer. As in Lee et *al.* study,[6] CP was found to be the best sequence for efficient polarization transfer between the two nuclei in this sample (rather than R-INEPT or D-HMQC). The $^{1}$H 90° pulse was 3.2 µs long, corresponding to a 78 kHz radiofrequency field (50 W). We observed that the "low-power" CP conditions, corresponding to $^{43}$Ca CP powers of less than 0.1 W (Figure 4), was the most efficient condition in HA_ENR. We note that this "low-power" condition was found to be less efficient than "high-power" CP conditions in a recent study of $^{43}$Ca complexes in a frozen solution.[7] However, we could not find a more efficient high-power condition despite lengthy optimizations.

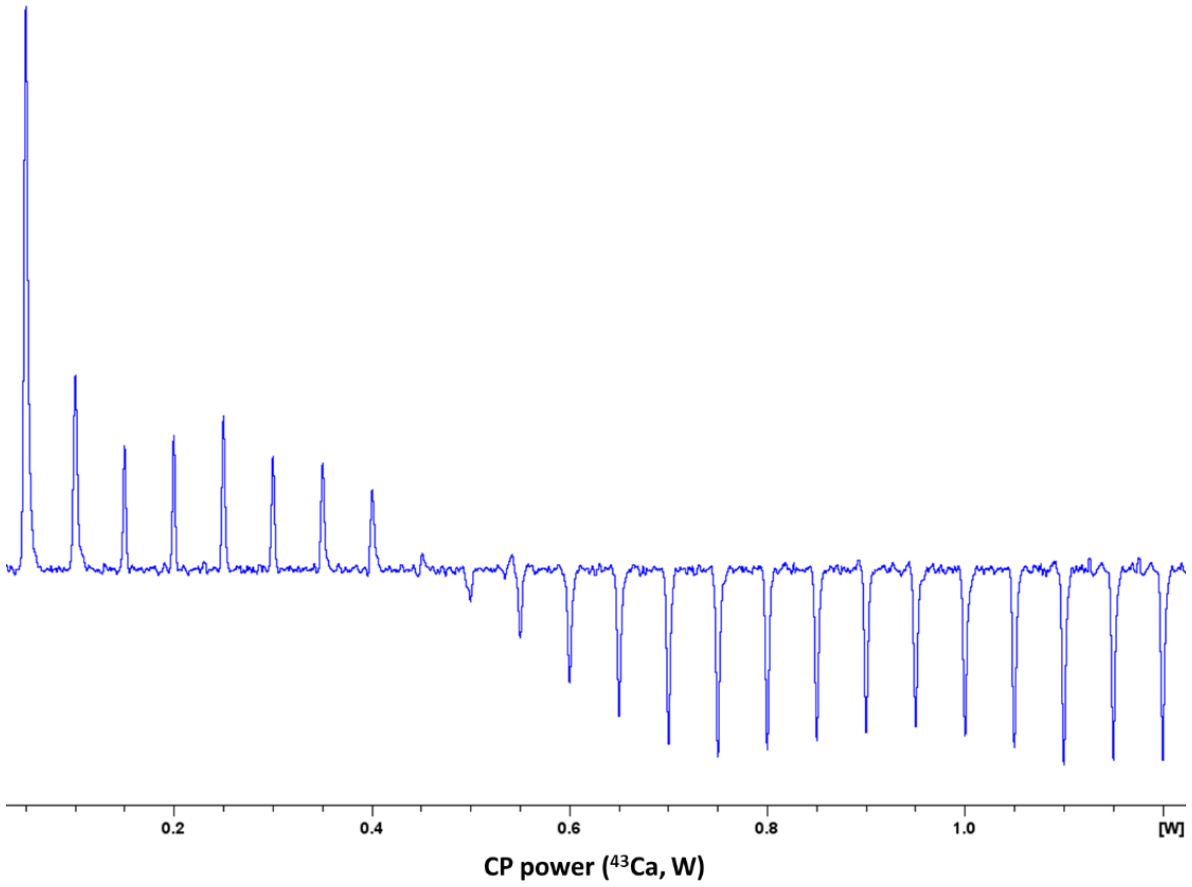


*Figure 4: $^{1}$H-$^{43}$Ca CPMAS intensities in HA_ENR as a function of the $^{43}$Ca CP power. Note the strong increase in intensity at 0.05 W. $^{1}$H: square spinlock, 1.25 W ($\omega_{rf}$ = 12.5 kHz), $\nu_r$ = 8.5 kHz, RD = 4 s, ns = 4, $t_{CP}$ = 3.0 ms. Note that optimizations of the $^{43}$Ca CP power around 0.05 W will be presented later in the manuscript (See Figure 6).*

## III.2. Experimental challenges and successive improvements

### III.2.1. CP dynamics and contact time

A first challenge was related to the choice of contact time in biological samples. Because the $^{43}$Ca acquisitions are extremely lengthy, no experimental measurement of the $^{1}$H-$^{43}$Ca CP dynamics can be realistically envisioned. Therefore, we attempted to estimate an optimal $t_{cp}$ value based on a series of assumptions.

The $^{1}$H – $^{43}$Ca dipolar coupling in apatites is small, with a "maximum" value of 0.4 kHz between $OH^-$ in the columns and the $Ca^{2+}$ sites of the crystalline structure ($d_{Ca-H}$ = 2.7 Å). This leads to a moderately long $^{1}$H-$^{43}$Ca polarization transfer, with a fitted $T_{CP}$ at 1.7 ms in HA_ENR (Figure 5). In this crystalline sample, the $T_{1\rho,CP}$ time constant of the $^{1}$H-$^{43}$Ca CPMAS experiment was measured at 11.9 ms. However, measurements of the $T_{1\rho}^{1H}$ in biological samples showed much lower values: for example, FCM81 -/- had a $T_{1\rho}^{1H}$ value of the $^{1}$H $OH^-$ resonance of only 3.5 ms. We can assume that the $T_{1\rho,CP}$ of the $^{1}$H-$^{43}$Ca CPMAS experiment is equal or lower than this value. Assuming additionally that the $T_{CP}$ rate is similar for both samples, and that $T_{1\rho,CP}$ is at most equal to $T_{1\rho}^{1H}$, we obtain the theoretical CP dynamics curve reported in Figure 5 (black squares).

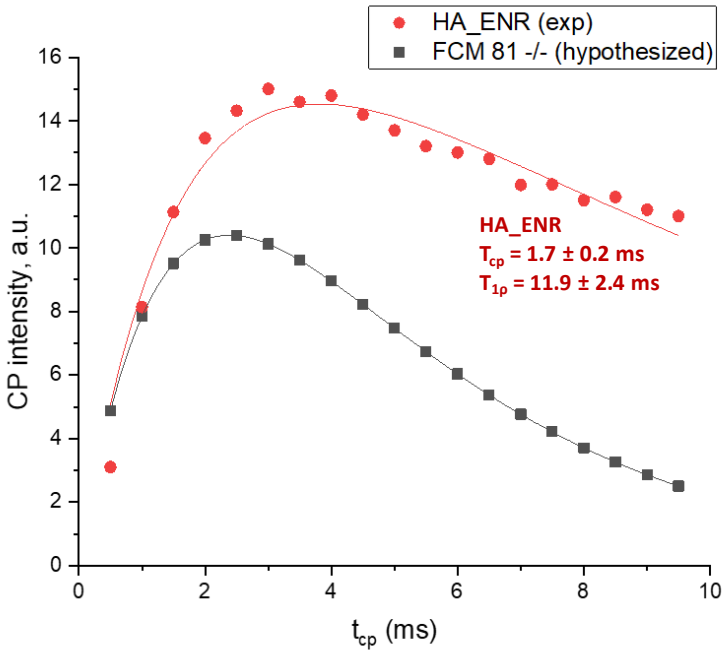


*Figure 5: Comparison between the experimental 1D CP dynamics of HA_ENR and the predicted dynamics of bone mineral. Red circles: experimental intensity of the $^{1}$H-$^{43}$Ca CPMAS spectra at various contact times. The red curve corresponds to a fit based on Eq. 4 of section I.2.1 in Chapter III, with the constants $I_0$, $T_{cp}$ and $T_{1\rho}$ optimized to match experimental data. Black squares: theoretical intensity based on Eq. 4 curve for FCM 81 -/- sample, hypothesizing a similar $T_{cp}$ rate (1.7 ms) and $I_0$, while $T_{1\rho,CP} = T_{1\rho}^{1H}(OH^-) = 3.5$ ms.*

Therefore, the long $t_{cp}$ value chosen in the Lee et *al.* study for mice molars (6 ms) may have been a factor contributing to the lack of signal.[6] Although we never achieved a sufficient signal/noise ratio in bone samples to empirically compare different contact times, we chose to primarily probe these biological samples at contact times ranging from 2.0 to 3.0 ms.

### III.2.2. Probe tuning

An issue that was encountered repeatedly in these experiments was a lack of reproducibility of the $^{1}H$-$^{43}Ca$ CPMAS experiments, either on synthetic or biological samples. Although the probe showed no apparent signs of instability, with stable tuning and matching conditions in overnight experiments, we initially found it impossible to reproduce $^{1}H$ – $^{43}Ca$ experiments across multiple days, despite reproducible $^{1}H$ spectra.

To troubleshoot this issue, we verified all CP optimizations on the HA_ENR sample, after failing to reproduce an experiment. We discovered that, although no visible detuning has occurred, the optimal $^{43}Ca$ spinlock power had changed overnight, decreasing from 0.075 W to 0.060 W (Figure 6). We then found that this optimal CP condition was unstable: successive detunings and retunings of the probe changed this optimum power, ranging from 0.085 W to 0.050 W.

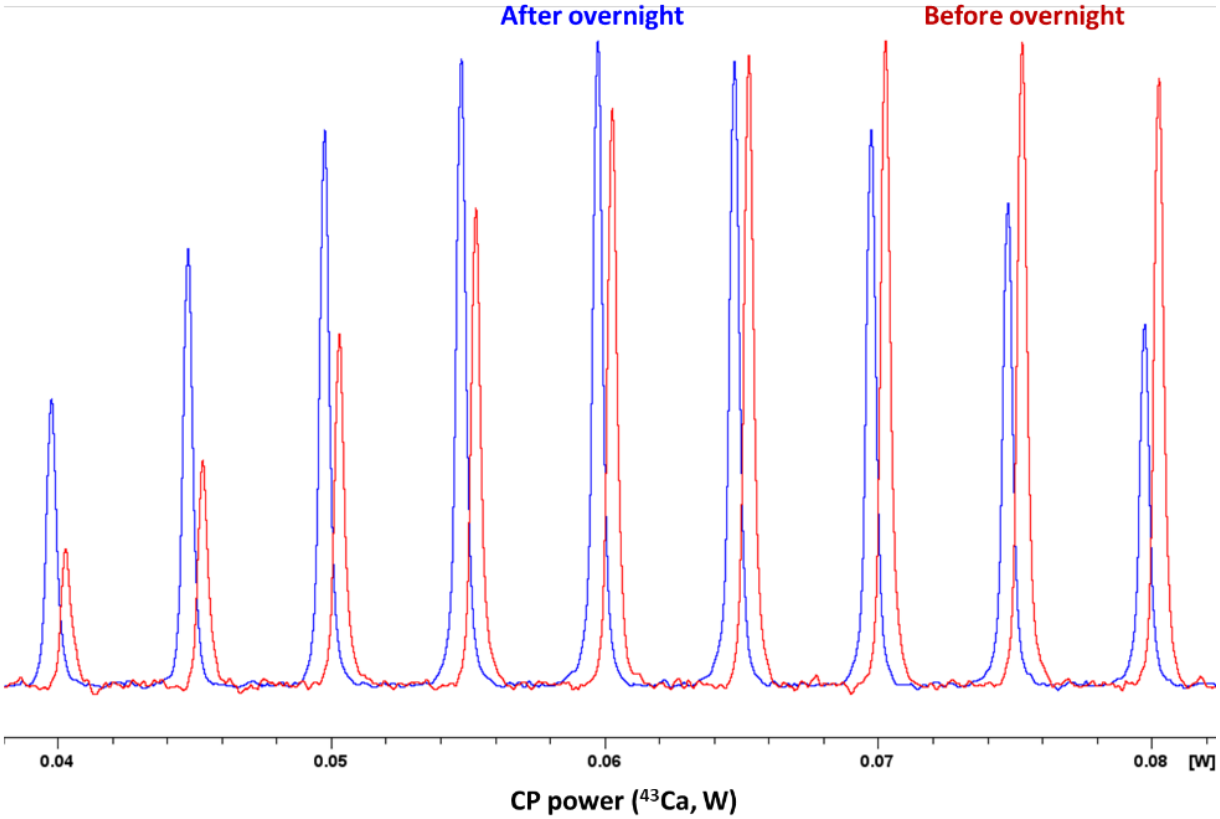


*Figure 6: Optimizations of the $^{43}Ca$ CP power on HA_ENR, before (red) and after (blue) an overnight experiment. Note the large difference in optimal power level between the two experiments.*

No such instability was observed for higher power pulses, but instabilities in the response of the preamplifier at these extremely low powers was problematic. This could be caused by small deviations in probe tuning, not visible on the TopSpin tuning utility, given the sensitivity of the CP powers to detuning and retuning.

This difficulty was solved in two steps. First, the indicated power of the preamplifier was artificially increased by adding a 20 dB attenuator at the back of the Y-channel. This lowers the power output of the channel 100-fold. As a result, the indicated power of the Y-channel is increased from 0.05-0.08 W to 5-8 W. This avoids setting the preamplifier to extremely low powers. In addition, the tuning of the $^{1}$H channel was made more precise by the use of oscilloscope measurements of the outgoing and reflected powers. To this end, a bidirectional coupler was installed on the $^{1}$H output of the preamplifier, which allowed for precise measurements of the reflected powers (Figure 7). The outgoing power was measured through a 20 dB attenuator, to avoid damage to the oscilloscope. Through minute changes to the tuning rods, a reflected intensity below 1% of the outgoing intensity could be achieved.

These two improvements together were found to greatly increase the reproducibility of these low-power experiments. No fluctuation of the optimum CP powers was observed after these solutions were implemented, and $^{1}$H – $^{43}$Ca CPMAS spectra were successfully reproduced. The optimized CP parameters were: a 1.0 W 90.100 ramped CP pulse on $^{1}$H, a 0.05 W CP pulse on $^{43}$Ca (with the preamplifier outputting 5 W due to the attenuator), with contact times of 2.0 ms.

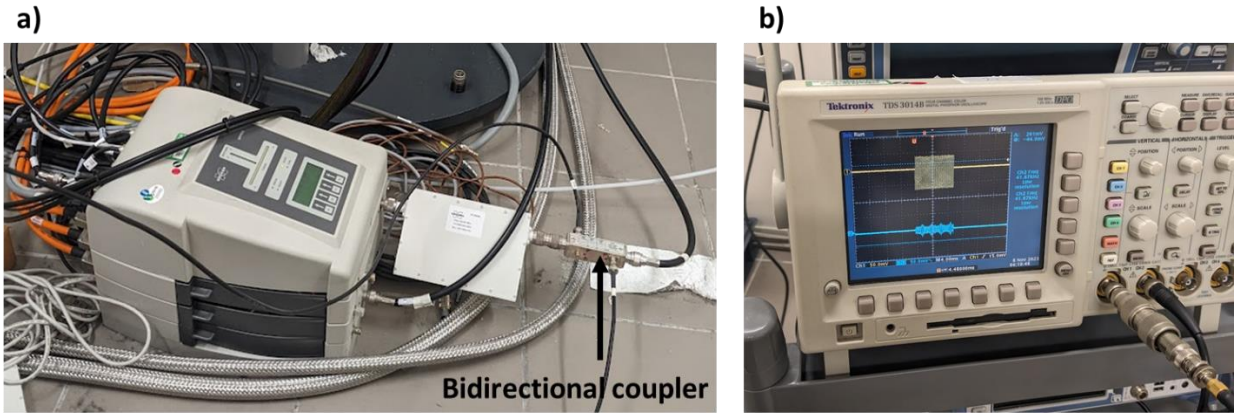


*Figure 7: a) Bidirectional coupler added to the $^{1}$H channel, connected to b) an oscilloscope, measuring the outgoing (yellow) and reflected (blue) signals. Here, the reflected power is approximately 1/500$^{th}$ of the outgoing power, indicating a very good tuning and matching of the $^{1}$H channel.*

Another important parameter when using this CP condition is the $^{43}$Ca irradiation frequency. Because of the extremely weak radiofrequency fields of the $^{43}$Ca CP pulse, the irradiation of the $^{43}$Ca spectrum is made significantly weaker. This was seen experimentally in the high dependance of the CP signal on the carrier frequency (Figure 8). Therefore, precisely tuning the carrier frequency can lead to an important increase in signal. Consequently, for optimized experiments

on bone samples, we chose to irradiate the samples with a $^{43}$Ca frequency of -120 Hz, which corresponds to the maximum of a $^{43}$Ca bone spectrum at this field.

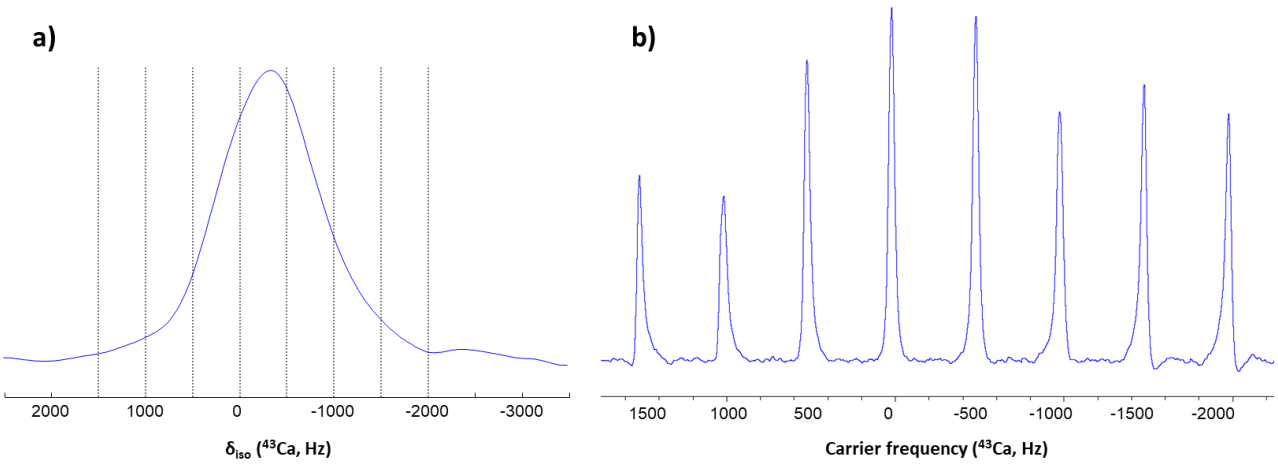


*Figure 8: a) $^{1}$H-$^{43}$Ca CPMAS spectra of HA_ENR. The vertical graduations divide the spectrum in 500 Hz increments. b). Variable-offset CP experiment with the carrier frequency incremented from 1500 to -2000 Hz by -500 Hz steps.*

## III.3. DNP-enhanced $^{1}$H-$^{43}$Ca NMR experiments

### III.3.1. Synthetic apatites

In these optimized conditions, it was possible to acquire a $^{1}$H – $^{43}$Ca CPMAS spectrum at natural abundance in 1 h for all synthetic samples. However, we found that the signal/noise ratio was significantly different between HA_BM and CHA_BM samples, when observed in similar experimental conditions (Figure 9). Despite extremely similar DNP enhancements, and $T_1$ rates, the CHA_BM sample exhibits a much lower signal level than the HA_BM sample. This is despite the fact that CHA_BM had a higher mass of sample in the rotor. Note that this comparison held true for all HA_BM and CHA_BM samples, with the calcium signal in CHA_BM being consistently much weaker than for its counterpart.

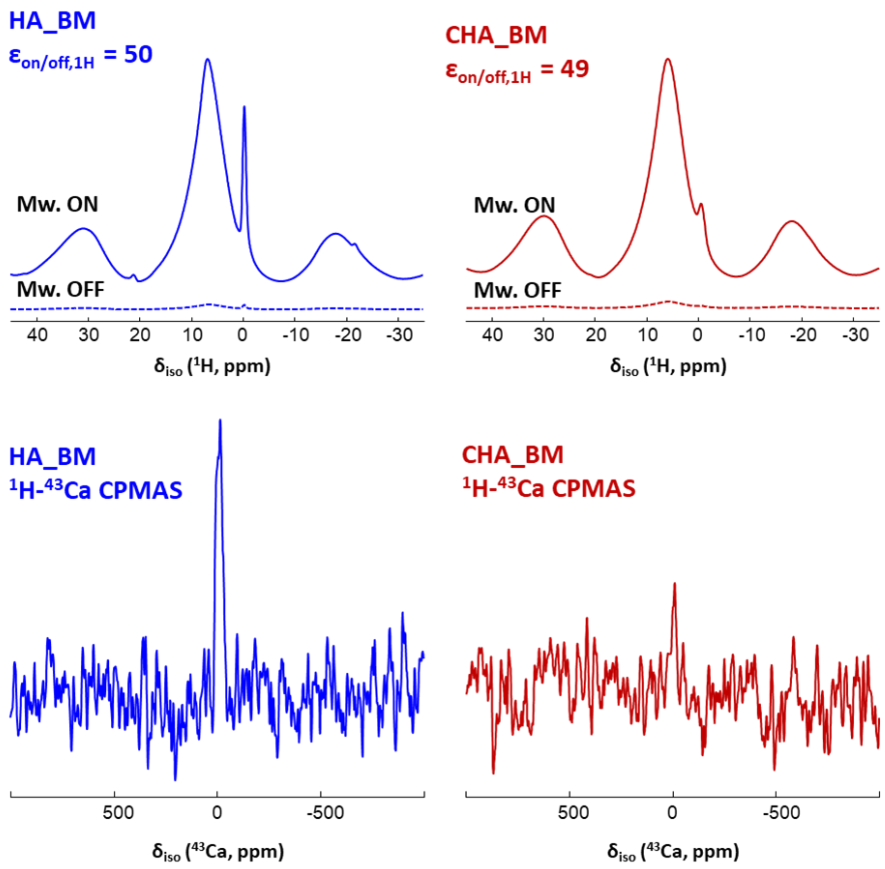


*Figure 9: Top : $^{1}H$ direct acquisitions of HA_BM and CHA_BM, with microwave irradiation switched on and off. Bottom = $^{1}H - ^{43}Ca$ CPMAS spectra of HA_BM and CHA_BM in comparable conditions, hyperpolarized with 10 mM AsymPolPOK in 60/30/10 $D_8$-Gly/$D_2O$/$H_2O$. RD = 1.5 s, ns = 2000, $t_{exp}$ = 1 h, $t_{cp}$ = 2.0 ms, $v_r$ = 8.5 kHz. $m_{HA\_BM}$ = 37 mg, $m_{CHA\_BM}$ = 45 mg.*

The choice of AsymPolPOK over AMUPol as a radical was made on the basis of the measured $\varepsilon_{on/off,1H}$ on biomimetic synthetic samples (Figure 10). For CHA_BM, although the difference in $^{43}Ca$ signal was not easely comparable for both radicals due to the extremely poor signal/noise ratio, the lower $\varepsilon_{on/off,1H}$ of AsymPolPOK versus AMUPol was compensated by a shorter $T_1$. However, because of the poor efficiency of AMUPol for HA_BM (similar $\varepsilon_{on/off,1H}$ but longer $T_1$), AsymPolPOK was deemed the better choice for the study of bone samples. Note, that in similar conditions, HA_BM and CHA_BM showed a lower signal/noise ratio than HA_CR and the sintered CHA_Ncomm.[6]

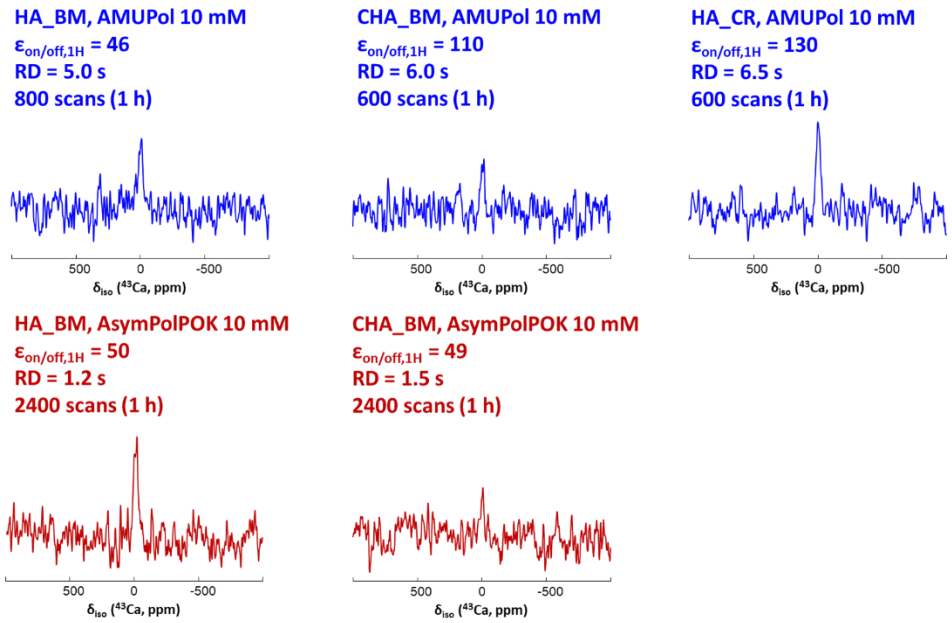


*Figure 10: $^{1}H - ^{43}Ca$ CPMAS spectra of HA_BM and CHA_BM using two different radicals: AMUPol 10 mM and AsymPolPOK 10 mM. $t_{cp}$ (CHA_BM) = 2.0 ms, $t_{cp}$ (HA_BM) = 4.0 ms. $^{1}H - ^{43}Ca$ CPMAS spectrum of HA_CR using AMUPol 10 mM with $t_{cp}$ = 4.0 ms is also shown for comparison.*

Note that the reasonable acquisition time for $^{1}H - ^{43}Ca$ CPMAS spectrum of HA_BM allowed to test a 2D $^{1}H$-$^{43}Ca$ CP-HETCOR experiment (Figure 11). This acquisition was very short in the F1 dimension, with only 16 slices recorded. As a result, the $^{1}H$ dimension is not resolved enough to discriminate different signals, but the wide $^{1}H$ contribution appears to be centred slightly above 0 ppm.

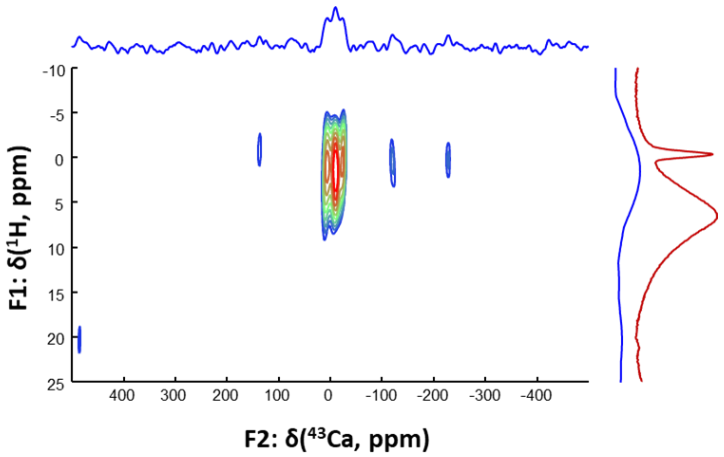


*Figure 11 : 2D $^{1}H$-$^{43}Ca$ CP-HETCOR spectrum of HA_BM, hyperpolarized with 10 mM AsymPokPOK in 60/30/10 $D_8$-Gly/$D_2O$/$H_2O$. RD = 1.5 s, ns = 2000, $t_{exp}$ = 1 h, $t_{cp}$ = 2.0 ms, $\nu_r$ = 10.0 kHz. $m_{HA\_BM}$ = 37 mg 16 increments were recorded in the indirect dimension with 3584 scans per increment. RD = 1s, $t_{exp}$ = 18 h. The blue spectra correspond to skyline projections of the 2D spectrum, whereas the red spectrum is a direct acquisition spectrum of the sample (with microwave irradiation)*

### III.3.2. Biological samples

Thanks to successive improvements, we managed to bring down the time required to acquire a natural-abundance $^{43}$Ca signal in all three synthetic samples to 1 h. For biological samples, however, the signal obtained in a few hours remained extremely weak. In these optimized conditions for biomimetic samples, the best signal was obtained for FCM 81 -/-, slightly above the noise level in 7 h (Figure 12, b). The signal of FCM 84 -/- was even weaker, with a signal at the noise level after 17 h of acquisition (Figure 12, c). The other samples gave even weaker (or undetectable) signal. As a result, $^{1}$H-$^{43}$Ca CPMAS spectra under DNP conditions could not be acquired significantly faster than a natural-abundance direct acquisition on a large rotor.[1,2] Moreover, its signal/noise ratio was much too low to consider acquiring $^{1}$H – $^{43}$Ca 2D correlation experiments.

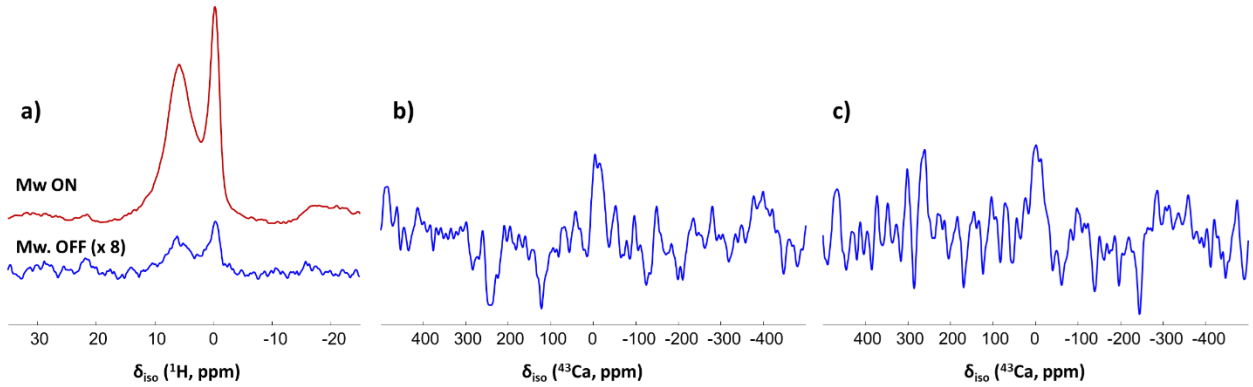


*Figure 12: a) $^{1}$H MAS spectra of of FCM 81 -/- through a 0.5 ms $T_{1\rho}$ filter, with microwave irradiation on (red) and off (blue). The $\varepsilon_{on/off,1H}$ is measured at 32. b) $^{1}$H-$^{43}$Ca CPMAS spectrum of FCM 81 -/-, acquired in 7 h, hyperpolarized with 40 mM AsymPolPOK in 60/30/10 $D_8$-Gly/$D_2O$/$H_2O$. $t_{cp}$ = 3.0 ms, ns = 20000, RD = 1.2 ms. c) $^{1}$H-$^{43}$Ca CPMAS spectrum of FCM 84 -/-, acquired in 17 h, hyperpolarized with 25 mM AsymPolPOK in 60/30/10 $D_8$-Gly/$D_2O$/$H_2O$. $t_{cp}$ = 3.0 ms, ns = 51400, RD = 1.2 ms.*

### III.3.3. Discussion

For apatitic samples, the signal/noise ratio of the previously published 2D $^{1}$H-$^{43}$Ca CP-HETCOR experiment[6] could not be reproduced. Note that the probe in this contribution is different to the probe of the original study due to technical difficulties.

Moreover, a number of factors could also explain this reduced signal. First, the biomimetic apatitic samples of this contribution are different as shown by their respective XRD signatures (Figure 13). HA_CR and CHAp_Ncomm samples show narrower diffraction peaks, indicating either larger coherence domains and/or lower degree of chemical disorder. This is consistent with the highest signal/noise ratio observed for HA_CR compared to all biomimetic samples. Moreover, HA_CR and CHAp_Ncomm samples do not exhibit a hydrated surface as biomimetic apatites. This could also explain the lack of signal observed for teeth in the initial study (Figure 3) and the lower $\varepsilon_{on/off,1H}$ (~ 30) obtained for the biological samples in this manuscript (which remain

comparable to other studies of bone *via* DNP-NMR,[9] but with shorter transverse relaxation delays due to the choice of radical).

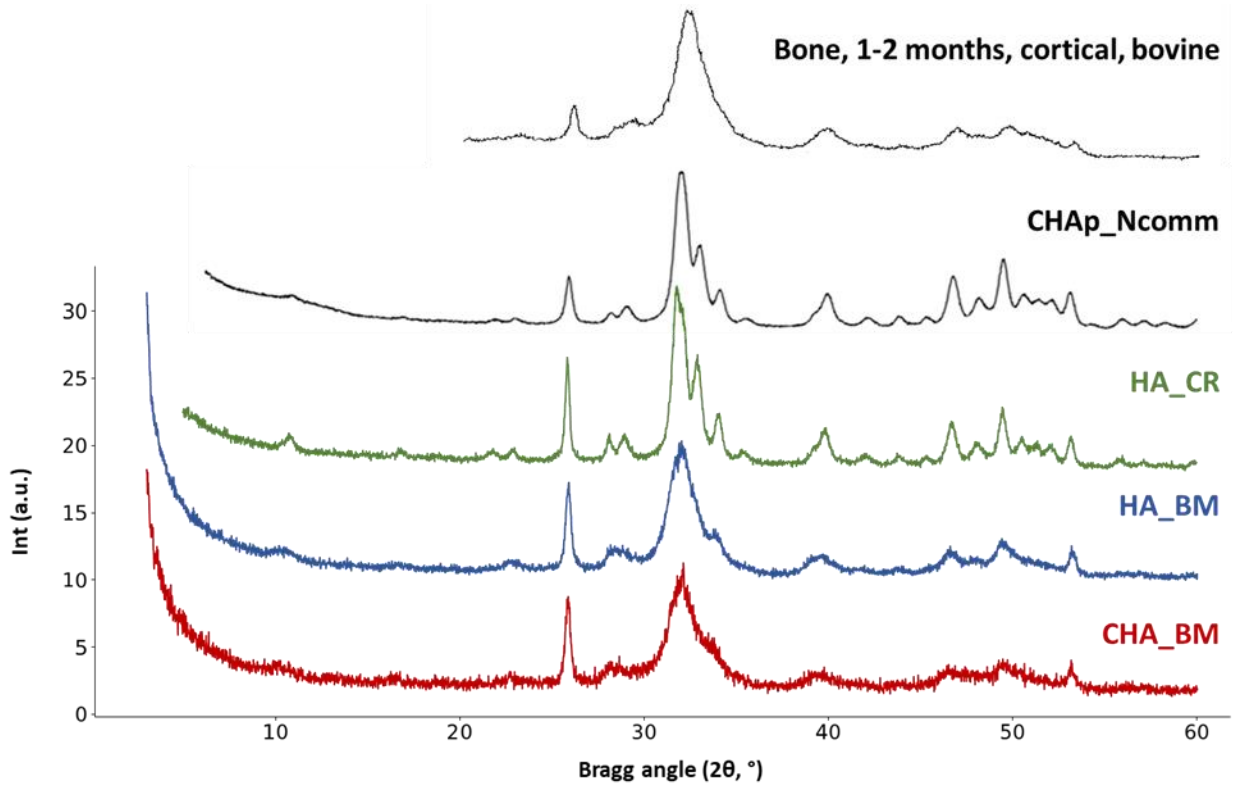


*Figure 13: XRD diffraction patterns for all three synthetic samples of this study, the CHAp_Ncomm from Lee et al.[6], and a typical bone pattern, reproduced from Kuhn* et al.[16]

While $\varepsilon_{on/off,1H}$ may be improved by a finely tuned choice of radical concentration and matrix, it does not explain alone the differences in $^{43}$Ca signal/noise ratios. Although the presence of the organic phase and $Ca^{2+}$ vacancies decreases the fraction of calcium in bones, this may also indicate an inherently lower efficiency of the $^{1}$H to $^{43}$Ca polarization transfer. Interestingly, while DNP-enhanced $^{1}$H-$^{31}$P CPMAS spectra of OCP were obtained with a very good signal/noise ratio (see Chapter II), several attempts to record $^{1}$H-$^{43}$Ca CPMAS (but also D-HMQC and R-INEPT) spectra remained unsuccessful, even on the $^{43}$Ca-enriched samples. This suggests that dynamical effects could also be in cause.

## IV. Perspectives

This study underlines the significant challenge that is still posed by DNP-enhanced $^{1}H$ – $^{43}Ca$ CPMAS NMR at natural abundance in biological materials. Even with a significantly hyperpolarized proton, the poor efficiency of the transfer and the difficulties inherent to the observation of an insensitive spin 7/2 nucleus complicates the study. Unfortunately, we can propose no obvious solution to improve the poor efficiency of these polarization transfers in bone samples. Determining exactly which factor is primarily responsible for the lower signal of CHA_BM could give us some direction. Finding an efficient high-power CP condition, although it has not yet worked with this probe configuration, may also still be a possibility. Otherwise, the development of extremely low temperature DNP could serve to push the sensitivity of the experiment even further.[17,18]

## V. References


(1) Laurencin, D.; Wong, A.; Chrzanowski, W.; Knowles, J. C.; Qiu, D.; Pickup, D. M.; Newport, R. J.; Gan, Z.; Duer, M. J.; Smith, M. E. Probing the Calcium and Sodium Local Environment in Bones and Teeth Using Multinuclear Solid State NMR and X-Ray Absorption Spectroscopy. *Phys. Chem. Chem. Phys.* **2010**, *12* (5), 1081–1091. https://doi.org/10.1039/B915708E.

(2) Xu, J.; Zhu, P.; Gan, Z.; Sahar, N.; Tecklenburg, M.; Morris, M. D.; Kohn, D. H.; Ramamoorthy, A. Natural-Abundance $^{43}$Ca Solid-State NMR Spectroscopy of Bone. *J. Am. Chem. Soc.* **2010**, *132* (33), 11504–11509. https://doi.org/10.1021/ja101961x.

(3) Michaelis, V. K.; Markhasin, E.; Daviso, E.; Herzfeld, J.; Griffin, R. G. Dynamic Nuclear Polarization of Oxygen-17. *J. Phys. Chem. Lett.* **2012**, *3* (15), 2030–2034. https://doi.org/10.1021/jz300742w.

(4) Perras, F. A.; Kobayashi, T.; Pruski, M. Natural Abundance 17O DNP Two-Dimensional and Surface-Enhanced NMR Spectroscopy. *J. Am. Chem. Soc.* **2015**, *137* (26), 8336–8339. https://doi.org/10.1021/jacs.5b03905.

(5) Perras, F. A.; Chaudhary, U.; Slowing, I. I.; Pruski, M. Probing Surface Hydrogen Bonding and Dynamics by Natural Abundance, Multidimensional, $^{17}$O DNP-NMR Spectroscopy. *J. Phys. Chem. C* **2016**, *120* (21), 11535–11544. https://doi.org/10.1021/acs.jpcc.6b02579.

(6) Lee, D.; Leroy, C.; Crevant, C.; Bonhomme-Coury, L.; Babonneau, F.; Laurencin, D.; Bonhomme, C.; De Paëpe, G. Interfacial Ca2+ Environments in Nanocrystalline Apatites Revealed by Dynamic Nuclear Polarization Enhanced $^{43}$Ca NMR Spectroscopy. *Nat Commun* **2017**, *8* (1), 14104. https://doi.org/10.1038/ncomms14104.

(7) Georges, T.; Chèvre, R.; Cousin, S. F.; Gervais, C.; Thureau, P.; Mollica, G.; Azaïs, T. 43Ca MAS-DNP NMR of Frozen Solutions for the Investigation of Calcium Ion Complexation. *ACS Omega* **2024**, *9* (4), 4881–4891. https://doi.org/10.1021/acsomega.3c08292.

(8) Goldberga, I.; Li, R.; Chow, W. Y.; Reid, D. G.; Bashtanova, U.; Rajan, R.; Puszkarska, A.; Oschkinat, H.; Duer, M. J. Detection of Nucleic Acids and Other Low Abundance Components in Native Bone and Osteosarcoma Extracellular Matrix by Isotope Enrichment and DNP-Enhanced NMR. *RSC Adv.* **2019**, *9* (46), 26686–26690. https://doi.org/10.1039/C9RA03198G.

(9) Azaïs, T.; Von Euw, S.; Ajili, W.; Auzoux-Bordenave, S.; Bertani, P.; Gajan, D.; Emsley, L.; Nassif, N.; Lesage, A. Structural Description of Surfaces and Interfaces in Biominerals by DNP SENS. *Solid State Nuclear Magnetic Resonance* **2019**, *102*, 2–11. https://doi.org/10.1016/j.ssnmr.2019.06.001.

(10) Lee, D.; Hediger, S.; De Paëpe, G. Is Solid-State NMR *Enhanced* by Dynamic Nuclear Polarization? *Solid State Nuclear Magnetic Resonance* **2015**, *66–67*, 6–20. https://doi.org/10.1016/j.ssnmr.2015.01.003.

(11) Kolodziejski, W.; Klinowski, J. Kinetics of Cross-Polarization in Solid-State NMR: A Guide for Chemists. *Chemical Reviews* **2002**, *102* (3), 613–628. https://doi.org/10.1021/cr000060n.

(12) Harris, R. K.; Becker, E. D.; Cabral de Menezes, S. M.; Goodfellow, R.; Granger, P. NMR Nomenclature: Nuclear Spin Properties and Conventions for Chemical Shifts: IUPAC

Recommendations 2001. *Solid State Nuclear Magnetic Resonance* **2002**, *22* (4), 458–483. https://doi.org/10.1006/snmr.2002.0063.
(13) Wong, A.; Laurencin, D.; Dupree, R.; Smith, M. E. Two-Dimensional 43Ca–1H Correlation Solid-State NMR Spectroscopy. *Solid State Nuclear Magnetic Resonance* **2009**, *35* (1), 32–36. https://doi.org/10.1016/j.ssnmr.2008.11.002.
(14) Sauvée, C.; Rosay, M.; Casano, G.; Aussenac, F.; Weber, R. T.; Ouari, O.; Tordo, P. Highly Efficient, Water-Soluble Polarizing Agents for Dynamic Nuclear Polarization at High Frequency. *Angewandte Chemie International Edition* **2013**, *52* (41), 10858–10861. https://doi.org/10.1002/anie.201304657.
(15) Mentink-Vigier, F.; Marin-Montesinos, I.; Jagtap, A. P.; Halbritter, T.; van Tol, J.; Hediger, S.; Lee, D.; Sigurdsson, S. Th.; De Paëpe, G. Computationally Assisted Design of Polarizing Agents for Dynamic Nuclear Polarization Enhanced NMR: The AsymPol Family. *J. Am. Chem. Soc.* **2018**, *140* (35), 11013–11019. https://doi.org/10.1021/jacs.8b04911.
(16) Kuhn, L.; Grynpas, M.; Rey, C.; Wu, Y.; Ackerman, J.; Glimcher, M. A Comparison of the Physical and Chemical Differences Between Cancellous and Cortical Bovine Bone Mineral at Two Ages. *Calcif. Tissue Int.* **2008**, *83*, 146–154. https://doi.org/10.1007/s00223-008-9164-z.
(17) Bouleau, E.; Saint-Bonnet, P.; Mentink-Vigier, F.; Takahashi, H.; Jacquot, J.-F.; Bardet, M.; Aussenac, F.; Purea, A.; Engelke, F.; Hediger, S.; Lee, D.; Paëpe, G. D. Pushing NMR Sensitivity Limits Using Dynamic Nuclear Polarization with Closed-Loop Cryogenic Helium Sample Spinning. *Chemical Science* **2015**, *6* (12), 6806–6812. https://doi.org/10.1039/C5SC02819A.
(18) Matsuki, Y.; Ueda, K.; Idehara, T.; Ikeda, R.; Ogawa, I.; Nakamura, S.; Toda, M.; Anai, T.; Fujiwara, T. Helium-Cooling and -Spinning Dynamic Nuclear Polarization for Sensitivity-Enhanced Solid-State NMR at 14 T and 30 K. *Journal of Magnetic Resonance* **2012**, *225*, 1–9. https://doi.org/10.1016/j.jmr.2012.09.008.

## Conclusion

Over the course of this study, solid state NMR was shown to be a powerful tool for the analysis of complex and disordered systems based on calcium phosphates. However, the results can prove resistant to simple answers and interpretations.

First, OCP's structure complexity was revealed by discrepancies observed between experimental NMR data and DFT calculations. Moreover, the appearance of new resonances in the $^{31}$P NMR spectra recorded at low temperature have led us to a comprehensive study based on the multinuclear $^{1}$H, $^{17}$O, $^{31}$P and $^{43}$Ca NMR spectra of OCP at low and high temperatures, and molecular dynamics simulations. Thanks to MD, we were able to prove the existence of dynamical effects in OCP at ambient temperature. Nonetheless, averaging NMR parameters over the MD did not allow the full interpretation of NMR signals. At low temperature, the number of resolved $^{31}$P sites appeared larger than the number of sites in the crystallographic cell, suggesting the presence of surface effects or of an even lower symmetry. As a result, we were not able to assign unambiguously all observed $^{31}$P sites with confidence, and two tentative assignments were proposed. This study shows the difficulties in calculating NMR parameters in disordered or mobile systems, such as hydrates. However, it also shows the power of variable-temperature NMR in highlighting dynamical effects in solids.

Second, in chapter III, we proposed a new NMR methodology for the comparative analysis of bone mineral of normal and $LPA_1$ deficient mice. For this purpose, we built our own method for the analysis of variable-$t_{cp}$ $^{1}$H-$^{31}$P CP-HETCOR spectra. This allowed for the processing of the data to be heavily automated, leading to faster and more in-depth comparisons between the samples. Using the theory of cross-polarization dynamics revealed some unexpected complexity: the I-S model for magnetization transfer from $^{1}$H to $^{31}$P through cross-polarization did not offer a reliable absolute quantification in the case of OCP, possibly due to dynamical effects. Nonetheless, extracting CP buildup parameters from the variable-$t_{cp}$ 2D fit of CP-HETCOR spectra of $OH^{-}$ ⋯ $PO_4^{3-}$, $H_2O$ ⋯ $(H)PO_4^{(2)3-}$ and $HPO_4^{2-}$ sites of biomimetic apatites and bone samples provided interesting results. First, the quantifications obtained for the different bone samples of the study were notably consistent, even if this result has to be considered with cautious since the validity of the underlying hypotheses of the I-S model on these systems is still questionable. Comparing the two groups (normal and $LPA_1$ deficient) against one another yielded no significant difference between the bone mineral components of +/+ and -/- mice. From the perspective of these $^{1}$H-$^{31}$P 2D NMR analyses, the bone minerals are therefore comparable in the two cases, down to an error margin of *ca.* 10% of the reported values. This expands on previous ATR-IR studies on these samples, concluding that the difference in bone quality reflected differing levels of porosity inside of the bone, rather than a different chemical composition of the mineralized tissue.

In addition, this study showed that a series of CP-HETCOR spectra at variable $t_{cp}$ could not be fitted with the same three frozen peaks at all contact times. $H_2O$ ⋯ $(H)PO_4^{(2)3-}$ and $HPO_4^{2-}$ peaks in particular, show a significative evolution of $\delta_{iso}(^{31}P)$ and $FWHM(^{31}P)$ with contact time, suggesting overlapping peaks with dissimilar CP dynamics, both in biomimetic apatites and bone samples. Consequently, two new fitting methods were developed to analyze these spectra.

A "point by point" method applied to 2D HETCOR acquired at higher magnetic field allowed to distinguish components of the signals with contrasting CP dynamics, in highly convoluted spectra. The strength of this method was that it allows us to visualize differences in dynamics in different areas of the spectrum without any initial assumption about its underlying components. A "3D fitting" method was used to confirm these findings. This suggested the existence of underlying signals in line with other studies showing that biomimetic apatites and bone mineral have at least two distinct sets of $H_2O$ and $HPO_4^{2-}$ signals: one originating from the disordered shell and the other from apatitic sites. Going further could require a systemic comparison of a wide range of samples. Yet, this first study of the 2D $^{1}H$-$^{31}P$ CP-HETCOR signal of apatitic calcium phosphates showed the value of the new methodology for the analysis of these data, and opens the way for a detailed decomposition of the NMR signals of bone.

Finally, thanks to successive improvements in the experimental set-up and acquisition conditions, natural-abundance $^{43}Ca$ NMR signal of synthetic apatites could be recorded in about one hour thanks to DNP enhancement. For biological samples, however, the signal obtained in a few hours remained weak and was therefore not sufficient to consider acquiring $^{1}H$ – $^{43}Ca$ 2D correlation experiments. Although the presence of the organic phase and $Ca^{2+}$ vacancies decreases the fraction of calcium in bones, this may also indicate an inherently lower efficiency of the $^{1}H$ to $^{43}Ca$ polarization transfer in the biological samples. A perspective could be the development of extremely low temperature DNP to push the enhancement further.

In conclusion, there are many avenues that could be explored to increase our understanding of biominerals and bone mineral. In addition to attempts to push further the limits of sensitivity (using $^{17}O$- and $^{43}Ca$-enriched samples or DNP-enhanced experiments) and resolution (using very high field spectrometers), there are also important aspects of bone mineral that can be studied at natural abundance using relatively low field instrumentation. The latter can benefit from the methodological developments presented in this manuscript. We hope that their application in future analyses can bring a better understanding of the structure of bone mineral and its link to bone health.